POLYMER/CERAMIC WIRELESS MEMS PRESSURE SENSORS FOR HARSH ENVIRONMENTS: HIGH TEMPERATURE AND BIOMEDICAL APPLICATIONS

A Dissertation
Presented to
The Academic Faculty

by

Michael A. Fonseca

In Partial Fulfillment
of the Requirements for the Degree
Doctor of Philosophy in the
School of Electrical and Computer Engineering

Georgia Institute of Technology
December 2007

POLYMER/CERAMIC WIRELESS MEMS PRESSURE SENSORS FOR HARSH ENVIRONMENTS: HIGH TEMPERATURE AND BIOMEDICAL APPLICATIONS

Approved by:

Dr. Mark G. Allen, Advisor
School of Electrical and Computer Engineering
Georgia Institute of Technology

Dr. Robert J. Butera
School of Electrical and Computer Engineering
Georgia Institute of Technology

Dr. Oliver Brand, Co-Advisor
School of Electrical and Computer Engineering
Georgia Institute of Technology

Dr. Gregory D. Durgin
School of Electrical and Computer Engineering
Georgia Institute of Technology

Dr. Elliot Chaikof
The Wallace H. Coulter Department of Biomedical Engineering
Georgia Institute of Technology and Emory University

Dr. Andrew F. Peterson
School of Electrical and Computer Engineering
Georgia Institute of Technology

Date Approved: November 7, 2007

Dedicated

To my parents and sisters for all their support and guidance throughout my life.

And to Amy, my soul-mate, friend, and wife.

ACKNOWLEDGEMENTS

First and foremost, I would like to express my sincere gratitude to my advisor Mark Allen. Dr. Allen allowed me to join his group first as an undergraduate as part of the Summer Undergraduate Research Program (SURE) directed by Dr. Gary May where Dr. Jennifer English and Dr. Martin Von Arx gave me leadership. Then, as a graduate student in Dr. Allen's group, I had the opportunity to mentor two undergraduates from SURE, Jacqueline A. Fairley and Claudio I. Estvez, who are now graduate students at the Georgia Institute of Technology. Additionally, while performing my research in wireless pressure sensors, Dr. Allen gave me the opportunity to join CardioMEMS, Inc, a medical device company, when it was just a start-up. I thank Dr. Allen for his leadership, direction, and opportunities, which allowed me to learn and grow as a scholar and in life. I thank my co-advisor Oliver Brand. Dr. Brand gave me the additional motivation needed to complete my graduate work. Dr. Brand's guidance and leadership in the completion of my dissertation process was invaluable. I sincerely thank Dr. Robert Butera, Dr. Gregory During, Dr. Elliot Chaikof, and Dr. Andrew Peterson for being members of thesis committee.

I would like to gratefully acknowledge Dr. Jay Yadav and Dr. Takao Ohki for their valuable technical input and assistance on abdominal aortic aneurysms and biomedical applications. I gratefully acknowledge the CardioMEMS staff, especially David Stern for his support during the development of wireless pressure sensors for biomedical applications. A special thanks to Jason Kroh and Jason White for their invaluable technical insight on wireless telemetry and catheter deliverability. I sincerely acknowledge Sandeep Yadav and Angad Singh for their continual support while working for CardioMEMS and pursuing my Ph.D. degree.

I would like to thank the members of the Microsensors and Microactuators (MSMA) group at the Georgia Institute of Technology for their support, advice, and friendship.

They introduced me to the nuances of our graduate student group and made graduate school enjoyable. A special thanks Dr. Martin Von Arx for helping me early on in my graduate career for his guidance and support. I would like to thank Dr. Jennifer English for her assistance in learning about wireless pressure sensors for high temperatures. I would also like thank Richard Shafer for all his valuable technical discussion and assistance with fabrication equipment. I would like to thank Benjamin King and Rubayeth Kamal for their assistance in fabrication and characterization of polymer-based sensors.

I would like to sincerely acknowledge the members of the Silicon-Based Microsystems group lead by Dr. Oliver Brand for their support during the completion of my graduate career as well as for welcoming me into the group. They gave me the motivation needed to finish my dissertation.

I would like to thank my loving wife Amy for her support throughout my graduate career, especially since our daughter Isabella was born. She has patiently supported me while working full time and pursuing my Ph.D. work. I thank my daughter for giving me boundless energy and then quickly absorbing it back. She has given me the joy only a parent knows. Finally, I would like to thank my parents and sisters for always giving me the love and support needed to accomplish my goals.

TABLE OF CONTENTS

APPENDICES

LIST OF TABLES

LIST OF FIGURES

LIST OF SYMBOLS OR ABBREVIATIONS

Abbreviations

951 AT	DuPont™ Microcircuit Materials, LTCC.
6160 Ag	DuPont™ cofireable conductor for 951 Green Tape™ system.
6142D Ag	DuPont™ cofireable conductor for 951 Green Tape™ system.
9141 Pt	DuPont™ cofireable conductor for alumina Green Tape™ system.
AAA	Abdominal Aortic Aneurysm.
AMD	Arithmetic Mean Distance.
AMSD	Arithmetic Mean Square Distance.
BJT	Bipolar Junction Transistor.
CHC	Ceramic Hermetic Chamber.
CMOS	Complementary Metal Oxide Semiconductor.
CT	Computed Tomography.
CTE	Coefficient of Thermal Expansion.
DC	Direct Current.
DI	Deionized water.
EMI	Electromagnetic Interference.
EVAR	Endovascular repair.
FDA	Food and Drug Administration.
FEA	Finite Element Analysis.
FEP	Fluorinated Ethylene Propylene.
flex-circuit	flexible-circuit-board.
GMD	Geometric Mean Distance.
HTCC	High-Temperature Co-fireable Ceramics.
IACUC	Institutional Animal Care and Use Committee.
IC	Integrated Circuits.

ID	Inner Diameter.
IOP	Intraocular Pressure.
IR	Infrared.
LCP	Liquid Crystal Polymer.
LTCC	Low-Temperature Co-fireable Ceramics.
MEMS	Micro Electromechanical Systems.
uEDM	Micro Electro Discharge Machining.
MRA	Magnetic Resonance Angiography.
OD	Outer Diameter.
PCB	Printed Circuit Board.
PolySi	PolySilicon.
ppr	Points per rotation.
PTFE	Polytetrafluoroethylene.
RF	Radio Frequency.
SOI	Silicone-On-Insulator.

Symbols

a	Plate radius for circular cavities or short rectangle edge for rectangular cavities.
A_{cap}	Capacitor electrode area.
a_e	Capacitor electrode radius for circular plates or width for rectangular plates.
A_{ove}	Planar spiral overlap area.
b	Long rectangle edge for rectangular cavities.
b_e	Rectangular capacitor electrode length.
C	Capacitor.
C_{eq}	Analytical model equivalent circuit capacitance.
C_0	Capacitance at zero applied pressure.
$C_{ove\ eq}$	Equivalent overlap capacitance for the analytical model.
C_{ove}	Planar spiral overlap capacitance.

C_{par}	Spiral inductor parasitic capacitance.
C_{plate}	Pressure variable parallel plate capacitance.
A_{plate}	Pressure variable parallel plate capacitance area.
C_s	Lumped element model sensor series pressure dependent capacitance.
C_{sub}	Spiral inductor substrate and environmental capacitance.
D	Flexural Rigidity.
d_{avg}	Spiral average fill diameter.
d_{in}	Spiral inner diameter.
d_i	Center pre-deflection for a diaphram.
D_n	Effective Flexural Rigidity.
d_{out}	Spiral outer diameter.
d_{01}	Center deflection for diaphram 1.
d_{02}	Center deflection for diaphram 2.
d_0	Center deflection for a diaphram.
ϵ	Dielectric constant.
E	Young's Modulus.
ϵ_{eff}	Effective dielectric constant.
ϵ_0	Free space permittivity.
ϵ_r	Relative dielectric constant.
f_{min}	Frequency minimum.
f_0	Resonant frequency at zero applied pressure.
h_i	Boundry between any two surfaces in a multilayered plate.
h_n	Effective Plate thickness.
k	Coupling coefficient.
k_m	Coupling coefficient between two planar spiral inductors.
k_a	Coupling coefficient between the antenna and planar spiral inductor.
L	Inductor.

λ	Gauge factor used to model DC resistance temperature dependence in metal.
L_a	Lumped element model antenna inductance.
LC	Inductive-Capacitive resonator.
L_{eq}	Analytical model equivalent circuit inductance.
ll	Spiral total length.
ll_{eff}	Spiral effective total length.
L_m	Lumped element model mutual inductance between the sensor and antenna.
L_{ma}	Coupling antenna and sensor mutual indcutance for the analytical model.
L_s	Lumped element model sensor series inductance.
ls	Spiral line spacing.
l_{seg}	Spiral segment length.
lt	Spiral line thickness.
lw	Spiral line width.
d_{Diff}	Mean of the difference between two measurements.
n	Spiral number of turns.
ν	Poisson's Ratio.
P	Pressure.
p_s	Spiral pitch.
Q	Quality Factor.
ρ	Resistivity.
r	Radial position for circular cavities or short axis for rectangular cavities.
R_c	Series resistance for the equivalent circuit of a lossy capacitor.
R_{eq}	Series resistance for the analytical modeling of resonant circuits.
r_{inc}	Incremental radius used to estimate the spiral length.
R_s	Lumped element model sensor series resistance.
ρ_s	Ratio of the separation of the average spiral diameter.

r_s	Spiral starting radius.
s_{Diff}	Standard deviation of the differences, d_{Diff}.
$tan\delta$	Loss Tangent.
$tan\delta_{media}$	Dielectric loss tangent for the surrounding medial of a sensor.
t_g	Gap Thickness.
t_{ins}	Polymer sensor insulation thickness.
θ_{inc}	Incremental angle used to calculate spiral length.
t_i	Multilayered Plate thickness for the i^{th} layer.
t_{m1}	Plate 1 thickness.
t_{m2}	Plate 2 thickness.
t_m	Plate thickness.
ω_{crit}	Frequency at which current crowding begins to become significant.
W_e	Electric energy density.
W_{media}	Percent electric energy density stored in the surrounding medial of a sensor.
X_c	Capacitor reactance.
Z_1	Input impedance looking into the coupling antenna.
z_n	Neutral surface for bending along the plate thickness.
$Z_{par\ eq}$	Spiral inductor equivalent parasitic capacitance.

Glossary

endoleak	Incomplete seal, with blood flow, by the endovascular graft and persistent growth or pressurization of the aneurysm sac without extragraft blood flow (endotension).
endotension	High pressure maintained within aneurysm sac with no evidence of a "leak" or blood flow outside of the graft.
FastCap	FastCap, v. 2.0 Porting Version 3.0, is a three dimensional capacitance extraction program. www.fastfieldsolvers.com.

FastHenry FastHenry, v. 3.0 Porting Version 3.2, is a three dimensional inductance extraction program. www.fastfieldsolvers.com.

FluoroEtch® Acton™ FluoroEtch® is a fluoropolymer pre-bonding etchant. The chemical etches the surface making the fluoropolymer bondable to other materials or itself. The chemical works by using a metallic sodium in the solution to react with the fluorine of the polymer, leaving the carbon-fluorine molecule unbalanced. The process should be performed in a nitrogen purged and oxygen-free enviroment because the solution is sensitive to moisture and oxygen.

gold standard In medicine, a gold standard test is a diagnostic test or benchmark that is regarded as definitive. This can refer to diagnosing a disease process, or the criteria by which scientific evidence is evaluated.

green Un-sintered ceramic material.

Kapton® DuPont™ Kapton® is a Polyimide film used for laminates.

Pyralux® DuPont™ Pyralux® is a B-staged modified acrylic sheet adhesive used primaraly to bond flexible innerlayers in multilayer lamination.

SpeedBoard® GORE™ SpeedBoard® C Prepreg is a low loss tangent, low dielectric constant thermoset prepreg used for laminates made from expanded PTFE (ePTFE) impregnated with thermoset resins.

stent graft Edovascular stent graft is a tubular device comprised of synthetic fabric supported by a metal structure (stent). These are used to support weak parts in ateries such as aneurysms.

SUMMARY

This dissertation presents an investigation of miniaturized sensors, designed to wirelessly measure pressure in harsh environments such as high temperature and biomedical applications. Current wireless microelectromechanical systems (MEMS) pressure sensors are silicon-based and have limited high temperature operation, require internal power sources, or have limited packaging technology that restricts their use in harsh environments. Sensor designs in this work are based on passive LC resonant circuits to achieve wireless telemetry without the need for active circuitry or internal power sources. A cavity, which is embedded into the substrate, is bound by two pressure-deformable plates that include a parallel-plate capacitor. Deflection of the plates from applied pressure changes the capacitance, thus, the resonance frequency varies and is a function of the applied pressure. The LC resonant circuit and pressure-deformable plates are fabricated into a monolithic housing that servers as the final device package (i.e. intrinsically packaged). This co-integration of device and package offers increased robustness and the ability to operate wirelessly in harsh environments. To intrinsically packaged devices, the fabrication approach relies on techniques developed for MEMS and leverage established lamination-based manufacturing processes, such as ceramic and flexible-circuit-board (flex-circuit) packaging technologies.

The sensor concept is further developed by deriving the electromechanical model describing the sensor behavior. The model is initially divided into the electromagnetic model, used to develop the passive wireless telemetry, and the mechanical model, used to develop the pressure dependence of the sensor, which are then combined to estimate the sensor resonance frequency dependence as a function of applied pressure. The derived analytical model allows parametric optimization of sensor designs. The sensor concept is demonstrated in two applications: high temperature and biomedical applications.

To demonstrate operation under pressure at temperatures greater than 300 ℃, the current limits for silicon-based MEMS sensors, devices fabricated from low temperature co-fireable ceramics (LTCC) and high temperature co-fireable ceramics (HTCC) using Ag and Pt metallization, respectively, were fabricated and characterized as a function of pressure and temperature. LTCC pressure sensors were operated up to 450 ℃ and up to 5 bars of pressure while HTCC devices demonstrated electrical functionality up to 600 ℃.

To demonstrate operation in biomedical implantable applications, polymer-based flexible designs were fabricated and characterized. The pressure sensors were fabricated from LCP, polyimide, PTFE substrates using Cu metallization. The sensors were bench-tested in simulated environments for body temperature and fluid, with results exhibiting resonance frequency drift due to the non-hermetic pressure-reference cavities and the polymer moisture absorption. Additionally, the resonance frequency and quality factor of the sensors were significantly reduced when operated in high-permittivity and high-loss dielectric environments. To reduce this performance degradation, a method to passivate the sensors was developed, which used an additional dielectric layer of low permittivity and dielectric loss was introduced. To minimize the sensor drift, this work investigated an alternate design by creating a composite polymer-ceramic sensor. The device retained the flexibility of the external polymeric package while incorporating a hermetic chamber to house the reference pressure and pressure-dependent capacitor. Furthermore, PTFE polymers were selected due to their low moisture absorption.

The polymer and polymer-ceramic sensors where characterized for reliability in hydrostatic air, fluid, and pulse pressure ($>$ 300 millions cycles simulating more than 7 years of pulse pressure cycles) fluid environments. Testing confirmed the reduction of frequency drift for polymer-ceramic pressure sensors compared to purely polymer-based pressure sensors. Finally, to demonstrate wireless continuous pressure measurements and catheter-based delivery *in vivo*, LCP-based pressure sensors were delivered into canine models with mock abdominal aortic aneurysms and monitored wirelessly over 30 days. LCP-based pressures sensors were used instead of the composite polymer-ceramic devices because at the time

of implant these were still being developed. However, the animal results confirmed both catheter deliverability and wireless telemetry in real biomedical applications.

CHAPTER 1

INTRODUCTION

The objective of the proposed research is to develop low-cost wireless RF pressure sensors fabricated from ceramic, polymer, or polymer/ceramic composite to operate in harsh environments such as high temperatures or biomedical applications, illustrated in Figure 1.1. To achieve highly simplified fabrication processes and designs for ultra-reliable sensor operation, a passive wireless sensor will be researched. The sensors will consist of an inductor (L) interconnected with pressure-variable capacitive (C) elements to form an LC resonant circuit; these can be packaged in a monolithic housing that servers as the final package and offers the potential to operate wirelessly in harsh environments (i.e. intrinsically packaged). To reduce cost, microelectromechanical system (MEMS)-based batch fabrication will be achieved through the micromachining of materials used in the established microelectronics packaging industry such as ceramic-packaging and flexible-circuit-board (flex-circuit) technology. Design, fabrication, and characterization issues of the proposed wireless pressure sensors will be researched, and *in vitro/vivo* testing will be utilized to demonstrate applicability in harsh environments.

Harsh environments can typically be subdivided into four categories, including high temperature, chemical, high loading, and biocompatible, which are listed in Table 1.1. Recent (2002) market projections (U.S. domestic) for harsh environment sensors are estimated at $5 billion, indicating a commercial need for these devices [1]. Two types of pressure sensors used to operate in harsh environments are high-temperature and biomedical pressure sensors. When comparing high-temperature and biomedical applications, several common design requirements can be identified, such as wireless telemetry, high reliability and batch fabrication for which MEMS-based approaches are well suited. However, MEMS devices

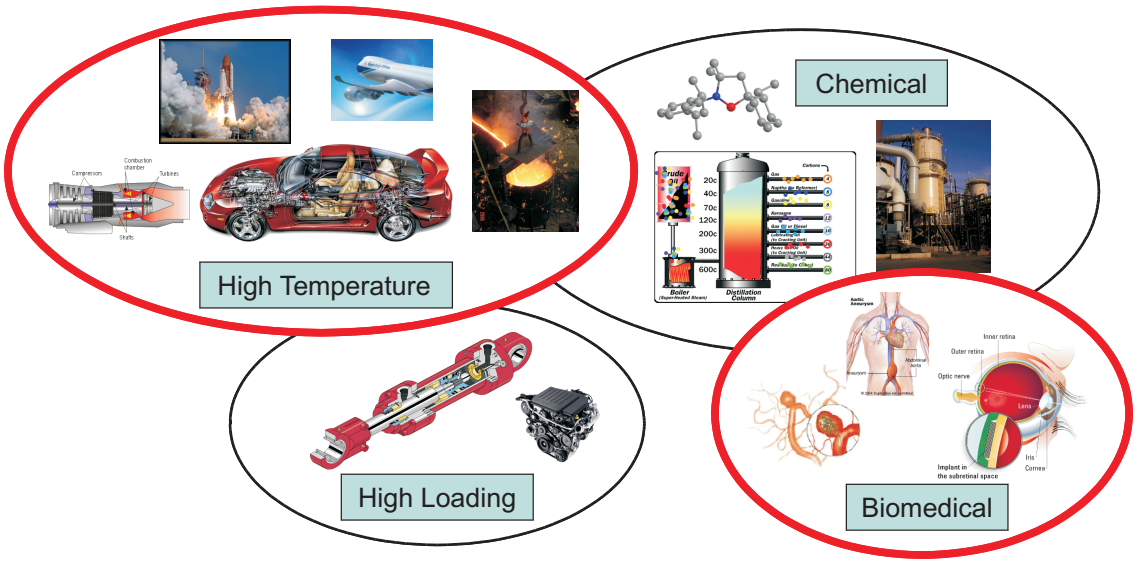

Figure 1.1: Harsh environments: high-temperature, high-loading, chemical, and biomedical.

often suffer from inadequate packaging technology, which can limit their use in harsh environments.

Table 1.1: General categories for harsh environments [1].

Category	**Characteristics**	**Typical Applications**
High-Temperature (Sensors and Electronics)	-55 to 600 ℃	Engines, Aircraft, Process Control, Environment Monitoring, Test and Measurement
Chemical Reactivity	Combustion Species	Engines, Chemical Plants, Well Logging, Fuel Cells, Power Generation
High-Loading and Vibration	> 300,000 G	Munitions, Test and Measurement
Biocompatibility	*In vivo*	Implantable Biomedical Devices

For high-temperature applications such as in the automotive [2], aerospace [3], and aeronautics [4] industries, illustrated in Figure 1.2, a critical unit of measure in system control is pressure. Consumer demand or government regulations are requiring low-cost, highly reliable wireless sensors to improve system performance and efficiency [2]. Although MEMS pressure sensors have been researched extensively, they have had limited use in these applications because of low-temperature operation, design complexity, or inadequate packaging technology. In this work, appropriate design, operation simplicity, material selection, and

fabrication processes resulting in intrinsically packaged wireless devices will be researched.

Similar to high-temperature applications, biomedical applications can benefit greatly from continuous wireless pressure monitoring for disease prevention, diagnosis, and treatment. A few of these diseases are illustrated in Figure 1.3. Applicability greatly increases when the sensors are permanently implanted through minimally invasive procedures, which is generally done through catheter delivery. Although rigid MEMS pressure sensors have been researched extensively for biomedical applications, they often have highly complex designs and fabrication processes or inadequate packaging technology. Additionally, rigid designs implementing wireless passive telemetry coupled with increased miniaturization for catheter deliverability limit detection distances because of reduced cross-sectional area (lower magnetic coupling). In contrast, flexible designs allow equivalent delivery sizes and larger cross-sectional area post delivery, increasing magnetic coupling. In this work, appropriate flexible designs, operation simplicity, material selection, and fabrication processes resulting in intrinsically packaged wireless devices are researched.

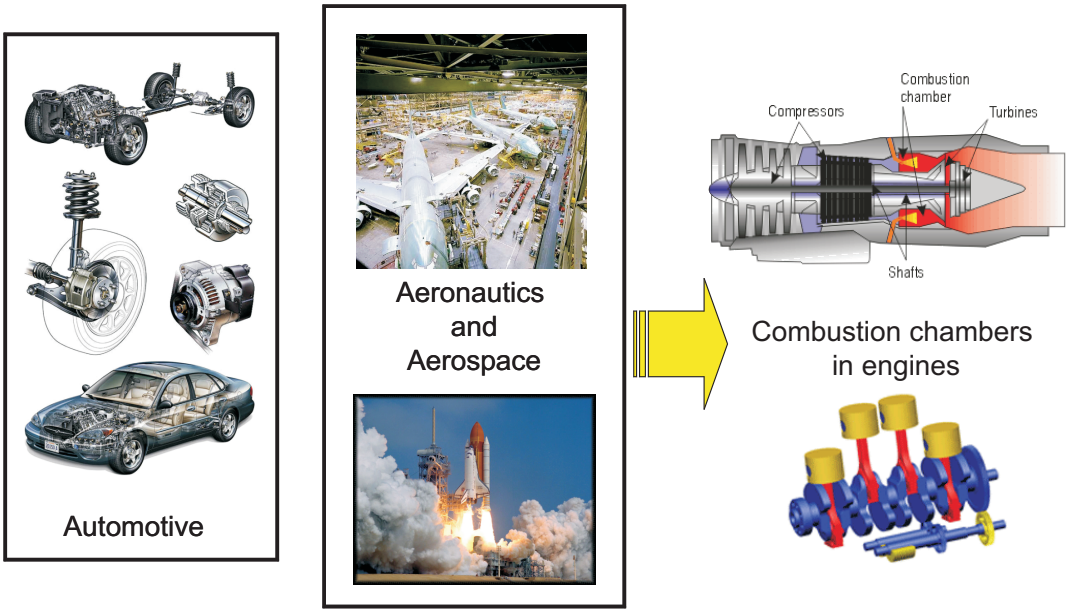

Figure 1.2: High-temperature applications including automotive, aerospace, and aeronautics industries.

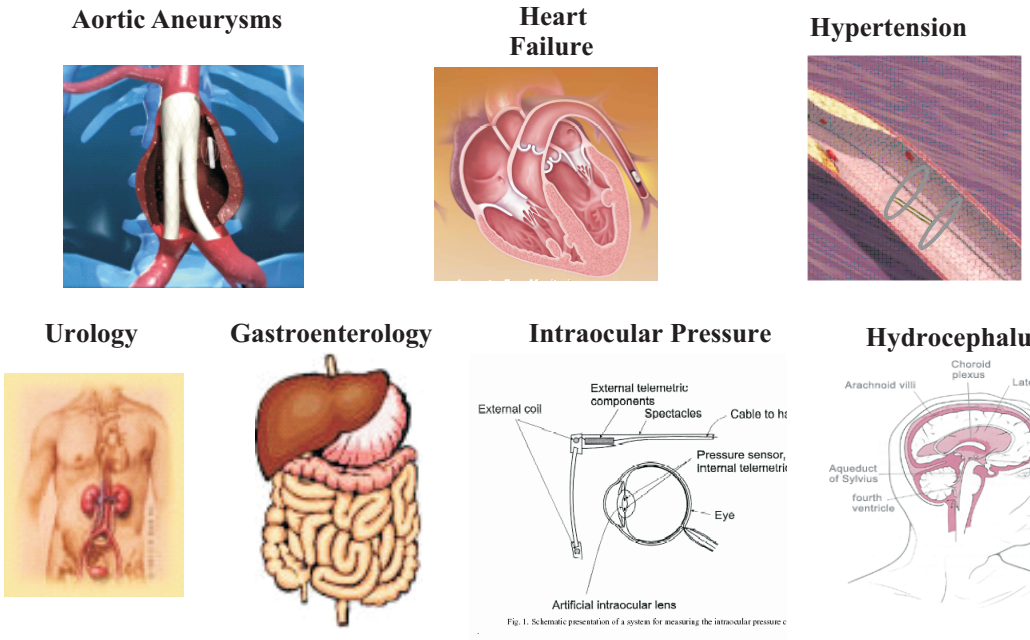

Figure 1.3: Biomedical applications that could benefit from wireless pressure sensing.

In this chapter, a detailed origin and history of wireless passive pressure sensors for high-temperature and biomedical applications are discussed in sections §1.1.1 and §1.1.2 respectively. Finally, section §1.2 presents the research objectives for rigid-ceramic and flexible-polymer pressure sensors.

1.1 Origin and History of the Problem

The origin of the problem is based on previously conducted dissertation work. The objective was to research wireless high-temperature pressure sensors [5]. As a continuation of this work, the challenge to increase the operational range beyond 400 ℃ will be investigated. The development of fabrication approaches to embed the circuitry within the ceramic substrates, achieving intrinsically packaged pressure sensors are researched. Additionally, similar wireless device architectures implemented in polymer/ceramic-based materials for use in biomedical applications are developed. Sections §1.1.1 and §1.1.2 detail the origin and history of passive wireless pressure sensors for the selected applications: high-temperature

and biomedical applications.

1.1.1 High-Temperature Applications

Wireless pressure measurement in harsh environments such as high temperatures has become increasingly critical in automotive, aerospace, and industrial applications [2–4]. Typical market drivers for high-temperature electronics are based on cost reduction through either direct or indirect cost savings from lower system costs, improved system maintenance, reduced machine down-time, or improved efficiency [6].

Typical temperatures for these applications can range from 200-1000 ℃, requiring the development of new low-cost sensor systems (i.e., sensor/device, package, and interrogation system). Great interest for MEMS-based sensors in high-temperature applications exists because of their micro-scale dimensions and potential for low fabrication cost, exemplified by current commercial MEMS accelerometers used in the automotive industry [7]. Many different MEMS-based wired and wireless approaches for high-temperature operation are currently being developed such as i) silicon-based piezoresistive sensors [8], ii) silicon-on-insulator (SOI) sensors [9, 10], iii) optically powered and fiber optic sensors [11–14], iv) wide-bandgap semiconductor-based sensors (SiC, diamond, and group III-nitrides) [6, 15–18], and v) passive ceramic sensors [19]. However, as will be discussed below, many of these approaches are limited because of material properties, availability of proper device packaging, or high cost of fabrication, requiring further development.

A great advantage of silicon-based devices is their widespread use and established manufacturing processes, which lower overall cost. Silicon devices generally require conventional microelectronics to achieve wireless telemetry, which are based on bipolar junction transistors (BJT) or complementary metal-oxide-semiconductor (CMOS) technologies. This circuitry ultimately limits the operational temperatures to < 150 ℃ because of excessive leakage currents [20]. Additionally, silicon mechanical properties deteriorate above 500 ℃

beyond which silicon starts to plastically deform [20]. Further advances in processing, using silicon fusion bonding to create an oxide layer that electrically isolates the sensing piezoresistor, extended the operation range for silicon-based sensors to 250 ℃ [8]. Compared to silicon, SOI-based devices were reported to have higher operating temperatures ranging from 200 ℃ [9] to 340 ℃ [10, 21]. However, their wireless circuitry generally requires supply voltages of several volts, which is undesirable in applications with limited power supply capabilities [11].

Fiber optic sensors fabricated from fused silica, sapphire, and SiC implementing extrinsic Fabry-Perot interferometry show great promise in high-temperature measurements with the potential to operate up to 1000 ℃ [13]. A similar fiber optic pressure sensor made entirely from fused silica demonstrated capabilities up to 710 ℃ [14]. Compared to electronic devices, fiber optic sensors have many advantages. They are immune to electromagnetic interference (EMI), are passive, and have high resolution and accuracy [14]. However, the fibers are wired into the sensing location, which can be unattractive for high pressure or chemically harsh environments where risks for leaks can occur. Additionally, the fragile nature of fibers requires robust packaging to survive the demanding industrial environment.

A different optical method uses a laser to wireless power a GaAs photodiode in a MEMS capacitive pressure sensor. The optically powered device uses an LC tuned oscillator to convert absorbed power into radio frequency (RF) energy and transmit it back to a receiving antenna. Although wireless telemetry for this scheme achieves a desirable distance of 1.5m, the devices are limited to 250 ℃ because of decreased performance of the GaAs photodiode and silicon tunnel diode at elevated temperatures [11]. Other limitations are the need for precise laser-photodiode alignment and the need for wavelength-transparent windows into the harsh environment for power transmission.

The operation limitation below 250 ℃ of silicon-based devices has triggered the development of higher-temperature semiconductor materials. Process development and material characterization for wide-bandgap materials, such as SiC, diamond, and group III-nitrides,

have demonstrated the potential for microelectronic circuitry to operate at elevated temperatures (> 300 ℃) [6]. The most mature wide-bandgap material is SiC used for the development of various high-temperature electronics and sensors [15, 16, 18, 22]. In 1998, Ned et al. [16] presented a 6H-SiC (a common polytype of SiC) pressure sensor operating at 600 ℃. The device used tangentially and radially oriented piezoresistors on a circular diaphragm. A Ti/TiN/Pt metalization with a layer of Au formed ohmic contacts. Gold wires were bonded from the sensor to external pins for electrical connections. Despite great strides in wide-bandgap semiconductor devices, they are limited by inadequate packaging technology. Although considerations for high-temperature packages have begun [17], more development is required to overcome many challenges such as [6] mechanical and electrical integrity of feedthroughs from thermal cycling, thermal expansion mismatches, and loss of package hermeticity. In addition, metal-to-semiconductor contacts require further development, since they can be affected by [6] atomic mixing, possible new phase formations (solid-state reactions), oxidation effects, and higher electromigration or thermomigration rates. Therefore, while high-temperature wide-bandgap semiconductor circuitry is advancing, further development in packaging is still required for wireless telemetry. In general, wide-bandgap semiconductor processes (cost, capabilities, and yields) and material availability are not at the same level as silicon, which reduces their use in cost-sensitive markets [6].

Finally, a completely passive wireless device without the need for contacts, feedthrough wires, or internal power supplies was discussed by English and Allen [19] in 1999. A passive *LC* resonant circuit for high-temperature operation was fabricated from low-temperature co-fireable ceramics (LTCC), an established process for the microelectronic packaging industry. The device used a pressure variable capacitor to modulate the resonant frequency of the oscillator. The fabrication approach used three green[1] sheets of LTCC material. The center sheet contained a circular opening to create buried cavities within the ceramic package. The sheets were assembled and laminated in an unfired state and then sintered at

[1]The term green is commonly used for un-sintered ceramic material

high temperatures (900 ℃) in a furnace. The sintering fused the LTCC material, forming a hermetic package. Copper planar spiral inductors were electrodeposited on the outside of the sintered sheets. Capacitor electrodes were fabricated over buried cavities on pressure-deflectable plates and connected to the inductors to form the LC resonator. Variation in pressure deflects the plates, changing the capacitance and thereby the resonant frequency. A pickup coil magnetically couples to the devices and allows detection of resonant frequencies. Devices were operated at 200 ℃ and in pressure ranges of 0-100 bar. Ultimately, the temperature range was limited because of the oxidation effects of the exposed copper metalization. Further research with this approach demonstrated operation up to 400 ℃ [5]. These devices were fabricated using screen-printable inks, instead of electrodeposited copper, on the outside of the device, which allowed for operation at higher temperatures. Although the circuitry was exposed to the environment, operation was increased up to the limitations of the selected materials. These devices show great potential for intrinsically packaged pressure sensors if implemented with higher-temperature materials and embedded circuitry. A comparison of various high-temperature pressure sensors is listed in Table 1.2.

1.1.2 Biomedical Applications

Compared to high-temperature applications, biomedical environments are mild with respect to pressure and temperature. Nevertheless, biomedical environments are equally harsh and can pose even greater demands on sensor designs given the potential risks to life. Many applications for *in vivo* pressure measurement exist and a few of them include intraocular [23–33], intravascular [34–37], intracranial [38], gastrointestinal [39–41], and bladder [42] pressure measurements. For many of these applications, implant miniaturization, biocompatibility, and wireless telemetry are critical because of increasing trends for minimally invasive procedures [43–46].

Table 1.2: Comparison of high-temperature pressure sensors.

Source	Type	Substrate	Temp [C]	Features	Drawbacks
[20]	CMOS	Si	150°	Low-cost, Established mfg., and wireless active telemetry	Low Temperature
[8]	Piezoresistive Fusion bonded	Si	250°		
[10, 21]	CMOS Capacitive	SOI	300°	Medium temperature range	Requires high voltage
[11]	Optically powered	Si	250°	Long detection range 1.5m	Low-temperature and precise optical alignment between source and device
[13, 14]	Fiber optic	SiC, SiO_2, Sapphire	1000°	High temperature operation and performance	Not wireless
[16]	Piezoresistive	SiC	600°	High temperature, potential for wireless active telemetry	Package technology, availability, and cost
[5, 19]	Capacitive	LTCC	400°	Intrinsically packaged, established mfg. processes, low-cos, and wireless passive telemetry	Exposed metal and medium temperature range

Great interest in MEMS-based wireless sensors for biomedical implants exists because of their micron-scale size, low power consumption, and potential for low fabrication costs [43]. Generally, capacitive-based sensors are preferred for wireless telemetry because of their high sensitivity to pressure, low noise, low temperature sensitivity, and low power consumption [47]. However, this only represents one part of the wireless system. Other essential building blocks are required that include the sensor, power source, signal processing unit, transmit/receive stage, and package [47]. Sensor design consideration for integrating or excluding these elements should be considered.

MEMS wireless technology for biomedical applications is typically subdivided into two types: active and passive telemetry. For active telemetry, integrated power supplies are required to power the integrated circuits (IC) [47]. However, the added system complexity increases packaging requirements [41] and reliability risks [48] and complicates operation [49]. Devices with internal power supplies have lifetime issues from constant replacement or recharging, which is undesirable or impractical in implantable biomedical applications.

Complex packaging technology is needed since it must isolate the active circuitry from harsh environments [4] while allowing the capacitive transducer to interact with the surrounding environment [48]. These constraints can become barriers towards applicability [47] since packaging technology for MEMS is at an infant stage compared to microelectronics [41]. In contrast, passive telemetry removes complexity and reduces risk by transferring power supplies and active circuitry from the implant to external electronics; this simplifies implant fabrication and package constraints since devices can be fabricated into the packaging materials [19].

Wireless passive MEMS pressure sensors are generally fabricated from silicon substrates implementing planar spiral inductors. These rigid devices coupled with catheter deliverability and increasing miniaturization constrain the size of the implant, which limits the passive telemetry distance. This is due to the reduction in mutual coupling (coupling coefficient) as the implant cross-sectional area decreases (lower magnetic flux capture cross-section). A potential solution is the development of flexible technology [50] that can be delivered in folded-up compact shapes and then expanded post-delivery. In the following sections, details of MEMS passive devices used in biomedical applications are discussed.

The simplest form of passive telemetry implements an LC circuit whose resonant frequency varies according to some environmental change. While some devices use variable inductors [51, 52], the majority of devices rely on variable capacitors for frequency modulation. Wireless passive telemetry exists for many different applications, including pressure [38, 49, 52–54], humidity [55–57], complex permittivity [58], strain [51], and flow [59] sensors. However, only a subset of these is suitable for biomedical implants because of additional reliability and biocompatibility constraints.

Wireless telemetry for biomedical applications has existed since the late 1950s. In 1957, Mackay and Jacobson [39] reported the "endoradiosonde," a radio transmitter that could be swallowed and used to transmit pressure and temperature data. In the same year, Farrar et al. [40] reported a telemetering capsule to study gastrointestinal pressure. A battery

within the devices powered an oscillator circuit whose frequency was variable to pressure. In 1967, miniaturization of "endoradiosondes" for intraocular implantation was achieved with the development of a new "transensor," discussed by Collins [23]. In this work, the devices implemented a passive LC circuit whose resonant frequency varied with pressure. A magnetically (inductively) coupled external loop allowed for wireless telemetry of the pressure-modulated frequency. This passive wireless scheme lends itself for very compact designs and high degree of simplicity, which are desirable characteristics for ultra-reliable operation in biomedical applications [46]. The "transensor" design consisted of a pair of hand-wound planar spiral coils spaced apart and mounted on opposite Mylar drumhead diaphragms. The coil self and mutual inductance, along with their associated distributed capacitance, formed the resonant circuit. The diaphragms were supported on the sides by a thin glass tube, approximately 1-2 mm tall. Changes in differential pressure across the diaphragms induced deflections, varying the space between the coils, and hence the resonant frequency. Although conventional macro-fabrication approaches were used, devices ranging from 2-6 mm in diameter were achieved. The "transensors" were used to continuously measure intraocular pressure (IOP) in over 70 animal implants.

Since then, many MEMS-based passive wireless implantable pressure sensors have been developed. In 1992, Rosengren et al. [25] reported a passive MEMS-based pressure sensor intended for the remote query of IOP. The device consisted of a silicon micromachined pressure-sensitive capacitor soldered to a hand-wound coil. Conventional micromachining of the capacitor used fusion bonding of two wafers; the bottom wafer had etched recesses in order to create buried cavities. The top wafer was thinned back to define a membrane of given thickness to achieve desirable pressure sensitivities. The handmade coil was fabricated from 50 μm diameter insulated gold wire, which was soldered to the capacitor, forming the LC circuit. In 1994, further performance improvements for this device [26] were achieved by reducing parasitic losses in the silicon-based capacitor structure. Finally, devices were coated in silicone rubber to electrically insulate them from eye fluid during successful IOP measurements within rabbit implants. Further advances in miniaturization, batch fabrication, and

improved performance of silicon-based pressure sensors were presented in [38, 49, 60, 61].

A commercially available passive pressure sensor for monitoring endovascularly repaired abdominal aortic aneurysms (AAA) was discussed by Allen [46] in 2005. The system uses minimally invasive catheter-based delivery to position the sensor within the aneurysm sack as a permanent implant. The sensors are fabricated from standard MEMS-based microfabrication techniques. On a lower fused silica substrate, an electrodeposited planar spiral coil forms the lower inductor. On a second fused silica substrate, an etched recessed area defines a deformable plate, which contains a second electrodeposited coil forming the upper inductor. The wafers were fusion bonded together to form hermetically sealed sensors. Careful control of the recess and electrodeposition allows for micron scale gaps between the upper and lower inductors. The application of pressure deflects the plate, changing the distance between inductors, thereby modulating the resonant frequency.

Table 1.3 lists a comparison of passive telemetry devices, most of which are rigid. Although rigid passive devices have applicability in biomedical applications, the development of flexible designs could expand medical diagnostic technology requiring increased miniaturization for minimally invasive procedures.

Table 1.3: Comparison of Passive Wireless Pressure Sensors.

Source	Materials	Size [mm]	Fabrication Approach	Application	Features
[23]	Mylar/Glass 44 AWG wire	6	hand-made	Intraocular pressure	Landmark miniaturization (1967)
[24, 25]	Si	2x2	MEMS capacitor and hand-wound coil		MEMS capacitor
[62]	Si, Cu, Al, Si_3N_4, PolySi, Glass	3x4	MEMS		Hartley oscillator
[27]	Si, Cu	4x4	MEMS		Harmonic Generation
[53]	Si, SiO_2,Al	3x3	MEMS	Pressure	Not biomedical
[19]	LTCC, Cu	30x30	MEMS	High-temperature pressure	Intrinsically packaged; Simple design for high reliability
[57]	Si, Polyimide, Ferrite, 44 AWG wire	1.5x7	MEMS capacitor and hand-wound coil	Humidity	MEMS capacitor
[56]	Si, Cu	1.5x8	MEMS		Integrated planar inductor
[54, 55, 58]	TiO_2, Cu, PCB, plexiglass	43x43	PCB	Humidity, pressure, and permittivity	Detection range
[49]	Si, Glass, Au	2.6x1.6	MEMS	Pressure	Absolute pressure and embedded circuitry
[52]	Ferrite, SiO_2, Glass, Epoxy, Cu	3x3	MEMS	Pressure	Inductively modulated
[38]	Si, Glass, Cu, Polyimide	6x6	MEMS	Intracranial pressure	Low-impedance interconnections
[51]	30 AWG wire	7.4x14.7	Hand made	Strain	Inductively modulated
[59]	304 Stainless Steel, Si	22x3	uEDM and MEMS	Flow rate	MEMS capacitor and integrated stent
[50]	Polyimide, Si	-	MEMS capacitor and flex-circuit	Blood pressure	Flexible package
[60, 61]	Si, SiO_2, Si_3N_4	1x1	MEMS	Biomedical	Distance and size
[46]	SiO_2, Cu	30x5	MEMS	AAA pressure	Distance, stability, and reliability

1.2 Thesis Outline

Chapter 2 developes the sensor concept and modeling. First, the sensor electromagnetic theory is presented, which includes a simplified lumped-element model and a more accurate semi-distributed analytical model. Although the model is not fully distributed, it is sufficient to capture most of the dominant effects for this work. Additionally, the analytical model is based on a literature survey of the electrical elements of inductance and capacitance. These form the basis for the electromagnetic model of the sensor. The electromagnetic model is verified through measurement of fabricated devices using both polymer and ceramic substrates. Next, a mechanical model for both circular and rectangular plates is presented and verified against results from Finite Element Analysis (FEA). Then, both the electromagnetic and mechanical models are integrated to form the electromechanical model and establish the pressure-dependent frequency of the LC resonator. Verification of the electromechanical model is achieved throughout the rest of the thesis. The derived model can be used to optimze design configurations implementing multi-layered planar spiral inductors that have distributed capacitances. The effects of temperature, humidity, and loss of dielectric materials used to fabricate the wireless pressure sensors are included.

Chapter 3 presentes the design, fabrication, and characterization of high-temperature pressure sensors. This included designs fabricated from low temperature cofireable ceramics LTCC with exposed and embedded circuitry operating up to 450 ℃, as well as high temperature cofireable ceramics (HTCC) with embedded circuitry operating up to 600 ℃. Devices fabricated from HTCC materials demonstrated feasability, operating in temperature ranges beyond that of conventional silicon-based sensors.

Chapter 4 defines the design space for the development of implantable wireless pressure sensors for biomedical applications. This chapter narrowes the design to a specific telemetry systems, method of delivery into the body, which is based on catheter-deliverability, and operational environment. The chapter concludes with a list of specific requirements for the sensor design. Using the model derived in Chapter 2, designs that achieve these

requirements are presented in Chapter 5 and Chapter 6.

Chapter 5 presentes the design, fabrication, and characterization of polymer-based pressure sensors fabricated from LCP, Kapton®, and PTFE substrates. These devices will have drift characteristics since they are fabricated from non-hermetic monolithic packages. This lead to the development of polymer-ceramice-based pressure sensors presented in Chapter 6.

Chapter 6 presentes the design, fabrication, and characterization of polymer-ceramic-based pressure sensors fabricated from PTFE and Zirconia ceramic substrates. Zirconia ceramic substrates are used to create hermetic chambers housing the reference pressure for the pressure sensor and metalized to form the pressure-variable capacitance. These are then embedded within the polymer layers and interconnected to the planar spiral inductors to complete the *LC* circuit. These devices have improved drift performance because of increased stability of the PTFE polymeric substrate and hermetic Zirconia chamber, which is demonstrated in the *in vitro* stability testing presented in Chapter 7.

Chapter 7 presentes *in vitro* sensor stability testing in hydrostatic air pressure environments for up to 60 hours, sensor stability testing in hydrostatic saline-fluid environments for up to 1300 hours, and sensor stability under cyclic saline-fluid pressure for over 300 millions pulses (simulating approximately 7 years of pulsation within the human body). In all cases of stability testing, the pressure sensors fabricated from polymer-ceramic substrates outperformed the polymer-based sensors. Besides bench testing and characterization, the feasibility of the design requirements for operation *in vivo* is presented in Chapter 8.

Chapter 8 presentes *in vivo* testing of an LCP-based pressure sensors in a mock-aneurysm in a canine model. At the time of animal protocol approval the PTFE-ceramic-based pressure sensors were still under development. Therefore, these were not available for implantation. Additionally, all the animal testing was performed by CardioMEMS, Inc staff as well as supplied equipment. The appropriate protocols and procedures specified by the Institutional Animal Care and Use Committee (IACUC) were followed. The results of the

animal study demonstrated catheter-deliverability of the developed wireless pressure sensors into a mock-aneurysm model in four canines. During and post-implant, continuous wireless pressure data-measurements from within the aneurysms were recorded for a time-frame of approximately 30 days. Both the delivery and continous measurement is succesfully demonstrated in this animal study.

Chapter 9 presents the conclusion and future outlook of this work.

CHAPTER 2

PRESSURE SENSOR DESIGN AND MODELING

The harsh environments introduced in Chapter 1 preclude the use of many pressure sensing technologies previously developed. These are either highly complex, implement silicon-based circuitry, are not compatible with wireless operation, or have unmet device packaging requirements, which limits their use within harsh environments. However, passive LC resonant circuit structures do not suffer from these limitations as they can be packaged in a monolithic housing that serves as the final package and offers the potential to operate wirelessly in harsh environments. An additional benefit of LC resonant circuits is that they greatly reduce sensor complexity and compactness [46], which is desirable for ultra-reliable operation in environments such as high-temperature or implantable biomedical applications.

The sensor design consists of a passive LC resonant circuit integrated into a package that contains a sealed embedded cavity with pressure deformable plates. A planar spiral inductor is integrated and embedded into the substrate. A parallel-plate capacitive element is interconnected with the inductive element to form the LC resonator. The capacitor is integrated into the mechanically deformable structures to create a pressure variable capacitive element. When the environmental hydrostatic pressure surrounding the sensors changes, the plates deflect and bring the electrodes of the capacitor closer or farther apart. In turn, the capacitance change of the system changes the resonance frequency. Therefore, the sensor's self-resonance frequency of the LC circuit is a function of the environmental pressure.

Two basic designs are used for this research, illustrated in Figure 2.1. The first design implements a single planar spiral inductor interconnected to a parallel plate capacitor, Figure 2.1a. Both L and C are fabricated on the outside of the substrate. The inductor and capacitor are interconnected with a via trace running on the outside of the substrate. The

second design uses two parallel spiral inductors and a parallel plate capacitor, Figure 2.1b. The inductors can be interconnected through a conducting via or simply be capacitively and inductively coupled. The circuitry is integrated and embedded within the substrate.

In the following sections, the electromagnetic model of LC resonant circuits is discussed for both a lumped and distributed element model as a means of describing the electromagnetic behavior of the sensors. In addition, the mechanical theory is presented for both circular and rectangular diaphragm structures in order to develop a mechanical deflection model. Finally, both electromagnetic and mechanical models are integrated to develop a generalized electromechanical model for the sensor.

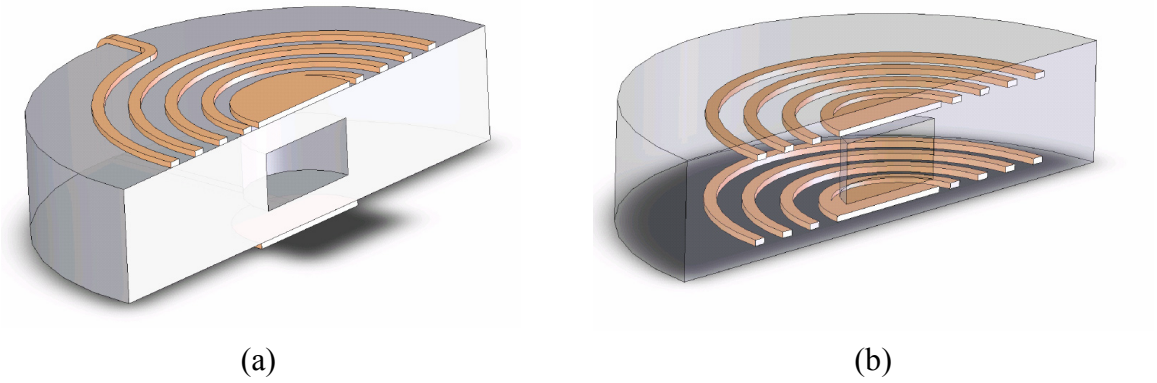

Figure 2.1: Pressure sensor concepts for a single planar spiral inductor external to the substrate (a), and two planar spiral inductors embedded within the substrate (b) (example shown is capacitively and inductively coupled, i.e. no via).

2.1 Sensor Electromagnetic Theory

The concept for the wireless pressure sensors implements an LC resonant circuit with pressure variable capacitance to wirelessly communicate with an external loop antenna. To gain further understanding of the electromagnetic behavior of the sensor and its interaction with the loop antenna, two electromagnetic modes are investigated. The first is a lumped element model, which can be used to simplify device behavior as it relates to the readout telemetry. The second is an analytical model with distributed elements, which are used

to design and optimize device performance as a function of physical characteristics and material properties.

2.1.1 Sensor Lumped Element Model

The lumped element model of the sensors, illustrated in Figure 2.2, includes a series inductance L_s, series capacitance C_s, and series resistance R_s. The resonant frequency for this circuit is given by

$$\omega_0 = 2\pi f_0 = \frac{1}{\sqrt{L_s C_s}} \tag{2.1}$$

and the quality factor Q is given by [5]

$$Q = \frac{\omega_0 L_s}{R_s} \ . \tag{2.2}$$

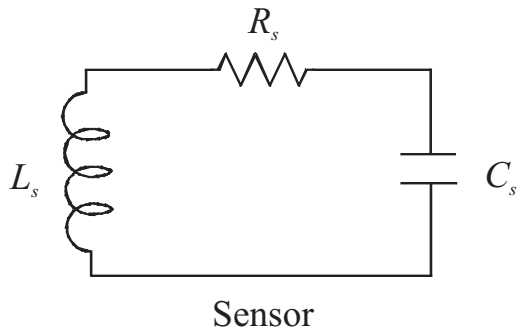

Figure 2.2: Electromagnetic lumped element model for an LC resonant circuit.

To interrogate the sensor, a loop-antenna of inductance L_a is magnetically coupled to L_s. This allows remote detection of the resonance frequency of the sensor. The sensor resonance and its coupling to the antenna is modeled from a two-port network using transformer theory, as shown in Figure 2.3 [63]. The coupling k between the sensor and the antenna is proportional to the mutual inductance L_m and is given by

$$k = \frac{L_m}{\sqrt{L_s L_a}} \ . \tag{2.3}$$

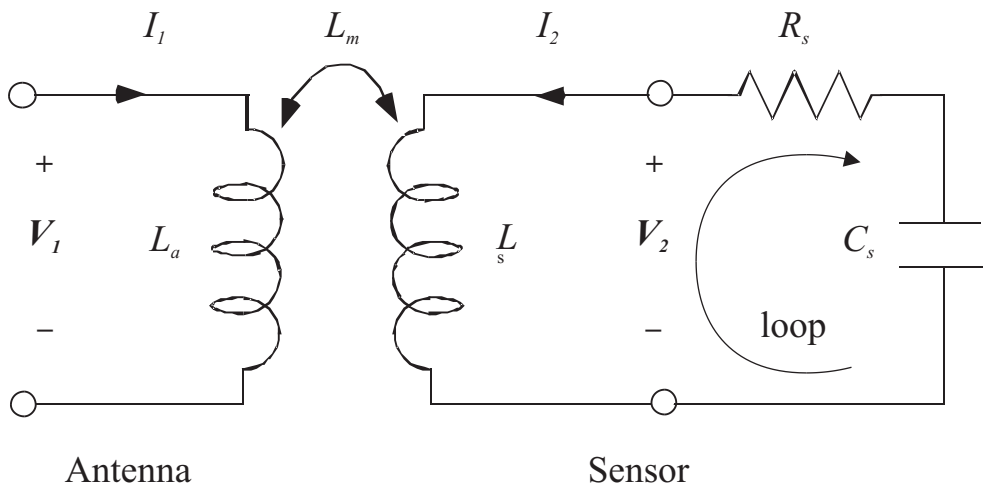

Figure 2.3: Lumped element model for an inductively coupled system containing a loop antenna and LC resonant circuit.

Analysis of the circuit in Figure 2.3 using transformer network theory and Kirchhoff's law, using phasor notation ($s = j\omega = j2\pi f_0$), yields the loop equations

$$V_1(s) = sL_aI_1 + sL_mI_2 \tag{2.4}$$

and

$$V_2(s) = sL_mI_1 + sL_sI_2 \ , \tag{2.5}$$

Using Kirchhoff's voltage law, the loop equation around the sensor is given by

$$-R_sI_2 - V_2 - \frac{1}{sC_s}I_2 = 0 \ . \tag{2.6}$$

Solving for I_2 in terms of I_1 by replacing V_2 in Eq. (2.6) with Eq. (2.5) yields the expression

$$I_2 = -\frac{C_sI_1L_ms^2}{1 + C_sR_ss + C_sL_ss^2} \ . \tag{2.7}$$

Replacing I_2 in Eq. (2.4) with Eq. (2.7) yields

$$V_1(s) = I_1s\left[L_a - \frac{C_sL_m^2s^2}{1 + C_ss(R_s + L_ss)}\right] \ . \tag{2.8}$$

Substituting L_m with the coupling coefficient k from Eq. (2.3), f_0 from Eq. (2.1), and Q from Eq. (2.2), the input impedance Z_1 looking into the antenna is given by

$$Z_1 = \frac{V_1}{I_1} = j2\pi fL_a\left[1 + k^2\frac{\left(\frac{f}{f_0}\right)^2}{1 - \left(\frac{f}{f_0}\right)^2 + \frac{j}{Q}\left(\frac{f}{f_0}\right)}\right] \ . \tag{2.9}$$

The result relates the sensor electrical characteristics such as the resonance frequency f_0, quality factor Q, and coupling coefficient k to a measurable impedance quantity Z_1. As long as one or all of the electrical characteristics of the sensor are a function of pressure or any other desirable physical parameter, these can be measured through the loop antenna impedance Z_1. This is achieved by measuring the impedance magnitude and phase, which are derived below. The general impedance for a circuit is defined as

$$Z = R + jX \ , \tag{2.10}$$

where R is the real part of the impedance and X, the reactance, is the imaginary part of the impedance and are defined as

$$Re(Z) = Z_R = R = |Z| \cos\theta \tag{2.11}$$

and

$$Im(Z) = Z_I = X = |Z| \sin\theta \ . \tag{2.12}$$

The magnitude and phase of the impedance Z are given by

$$|Z| = \sqrt{(Re(Z))^2 + (Im(Z))^2} \tag{2.13}$$

and

$$\angle Z = \arctan\left[\frac{Im(Z)}{Re(Z)}\right] \ . \tag{2.14}$$

By defining $\Omega = f/f_0 = \omega/\omega_0$, Eq. (2.9) can be re-written as

$$Z_1 = j\omega L_a \left[1 + k^2\Omega^2 \left(\frac{(1-\Omega^2) - j\frac{\Omega}{Q}}{(1-\Omega^2)^2 + \frac{\Omega^2}{Q^2}}\right)\right] \ , \tag{2.15}$$

where the magnitude and phase of Z_1, using Eq. (2.13) and Eq. (2.14), are given by

$$|Z_1| = \sqrt{\left[\frac{L_a\omega k^2\Omega^3}{Q\left((1-\Omega^2)^2 + \frac{\Omega^2}{Q^2}\right)}\right]^2 + \left[L_a\omega\left(1 + \frac{k^2\Omega^2(1-\Omega^2)}{(1-\Omega^2)^2 + \frac{\Omega^2}{Q^2}}\right)\right]^2} \tag{2.16}$$

and

$$\angle Z_1 = \arctan\left[\frac{(1-\Omega^2) + \frac{\Omega^2}{Q^2} + k^2\Omega^2(1-\Omega^2)}{\frac{k^2\Omega^3}{Q}}\right] \ . \tag{2.17}$$

Table 2.1: Example circuit-antenna system used to illustrate the input impedance derived in Eq. (2.9).

Input	Value
f_0	35 MHz
Q	40
k	0.1
L_a	1 μH

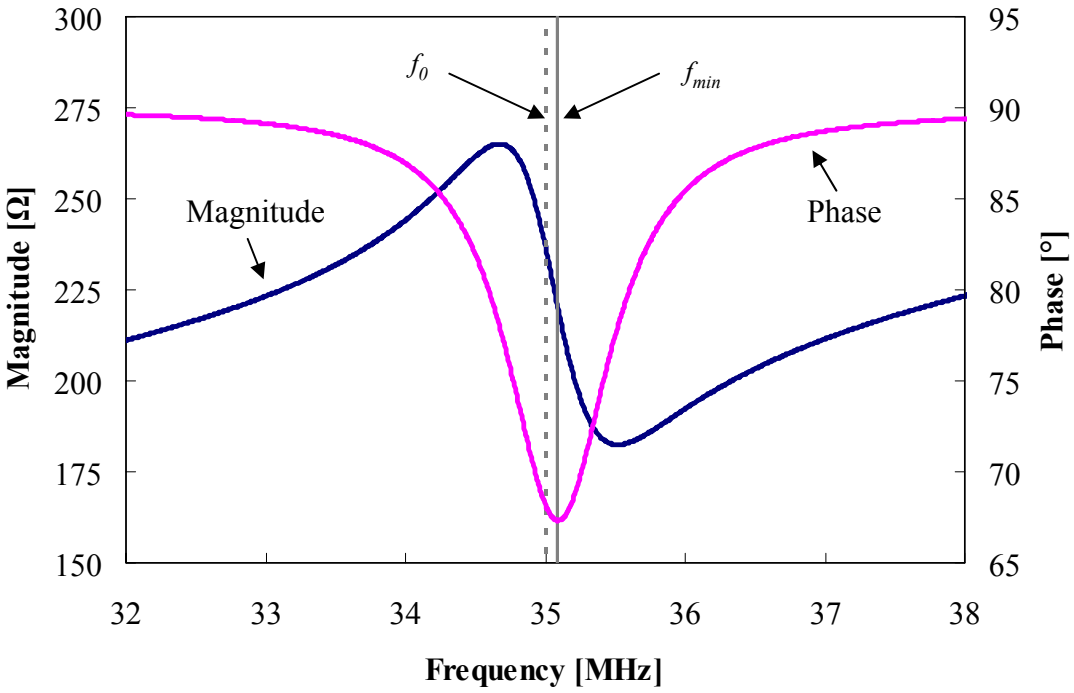

Figure 2.4: Magnitude and phase of input impedance for a LC circuit-antenna system with electrical parameters described in Table 2.1.

This model can then be used to extract f_0, Q, and k by measuring Z_1 as a function of frequency f. An example of the input impedance for a system with electrical parameters in Table 2.1 is illustrated in Figure 2.4.

From analysis of Figure 2.3 and from electromagnetic theory, it is expected that the minimum resonance frequency f_{min} extracted from the measured impedance phase Eq. (2.17) will be offset by the mutual inductance of the antenna L_a coupled through k to the sensor inductance L_s. This coupling acts to raise the resonant frequency of the coupled system compared to the self-resonance frequency of the sensor. The difference is illustrated in Figure 2.4, with $f_0 = 35$ MHz and $f_{min} = 35.09$ MHz, calculated from the phase. This effect can be further understood by investigating the input impedance Z_1 phase frequency minimum f_{min}. The frequency minimum f_{min} is found from the partial derivative of the phase with respect to Ω and setting it equal to zero. Using the chain rule, the derivative is

$$\frac{\partial}{\partial\Omega}\left[\angle Z_1\right] = \underbrace{\frac{\partial}{\partial\Omega}\left[\arctan\left(\frac{1}{f(\Omega)}\right)\right]}_{\neq 0} \cdot \frac{\partial}{\partial\Omega}\left[\frac{1}{f(\Omega)}\right] = 0 \ . \tag{2.18}$$

Since the first argument of the chain rule results in a non-zero term for physical values of Ω, solving for f_{min} reduces to solving for Ω. This is achieved from

$$\frac{\partial}{\partial\Omega}\left[\frac{1}{f(\Omega)}\right] = 0 \ , \tag{2.19}$$

where $f(\Omega)$ is defined as

$$f(\Omega) = \frac{\frac{k^2\Omega^3}{Q}}{(1-\Omega^2) + \frac{\Omega^2}{Q^2} + k^2\Omega^2(1-\Omega^2)} \tag{2.20}$$

and

$$\Omega = \frac{\omega_{min}}{\omega_0} = \frac{f_{min}}{f_0} \ . \tag{2.21}$$

Solving Eq. (2.19) for Ω and discarding nonphysical roots, the following expression is determined

$$\Omega = \sqrt{\frac{(2 - Q^{-2} - k^2) - \sqrt{(Q^{-2} - 2 + k^2)^2 - 12(k^2-1)}}{2(k^2-1)}} \tag{2.22}$$

Further simplification is achieved by taking the Taylor series expansion of Eq. (2.22) about Ω for small values of k and large values of Q (derivation found in Appendix A, section

§A.1). The result yields a simple equation relating f_{min}, the measured quantity, with f_0 the resonance of the sensor as a function of k and Q.

$$f_{min} = f_0 \left(1 + \frac{k^2}{4} + \frac{1}{8Q^2}\right) \tag{2.23}$$

From Eq. (2.23) it is clear that as the coupling k becomes small and approaches zero and the quality factor Q increases and approaches infinity, f_{min} approaches f_0. For practical values of k and Q, the difference between f_{min} and f_0 is small. Typical values for devices intended for biomecial applications, with zero separation distance between the sensor and antenna, have k <0.07 and Q ranging from 30-70. Using these values, the expected difference between f_{min} and f_0 is 0.16% to 0.17%, which is 57 to 60 kHz for a sensor with f_0 equal to 35 MHz. As the k drops below 0.01, the difference in frequency is less than 0.01%. Using a pressure sensitivity of 10 kHz·mmHg^{-1}, the error introduced from using f_{min} will have a maximum of 6 mmHg for zero separation distance. For practical applications, the separation distance between the antenna and sensor will be more than a few centimeters, reducing the error further.

2.1.2 Sensor Analytical Modeling

Analytical models are useful to predict performance characteristics of designs having specific requirements or narrow design spaces. In this work, use of analytical models to design pressure sensors for biomedical applications is required to meet a reduced design space, as will be discussed in Chapter 4. The model presents an improvement beyond the lumped element model, which is primarily used for curve fitting because it allows for geometric design of the different circuit elements that make up the sensors. The development of the analytical model begins by deriving the models for planar spiral inductors in section §2.1.3 and parallel plate capacitances for overlapping planar spirals in section §2.1.4. Then, these are integrated to form the LC resonant circuit model of the sensor in section §2.1.5. Finally, the models are verified in section §2.1.6 by fabricating devices with geometries and materials that will be used to fabricate pressure sensors.

2.1.3 Analytical Model for Planar Spiral Inductors

Most inductor models implement a π equivalent circuit, illustrated in Figure 2.5, with series inductance L_s, series resistance R_s, and parasitic capacitance C_{par}. C_{par} is the winding-to-winding capacitance, which when combined with L_s results in the self-resonant frequency of the planar spiral inductor. The π circuit models found in literature generally have substrate impedances to ground when a ground plane exists. These were left out in Figure 2.5 for simplicity. For the designs in this work, grounding planes are not implemented, however, environmental and other substrate effects will be included in the model by adding a parallel circuit element later in this section.

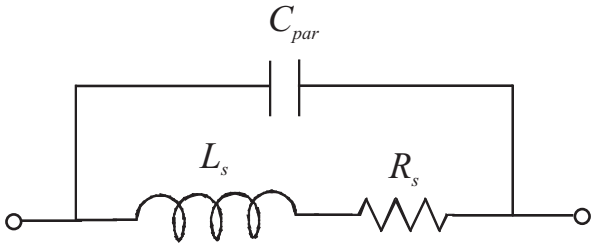

Figure 2.5: Simplified π model for a planar spiral inductor with series resistance R_s and inductance L_s, and parasitic capacitance C_{par}.

Analysis of the circuit in Figure 2.5 yields the planar spiral impedance given by

$$Z_{spiral} = \frac{R_s + j\left[L_s\omega - C_{par}R_s^2\omega - C_{par}L_s^2\omega^3\right]}{1 - 2C_{par}L_s\omega^2 + (C_{par}R_s\omega)^2 + (C_{par}L_s)^2\omega^4} \ . \tag{2.24}$$

From Eq. (2.24), the self-resonance can be found by setting the imaginary part equal to zero and solving for ω, resulting in

$$f_{0\ Spiral} = \frac{1}{2\pi\sqrt{L_sC_{par}}}\sqrt{1 - \frac{C_{par}R_s^2}{L_s}} \ . \tag{2.25}$$

Additionally, from Eq. (2.24) the quality factor can be calculated as

$$Q_{Spiral} = \frac{Im[Z_{spiral}]}{Re[Z_{spiral}]} = \frac{\omega L_s}{R_s}\left[1 - \underbrace{\frac{C_{par}R_s^2}{L_s} - C_{par}L_s\omega^2}_{\text{Capacitive loss factor}}\right] \ , \tag{2.26}$$

where the first term accounts for the magnetic energy stored and the second term is the capacitive loss factor describing the reduction in Q due to an increase in peak electrical energy with frequency and zero value of Q at the self-resonance [64].

There are many approaches to calculating the inductance of planar spirals in the literature [65–85]; however, after further consideration, it was found that a current sheet approach [73, 85] was the most suitable for this work. The current sheet approximation uses finite width conductive sheets with infinitesimal thickness. This method, first introduced in the early 1900 by Nagaoak [85], is suitable for geometries where the conductor thickness is much smaller than its length or width. The current sheet approach uses geometric mean distance (GMD), arithmetic mean distance (AMD), and arithmetic mean square distance (AMSD), to describe the planar spiral inductor geometry [73]. Although this method has already been derived by [85] for various inductor shapes, a summary for circular planar spiral inductors is presented below.

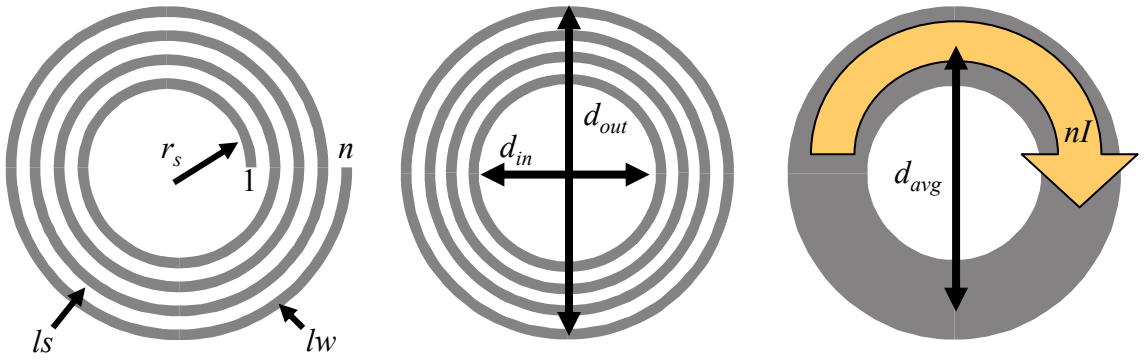

$$\rho_s = (d_{out} - d_{in}) / (d_{out} + d_{in}) \qquad ls \leq 3lw$$

$$\rho_s d = nlw + (n\text{-}1)ls$$

Figure 2.6: Analytical modeling of concentric current sheets by transforming a circular planar spiral (a), to concentric conductor filaments (b), and to a current sheet (c).

The derivation begins by representing the spiral inductor, Figure 2.6a, by concentric circular conductors, Figure 2.6b. In Figure 2.6a, the spiral number of turns is n, line spacing

is ls, line width is lw, and starting radius is r_s, while in Figure 2.6b and Figure 2.6c the equivalent spiral representations have inner, outer, and average diameters d_{in}, d_{out}, and d_{avg} respectively. The mutual inductance between the circular filaments can be found from

$$M_{circfil} = \frac{\mu d_{avg}}{2} \left[(2-m)K(m) - 2E(m) \right] \ , \tag{2.27}$$

where the average diameter d_{avg} is

$$d_{avg} = \frac{d_1 + d_2 + \ldots + d_n}{n} \ , \tag{2.28}$$

and $K(m)$ and $E(m)$ are the complete elliptical integrals of the first and second kind, respectively, with argument $m = (1 - \rho_s^2)$. The ratio of the separation of the average diameter ρ_s is given by

$$\rho_s = \frac{d_{out} - d_{in}}{d_{out} + d_{in}} \ . \tag{2.29}$$

The series expansion of Eq. (2.27) yields a simpler expression

$$M_{circfil} \approx \frac{\mu d_{avg}}{2} \left[ln\left(\frac{1}{\rho_s}\right) - 0.6 + 0.7\rho_s^2 \right] \ . \tag{2.30}$$

The self inductance of a single current sheet takes advantage of GMD and AMSD concepts, illustrated in Figure 2.6c, and is approximated by

$$L_{circsheet} \approx \frac{\mu d_{avg}}{2} \left[ln\left(\frac{d_{avg}}{w}\right) + 0.9 + 0.2\frac{w^2}{d_{avg}^2} \right] \ , \tag{2.31}$$

with average diameter d_{avg} and sheet width w. Using similar techniques, the mutual inductance for n current sheets is estimated. Once combining both mutual inductance and self inductance for all concentric circuloar rings, the expression for the low frequency inductance, L_s, of a circular planar spiral inductor with n turns is given by

$$L_s = \frac{\mu n^2 d_{avg}}{2} \left[ln\left(\frac{2.46}{\rho_s}\right) + 0.2\rho_s^2 \right] \ , \tag{2.32}$$

where the coefficients 2.46 and 0.2 are empirically found in [85]. To verify Eq. (2.32), FastHenry simulations were performed. Figure 2.7 illustrates a comparison between FastHenry simulations and analytical results from Eq. (2.32), showing good agreement.

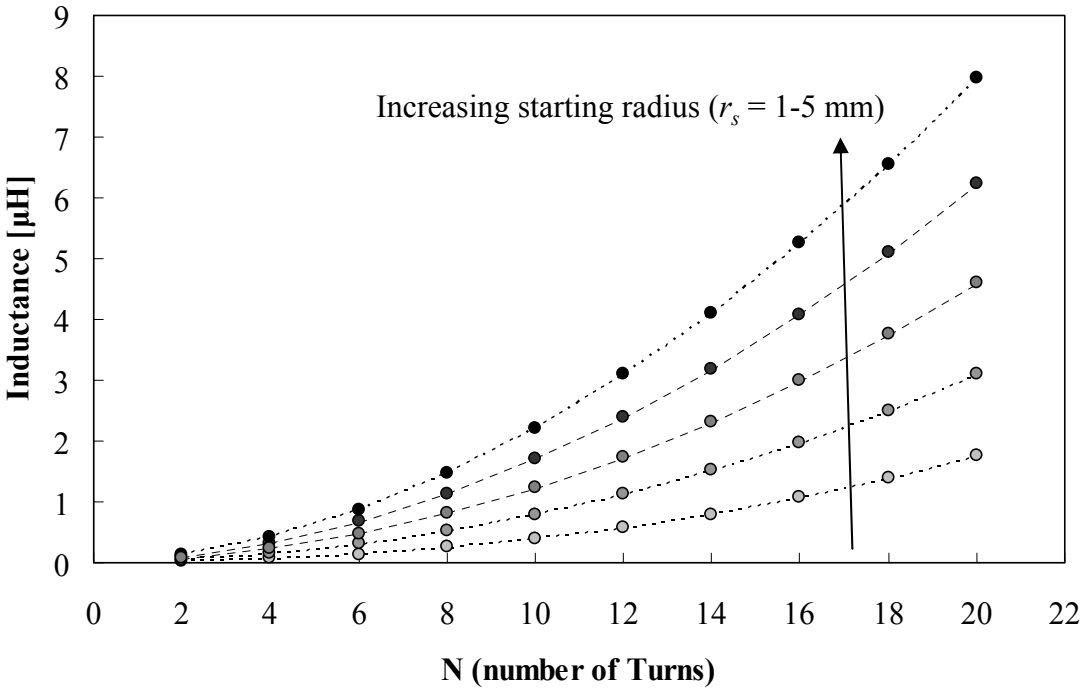

Figure 2.7: FastHenry simulation (dots) compared to the analytical model of Eq. (2.32) (dash-line) for spirals with $r_s = 1 - 5$mm, $lt = 17\mu$m, $lw/ls = 1$, and with a pitch $p_s = 120\mu$m.

The frequency-dependent inductance of the circuit in Figure 2.5 is calculated from [84] as

$$L_{eq}(f) = \frac{L_s}{1 - L_s C_{par}(2\pi f)^2} \ , \tag{2.33}$$

where C_{par} is the inductor parasitic self-capacitance, illustrated in Figure 2.8. The right side of Figure 2.8 illustrates the geometry used to calculate concentric rings for modeling of inductance while the left side illustrates the fringe field and the effective relative permittivity ϵ_{eff} when different dielectrics are used.

The methods used above (GMD, AMD, and AMSD) to estimate the inductance of planar spirals do not rely on the length of the spiral. To estimate the length, two approaches can be used. The first mothod uses the circumfernce of each concentric circle which are then added to calculate the total length. The second method devides the spiral-turns into small segments, then the length of each segment is estimated, and finally they are added together. The second mothod is used in this work because it provides greater accuracy and is required

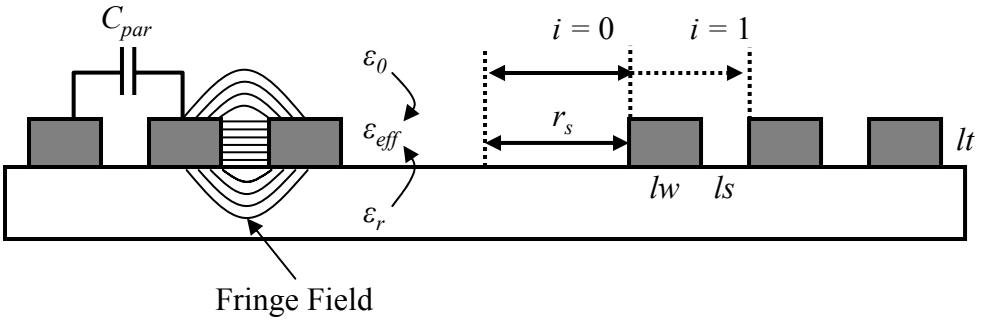

Figure 2.8: Geometry used to estimate the parasitic self-capacitance of a planar spiral inductor.

to calculate the complex parasitic sefl-capacitance of the sprial inductance. This is done by first defining the number of segments or points per rotation (*ppr*) for each turn. The length of each segment is calculated using the Pythagorean theorem and the array of lengths is added together.

The accuracy of the length will be dependent on the number of segments. To illustrate this, Figure 2.9 graphs three spirals with increasing *ppr* using values of 10, 30, and 60. For the spiral with *ppr* of 10, the segments are clearly visible. As *ppr* increases, the spiral approaches the ideal circular spiral. For the purposes of this work, $ppr > 30$ are implemented and for modeling *ppr* of 60 are used.

The length of each segment is calculated from the x,y coordinates of each segment. We begin by defining the spiral pitch (p_s) and incremental radius (r_{inc}) and angle (θ_{inc}) change per segment, defined as

$$p_s = lw + ls \tag{2.34a}$$

$$r_{inc} = \frac{lw + ls}{ppr} \tag{2.34b}$$

$$\theta_{inc} = \frac{2\pi}{ppr} \ . \tag{2.34c}$$

Using Eq. (2.34), the coordinates for each segment are defined as

$$x_{(i,j)} = \left[r_s + p_s n_i + \frac{lw}{2} + j r_{inc} \right] \cos(0 + j\theta_{inc}) + \Delta_{offset} \tag{2.35a}$$

$$y_{(i,j)} = \left[r_s + p_s n_i + \frac{lw}{2} + j r_{inc} \right] \sin(0 + j\theta_{inc}) + \Delta_{offset} \ , \tag{2.35b}$$

where r_s is the starting radius, p_s is the pitch, lw is the line width, n_i is the i^{th} turn evaluated from $i = 0$ to $i = (n-1)$, and jr_{inc} and $j\theta_{inc}$ are the j^{th} radial and angular increments evaluated from $j = 0$ to $j = ppr$. The value of Δ_{offset} is used to radially offset the center of the spiral to the first quadrant of the x, y plane, with both having a value of $\geq r_s + \frac{lw}{2} + np$ to make all x, y coordinates positive.

Using the coordinates from Eq. (2.35), the differential between the start (i, j) and end $(i+1, j+1)$ coordinates are given by

$$\Delta x_{(i,j)} = x_{(i+1,j+1)} - x_{(i,j)} \tag{2.36a}$$

$$\Delta y_{(i,j)} = y_{(i+1,j+1)} - y_{(i,j)} \ . \tag{2.36b}$$

The length of each segment (l_{seg}) can be calculated using the Pythagorean theorem, shown below

$$l_{seg(i,j)} = \sqrt{\Delta x_{(i,j)}^2 + \Delta y_{(i,j)}^2} \ . \tag{2.37}$$

The length of the spiral (ll) is given by

$$ll = \sum_{i=1}^{i=n} \sum_{j=1}^{j=ppr} l_{seg(i,j)} \ , \tag{2.38}$$

where the innermost summation in Eq. (2.38) calculates the length per turn and outermost summation calculates the total length.

The parasitic self-capacitance of a planar spiral is complex to calculate due to the high level of distribution. In literature, analytical equations have had little success in estimating the spiral self capacitance. Some of the methods used include parallel plate theory [67], electric energy stored by using a linear voltage profile that is a function of the spiral turn length ratio [84, 86, 87]. However, in most of the literature, which considers devices built

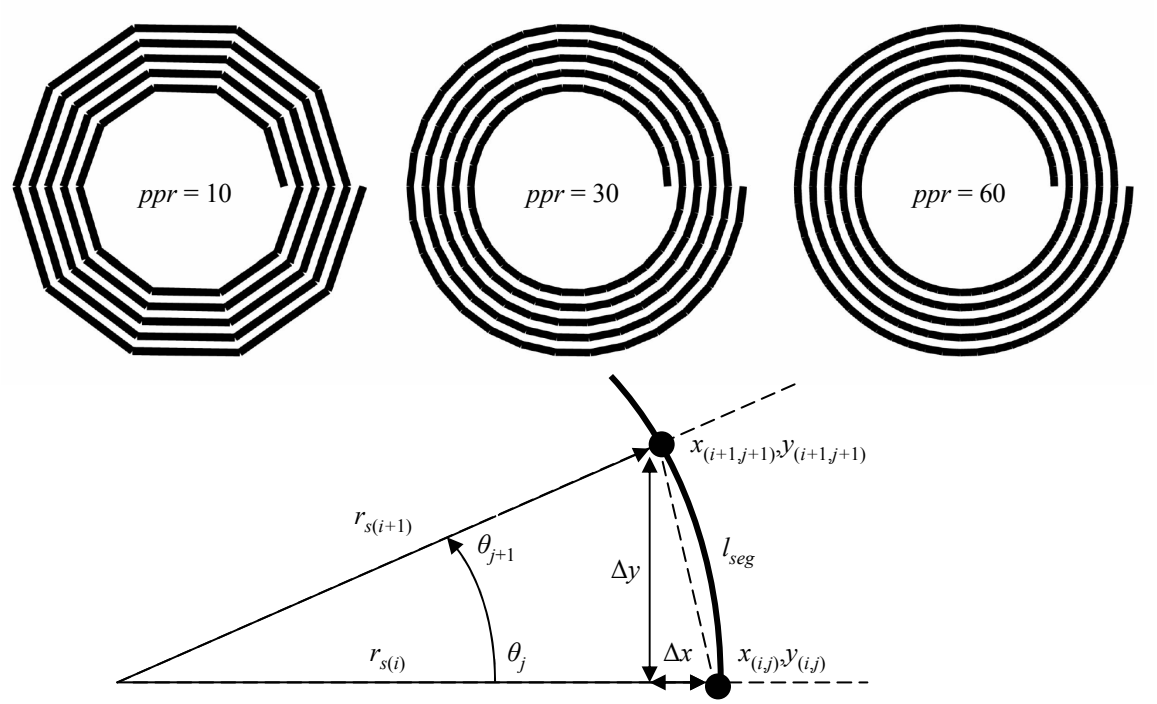

Figure 2.9: Three spirals with increasing *ppr* (top) and geometry used to define each segment length (bottom).

on silicon, this parasitic capacitance is ignored since substrate losses are a more dominant effect [67].

For this work, even though the substrate is not silicon, the spiral self-capacitance accounts for a small part of the system capacitance when two or more spirals are overlapped to form the sensor architecture. For this reason, a curve fitting approach is used to analytically estimate the self-capacitance. This was achieved by first modeling the capacitance for various structures of interest using FastCap. Capacitance sensitivity to line thickness (lt), starting radius (r_s), line width to line spacing ratio (lw/ls), and pitch (p_s) were investigated and are graphed Figure 2.10.

From Figure 2.10 it is clear that the spiral self-capacitance varies as a function of pitch (p_s) and starting radius (r_s) and not the line thickness (lt) or line width to line spacing ratio (lw/ls). The capacitive increase due to pitch p_s or starting radius r_s is due to an increase in the overall length of the spiral. The lack of sensitivity to line thickness lt and

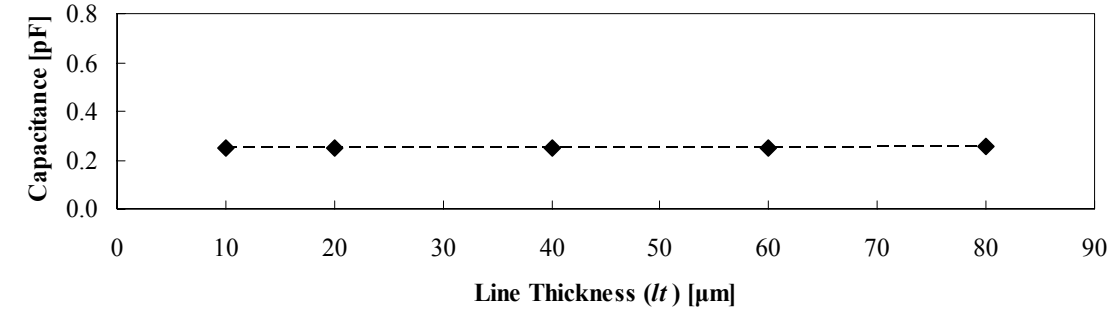

(a) $p_s = 120\mu$m, $n = 10$, $lw/ls = 1$

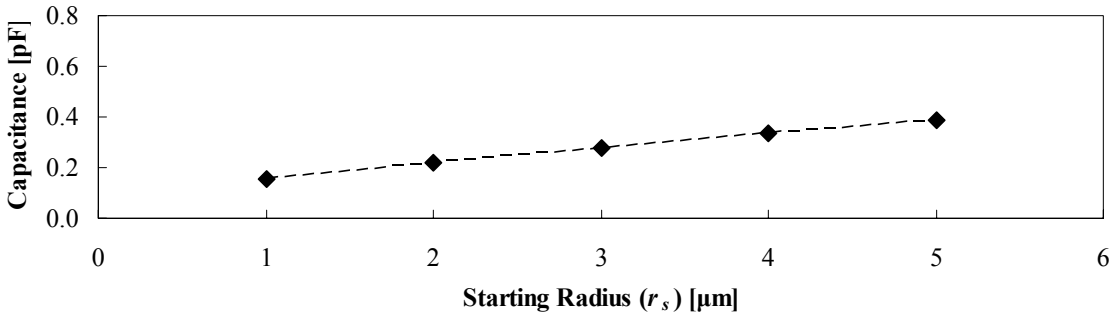

(b) $p_s = 120\mu$m, $n = 10$, $lw/ls = 1$

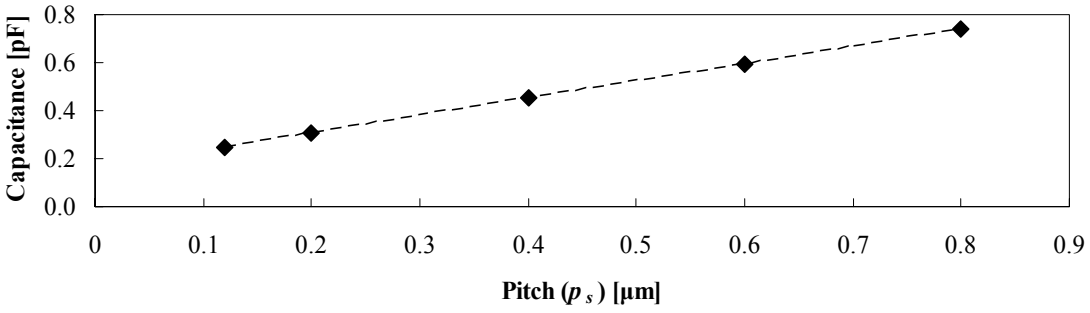

(c) $n = 10$, $lw/ls = 1$

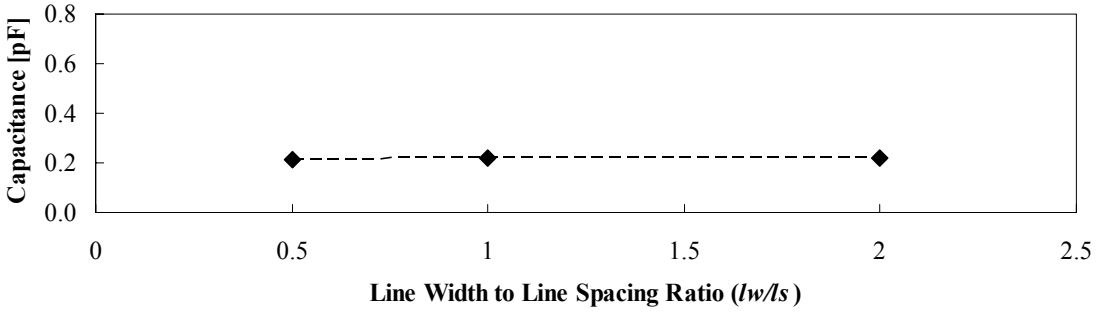

(d) $p_s = 120\mu$m, $n = 10$

Figure 2.10: FastCap results for planar spiral self-capacitances for variable (a) line thickness lt, (b) starting radius r_s, (c) pitch p_s, and (d) line width to line spacing ratio lw/ls.

line width to line spacing ratio lw/ls is likely due to the fringe electric field from the top and bottom surfaces of the spiral trace, illustrated in Figure 2.8.

From the modeling done in Figure 2.10, it can be shown that the self-capacitance is primarily a function of the spiral length. To derive an analytical equation for C_{par}, the electric energy stored in a spiral-turn is used and is defined as

$$E_i = \frac{C_i \Delta V^2}{2} = \frac{\epsilon \cdot ll_i \cdot lt}{2ls} \cdot \frac{\Delta V^2}{n^2} \ , \tag{2.39}$$

where ll_i is the turn length, the voltage per turn is a function of the number of turns, and the total voltage drop across the spiral is ΔV. The energies can summed for all the turns and the equivalent capacitance can be extracted as

$$C_{par-equivalent} = 2 \cdot \sum_{i=1}^{i=n} \frac{E_i}{\Delta V^2} = \frac{\epsilon \cdot ll \cdot lt}{ls} \cdot \frac{1}{n^2} \ , \tag{2.40}$$

where ll is the total length of the spiral. Eq. (2.40) includes an inverse proportionality to the number of turns squared. From a data set generated from FastCap, Eq. (2.40) can be modified to

$$C_{par} = \epsilon_0 \cdot \epsilon_{eff} \cdot ll_{eff} \cdot \frac{1}{n^k} \ , \tag{2.41}$$

where ϵ_0 is the permittivity of free space and ϵ_{eff} is the effective relative permittivity, n is the number of turns, k is a fitting variable, which is a function of the starting radius r_s and pitch p_s, and ll_{eff} is the spiral effective total length. the effective length is defined as

$$ll_{eff} = ll - \frac{ll_1 + ll_n}{8}, \tag{2.42}$$

where ll is the total length and ll_1 and ll_n are the lengths of the first and last turn of the spiral. The effective length ll_{eff} is used to reduce the capacitance since the first and last turns do not contribute as much capacitance as the inner turns. Figure 2.11 graphs a comparison between Eq. (2.41) and FastCap versus the number turns n and starting radius r_s, with reasonable agreement, for constant pitch of $p_s = 120\mu$m. The fitting coefficient used for Figure 2.11 is $k(r_s) = 20r_s + 0.78$, which is only a function of r_s because the pitch was held constant. In fact, k also varies with pitch. Therefore, k can be found using the method above for different values of r_s and p_s. Although Eq. (2.41) has no real physical

meaning, it is sufficient for the modeling required in this work since C_{par} is generally small.

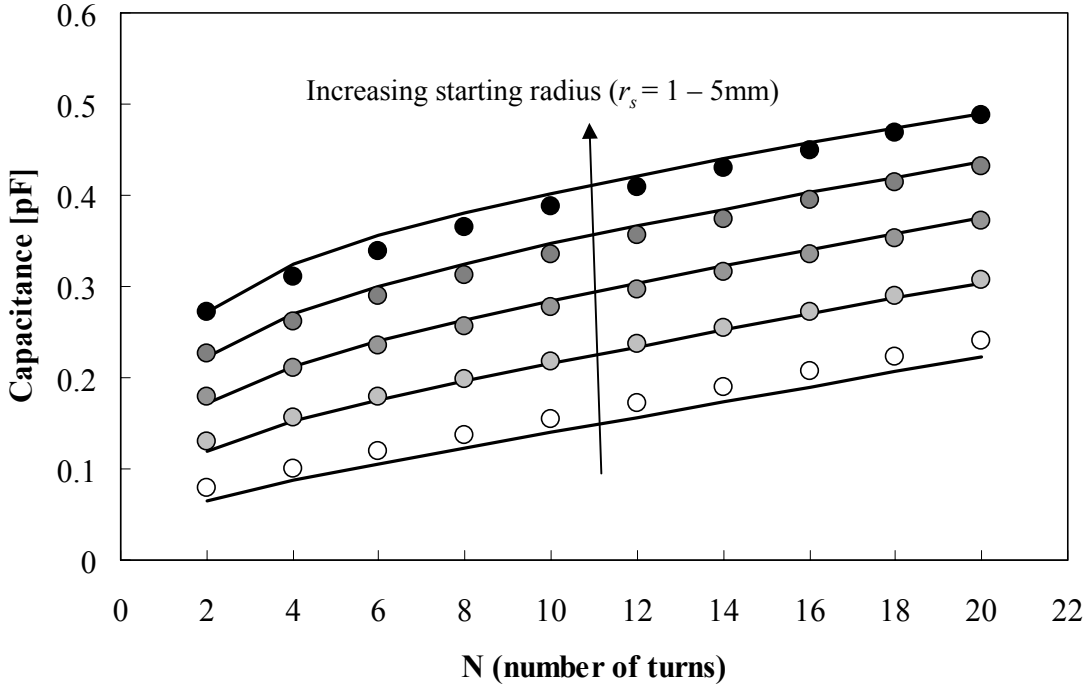

Figure 2.11: Spiral self-capacitance versus number of turns n for starting radius from $r_s = 1$ mm to $r_s = 5$ mm and constant pitch $p_s = 120$ μm. FastCap results shown as circles and Eq. (2.41) shown as the line.

The frequency-dependent series resistance $R(\omega)$ is modeled through the approximate analytical equation [80]

$$R(\omega) \approx R_s \left[1 + \frac{1}{10} \left(\frac{\omega}{\omega_{crit}} \right)^2 \right] , \tag{2.43}$$

where R_s is the DC resistance, calculated from

$$R_s = \frac{\rho \cdot ll}{lw \cdot lt} , \tag{2.44}$$

and ω_{crit} is the frequency at which current crowding becomes significant, and is calculated from [80]

$$\omega_{crit} = \frac{3.1 \cdot \rho \cdot (lw + ls)}{\mu_0 \cdot lw^2 \cdot lt} , \tag{2.45}$$

where ρ is the metal resistivity, ll is the spiral length, μ_0 is the permeability of free space, lw is the line width, lt is the line thickness, and ls is the line spacing. Eq. (2.43) presents a

good approximation to compute and consider the losses due to proximity and skin-depth as it relates to the distribution of the current density within the conductor, which is sufficient for this work. A more precise analytical model for these effects is found in [84].

The frequency dependent resistance $R(\omega)$ from Eq. (2.43) is not directly measured without the effects of the self-resonance of the spiral. From Eq. (2.24) we observe that the real part of the impedance is

$$Re[Z_{spiral}] = \frac{R(\omega)}{1 - 2C_{par}L_s\omega^2 + (C_{par}R_s\omega)^2 + (C_{par}L_s)^2\omega^4} \ , \tag{2.46}$$

where R from Eq. (2.24) is replaced with $R(\omega)$ from Eq. (2.46).

To verify the analytical model of Figure 2.5, circular planar spiral inductors were fabricated on ceramic and polymeric substrates and measured using an HP4194A impedance analyzer. This was done by probing the spiral at each end to measure the impedance. The geometrical and material characteristics of the spirals are listed in Table 2.2 and illustrated in Figure 2.12.

Table 2.2: Planar spiral geometrical (measured) and material characteristics used to verify analytical models.

Characteristic	**Design1**	**Design2**	**Design3**
n	12	14.5	9
lw [μm]	55	55	435
ls [μm]	67	67	430
lt [μm]	17	17	30
r_s [mm]	3.8	3.8	4.19
Substrate	75 μm PTFE	75 μm PTFE	500 μm Alumina
ϵ_r	2.2	2.2	9
ρ [Ωm]	1.72×10^{-8}	1.72×10^{-8}	1.27×10^{-7}

From the impedance analyzer measurements for the designs described above, the electrical characteristics, such as self-resonance, series inductance, parasitic self-capacitance, and resistance were measured and compared to the analytical models. The results are summarized in Table 2.3. The measured frequencies, inductances, resistances, and quality factors are direct measurements using the impedance probe of the impedance analyzer while the

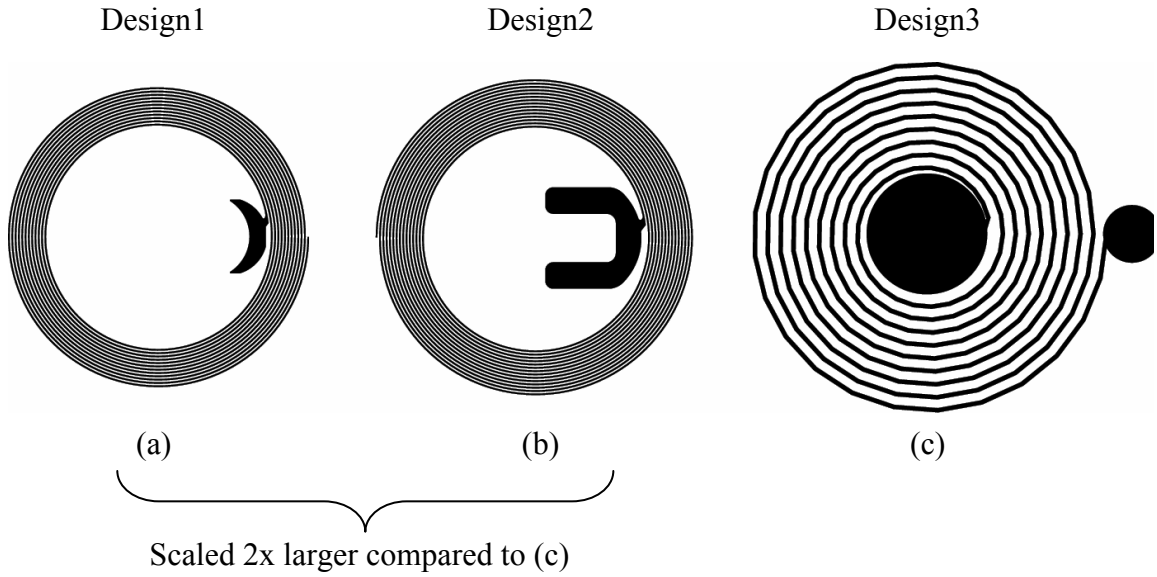

Figure 2.12: Planar spiral inductors for Design1 (a), Design2 (b), and Design3 (c) used to verify analytical modeling. Designs 1 and 2 are used in polymeric based designs while Design3 is used for ceramic designs. These are discussed in subsequent chapters.

capacitance was extracted from the frequency and inductance measurements. The probe had a parasitic capacitance of 1.536 pF, which lowered the resonant frequencies during the impedance measurement. The frequencies, which are listed in Table 2.3, were used to calculate the capacitance from which the probe parasitic capacitance was subtracted yielding the spiral self-capacitance.

Table 2.3: Planar spiral analytical model result summary.

Design	f_0 **[MHz]**		L_s **[μm]**		R_s **[Ω]**		C_{par} **[pF]**	
	Meas.[a]	Eq. (2.25)	Meas.	Eq. (2.32)	Meas.	Eq. (2.44)	Meas.[b]	Eq. (2.41)[c]
Design1	77.86	77.62	2.3	2.24	6.93	6.4	0.330	0.341
Design2	64.45	64.63	3.28	3.2	9.05	7.96	0.371	0.364
Design3	86.96	86.11	1.47	1.42	4.72	4.53	0.804	0.848

[a] These frequencies include the impedance analyzer probe parasitic capacitance of 1.536 pF.
[b] The measured C_{par} is extracted from the self-resonance and measured series inductance.
[c] In Eq. (2.41), ϵ_{eff}= 1 was used instead of estimating the actual ϵ_{eff}.

The measured low-frequency inductances for the three designs are 2.3 μH, 3.28 μH, and 1.47 μH, and are compared to the analytical model results from Eq. (2.32), which are 2.24 μH, 3.2 μH, and 1.42 μH, for Desing1, Design2, and Design3 respectively. The results of

Eq. (2.32) compare well with the measured inductance and are within 3.5% of each other as well as results from FastHenry.

The measured parasitic self-capacitance in Table 2.3 is extracted from the self-resonance and measured inductances, and are 0.33 pF, 0.371 pF, and 0.804 pF, which are in good agreement with Eq. (2.41) estimates of 0.341 pF, 0.364 pF, and 0.848 pF for Design1, Design2, and Design3 respectively. The calculated values from Eq. (2.41) are within 5% of the measured value and results from FastCap. Figure 2.13 graphs a comparison of simulations performed on FastHenry and FastCap, the analytical model, and measurements for spirals from Design1 and Design2.

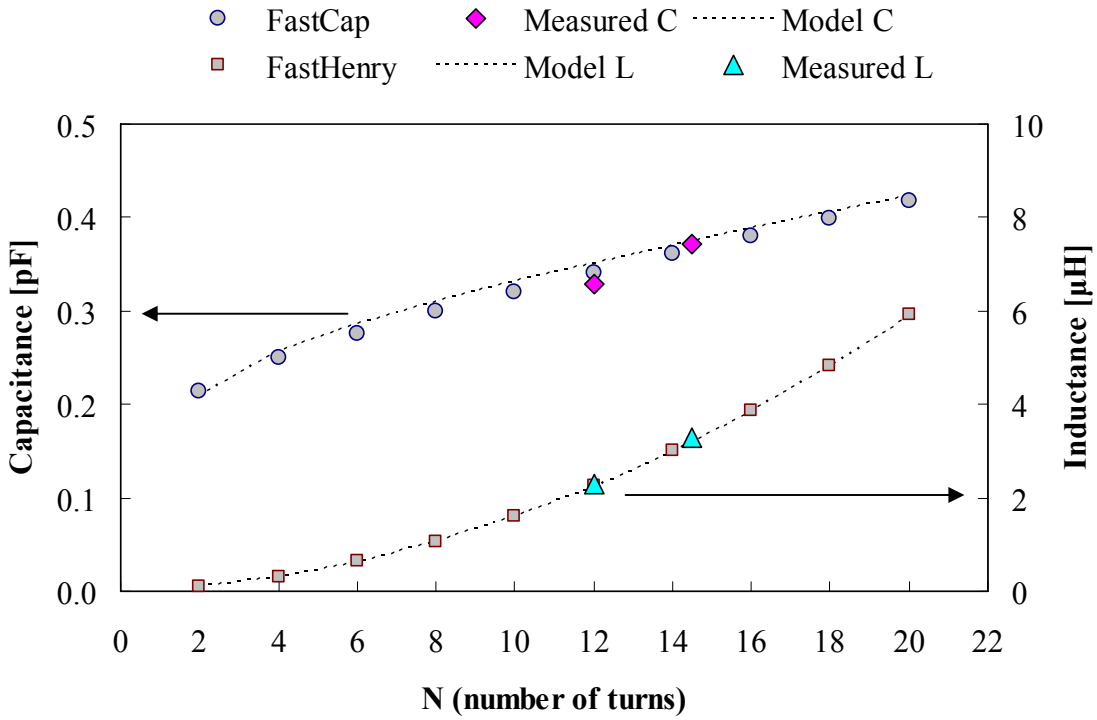

Figure 2.13: Comparison of FastHenry and FastCap simulations, analytical modeling, and measurement to spiral Design1 and Design2 from Table 2.2.

The series resistance was also verified against impedance analyzer measurements for the designs described in Table 2.2. The measured DC resistances are 6.93 Ω, 9.05 Ω, and 4.72 Ω, which are in good agreement with Eq. (2.44) estimates of 6.4 Ω, 7.96 Ω, and 4.53 Ω, for Design1, Design2, and Design3 respectively. The calculated DC resistance values are

within 12% of the measured values. This difference is likely due to variations in spiral line dimensions and actual resistivity of the metal compared to the resistivity found in literature.

The resonant frequencies, measured with an impedance probe and including the probe parasitic capacitance of 1.536 pF, are 77.86 MHz, 64.45 MHz, and 86.96 MHz, and are compared to the analytical model results from Eq. (2.25), which are 77.62 MHz, 64.63 MHz, and 86.11 MHz, for Desing1, Design2, and Design3 respectively. The calculated frequencies are within 1% of the measured values with excellent agreement.

The inductance as a function of frequency was measured and compared to Eq. (2.33). The estimated value of C_{par} plus the probe parasitic capacitance was used for Eq. (2.33). Figure 2.14 graphs the measured and calculated frequency-dependent inductance with good agreement even up to the self-resonance. Figure 2.15 compares Eq. (2.43), Eq. (2.46), and the measured real part of the impedance with good agreement up to the self-resonance for Design1. Similar results were achieved for Design2 and Design3.

Finally, the quality factor of the equivalent circuit shown in Figure 2.5 and defined in Eq. (2.26) is verified. Figure 2.16 graphs the measured and predicted Q values as a function of frequency for Design1 with good agreement up to the self-resonance. Similar results were achieved for Design2 and Design3.

2.1.4 Overlap Capacitance between two Spirals

In Figure 2.1, two sensor concepts were introduced. The concept from Figure 2.1b implements two planar spiral inductors overlapping each other. This requires the calculation of the overlap capacitance between the spiral inductors. The analytical estimation, using parallel plate theory, of the overlap capacitance C_{ove} is given by [88]

$$C_{ove} = \frac{\epsilon A_{ove}}{t_g} \ , \tag{2.47}$$

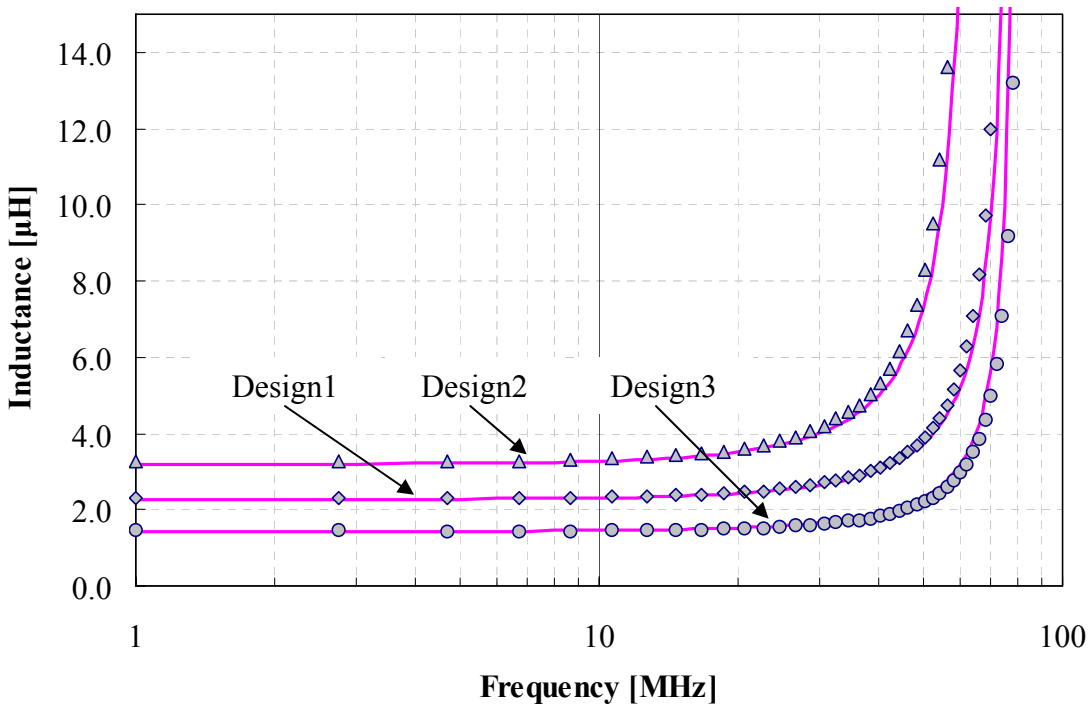

Figure 2.14: Measured and calculated (from Eq. (2.33)) frequency dependent inductance for planar spiral inductors. The solid lines represent the model while the measured data are represented by diamonds for Design1, triangles for Design2, and circles for Design3.

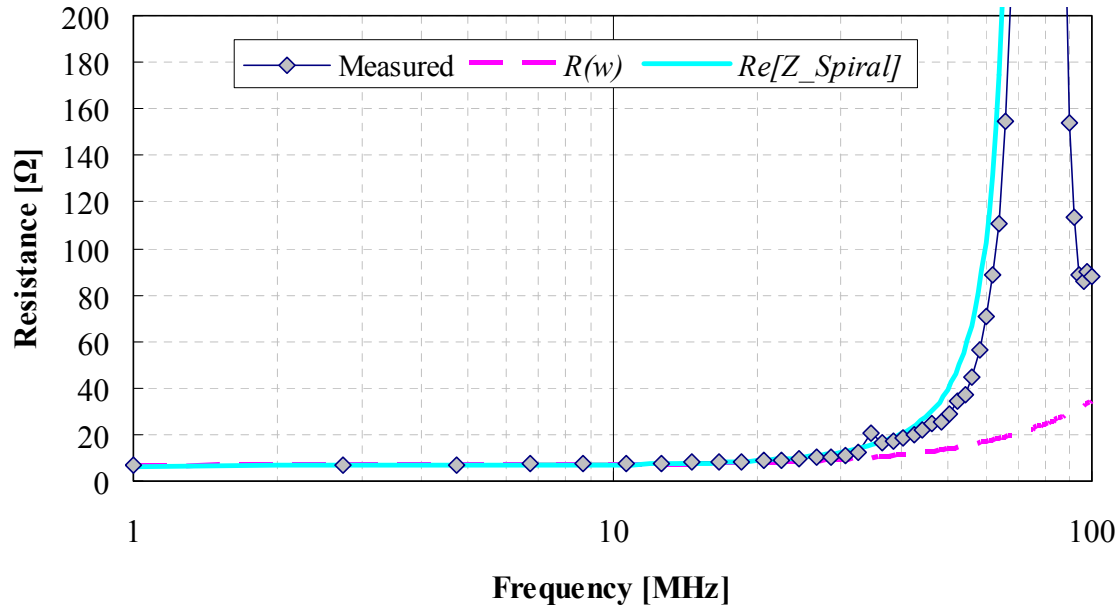

Figure 2.15: Comparison of measured real part of the coil impedance (diamonds) compared to $R(\omega)$ from Eq. (2.43) (dashed line) and $Re[Z_{spiral}]$ from Eq. (2.46) (solid line) for Design1.

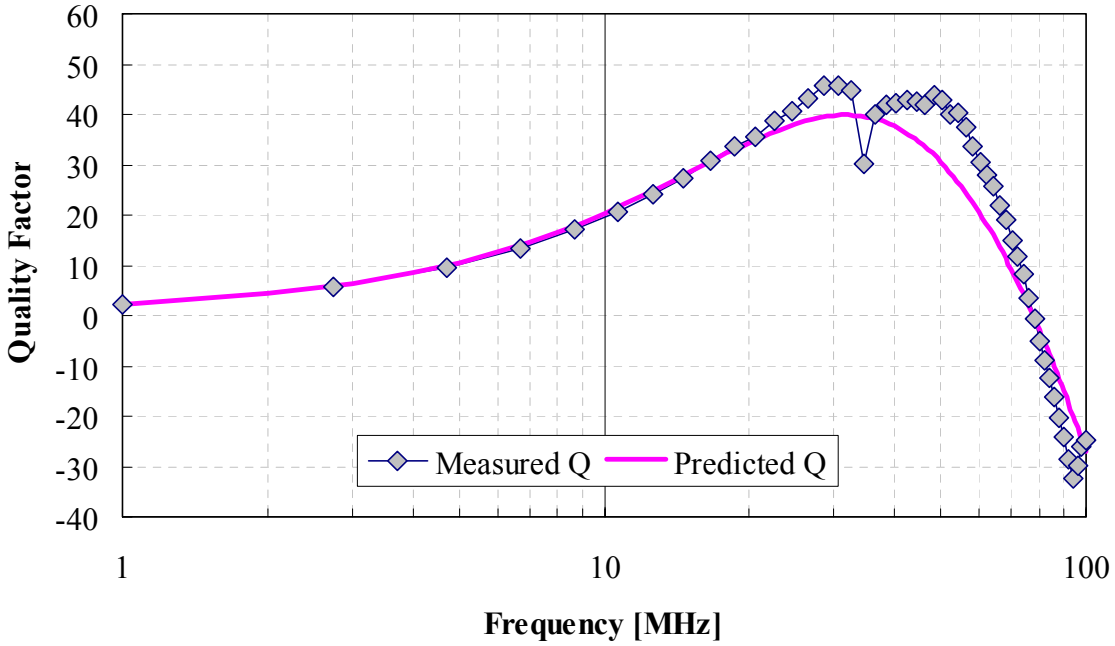

Figure 2.16: Comparison of measured (diamonds) and predicted (solid line) quality factor Q (from Eq. (2.26)) for Design1.

where t_g is the the gap between the coils, A_{ove} is the overlap area between two planar spirals, and ϵ is the dielectric constant of the substrate separating the coils. To take into account the dielectric loss, a complex permittivity ϵ is used, given by

$$\epsilon = \epsilon' - j\epsilon'' = |\epsilon|\, e^{-j\delta} \ , \tag{2.48}$$

where ϵ' is real part of the permittivity and ϵ'' is the imaginary part accounting for the dielectric loss. In phasor notation, δ is the dielectric loss angle. For good dielectrics with $\epsilon' >> \epsilon''$, the approximation

$$\frac{\epsilon''}{\epsilon'} = \tan\delta \tag{2.49}$$

allows further simplification, where $tan\delta$ is the loss tangent or dissipation factor. Using the approximation from Eq. (2.49) in Eq. (2.48), the complex permittivity can be rewritten as

$$\epsilon = \epsilon_0\epsilon_r(1 - j\tan\delta) \ . \tag{2.50}$$

By replacing ϵ in Eq. (2.50) for Eq. (2.47), the complex impedance shown in Figure 2.17 is defined as

$$Z^*_{ove} = R_c - jX_c = \left[j\omega\left(\epsilon_0\epsilon_r(1 - j\tan\delta)\frac{A_{ove}}{t_g}\right)\right]^{-1} \ , \tag{2.51}$$

where R_c is the capacitance series resistance, defined as

$$R_c = \frac{t_g}{\omega\epsilon_0\epsilon_r \cdot \tan\delta \cdot A_{ove}} \ , \tag{2.52}$$

and X_c is the capacitance reactance, defined as

$$X_c = \frac{t_g}{\omega\epsilon_0\epsilon_r \cdot A_{ove}} \ . \tag{2.53}$$

The circuit in Figure 2.17 was chosen to be in series instead of parallel because of the desired current flow at low and high frequencies. The series model requires all the current to flow through both elements while the parallel model allows for current flow in the resistor even when the capacitive impedance is very high. Since the substrate materials in this work are considered good dielectrics, they should not necessarily conduct when the capacitive impedance is high, the series model is used in this work.

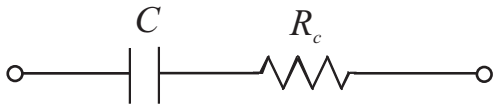

Figure 2.17: Equivalent circuit model for overlap capacitance including the dielectric loss, represented by the series resistance.

For circular planar spiral inductor geometries used in this work, the overlap area A_{ove} is not simply the area of one spiral. The counter rotation of the coils required for constructive mutual coupling reduces the overlap between the spirals. Without the counter rotation, the coupling would act to cancel the magnetic field. Figure 2.18a illustrates two stacked circular planar spirals; from this it is clear that the entire coil area is not completely overlapping. The top and bottom portion of the coil is offset by the pitch of the coil while the sides are completely overlapping. To estimate the overlap area, geometric intersection of the two coils is performed, resulting in Figure 2.18b.

Calculating the area of one spiral and the intersected area from Figure 2.18b, the calculated ratio of the two is given by $A_{intersect}/A_{spiral}$. The overlap ratio was calculated for designs with 2-20 turns and coil pitch of 120 and 300 μm, which is graphed in Figure 2.19.

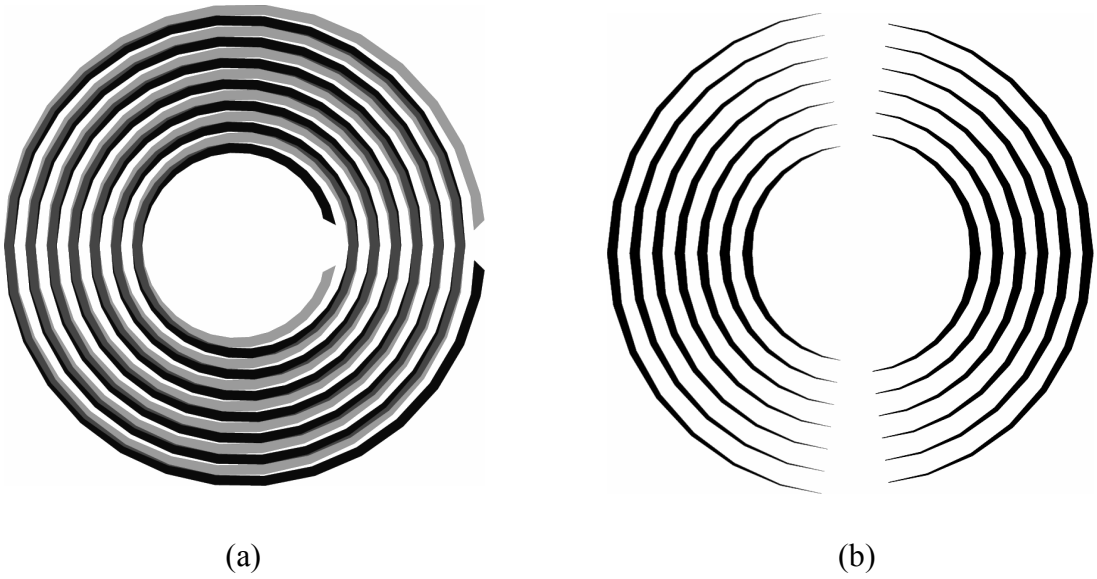

Figure 2.18: Example demonstrating the overlap area for circular planar spiral inductors used in this research: two stacked circular planar spirals inductors (a) and the geometric intersection (b) resulting in the overlap area.

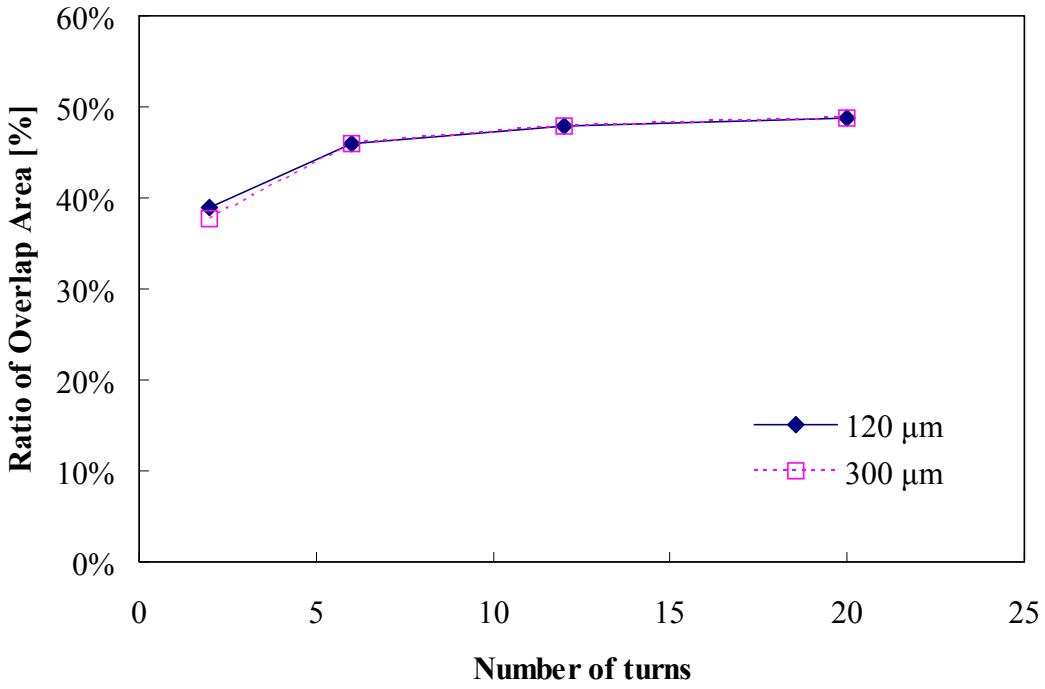

Figure 2.19: Ratio of spiral overlap area as a function of the number of turns. The ratio calculation includes spirals with 120 and 300 μm pitch (ls/lw ratio of 1) and r_s of 3.8 and 4 mm respectively.

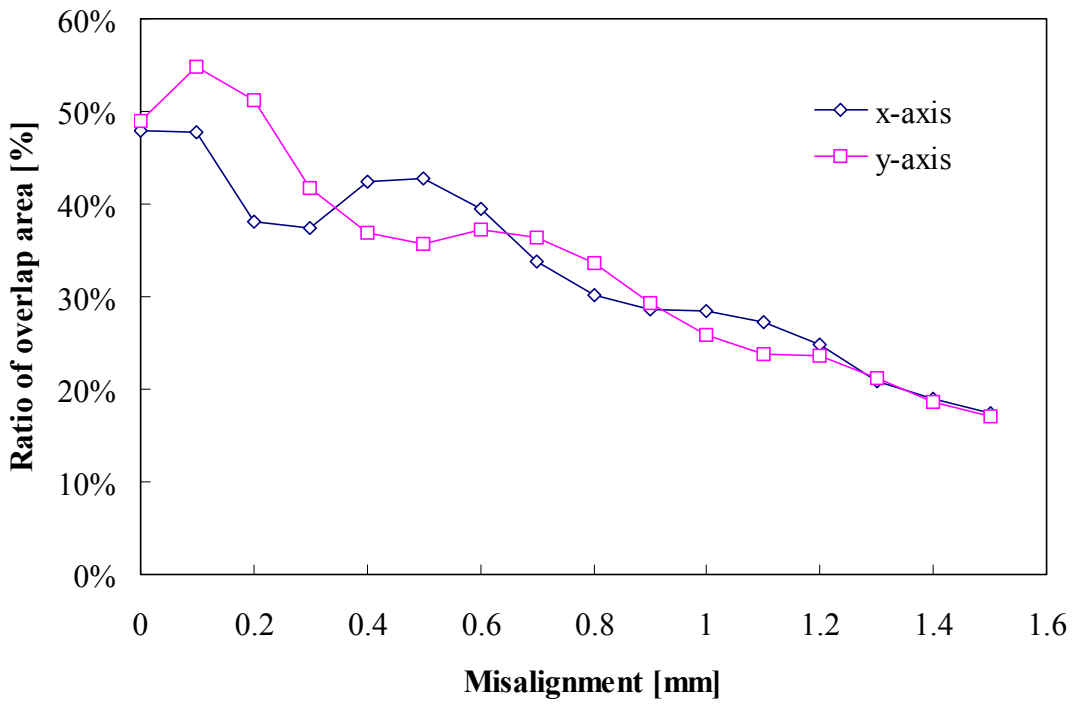

Figure 2.20: Ratio of spiral overlap area as a function of misalignment between the two spirals. The spirals in this calculation have a pitch of 120 μm, r_s of 3.8 mm, and ls/lw ratio of 1. One spiral was misaligned by sweeping it in 100 μm intervals along the x and y axis.

As the number of turns increases, the ratio approaches 50%. The sensitivity of alignment between the spirals was calculated by offsetting one spiral in 100 μm increments and estimating the area overlap ratio, graphed in Figure 2.20. At 400 μm of misalignment, the overlap ratio is reduced by 10%. For most of the spiral designs considered in this work the ratio can be approximated to 45%. Using this approximation, the general analytical solution for the overlap area A_{ove} of circular planar spiral geometries used in this work is given by

$$A_{ove} = 0.45 \cdot lw \cdot ll \ , \tag{2.54}$$

where lw is the line width and ll is the spiral length from Eq. (2.38). Replacing Eq. (2.54) in Eq. (2.47) yields

$$C_{ove} = \frac{0.45 \cdot \epsilon \cdot lw \cdot ll}{t_g} \ . \tag{2.55}$$

where the complex permittivity ϵ was not replaced by Eq. (2.50) for simplicity. Verification of Eq. (2.55) will be presented in the next section §2.1.5.

2.1.5 Sensor *LC* Resonant Circuit Model

In previous sections, the inductor and capacitor models were discussed separately. Next, they are combined to create the sensor LC resonant circuit model, whose cross-section is illustrated in Figure 2.21. The circuit for this model is not a fully distributed element model, however, sufficient distribution is included to account for many of the desired effects.

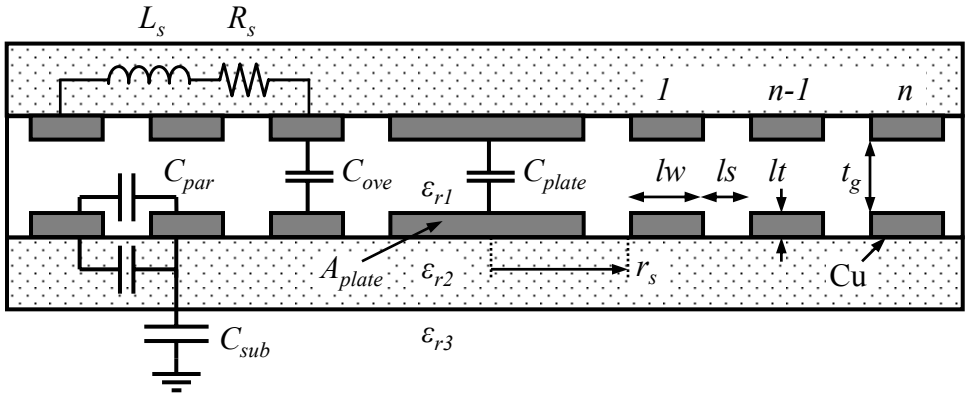

Figure 2.21: Cross-sectional view of a LC resonant circuit used to illustrate the distributed elements of the model.

In Figure 2.21, two oppositely wound planar spiral inductors L_s are separated by a gap t_g. The spirals have a series resistance R_s and parasitic self-capacitance C_{par}. The gap allows for capacitive coupling through the overlap capacitance of C_{ove} between the two spirals as well as magnetic coupling through the mutual inductance L_m (not drawn). The spirals are also connected to a parallel plate capacitor C_{plate}, which will become the pressure-variable capacitance. Although devices can be fabricated to make the overlap capacitance C_{ove} the sensing capacitance, by fabricating them on pressure deformable plates, this concept is not pursued further in this work. However, this type of pressure sensitive device was introduced in [23], and more recently presented in [46].

Figure 2.22 graphs the general circuit for the analytical LC resonant circuit model. This circuit represents the sensor concept graphed in Figure 2.1b, a sensor with embedded circuitry and no ohmic via interconnect. Also, the four nodes listed (1-4) have substrate impedances. These were left out to simplify the circuit and will be discussed later in this section.

The circuit in Figure 2.22 includes the parasitic self-capacitance C_{par}, series resistance R_s and inductance L_s, derived in section §2.1.3 for each planar spiral inductor. The equivalent overlap capacitance $C_{ove\ eq}$ in Figure 2.22 includes two separate capacitive elements in parallel that are added together. One element is the planar spiral overlap capacitance C_{ove} derived in section §2.1.4. The other is the pressure-variable parallel plate capacitance C_{plate}. The value of $C_{ove\ eq}$ in the circuit of Figure 2.22 is given by

$$C_{ove\ eq} = \tfrac{1}{2}\left(C_{ove} + C_{plate}\right) \ , \tag{2.56}$$

where C_{plate} is given by

$$C_{plate} = \frac{\epsilon A_{plate}}{t_g} \ , \tag{2.57}$$

where the plate area is A_{plate} and the plate gap is t_g. In Eq. (2.56), the sum of the capacitances is divided by a factor of two to distribute the capacitance into two elements in the circuit shown in Figure 2.22.

From Figure 2.22, other sensor concepts can be represented by simplifying the circuit. One case has the spiral terminals connected through an ohmic via thereby removing one of the $C_{ove\ eq}$ elements, illustrated in Figure 2.23a. For this case, the remaining value of the $C_{ove\ eq}$ is not necessarily divided by two as in Eq. (2.56). Another case implements only one spiral inductor, which is connected to $C_{ove\ eq}$ simplifying the circuit to Figure 2.23b, where $C_{ove\ eq}$ reduces to C_{plate}.

To simplify current mesh analysis of Figure 2.22, the circuit is rearranged to an equivalent circuit graphed in Figure 2.24, where C_{sub} is introduced as the substrate and environmental impedance. Although C_{sub} is graphed as a capacitor in Figure 2.24, it can include losses

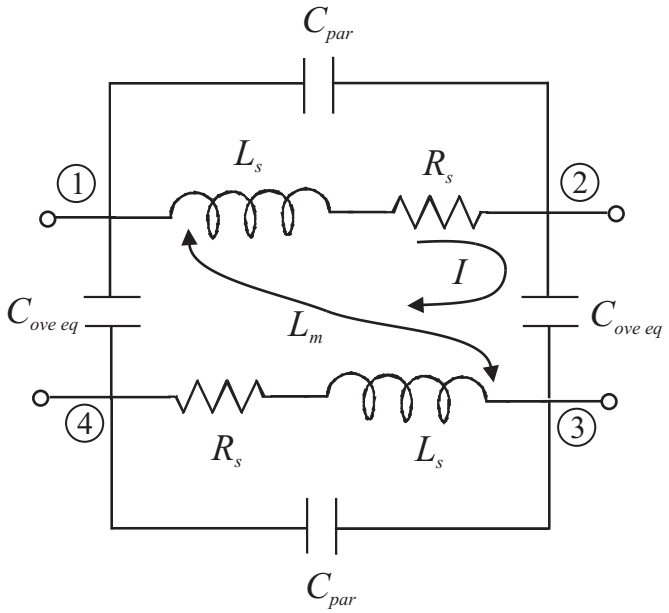

Figure 2.22: Circuit model for a sensor with two planar spiral inductors that are capacitively and inductively coupled.

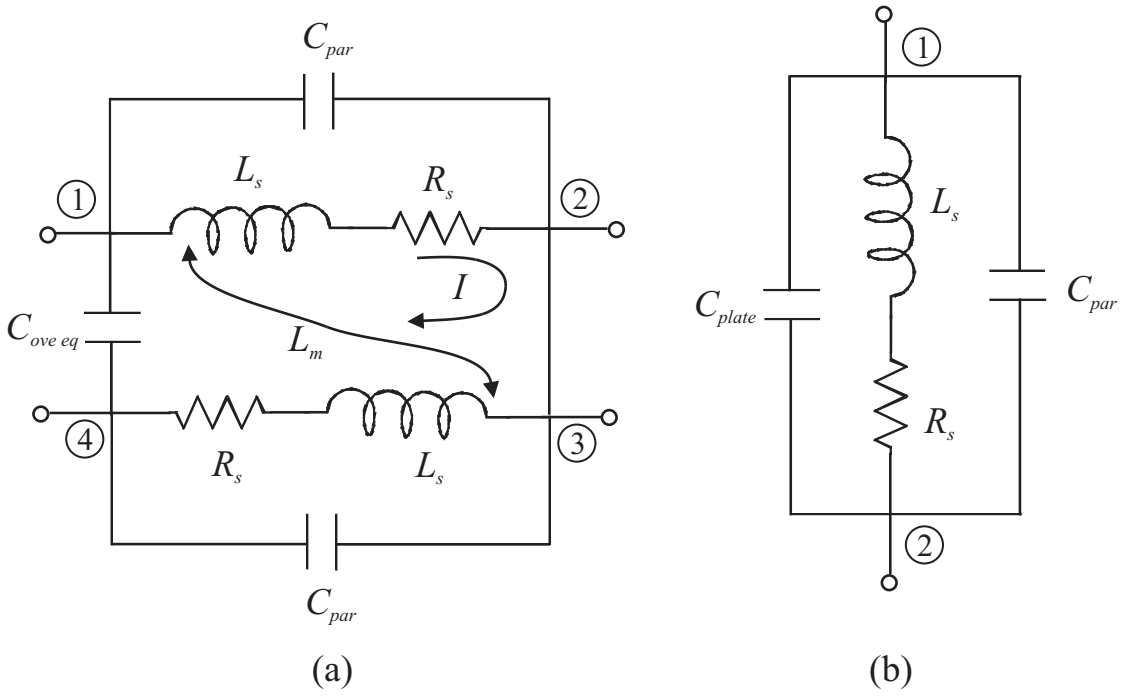

Figure 2.23: Circuit model for a sensor with two planar spirals interconnected through a via (a), and for a sensor with one spiral (b).

depending on several factors such as the substrate, sensor coating, or surrounding environment. For now it will be left as an ideal capacitor as C_{sub}.

All mesh currents in Figure 2.24 are drawn to flow in the clockwise direction, and the voltages and currents V_2, V_3 and I_2, I_3 are across the series inductance L_s and series resistance R_s for each spiral respectively. The other two labeled currents, I_4 and I_5, are mesh analysis currents. The inductances are coupled to each other by the mutual inductance L_m, which is drawn to indicate constructive coupling of the magnetic flux through each spiral. An important aspect of this model is that the symmetry of the circuit generates voltages of equal magnitude and opposite phase at the labeled nodes. The voltage drop from node 1 to 2 is equal to the voltage drop from nodes 3 to 4. Therefore, the voltage at node 1 is equal in magnitude as node 4 but out of phase by 180°. The same occurs with nodes 2 and 3.

The inductances of each planar spiral L_s are also coupled to an external antenna L_a through the mutual inductance L_{ma}. The antenna L_a has a voltage V_1 and current I_1, not graphed in Figure 2.22 or Figure 2.24. However, the coupling of the antenna is equivalent to that of Figure 2.2 in section §2.1.1.

Analysis of the circuit in Figure 2.24 begins by defining the voltages across the spirals and antenna as

$$V_1 = sLaI_1 + sL_{ma}I_2 + sL_{ma}I_3 \tag{2.58a}$$

$$V_2 = R_sI_2 + sL_sI_2 + sL_mI_3 + sL_{ma}I_1 \tag{2.58b}$$

$$V_3 = R_sI_3 + sL_sI_3 + sL_mI_2 + sL_{ma}I_1 \ , \tag{2.58c}$$

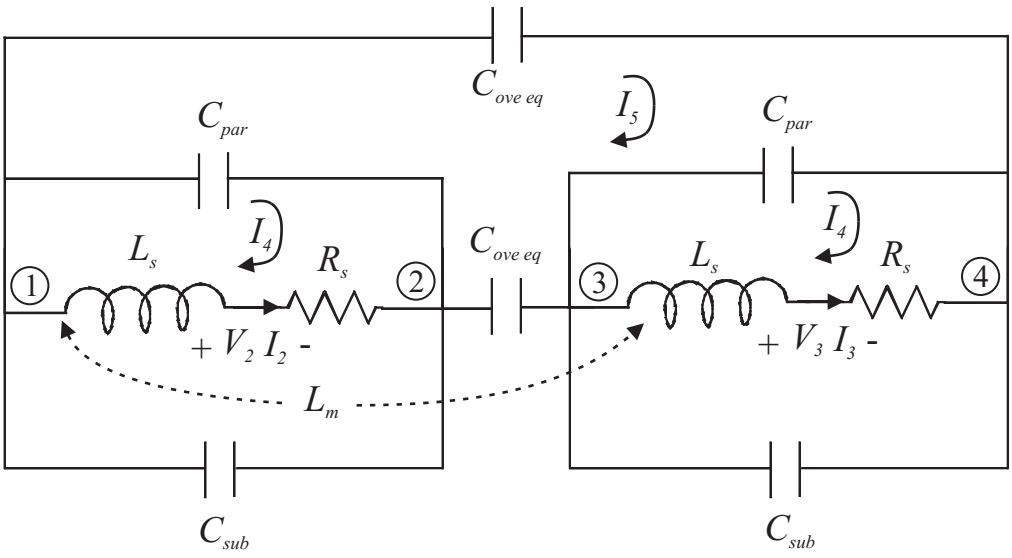

Figure 2.24: Circuit model for a sensor with two planar spiral inductors that are capacitively and inductively coupled. This circuit is equivalent to Figure 2.22 and was rearranged to simplify mesh analysis.

where $V_2 = V_3$. Next, we can combine C_{par} and C_{sub} from Figure 2.24 in parallel as $Z_{par\ eq}$. Therefore, the mesh equations are given by

$$-V_2 + Z_{par\ eq}(I_4 - I_5) = 0 \tag{2.59a}$$

$$Z_{ove\ eq}I_5 - V_3 + Z_{ove\ eq}I_5 - V_2 = 0 \tag{2.59b}$$

$$-V_3 + Z_{par\ eq}(I_4 - I_5) = 0\ , \tag{2.59c}$$

where the impedance Z_* represents the impedance for each circuit element and * is one of the elements ($_{par\ eq},\ _{ove\ eq}$) in Eq. (2.59). Now we solve for I_5 from Eq. (2.59b) and replace the impedances back to circuit elements, resulting in

$$I_5 = C_{ove\ eq}s(I_3R_s + I_2L_ms + I_3L_ss + I_1L_{ma}s)\ . \tag{2.60}$$

Replacing I_5 back into Eq. (2.59) and solving for I_4 from Eq. (2.59c) yields

$$I_4 = (C_{ove\ eq} + C_{par} + C_{sub})s(I_3R_s + I_2L_ms + I_3L_ss + I_1L_{ma}s)\ . \tag{2.61}$$

Now, setting $I_3 = -I_4$ and solving for I_3 results in

$$I_3 = -\frac{(C_{ove\ eq} + C_{par} + C_{sub})(I_2L_m + I_1L_{ma})s^2}{1 + (C_{ove\ eq} + C_{par} + C_{sub})s(R_s + sL_s)}\ , \tag{2.62}$$

which is a function of I_2 and I_1. Replacing I_3 back into I_4 and setting $I_2 = -I_4$ and solving for I_2 equals

$$I_2 = -\frac{C_{eq} I_1 L_{ma} s^2}{1 + C_{eq} s(R_s + L_{eq} s)} \tag{2.63}$$

where the terms C_{eq} and L_{eq} are the equivalent capacitance and inductance respectively, and are defined as

$$C_{eq} = C_{ove\ eq} + C_{par} + C_{sub} \Longrightarrow \tfrac{1}{2}\left(C_{ove} + C_{plate}\right) + C_{par} + C_{sub} \tag{2.64a}$$

$$L_{eq} = L_m + L_s \Longrightarrow L_s(1 + k_m)\ , \tag{2.64b}$$

where k_m is the coupling coefficient between the two planar spiral inductors. In Eq. (2.64a), the factor of $\frac{1}{2}$ in front of C_{ove} and C_{plate} is due to the fact that the total capacitance is split up into two separate distributed elements $C_{ove\ eq}$ for the circuit in Figure 2.24.

Substituting I_2 and I_3 from Eq. (2.63) and Eq. (2.62) into Eq. (2.58a) results in the input impedance Z_1, which is given by

$$Z_1(s) = \frac{V_1}{I_1} = L_a s - \frac{2 C_{eq} L_{ma}^2 s^3}{1 + C_{eq} R_s s + C_{eq} L_{eq} s^2}\ . \tag{2.65}$$

Eq. (2.65) links the analytical models derived in sections §2.1.3 and §2.1.4 and the measurable quantity of the input impedance of the loop antenna L_a. In addition, Eq. (2.65) is similar to Eq. (2.8) from section §2.1.1 except for the factor of 2, which is due to the antenna being coupled to two spiral inductors. Further simplification of Eq. (2.65) is achieved by defining

$$f_0 = \frac{1}{2\pi\sqrt{L_{eq} C_{eq}}} \tag{2.66a}$$

$$Q = \frac{\omega_0 L_{eq}}{R_s} \tag{2.66b}$$

$$L_{ma} = k_a \sqrt{L_a L_s} \tag{2.66c}$$

$$L_m = k_m L_s\ , \tag{2.66d}$$

where k_a is the coupling coefficient between the antenna and planar spirals and k_m is the coupling coefficient between the two planar spirals. Also, in Eq. (2.66b) the series resistance

R_s is equal to the total loss. Replacing s with $s = j\omega = j2\pi f$, Eq. (2.65) can be rewritten as

$$Z_1(f) = j2\pi f L_a \left[1 + k_a^2 \left(\frac{2}{1+k_m} \right) \cdot \left(\frac{\left(\frac{f}{f_0}\right)^2}{1 - \left(\frac{f}{f_0}\right)^2 + \frac{j}{Q}\left(\frac{f}{f_0}\right)} \right) \right] . \tag{2.67}$$

Eq. (2.67) is equivalent to Eq. (2.9) in section §2.1.1. The factor of $2/(1 + k_m)$ next to the coupling coefficient k_a takes into account the energy absorbed by the planar spirals L_s from the coupling antenna L_a. This is due to the antenna L_a being coupled to two planar spiral inductors, hence the factor of 2, and is also proportional to the coupling coefficient k_m between the two planar spirals. When the two planar spirals are strongly coupled (effectively almost becoming one single inductor of inductance $L_{eq} = L_s + L_m$), the factor $2/(1 + k_m)$ approaches unity as k_m approaches unity. As the spirals become poorly coupled (the spirals are closer to individual inductors of inductance L_s), the factor approaches 2 as k_m approaches zero.

For the case when there exists a via interconnect, graphed in Figure 2.23a, the same circuit analysis is performed, resulting in Eq. (2.65) for input impedance Z_1 of the antenna L_a. However, the equivalent capacitance C_{eq} is redefined as

$$C_{eq} = 2C_{ove\ eq} + C_{par} + C_{sub} = 2\left(C_{ove} + C_{plate}\right) + C_{par} + C_{sub} . \tag{2.68}$$

In this case, the factor of $\frac{1}{2}$ in front of C_{ove} and C_{plate} used Eq. (2.64a) is not necessary because the capacitance values are lumped into one circuit element as shown in Figure 2.23a.

Finally, for the case where there is only one planar spiral (see the concept described in Figure 2.1a), with the circuit shown in Figure 2.23b, the factor of $2/(1 + k_m)$ in the impedance disappears. Additionally, L_{eq} reduces to L_s and C_{eq} reduces to C_{plate}. This result is equivalent to the model derived in section §2.1.1 Eq. (2.9).

To include the losses from imperfect dielectrics, Eq. (2.65) can be modified to include the equivalent resistance R_{eq} due to dielectric dissipation, which was derived in section §2.1.4

in Eq. (2.51). Thus C_{eq} in Eq. (2.65) is replaced with $C_{eq} - jR_{eq}$, which results in

$$Z_1(s) = L_a s - \frac{2(C_{eq} - jR_{eq})L_{ma}^2 s^3}{1 + (C_{eq} - jR_{eq})R_s s + (C_{eq} - jR_{eq})L_{eq} s^2} \ , \tag{2.69}$$

where R_{eq} is defined as

$$R_{eq} = R_{ove\ eq} + R_{par} + R_{sub} \ . \tag{2.70}$$

Each resistance in Eq. (2.70) is associated with a specific dielectric section of the design. This allows for more effective modeling of various loss effects. Simplification of Eq. (2.69) is performed in a similar fashion to Eq. (2.65). However, the use of numerical solvers, such as MATLAB, will be sufficient to calculate the complex impedance from Eq. (2.69).

The model derived above can be used to guide sensor design for optimal operation of a given characteristic. To illustrate this, Eq. (2.66) is used to calculate sensor self resonance frequency and quality factors for designs whose starting radius ranges from r_s = 1 to 5 mm versus the number of turns n, illustrated in Figure 2.25. The designs use a pitch of p_s = 120 μm, line width of lw = 60 μm, line spacing of ls = 60 μm, line thickness of lt = 20 μm, relative permittivity of ϵ_r = 2.1, and loss tangent $tan\delta = 4x10^{-4}$. As expected, the frequency decreases with increasing r_s due to the increased inductance and the quality factor maximum shifts down with number of turns since the L_m/R_s ratio maximum occurs at a lower number of turns.

Similarly, r_s can be held constant while the relative permittivity and loss tangent can be varied. This is useful for designing complex systems that include different materials or to capture device behavior when fabricated from materials whose dielectric properties change with temperature, moisture, or any other physical variable. Using the model, the dielectric properties are varied from ϵ_r = 1 to 5 and $tan\delta = [1x10^{-4}\ 1x10^{-3}\ 1x10^{-2}\ 1x10^{-1}]$, and the results are graphed in Figure 2.26 and Figure 2.27 respectively. As the permittivity increases, so does the frequency. The quality factor reduces with increasing permittivity even though the loss tangent was held constant because the higher permittivity induces greater dielectric loss in the system through the displacement current. For the case with constant permittivity and varying loss tangent, the frequency remains constant since it does

not vary with $tan\delta$ and the quality factor decreased. These results are in agreement with electromagnetic theory of dielectric loss. It should be noted that C_{sub}, in Figure 2.21, is ignored for the calculations above because it is assumed that devices are surrounded by air. C_{sub} will be used to model changes of surrounding media in Chapter 4, §4.4 and verified in Chapter 5, §5.1.6.

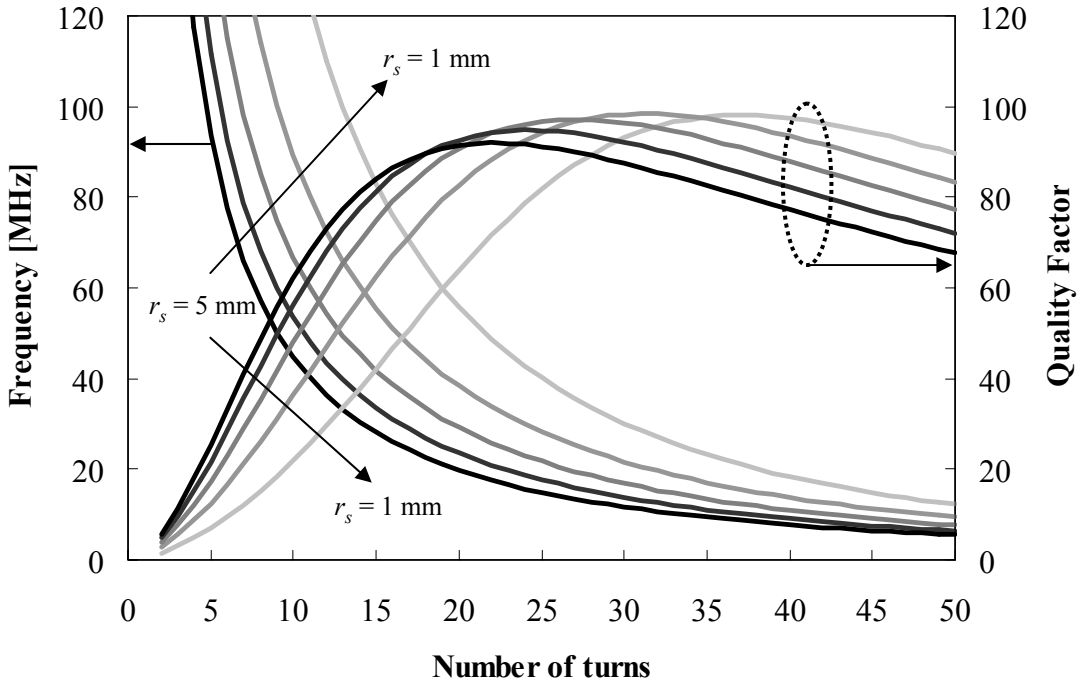

Figure 2.25: Example parametric sweep of number of turns n and spiral starting radius r_s while the pitch, line width, line spacing, line thickness, relative permittivity, and loss tangent were held constant.

2.1.6 Sensor Electromagnetic Model Verification

To verify Eq. (2.65) through Eq. (2.67), several non-pressure sensitive devices were fabricated from PTFE polymeric substrates. The fabricated devices implement two planar spirals, described by the concept in Figure 2.1b and the equivalent circuit in Figure 2.24, which means they do not implement a via interconnection between the spirals. The device geometric and material characteristics, described by the cross-sectional view in Figure 2.21,

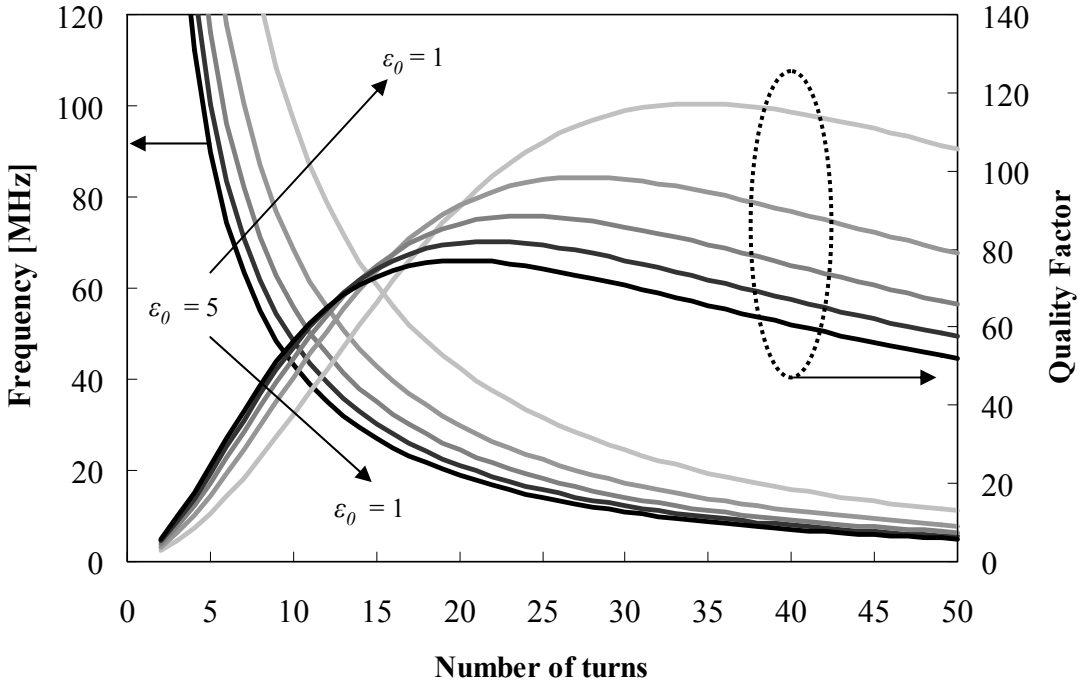

Figure 2.26: Example parametric sweep of number of turns n and substrate relative permittivity ϵ_r while the starting radius, pitch, line width, line spacing, line thickness, and loss tangent were held constant.

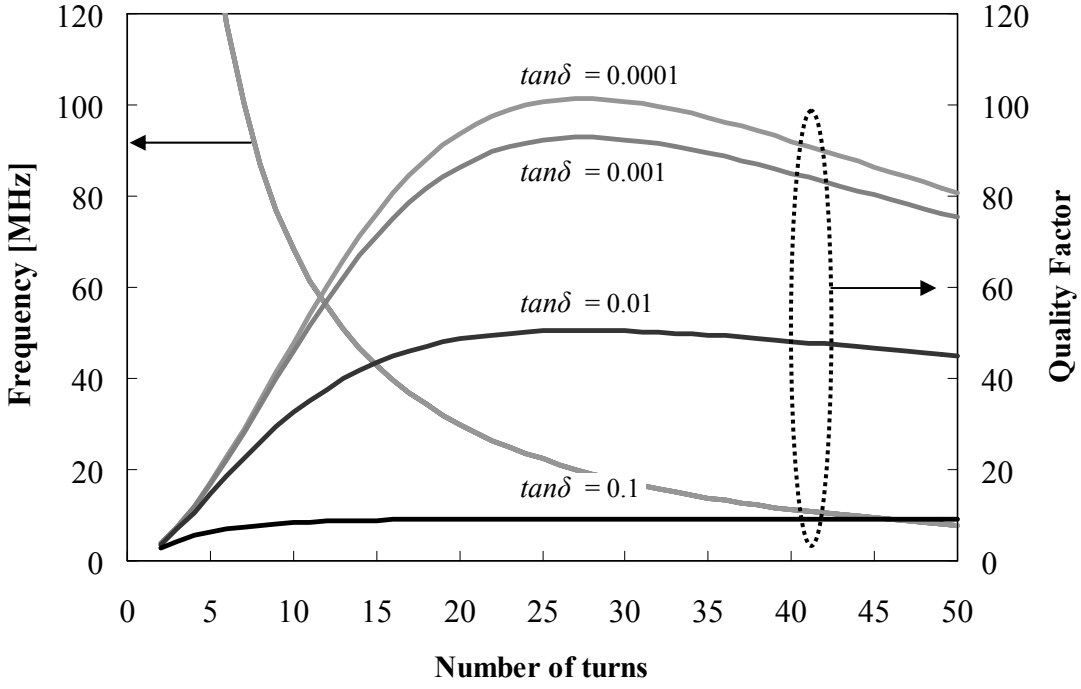

Figure 2.27: Example parametric sweep of number of turns n and substrate loss tangent $tan\delta$ while the starting radius, pitch, line width, line spacing, line thickness, and relative permittivity were held constant.

are summarized in Table 2.4. Using Table 2.4 and the analytical model described in section §2.1.5, circuit-element values for Designs1-5 (D1-D5) were calculated and are summarized in Table 2.5.

Table 2.4: Planar spiral geometrical (measured) and material characteristics used to verify the analytical model.

Characteristic	**D1**	**D2**	**D3**	**D4**	**D5**
n	12	14	15	16	17
lw	54.5 μm				
ls	66.7 μm				
lt	17 μm				
r_s	3.8 mm				
Substrate	75 μm thick PTFE				
t_g	110 μm PTFE				
PTFE ϵ_r [a]	2.06				
PTFE $tan\delta$ [a]	0.0008				
Cu ρ [a]	1.72×10^{-8} Ωm				
A_{plate}	13.92 μm^2				

[a] From supplier literature or bulk material property.

From the circuit elements in Table 2.5, the impedance magnitude and phase can be calculated from Eq. (2.69). The impedance comparison between the model and measured data for design D3 from Table 2.4 are graphed in Figure 2.28. The antenna L_a for these measurements had an inductance of 0.56 μH. Additionally, the coupling coefficient k_a between the antenna and planar spirals was extracted from the measurements with a value of 0.083. Both the antenna inductance and coupling values were used in Eq. (2.69) to calculate the model impedance. The calculated resonance frequency f_0 is 37.60 MHz and is 1.17% lower than the measured value of 38.05 MHz. The difference in f_0 is attributed to variation in the overall gap between the spirals. The calculated quality factor Q is 79 and is 9.43% higher than the measured value of 72.2. The error in Q is likely due to inaccuracies in metal resistivity and polymer loss tangent as well as metal-trace dimensions.

The measured and calculated resonant frequencies f_0 for designs in Table 2.4 are plotted versus the number of turns in Figure 2.29a. The variation in frequency between the

Table 2.5: Summary of analytically calculated circuit parameters for five LC resonant circuits with different number of spiral turns.

Characteristic	**Eq.**	**D1**	**D2**	**D3**	**D4**	**D5**
L_s [μH]	Eq. (2.32)	2.24	2.99	3.40	3.84	4.31
L_{eq} [μH]	Eq. (2.64b)[a]	4.14	5.52	6.29	7.10	7.97
C_{par} [pF]	Eq. (2.41)	0.73	0.77	0.79	0.81	0.82
R_s [Ω]	Eq. (2.44)	6.37	7.63	8.28	8.95	9.63
$R(f_0)$ [Ω]	Eq. (2.43)	12.11	12.46	12.74	13.08	13.47
$Re[Z_{spiral}]$ [Ω]	Eq. (2.46)	16.88	17.27	17.61	18.03	18.51
C_{ove} [pF]	Eq. (2.55)	1.40	1.67	1.81	1.96	2.11
C_{plate} [pF]	Eq. (2.57)	2.31				
C_{eq} [pF]	Eq. (2.64a)[b]	2.58	2.76	2.85	2.94	3.03
R_{eq} [Ω]	Eq. (2.70)[b]	1.01	1.13	1.19	1.24	1.30
f_0 [MHz]	Eq. (2.66a)	48.65	40.77	37.60	34.83	32.38
Q	Eq. (2.66a)[c]	70.8	76.9	79.0	80.6	81.8

[a] Assumes k_m for stacked planar spirals is 0.85 [88].
[b] C_{eq} is calculated with C_{sub} equal to zero.
[c] For Q, R_s from Eq. (2.66a) is replaced with $Re[Z_{spiral}] + R_{eq}$.

measured and calculated values is likely due to observed inaccuracies during fabrication. Fabrication was done in batch process in a 4x4 array. During lamination, non-uniform pressure resulted in gap gradients between the bonded layers. The quality factor Q for each design is plotted versus number of turns, graphed in Figure 2.29b. It is expected that improved accuracy of the predicted Q can be achieved by taking into account geometrical variations (defects of the metal trace that are not easily measured) or material properties for which bulk properties are used. Additional verification of the electromagnetic model is performed throughout subsequent chapters.

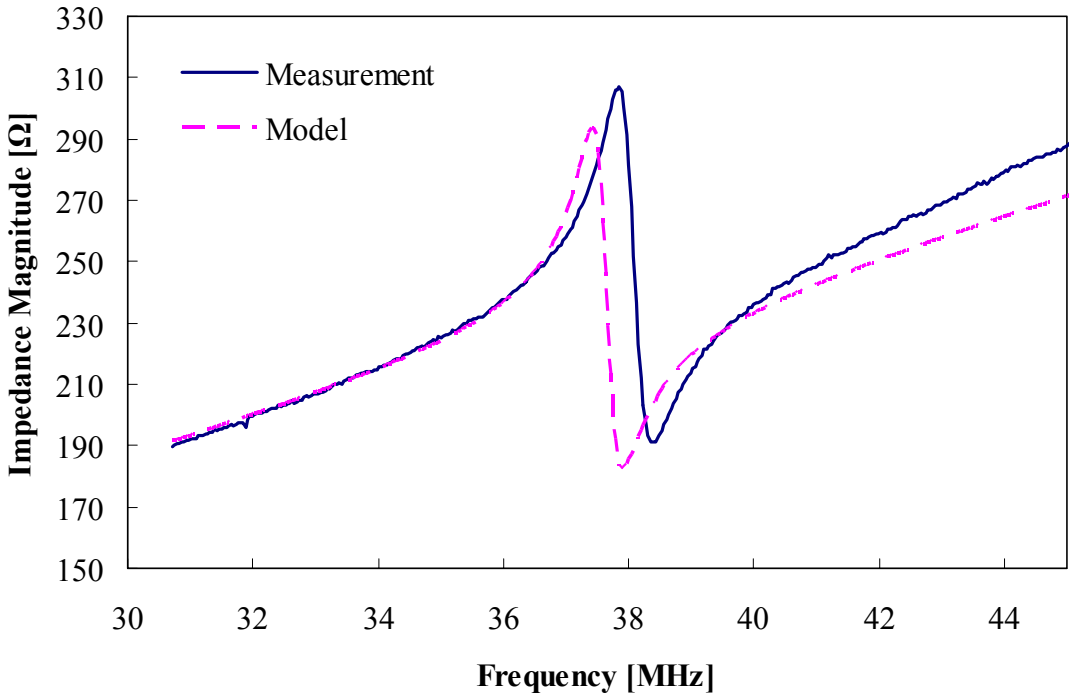

(a) Magnitude

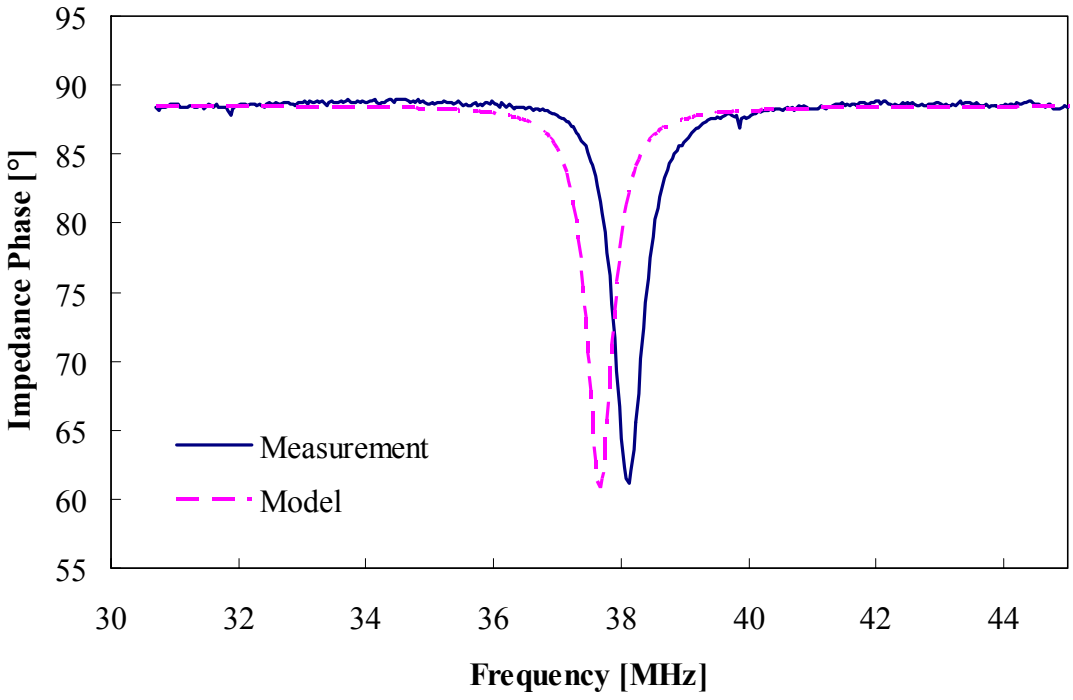

(b) Phase

Figure 2.28: Graph of impedance magnitude and phase vs. frequency for design D3 from Table 2.4.

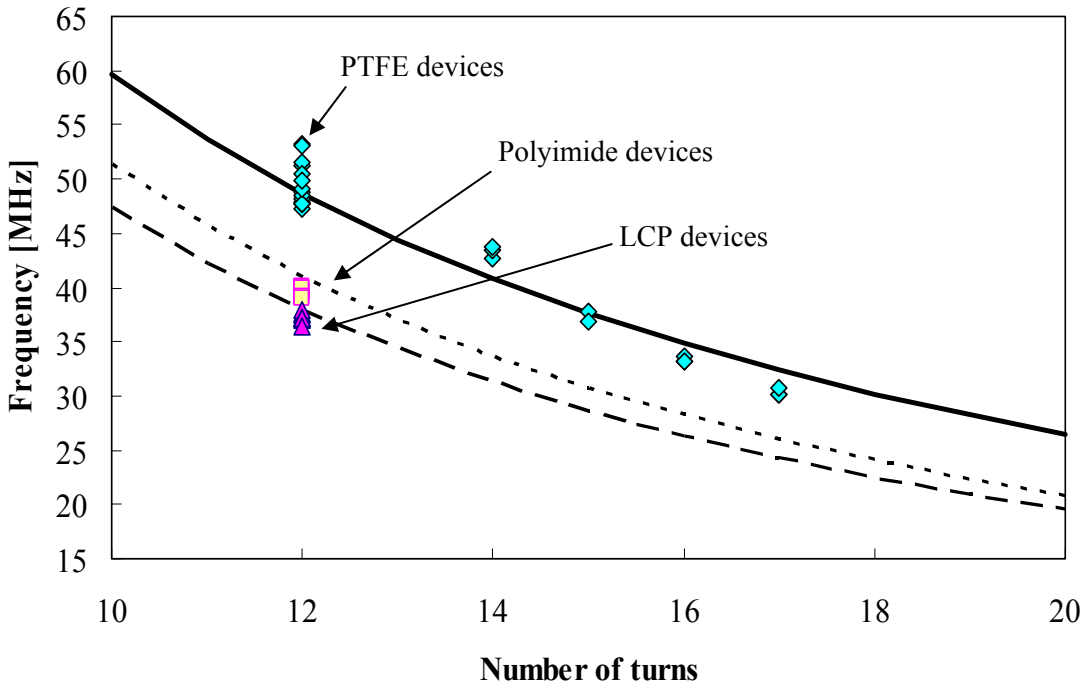

(a) Resonance frequency f_0

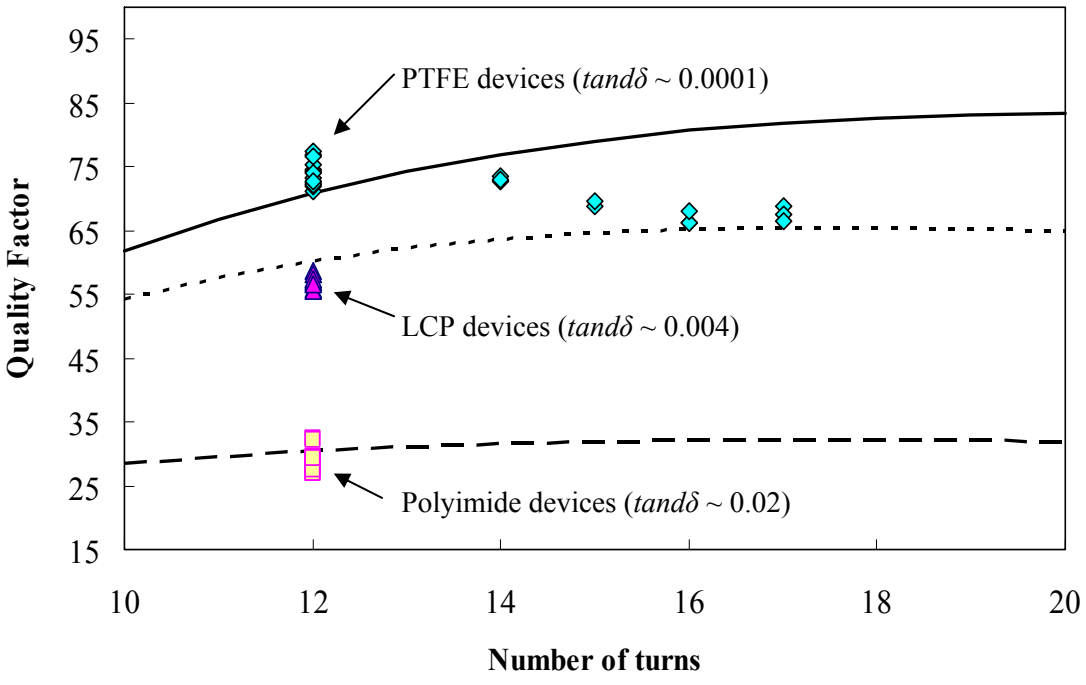

(b) Quality factor Q

Figure 2.29: Graph of frequency f_0 and quality factor Q vs. number of turns comparing measured data and the analytical model from Eq. (2.66) for PTFE, Polyimide, and LCP substrates.

2.2 Sensor Mechanical Theory

Wireless pressure sensor designs in this work implement an embedded cavity enclosed by two pressure deformable plates. To gain further understanding of the deflection of the mechanical structures for both circular and rectangular shapes, two models are investigated. These are a circular plate model and a rectangular plate model.

The cross-sectional view used for the models described above is illustrated in Figure 2.30. The illustration includes diaphragms of different thickness for cases where one plate dominates the mechanical behavior. For the cases where both diaphragms are equal, the models are simplified. Each diaphragm has a center deflection d_{01} and d_{02} corresponding to each thicknesses of t_{m1} and t_{m2}. The axis r in Figure 2.30 is zero at the center of the plate and a at the diaphragm edge. These are separated by a gap t_g, which determines the maximum total center deflection and ultimately the dynamic range of the pressure sensor. The diaphragm boundary conditions are clamped at the edges since they are made of the same material as the rest of the substrate, with Young's modulus E and Poisson's ratio of ν.

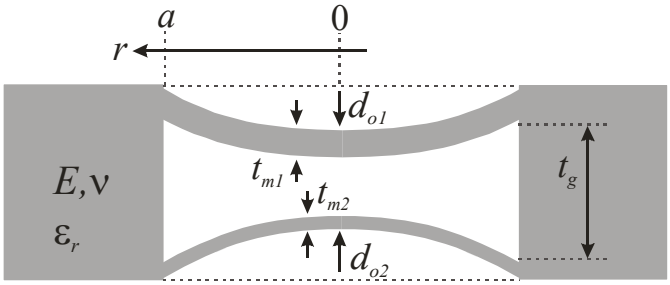

Parameter	Description
t_g	Gap thickness
a	Plate edge on axis r
r	Plate axis
d_{01}	Center deflection for plate 1
d_{02}	Center deflection for plate 2
t_{m1}	Diaphragm 1 thickness
t_{m2}	Diaphragm 2 thickness
E	Young's modulus
ν	Poisson's ratio
ϵ_r	Relative dielectric constant

Figure 2.30: Schematic cross-section of a sealed cavity structure enclosed by two pressure-deformable diaphragms used for the development of sensor mechanical theory.

2.2.1 Plate Flexural Rigidity

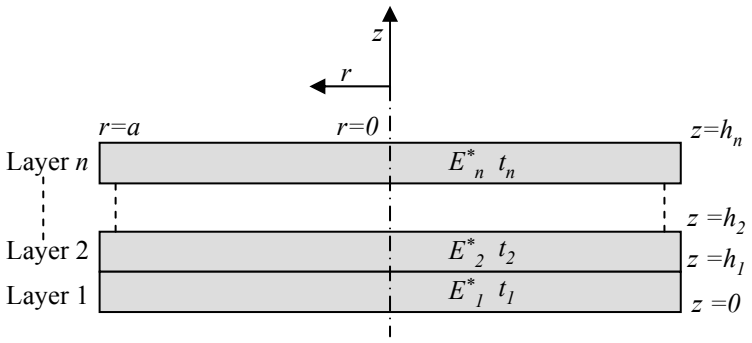

Figure 2.31: Schematic showing the cross-sectional view of a multilayered plate.

The flexural rigidity of a diaphragm defines the bending stiffness when a mechanical load is applied. For the case where a single material is used, the flexural rigidity is given by

$$D = \frac{Et_m^3}{12(1-\nu^2)} \ , \tag{2.71}$$

where E is the Young's modulus, ν is Poisson's ratio, and t_m is the diaphragm thickness. Since some devices will use laminated sheets of different materials to fabricate the sensors, multilayered composite diaphragms are considered, illustrated in Figure 2.31. Therefore, the effective flexural rigidity D_n and effective thickness h_n for n layers are considered, and whose analytical equations were derived in [89]. These are given below for reference. The derivation begins by defining the neutral surface for bending z_n

$$z_n = \frac{\sum_{i=1}^{n} E_i^* t_i (h_{i-1} + \frac{t_i}{2})}{\sum_{i=1}^{n} E_i^* t_i} \ , \tag{2.72}$$

where t_i is the i^{th} layer thickness. The modulus is redefined as

$$E_i^* = \frac{E_i}{1-\nu_i^2} \ . \tag{2.73}$$

The surface interface between any two layers h_i is defined as

$$h_i = \sum_{j=1}^{i} t_j \ , \tag{2.74}$$

where $i = 1 \ldots n$ for Eq. (2.74). The flexural rigidity of a multilayered plate D_n is given by

$$D_n = \sum_{i=1}^{n} E_i^* t_i \left[h_{i-1}^2 + h_{i-1} t_i + \frac{t_i^2}{3} - \left(h_{i-1} + \frac{t_i}{2} \right) z_n \right] . \tag{2.75}$$

Eq. (2.72) and Eq. (2.75) above can be simplified for a monolayered plate with uniform material for n layers, yielding

$$z_n = \frac{h_n}{2} \tag{2.76}$$

and

$$D_n = \frac{E^* h_n^3}{12} . \tag{2.77}$$

From this result it is obvious that Eq. (2.77) is equivalent to Eq. (2.71). Two special cases of interest for the effective flexural rigidity are $n = 2$ and $n = 3$. Both z_n and D_n for these cases are given below. For a bilayer diaphragm ($n = 2$), Eq. (2.72) and Eq. (2.75) simplify to

$$z_n = \frac{E_1^* t_1^2 + E_2^* t_2 (2t_1 + t_2)}{2(E_1^* t_1 + E_2^* t_2)} \tag{2.78}$$

and

$$D_n = E_1^* t_1^2 \left(\frac{t_1}{3} - \frac{z_n}{2} \right) + E_2^* t_2 \left[t_1^2 + t_1 t_2 + \frac{t_2^2}{3} - \left(t_1 + \frac{t_2}{2} \right) z_n \right] . \tag{2.79}$$

For a trilayer diaphragm ($n = 3$), Eq. (2.72) and Eq. (2.75) simplify to

$$z_n = \frac{E_1^* t_1^2 + E_2^* t_2 (2t_1 + t_2) + E_3^* t_3 (2t_1 + 2t_2 + t_3)}{2(E_1^* t_1 + E_2^* t_2 + E_3^* t_3)} \tag{2.80}$$

and

$$\begin{aligned} D_n = E_1^* t_1^2 \left(\frac{t_1}{3} - \frac{z_n}{2} \right) &+ E_2^* t_2 \left[t_1^2 + t_1 t_2 + \frac{t_2^2}{3} - \left(t_1 + \frac{t_2}{2} \right) z_n \right] \\ &+ E_3^* t_3 \left[t_1^2 + t_2^2 + t_1 t_3 + t_2 t_3 + \frac{t_3^2}{3} - \left(t_1 + t_2 + \frac{t_3}{2} \right) z_n \right] . \end{aligned} \tag{2.81}$$

2.2.2 Circular Plate Theory

For the case where the cavity is bounded by a circular plate, the plate radius is equal to a along the radial axis r when using cylindrical coordinates. The shape of the deflected surface for either the top or bottom plate in Figure 2.32 can be represented by [90]

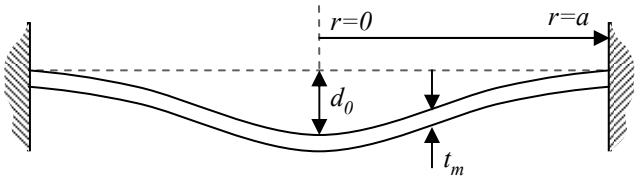

Figure 2.32: Schematic showing the cross-sectional view of a circular plate with clamped edges.

$$d(r) = d_0 \left(1 - \frac{r^2}{a^2}\right)^2 \ , \tag{2.82}$$

where d_0 is the center deflection and $d(r)$ is the deflection as a function of radius r. Using the energy method, an approximate expression for the center deflection of thin plates is derived. The expression assumes both bending and stretching of a uniformly loaded circular plate and is given by [90] [1]

$$d_0 = \frac{Pa^4}{64D} \underbrace{\frac{1}{1 + 0.488\left(\frac{d_0}{t_m}\right)^2}}_{\text{Stretching Factor}} \ , \tag{2.83}$$

where P is a uniformly applied pressure load, t_m is the corresponding plate thickness and D is flexural rigidity. The last term on the right hand side of Eq. (2.83) represents the effect of stretching of the middle surface on the deflection. Solving for d_0 results in the center deflection of the plate and the solution is given in Appendix A, section §A.2 Eq. (A.9). By investigating the limits of the ratio of d_0/t_m, Eq. (2.83) can be simplified to equations that assume small and large plate center deflection compared to the plate thickness, which are derived below.

For the case when the deflection is small compared to the plate thickness ($d_0 << t_m$), Eq. (2.83) above simplifies to

$$d_0 = \frac{Pa^4}{64D} \ , \tag{2.84}$$

which is exactly the maximum center deflection for pure bending of a circular plate with clamped edges. Alternatively, if the deflection becomes large compared to the plate thickness

[1] Eq. (2.83) assumes ν=0.3 as part of simplification during the derivation.

($d_0 >> t_m$), Eq. (2.83) above simplifies to [90]

$$d_0 = 0.662a\sqrt[3]{\frac{Pa}{Et_m}} \ . \tag{2.85}$$

To illustrate circular plate deflection, an example design is used with the equations derived above. The geometrical design parameters for the example are listed in Table 2.6 [2]. Using Table 2.6, models for center deflection of the full model Eq. (2.83), small deflection Eq. (2.84), and large deflection Eq. (2.85) were calculated. Additionally, finite element analysis (FEA) was performed to compare to the analytical models, and the results are graphed in Figure 2.34a. Good correlation between the full analytical model and FEA is found. The transition from small to large deflection for this example is illustrated in Figure 2.34b. From Figure 2.34b it can be determined that for ratios of $d_0/t_m < 0.5$ the small deflection assumptions result in deflection errors of $< 10\%$. For ratios of $d_0/t_m > 1.9$, large deflection assumptions can be used with deflection errors of $< 10\%$. For the ratio range of $0.5 < d_0/t_m < 1.9$, the full deflection model or FEA models should be used. It should be noted that the ratios calculated above apply to the specific examples given. These can be recalculated as necessary with new examples.

Table 2.6: Example design used for deflection modeling of circular plates.

Input	Value
a	4.19 mm
t_m	100 μm
E	152 GPa
ν	0.17

2.2.3 Rectangular Plate Theory

For the case where the cavity is bounded by a rectangular plate, we shift from cylindrical coordinates to cartesian coordinates. The short side of the rectangle lies along the y axis having a width of a and the long side of the plate lies along the x axis having a length of b.

[2] The values used in Table 2.6 are discussed further in Chapter 3 for LTCC sensor designs.

The rectangular plate is illustrated in Figure 2.33. Unlike circular plates, the deflection of a rectangular plate is more involved. Therefore, we begin with an expression for the center deflection of thin plates ($d_0 << t_m$). The expression assumes bending of a uniformly loaded rectangular plate with clamped edges and is given for various ratios of b/a [90] [3]

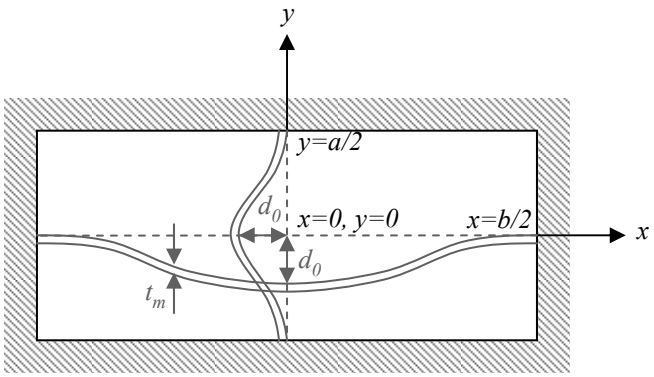

Figure 2.33: Schematic showing the top and cross-sectional view of a rectangular plate with clamped edges.

$$d_0 = \alpha \frac{Pa^4}{D} \begin{cases} \alpha = 0.00126 & b/a = 1.0 \\ \alpha = 0.00220 & b/a = 1.5 \\ \alpha = 0.00254 & b/a = 2.0 \\ \alpha = 0.00260 & b/a = \infty \end{cases}, \tag{2.86}$$

where P is a uniformly applied pressure load, α is the b/a coefficient, and D is the flexural rigidity.

For the case when the deflection is large compared to the plate thickness ($d_0 >> t_m$), the membrane theory is used to determine the center deflection. The center deflection is given by [90] [4]

$$d_0 = 0.401a \sqrt[3]{\frac{Pa}{2Et_m}} \ . \tag{2.87}$$

To get an approximate solution for the deflection that includes both bending and stretching of a rectangular plate with clamped edges, a method consisting of a combination of

[3] Eq. (2.86) assumes ν=0.3 as part of simplification during the derivation.
[4] Eq. (2.87) is the deflection for a square plate.

known solutions for small deflection and membrane theory is used [90]. The method assumes that the load P can be resolved into two parts: one is the balance of bending and shearing stresses and the second is the balance of the membrane stresses. The sum of these two loads is

$$P = \underbrace{\frac{Dd_0}{0.0026a^4}}_{\text{Bending}} + \underbrace{\left(\frac{d_0}{0.401a}\right)^3 \frac{2Et_m}{a}}_{\text{Stretching}} . \tag{2.88}$$

Solving for d_0 in (2.88) results in the center deflection for a rectangular plate that includes both bending and stretching. The solution is achieved through numerical methods and is therefore not included below, however, it is listed in Appendix A, section §A.3 Eq. (A.11).

To illustrate rectangular plate deflection, an example design is used to verify the equations derived above. The geometrical design parameters are listed in Table 2.7. Using Table 2.7, models for center deflection of the full model Eq. (2.88), small deflection Eq. (2.86), and large deflection Eq. (2.87) were calculated. Additionally, FEA was performed to compare to the analytical models, and the results are graphed in Figure 2.35a. Again, a good correlation between the full analytical model and the FEA data is found. The transition from small to large deflection for this example is illustrated in Figure 2.35b. From Figure 2.35b it can be seen that for ratios of $d_0/t_m < 0.37$, small deflection assumptions result in deflection errors of $< 10\%$. For ratios of $d_0/t_m > 2.06$, large deflection assumptions can be used with deflection errors of $< 10\%$. For the ratio range of $0.37 < d_0/t_m < 2.06$, the full deflection model or FEA models should be used.

Table 2.7: Example design used for deflection modeling of circular plates.

Input	**Value**
a	2 mm
b	7 mm
b/a	3.5
t_m	50 μm
E	2.26 GPa
ν	0.33

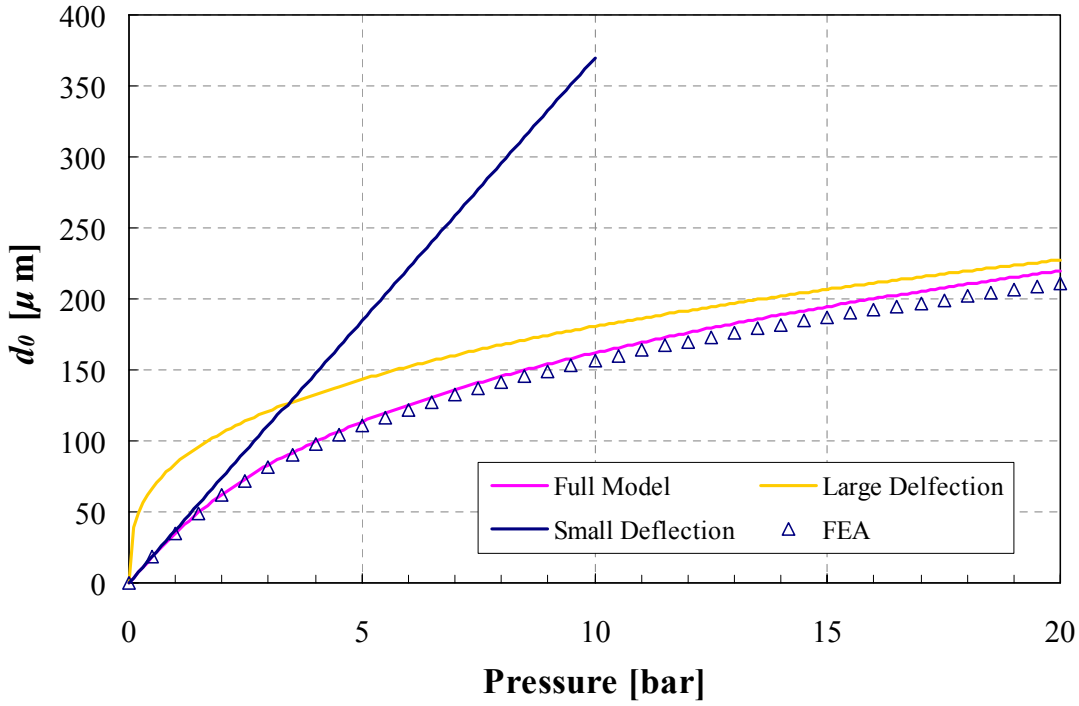

(a) Mechanical modeling of a circular plate with analytical and FEA models.

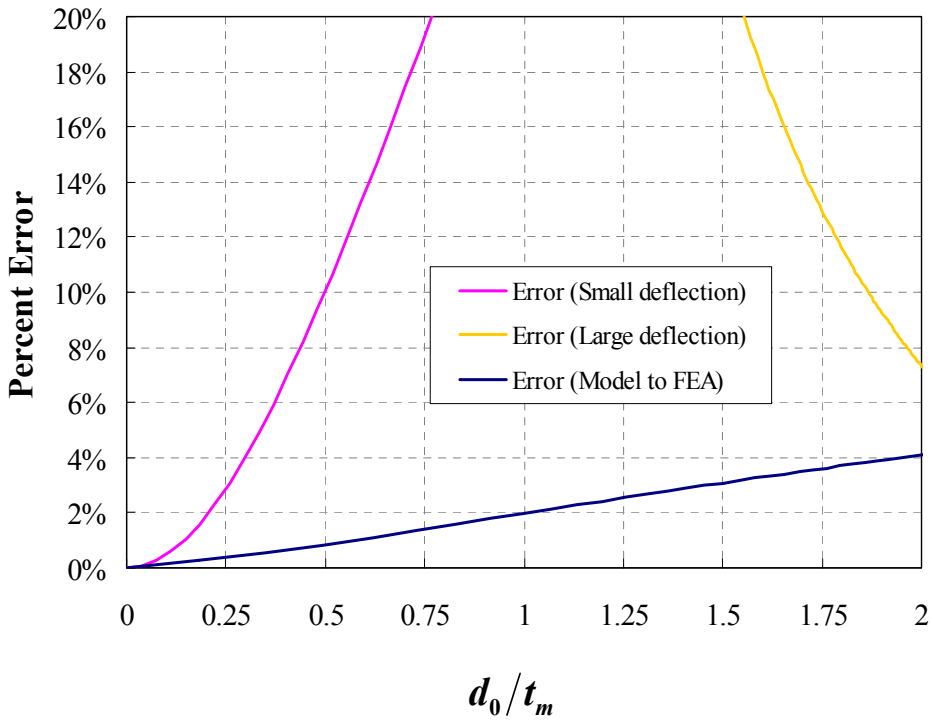

(b) Transition from small to large deflection for mechanical modeling of circular plates.

Figure 2.34: Mechanical modeling of (a) deflection of circular plates and (b) errors by simplified small and large deflection models.

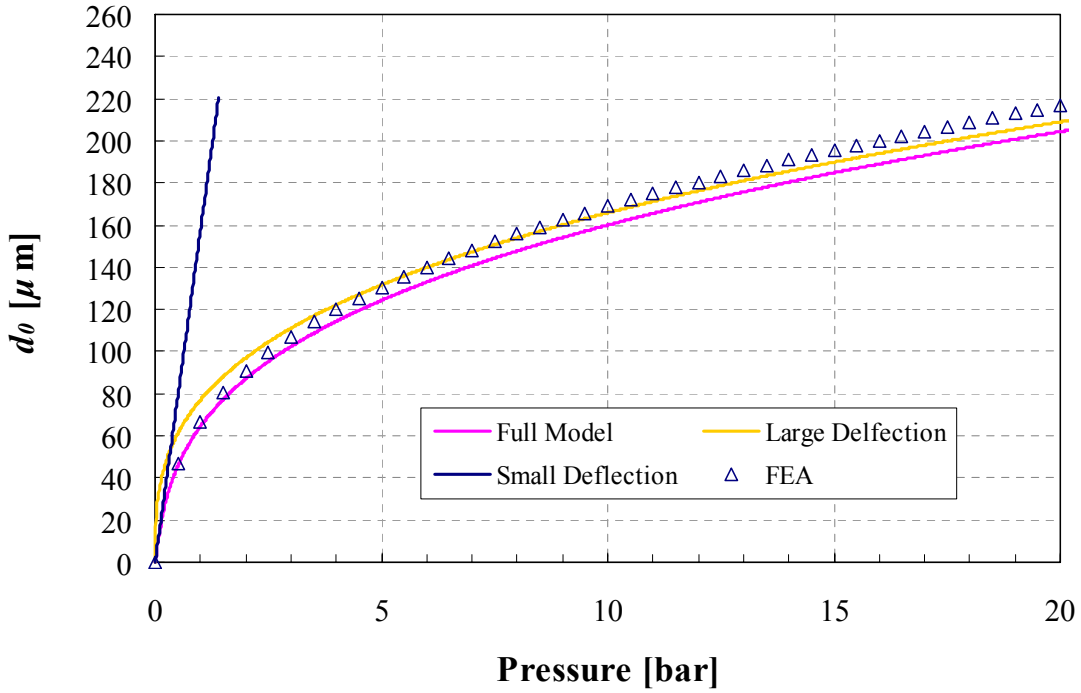

(a) Mechanical modeling of a rectangular plate with analytical and FEA models.

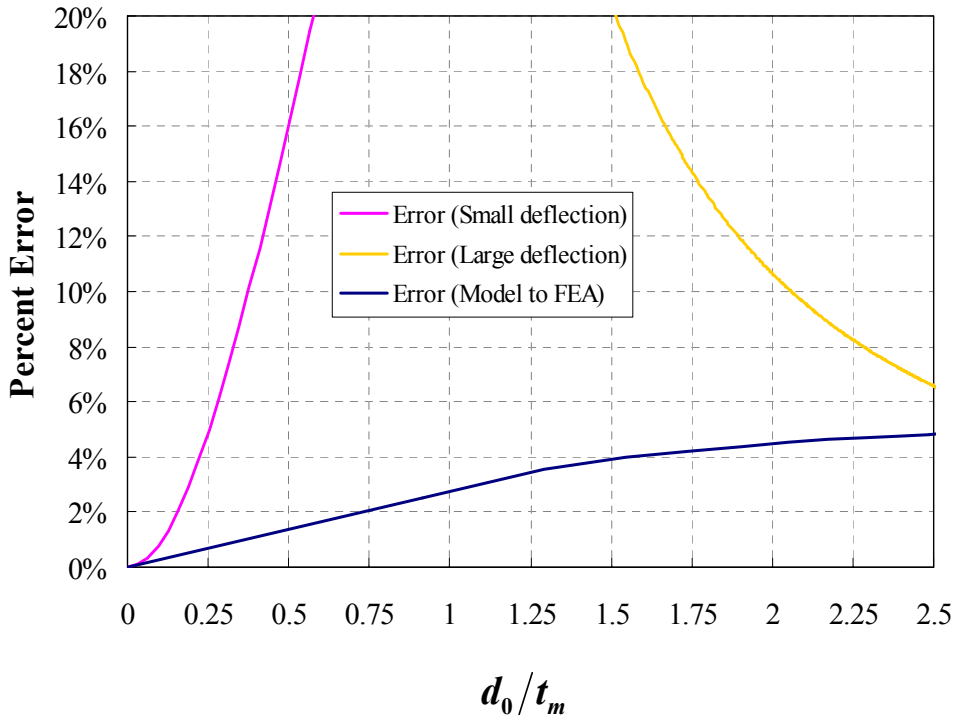

(b) Transition from small to large deflection for mechanical modeling of rectangular plates.

Figure 2.35: Mechanical modeling of (a) deflection of rectangular plates and (b) errors by simplified small to large deflection models.

2.3 Sensor Electromechanical Theory

To achieve pressure sensitivity, the devices have a cavity enclosed by two diaphragms, t_{m1} and t_{m2}, which are separated by a gap t_g, illustrated in Figure 2.30. The diaphragms contain metal electrodes that form the pressure variable capacitance. In this section the electromechanical model that accounts for a variable capacitance as a function of pressure is discussed. Then, the capacitance is integrated into the calculation of the pressure variable resonance frequency $f_0(P)$.

In sections §2.1 and §2.2 the sensor electromagnetic and mechanical models are derived. To integrate these into a single model, an electromechanical model is derived. This is done by modifying the capacitance C_{plate}, discussed in section §2.1.5 Eq. (2.57), to incorporate gap variability due to changes in pressure P.

The derivation begins by redefining C_{plate}. Four different cases for the pressure variable capacitance are considered in this work, graphed in Figure 2.36. The first is for devices whose circuitry is external to the package as shown in Figure 2.36a. The second and third are for devices with embedded circuitry, and two types are considered. Type 1 has both electrodes facing each other opposite the gap t_g, illustrated in Figure 2.36b. Type 2 has one electrode embedded within a diaphragm while the other electrode is inside the cavity, shown in Figure 2.36c. This type eliminates the possibility of the electrodes shorting when high pressure is applied and the diaphragms go into touch-mode. The fourth and final case is for embedded chambers. This configuration is for the case when the packaging substrate, represented by ϵ_{r2} in Figure 2.36d, is not hermetic. By embbeding a hermetic chamber within the non-hermetic packaging substrate, it is possible to fabricate a more stable sensor. Although the case where both electrodes are embedded within the diaphragms are not specifically listed, they can be calculated in a similar fashion.

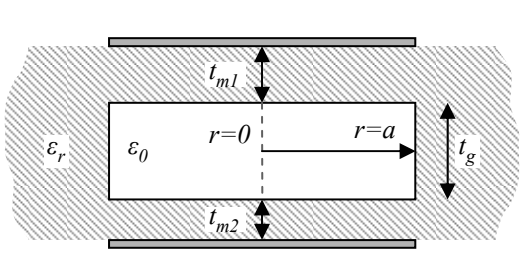

(a) Exposed circuitry model.

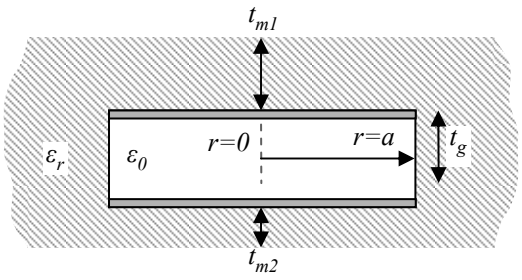

(b) Type 1 embedded circuitry model.

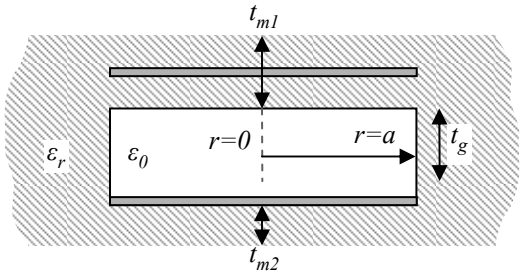

(c) Type 2 embedded circuitry model.

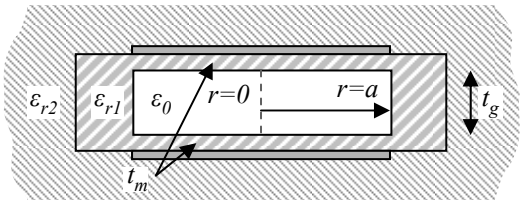

(d) Embedded chamber model.

Figure 2.36: Cross-section of pressure-variable capacitance models for (a) exposed circuitry, (b) Type 1 embedded circuitry, (c) Type 2 embedded circuitry, and (d) embedded chambers.

2.3.1 Circular Diaphragms

The circular parallel plate capacitances C_0 for the cases in Figure 2.36 are given by

$$C_0 = \frac{\epsilon_0 \pi a^2}{t_g + \frac{1}{\epsilon_r}(t_{m1} + t_{m2})} + \frac{\epsilon_0 \epsilon_r \pi (a_e^2 - a^2)}{t_g + t_{m1} + t_{m2}} \qquad \text{Case a: Figure 2.36a} \tag{2.89a}$$

$$C_0 = \frac{\epsilon_0 \pi a^2}{t_g} + \frac{\epsilon_0 \epsilon_r \pi (a_e^2 - a^2)}{t_g} \qquad \text{Case b: Figure 2.36b} \tag{2.89b}$$

$$C_0 = \frac{\epsilon_0 \pi a^2}{t_g + \frac{t_{m1}}{2\epsilon_r}} + \frac{\epsilon_0 \epsilon_r \pi (a_e^2 - a^2)}{t_g + \frac{t_{m1}}{2}} \qquad \text{Case c: Figure 2.36c} \tag{2.89c}$$

$$C_0 = \frac{\epsilon_0 \pi a^2}{t_g + \frac{2t_m}{\epsilon_{r1}}} + \frac{\epsilon_0 \epsilon_{r1} \pi (a_e^2 - a^2)}{t_g + 2t_m} \qquad \text{Case d: Figure 2.36d} \tag{2.89d}$$

where a is the radius of the diaphragm and a_e is the radius of the electrode. The capacitances in Eq. (2.89) are the sum of two terms. The first term accounts for the capacitance going through the embedded cavity and assumes the capacitive electrodes have a radius equal to the diaphragm radius a. The second term represents the fringe field through the substrate for the cases when the electrodes are larger than the diaphragm and is only valid for $a_e > a$. When $a_e < a$, the second term is removed and a is replaced with a_e in the first term. Note that deflection is still calculated with a and not a_e.

To estimate the change in capacitance due to changes in pressure, a model that includes the non-uniform deflection of the plate is used. The non-uniformity is illustrated in Figure 2.32 for circular plates, where the maximum deflection occurs at $r = 0$ and minimum deflection occurs at $r = a$. The pressure variable capacitance is obtained by integrating [91]

$$C_{plate}(P) = \epsilon_0 \int_0^{2\pi} \int_0^a \frac{r dr d\theta}{t^* - d(r)} \begin{cases} t^* = t_g + \frac{1}{\epsilon_r}(t_{m1} + t_{m2}) & \text{for Case a} \\ t^* = t_g & \text{for Case b} \\ t^* = t_g + \frac{tm1}{2\epsilon_r} & \text{for Case c} \\ t^* = t_g + \frac{2t_m}{\epsilon_{r1}} & \text{for Case d} \end{cases}, \tag{2.90}$$

where $d(r)$ is the deflection as a function of radius r and is given by Eq. (2.82). After integrating, Eq. (2.90) can be simplified to [92]

$$\begin{aligned} C_{plate}(P) &= \frac{C_0}{\sqrt{\gamma}} \tanh^{-1}(\sqrt{\gamma}) \\ \gamma &= \frac{d_{01} + d_{i1} + d_{02} + d_{i2}}{t^*} \ . \end{aligned} \tag{2.91}$$

where d_i is the initial center diaphragm pre-deflection and t^* is defined in Eq. (2.90). The term d_i was included because generally the diaphragms have an initial pre-deflection that is set during fabrication or from an initial pressure differential for devices with vacuum in the embedded chamber. On the other hand, d_{01} and d_{02} denote the center deflection of the top and bottom membranes under applied pressure.

2.3.2 Rectangular Diaphragms

The rectangular parallel plate capacitances C_0 for the cases in Figure 2.36 are given by

$$C_0 = \frac{\epsilon_0 ab}{t_g + \frac{1}{\epsilon_r}(t_{m1} + t_{m2})} + \frac{\epsilon_0 \epsilon_r (a_e b_e - ab)}{t_g + t_{m1} + t_{m2}} \qquad \text{Case a: Figure 2.36a} \tag{2.92a}$$

$$C_0 = \frac{\epsilon_0 ab}{t_g} + \frac{\epsilon_0 \epsilon_r \pi (a_e b_e - ab)}{t_g} \qquad \text{Case b: Figure 2.36b} \tag{2.92b}$$

$$C_0 = \frac{\epsilon_0 ab}{t_g + \frac{t_{m1}}{2\epsilon_r}} + \frac{\epsilon_0 \epsilon_r (a_e b_e - ab)}{t_g + \frac{t_{m1}}{2}} \qquad \text{Case c: Figure 2.36c} \tag{2.92c}$$

$$C_0 = \frac{\epsilon_0 ab}{t_g + \frac{2t_m}{\epsilon_{r1}}} + \frac{\epsilon_0 \epsilon_{r1} (a_e b_e - ab)}{t_g + 2t_m} \qquad \text{Case d: Figure 2.36d} \tag{2.92d}$$

where in this case a is the width and b is the length of the diaphragm and a_e is the width and b_e is the length of the electrode. In Eq. (2.92), the first term accounts for the capacitance going through the embedded cavity and assumes the capacitive electrodes have an area equal to the diaphragm area A_{plate}. The second term represents the fringe field through the substrate for the cases when the electrodes are larger than the diaphragm and is only valid for $a_e b_e > ab$. When $a_e b_e < ab$, the second term is removed and a and b are replaced with a_e and b_e in the first term. Note that deflection is still calculated with ab and not $a_e b_e$.

To estimate the change in capacitance due to changes in pressure, the same equation, Eq. (2.91), derived for circular plates is used. Although Eq. (2.91) was derived assuming radial symmetry, it is sufficient to capture the expected change in capacitance as a function of the maximum center deflection for rectangular plates. Therefore, Eq. (2.91) along with the center deflections for rectangular plates will be used in subsequent chapters for analytical modeling.

2.3.3 Pressure Variable Resonant Frequency

The pressure-dependent resonant frequency is derived by redefining C_{eq} in Eq. (2.66a). C_{eq} is redefined as a function of pressure by

$$C_{eq}(P) = \frac{C_{ove} + C_{plate}(P)}{2} + C_{par} + C_{sub} \ . \tag{2.93}$$

Eq. (2.93) assumes the sensor concept without via interconnects between the planar spiral (Figure 2.24). Therefore, for the rest of the concepts discussed in section §2.1.5, the pressure-dependent C_{eq} is derived by replacing C_{plate} with $C_{plate}(P)$. The pressure-dependent frequency can be rewritten from Eq. (2.66a) by using Eq. (2.93) and is given by

$$f_0(P) = \frac{1}{2\pi\sqrt{L_{eq}C_{eq}(P)}} \ . \tag{2.94}$$

CHAPTER 3

HIGH-TEMPERATURE PRESSURE SENSORS

Several sensor designs were developed and characterized to advance ceramic-based passive pressure sensors for wireless telemetry in high-temperature harsh environments. Two types of ceramic material were used to design and research pressure sensors, namely low temperatue co-fireable ceramic (LTCC) and high temperature co-fireable ceramic (HTCC) materials. Designs researched include exposed and embedded circuitry sensors with one or two planar spiral inductors interconnected to parallel plate capacitors. The list below provides research objectives for passive wireless ceramic pressure sensors for high-temperature applications.

- Implement passive LC resonant circuits for wireless telemetry.
- Use parallel-plate capacitors fabricated on and integrated into pressure-deflectable diaphragms.
- Leverage standard microelectronics ceramic packaging technology used for ICs to achieve batch-fabrication.
- Fabricate devices from high-temperature ceramic materials.
- Leverage multi-layer fabrication approaches to achieve embedded passives.
- Use materials with the potential for micro-fabrication processes to create micro-scale mechanical and electrical features.

Section §3.1 gives a brief summary of bulk material properties for LTCC and HTCC as well as the characterization of the electrical properties as a function of temperature. Section §3.2 discusses the development of pressure sensors fabricated on LTCC substrates while section §3.3 discusses sensors fabricated on HTCC substrates. Finally, section §3.4 summarizes the results and conclusions.

3.1 Material Properties of LTCC and HTCC

In this section, the material properties of 96% alumina HTCC (supplied by Richard E. Milstler, Inc) will be compared to DuPont™ 951 AT LTCC laminate. The bulk material properties for the ceramic substrates selected in this research are listed in Table 3.1. To compare the electrical properties, parallel plate capacitors were fabricated and characterized versus temperature. From the impedance measurements, the permittivity and conductivity were extracted and are graphed in Figure 3.1 and Figure 3.2 respectively.

One of the limitations of 951 AT LTCC is that the permittivity and conductivity at frequencies $\geq$ 10 MHz increases substantially for temperatures above 300 ℃. In addition, at temperatures above 500 ℃ the LTCC material creeps [5]. In contrast, the alumina HTCC permittivity behaves more linearly over similar temperature ranges and has lower variation.

Table 3.1: LTCC and HTCC Material Properties [93, 94].

Property	**951 AT LTCC**	**Alumina HTCC**
Flexural Strength [MPa]	320	325
E [GPa]	152	380
Poisson's Ratio	0.17	0.24
Density [g·cm^3]	3.1	3.7 - 3.97
CTE [ppm·C^{-1}]	5.8	7.7
Unfired thickness [μm]	114±8	100 or 200
X,Y Shrinkage [%]	12.7±0.3	15
Z Shrinkage ([%]	15±0.5	15
ϵ_r	7.8	9
$tan\delta$	0.014	0.0001

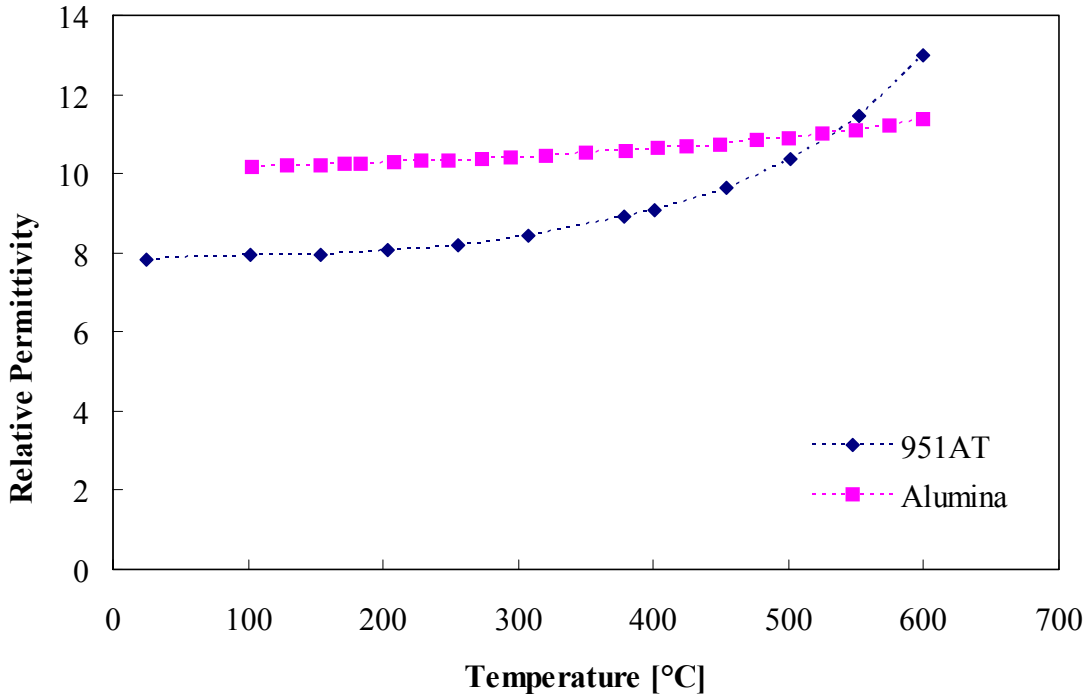

Figure 3.1: LTCC and HTCC ceramic permittivity versus temperature.

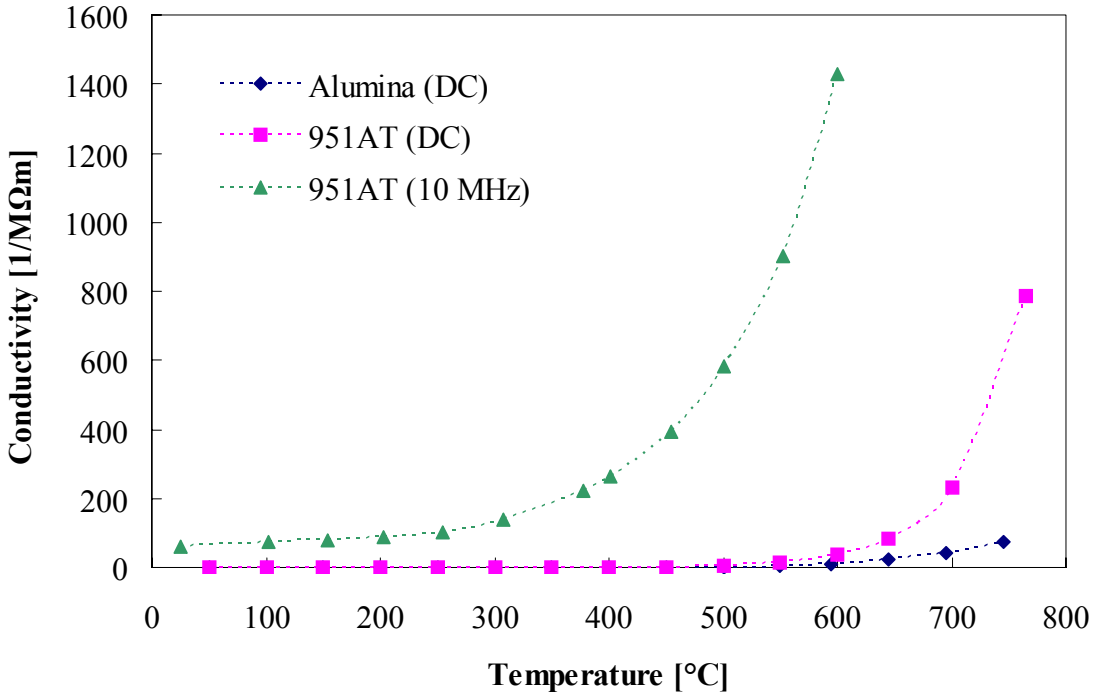

Figure 3.2: LTCC and HTCC ceramic conductivity versus temperature.

3.2 Development of LTCC Pressure Sensors

Initial device designs were implemented in LTCC materials because of material availability and standard fabrication processes, which allowed for rapid development. Two basic designs are considered, yielding exposed and embedded circuitry sensors. Section §3.2.1 provides a brief summary of the exposed circuitry sensor presented in [5]. Section §3.2.2 presents a detailed account of the development of embedded circuitry pressure sensors fabricated on LTCC substrates. Finally, section §3.2.4 concludes the results for LTCC based sensors.

3.2.1 Exposed Circuitry Sensors

As mentioned in section §1.1, the development of high-temperature pressure sensors originates from previous dissertation work [5]. The overlap between [5] and this work is the design and fabrication of sensors from LTCC materials with exposed circuitry using screen printable inks. More specifically, the overlap is the development of screen-printable inks for metalization as opposed to electro-deposited Cu [5]. The use of screen-printable inks allows for metalization to occur prior to sintering, which permits embedded circuitry, and will be discussed in the subsequent section §3.2.2. This section will provide a summary of the developed work done for exposed circuitry sensors; however, a detailed account for these pressure sensors is given in [5]

3.2.1.1 Design and Fabrication

The sensor design implements a single planar inductor and a pressure sensitive capacitor. A schematic and top-view photograph of the wireless pressure sensor is shown in Figure 3.3. The sensor consists of two diaphragms separated by a vacuum-sealed cavity of gap size t_g. The stack of diaphragms and cavity is enclosed by two electrodes that form a capacitor, illustrated in Figure 3.3a. External to the substrate, a planar spiral inductor-coil

is electrically connected to the capacitor. These components form a passive LC resonator with pressure dependent resonant frequency f_0.

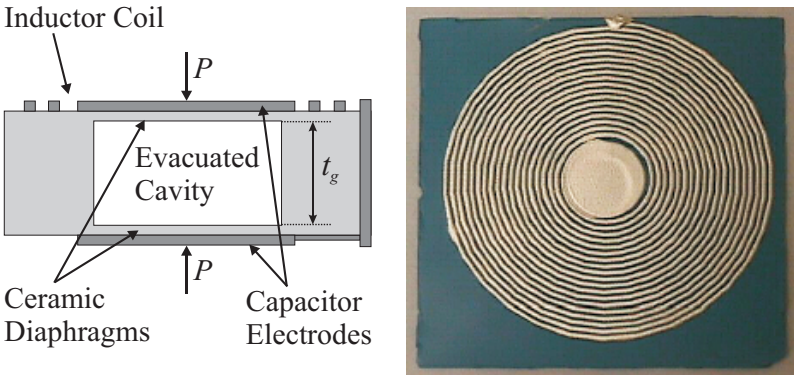

Figure 3.3: Schematic cross-section (a) and top-view photograph (b) of an exposed circuitry ceramic pressure sensor with silver screen printed conductors.

The planar-spiral inductor and diaphragm, shown in Figure 3.4 and Figure 2.30 respectively, have geometrical design values given in Table 3.2.

Table 3.2: Circular planar spiral inductor and mechanical diaphragm geometrical design parameters for exposed circuitry LTCC pressure sensors.

Parameter	**Value**
n	19
lw	400 μm
ls	400 μm
lt	50 μm
r_s	4.5 mm
Metal	6160 Ag
a	4.5 mm
a_e	4.6 mm
t_m	190 μm
t_g	190 μm

The fabrication process, illustrated in Figure 3.5, is based on lamination and sintering of ceramic tape. The substrate, which includes the buried cavity and diaphragms, is composed of three sections of ceramic sheets of 951 AT ceramic tape [94]. The top and bottom sections

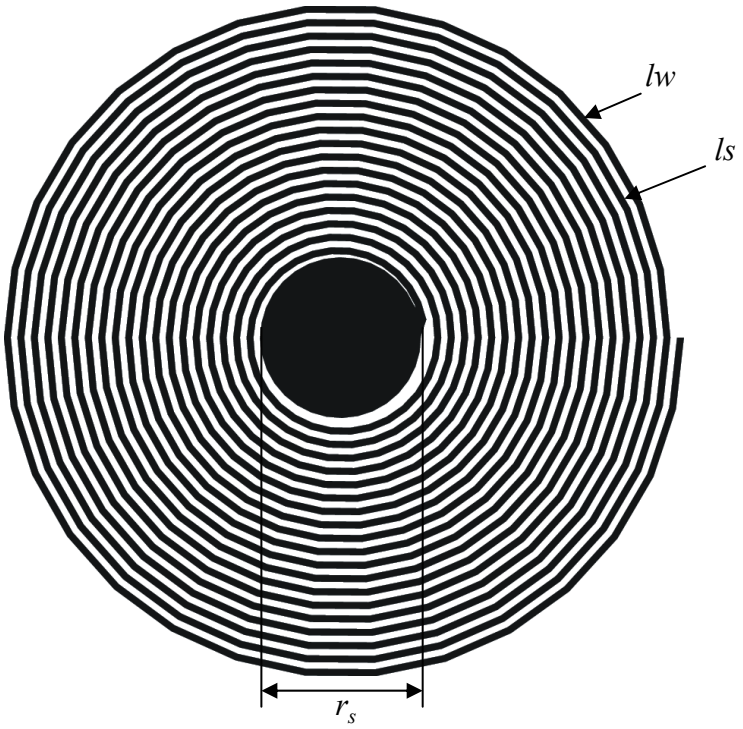

Figure 3.4: Circular planar spiral inductor design for exposed circuitry LTCC pressure sensors.

(see Figure 3.5 step 1), consist of two layers of ceramic sheets and create the pressure sensitive diaphragms of the mechanical structure. The inner layer, which also has two sheets, contains a circular hole of radius a. To form the sensor, the ceramic sheets were laminated together, shown in Figure 3.5, step 2, in a hot vacuum press for 10 minutes. The press temperature used was 70 ℃ with a pressure of 3000 psi (9.38 tons for an area of 6.25 in^2). After lamination, the sample was cut down to a square approximately 4 cm on a side prior to firing. The sample was fired in a box furnace in air for 30 minutes at 500 ℃ (5 ℃ $\cdot min^{-1}$ ramp rate) to bake off the organics and then for 20 minutes at 850 ℃ (5 ℃ $\cdot min^{-1}$ ramp rate) to melt the glass particles and harden the sample, shown in Figure 3.5, step 3 [94]. After sintering, the metalization was screen-printed with DuPont™ 6160 Ag to form the electrical circuit, shown in Figure 3.5, step 4. Further details of the fabrication process and equipment are described in Appendix B, section §B.1.1 and Appendix C, section §C.1 respectively.

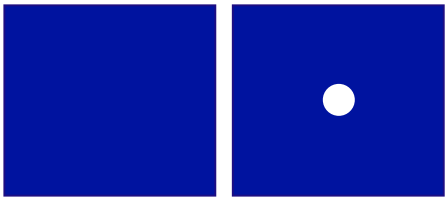

1. Cut samples of green tape.

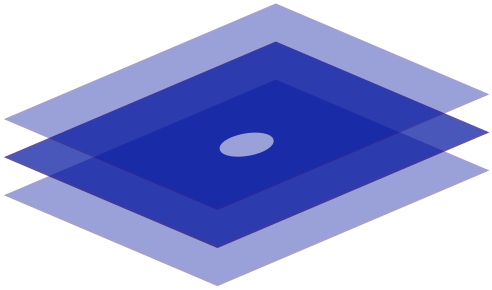

2. Laminate sections.

3. Sinter sample at high temperature.

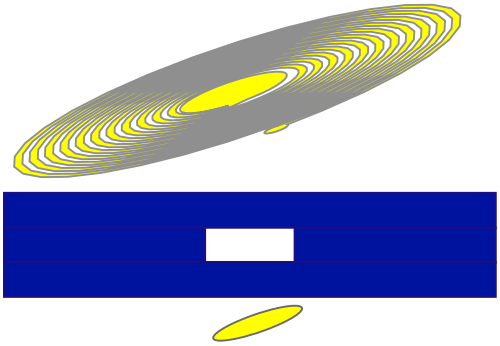

4. Screen print circuitry.

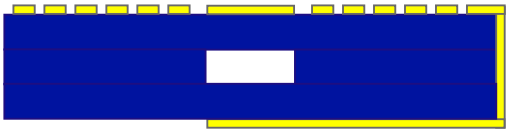

5. Cure ink; sample is ready to test.

Figure 3.5: Fabrication process for exposed circuitry sensor.

Devices described above and fabricated with exposed circuitry were characterized as a function of pressure and temperature. The results presented in [5] demonstrated operation up to 400 ℃ in pressure ranges from 1-7 bar, for designs fabricated with screen-printing technology. To advance the operational range of pressure sensors beyond 400 ℃ for high temperature harsh environments, section §3.2.2 will present the development of embedded circuitry designs fabricated in LTCC substrates.

3.2.2 Embedded Circuitry Sensors

The embedded circuitry protects the metal elements from exposure to the high-temperature harsh environment, which was the main drawback of the ceramic pressure sensors in [19]. The design implements two planar spiral inductors and a pressure variable capacitor. The next sections discuss the design, fabrication and characterization of embedded circuitry LTCC sensors.

3.2.2.1 Design and Fabrication

Similar to devices designed with exposed circuity, devices with embedded circuitry have three essential parts to the design, which include formation of a flexible membrane, a sealed cavity, and the integration of an LC resonant circuit. The major differences between this design and the previously mentioned design in §3.2.1 is the completely embedded circuitry, introduced in section §2 Figure 2.1b. Other key differences are the use of two oppositely wound coils interconnected through a buried via and the use of an evacuation channel to generate vacuum within the cavity. Another design aspect was the addition of a ceramic sheet over one of the embedded capacitive electrodes. This was done to eliminate potential electrical shorting when the buried electrodes go into touch mode at high pressures, shown in Figure 2.36c. For this design a schematic cross-sectional view is illustrated in Figure 3.6.

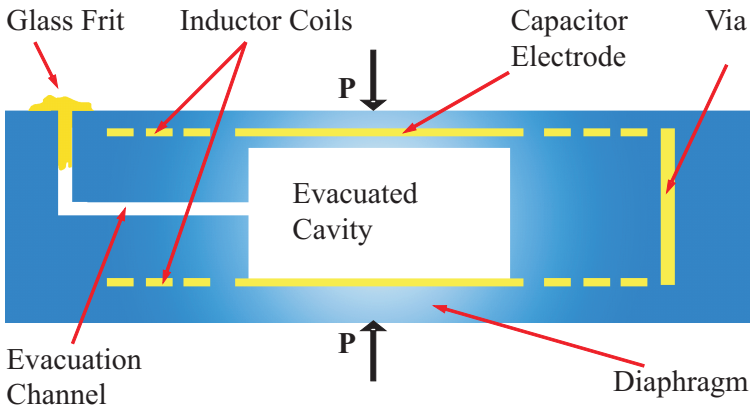

Figure 3.6: Schematic cross-sectional view of an embedded circuitry ceramic pressure sensor.

The fabrication process, illustrated in Figure 3.7, is based on lamination and sintering of screen-printed DuPont™ 951 AT LTCC. The first step is to laser-cut the green tape using an IR Laser system. The laser is used to cut accurate cavity, via, and alignment holes as well as the evacuation channel, as illustrated in Figure 3.7, step 1. Detailed schematic layout and geometrical values used for laser cutting this design are graphed in Appendix B section §B.1.1, Figure B.1, where the cavity radius a is 4.16 mm, the channel length is 8.85 mm, the channel exit hole is 1 mm in diameter, and the via is also 1 mm in diameter. The cut pattern also includes 4 alignment holes for the press blocks, shown in Appendix B, Figure B.2.

To achieve embedded passives within the substrate, DuPont™ 6142D Ag conductor was screen-printed while the ceramic tape was in a green state, illustrated in Figure 3.7, step 1. The top section uses two sheets to embed the top planar spiral and electrodes, which are screen-printed on the underside of the top-most sheet, shown in Figure 3.7, step 2. The wet ink is allowed to dry in an oven at 120 ℃ for 5 minutes prior to lamination. The middle section defines the cavity and is between one and three sheets thick. An evacuation channel exits the cavity along the plane of the sheets, and is long enough to traverse beyond the planar spiral inductor before making a 90° turn through the top section (see Figure 3.6). The bottom section has a second sheet separating the spiral from the evacuation channel,

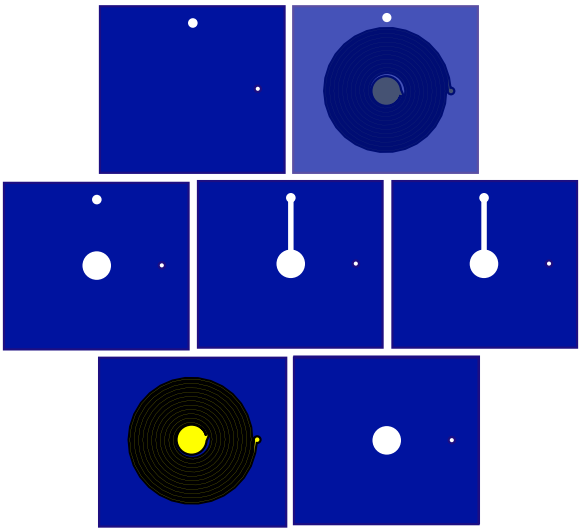

1. Laser-cut samples of green tape. Then screen-print top and bottom coils

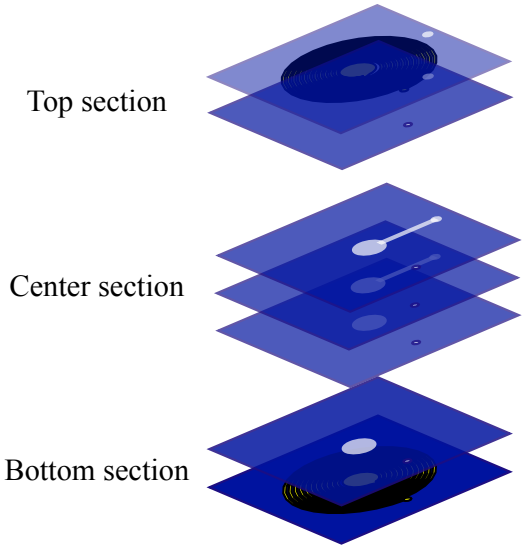

2. Laminate all three sections seperately.

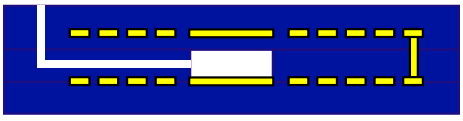

3. Laminate sections together and screen-print via interconnect. Then sinter laminated sample.

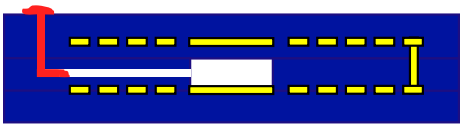

4. Plug evacuation channel with glass frit and melt to seal channel.

Figure 3.7: Fabrication process for embedded circuitry sensor.

shown in Figure 3.7, step 2. This sheet also has a hole cut at the electrode so as to not increase the diaphragm thickness. The same screen mask pattern from the top section is used to screen-print the coil on the bottom section; this is done on the top side of the bottom section, graphed in Figure 3.7, step 2. The coils are printed on opposite sides of the top and bottom sheets, illustrated in Figure 3.7, step 1, so that when they are assembled, the spiral rotations are in opposite directions and have complimentary magnetic flux. Alternatively, if the coils have spiral rotation in the same direction, the magnetic flux from each coil would cancel each other.

Assembly of the device begins by vacuum laminating the top and middle sections separately (and the bottom section if it is using more than one sheet), illustrated in Figure 3.7, step 2. This ensures that areas over the cavity and channels are well laminated before final assembly. The press temperature used was 70 ℃ with a pressure of 3000 psi (9.38 tons for an area of 6.25 in^2). The bottom and middle sections are then assembled in the press blocks and vacuum laminated, illustrated in Figure 3.7, step 2. A brass or stainless steel stencil, with a hole located at the site of the via interconnect, is placed over the stack of sheets in the press blocks. The stencil masks the entire substrate except for the via hole. Next, DuPont™ 6160 Ag conductor is used to fill the via hole, which is then allowed to dry in an oven at 120 ℃ for 5 minutes. The top section is assembled over the bottom and middle sections to form the final stack and laminated in the press without vacuum. Contact between the top metal spiral and via during lamination is sufficient to ensure the metla melts and creates a contact during sintering. The laminated stack is sintered in a box furnace in air for 30 minutes at 500 ℃ (5 ℃ $\cdot min^{-1}$ ramp rate) to bake off the organics and then for 20 minutes at 850 ℃ (5 ℃ $\cdot min^{-1}$ ramp rate) to melt the glass particles and harden the sample [94]. The assembly is illustrated in Figure 3.7, step 3. The final step is to evacuate the cavity and seal it with glass. This is done by placing ELAN #19 glass frit (powdered glass) over the exit hole of the evacuation channel. The sample is placed in a vacuum tube furnace and heated 790 ℃ (2 ℃ $\cdot min^{-1}$ ramp rate) and held for 30 minutes to melt the glass particles. The glass frit (ELAN #19) was chosen because the CTE of 56

ppm closely matches 58 ppm of LTCC. Additionally, the powder average grain size is 20 μm, which is well suited for filling the evacuation channel, which can have a cross-section of 500x100 μm. Further details of the fabrication process and equipment are described in Appendix B, section §B.1.2 and Appendix C, section §C.1. A fabricated device top view and cavity and via cross-sectional view are illustrated in Figure 3.8.

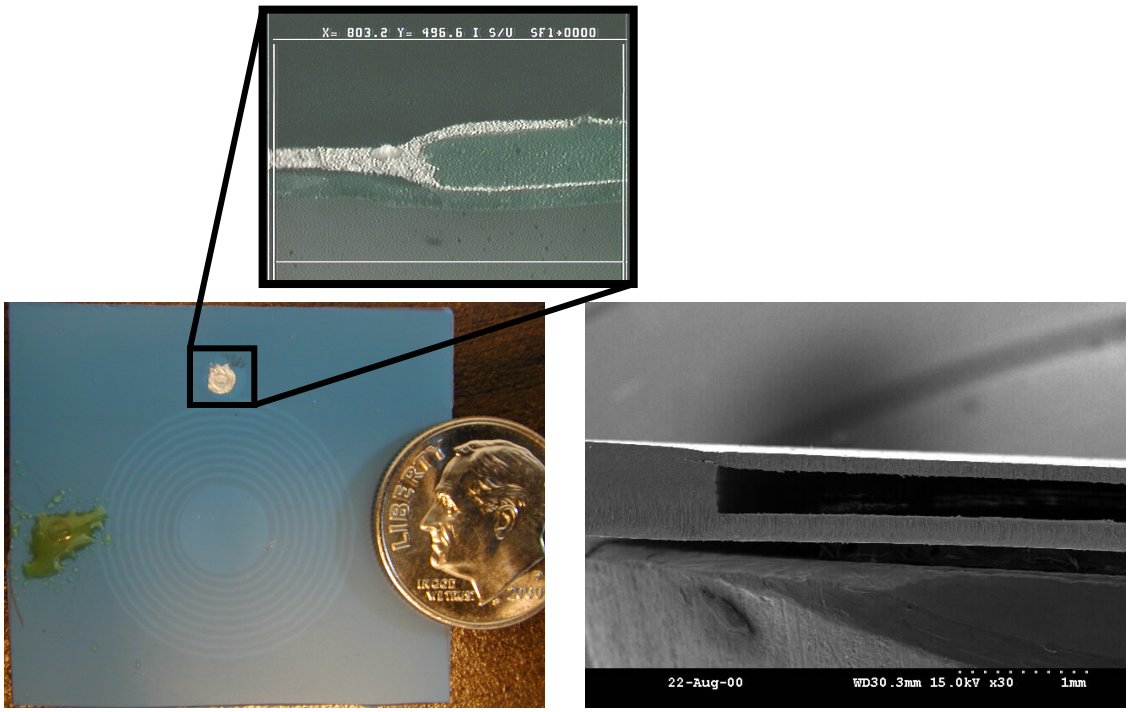

Figure 3.8: Embedded-circuitry ceramic pressure sensor top view (a) with detailed view of via interconnect cross-section and SEM photomicrograph of buried cavity (b).

3.2.2.2 Modeling and Characterization

The planar spiral inductor and mechanical diaphragm, graphed in Figure 3.9 and Figure 2.30, have geometrical design values that are given in Table 3.3. Using the model for inductance derived in section §2.1.3, the calculated series inductance L_s, series resistance R_s, and self-capacitance C_{par} can be calculated for the spiral given in Figure 3.9, and are 1.39 μH

[Eq. (2.32)], 4.0 Ω [Eq. (2.46)], and 4.77 pF [Eq. (2.41)] respectively. The measured inductance and DC resistance of 1.48 μH and 4.58 Ω compare well with the model estimates. A single inductor was fabricated on a ceramic LTCC substrate and characterized as a function of temperature. Figure 3.10a graphs the measured inductance versus temperature and Figure 3.10b graphs the measured DC resistance versus temperature. As expected, the DC resistance has a linear dependence with temperature. Also, from Figure 3.10a, the inductance varies insignificantly with temperature. To extract the intrinsic material property from the measured metal ink, the DC resistance from Eq. (2.44) can be approximated as [5]

$$R_s(T) = \frac{\rho(1 + \lambda\Delta T)}{lw \cdot lt} \cdot ll \ , \tag{3.1}$$

where the term λ is the temperature coefficient and ΔT is the change in temperature. From Figure 3.10b, the gauge factor is determined to be 0.0031 ℃ $^{-1}$ or 3100 ppm ℃ $^{-1}$.

Table 3.3: Circular planar spiral inductor and mechanical diaphragm geometrical design parameters for embedded circuitry LTCC pressure sensors.

Parameter	**Value**
n	9
lw	300 μm
ls	600 μm
lt	16 μm
Metal	6142D Ag
r_s	4.2 mm
a	3.6 mm
a_e	4.0 mm
t_{m1}	190 μm
t_{m2}	95 μm
t_g	380 μm

The pressure variable capacitance C_{plate} for the pressure sensor consists of the top and bottom metal electrodes separated by a cavity with gap t_g, shown in Figure 3.6. The top metal electrode is also covered by a sheet of ceramic. The capacitance at zero applied pressure is given from Eq. (2.89c) and is equal to 2.62 pF. However, this assumes no initial pre-deflection. Although the pre-deflection was not measured for this device, it is possible to assume a pre-deflection (pre-deflection arises from the fabrication process and the

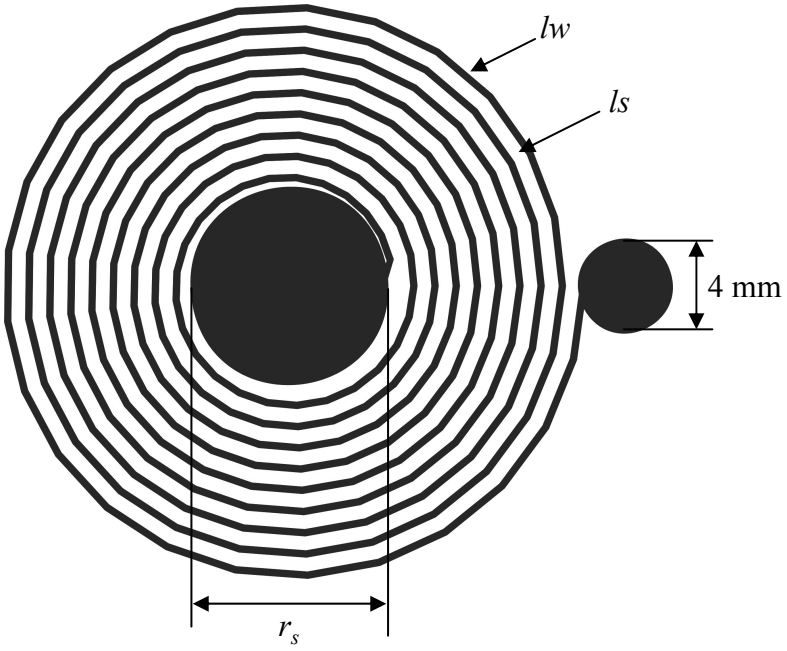

Figure 3.9: Circular planar spiral inductor design for embedded circuitry LTCC pressure sensors.

pressure differential between the cavity and atmospheric pressure) of $d_i \approx 220$ μm for both diaphragms (d_{01} + d_{02}). With this value, a pre-deflected capacitance is calculated from Eq. (2.91) equal to $C_{plate}(P)_{P=0} = 3.4$ pF, where (P=0) represents zero applied pressure beyond atmospheric pressure. Using Eq. (2.83) and Eq. (2.91), the deflections d_{01} and d_{02} and the pressure-dependent capacitance $C_{plate}(P)$ are calculated respectively. Figure 3.11 graphs the deflections for d_{01} and d_{02} versus pressure with deflections of 14.2 and 82.8 μm at 5 bars respectively. Figure 3.12 graphs the pressure variable capacitance $C_{plate}(P)$ versus pressure.

The sensor is placed in the plane of a loop antenna L_a and the impedance is measured. The inductance of the antenna L_a was estimated as 0.876 μH. Using the model derived in section §2.1.5, the impedance magnitude and phase of the sensor can be calculated from Eq. (2.65) and are graphed in Figure 3.13a and Figure 3.13b respectively. Below and above resonance, the phase is close to the ideal value of 90° for an inductor and the magnitude depends linearly on the frequency. The data in Figure 3.13 was taken at atmospheric

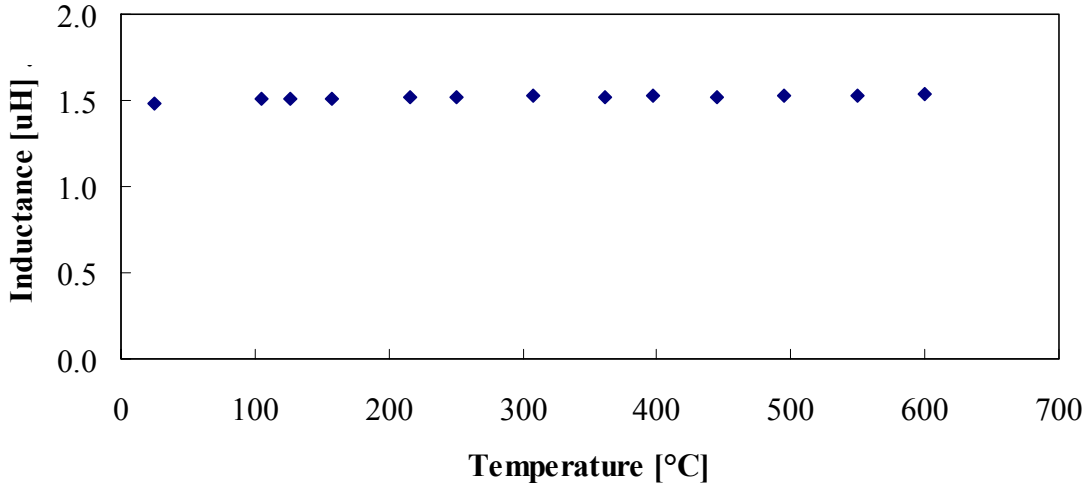

(a) Inductance versus temperature.

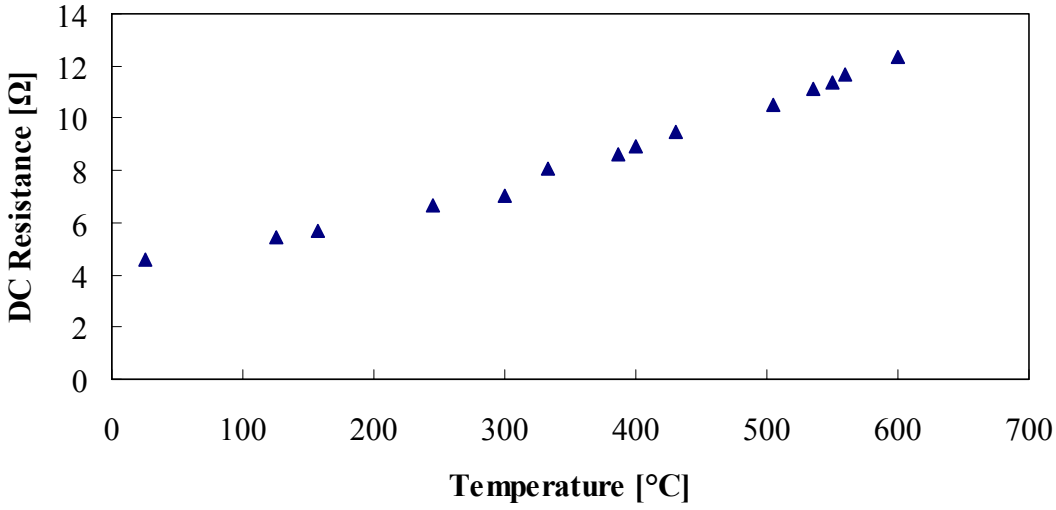

(b) DC resistance versus temperature.

Figure 3.10: Measured inductance and capacitance versus temperature for components fabricated on LTCC ceramic.

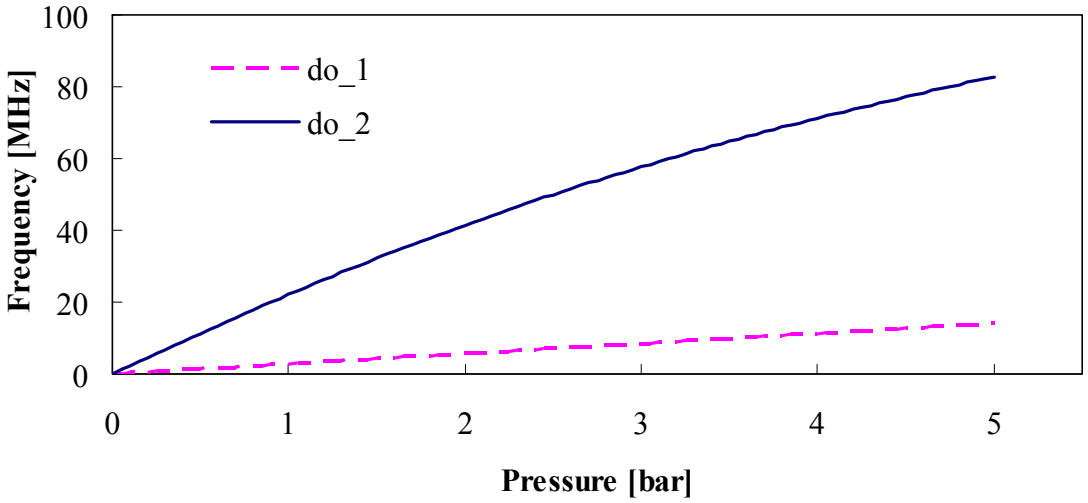

Figure 3.11: Center deflection versus pressure for embedded circuitry LTCC designs.

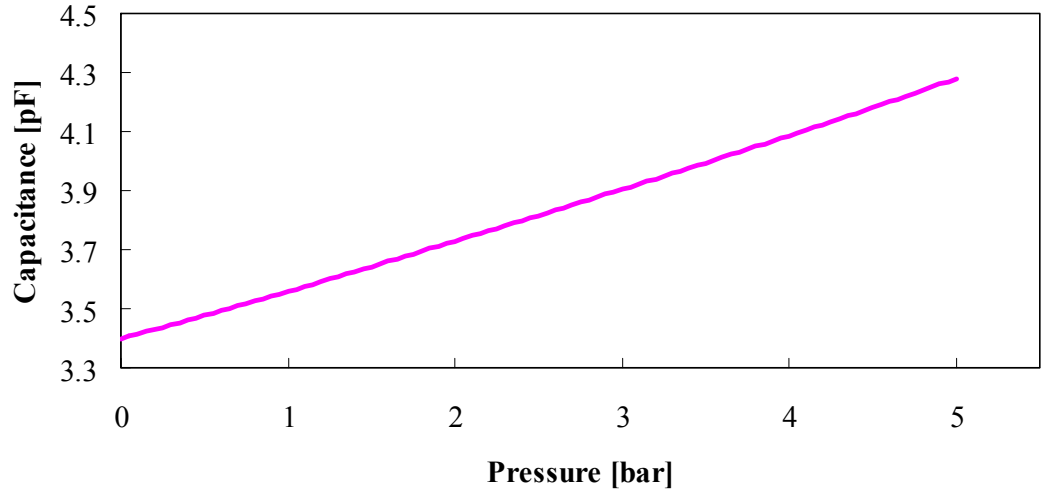

Figure 3.12: Pressure variable capacitance versus pressure for embedded circuitry LTCC designs.

pressures. At resonance, the sensor induces a change in impedance phase and magnitude. The phase minimum f_{min} occurs at 16.63 MHz. Curve fitting, using Eq. (2.9), was used to extract frequency, coupling coefficient, and quality factor from the measured data, shown in Figure 3.13 as the solid line termed Data fit. The resonance frequency f_0, the coupling coefficient k, and the quality factor Q obtained from the fit are 16.52 MHz, 0.157, and 36.1 respectively. Note that the phase minimum f_{min} is 0.67% higher than f_0. The difference is discussed in section §2.1.1, Eq. (2.23).

The calculated and measured self-resonances are 16.8 and 16.52 MHz, which are in good agreement. The difference of 1.7% in frequency is likely due to higher than predicted parastic self-capacitance C_{par} of the spiral and higher fringe electric field from the plate capacitance C_{plate}. The calculated and measured quality factors Q are 36.4 and 36.1 respectively, which are also in good agreement. The variation in Q is likely due to spiral trace thickness lt and width lw variation from the screen printing process.

Sensor measurements as a function of pressure and temperature were taken using a Parr pressure/temperature vessel, illustrated in Figure 3.14a. The pressure can be controlled from atmospheric pressure up to 194 bar using a nitrogen gas tank, a Fisherbrand regulator, and an Ashcroft pressure gauge. The temperature can be controlled from room temperature up to 800 ℃ using a Waslow 4780 temperature controller and a thermocouple placed in proximity with the sensor. A computer with LabVIEW software is used to log antenna impedance magnitude and phase data. This system, shown in Figure 3.14b, is described in greater detail in [5].

Since the vessel is made of metal, the antenna must be placed inside the chamber for all the measurements. In the cases where there is no metal between the sensor and the antenna, the antenna can be placed outside of the harsh environment. However, even in the case where the antenna must be exposed to the harsh environment, the wireless scheme is advantageous since it eliminates the need for potentially unreliable high temperature contacts to be made with the sensor, and also allows for the possibility of the sensor to

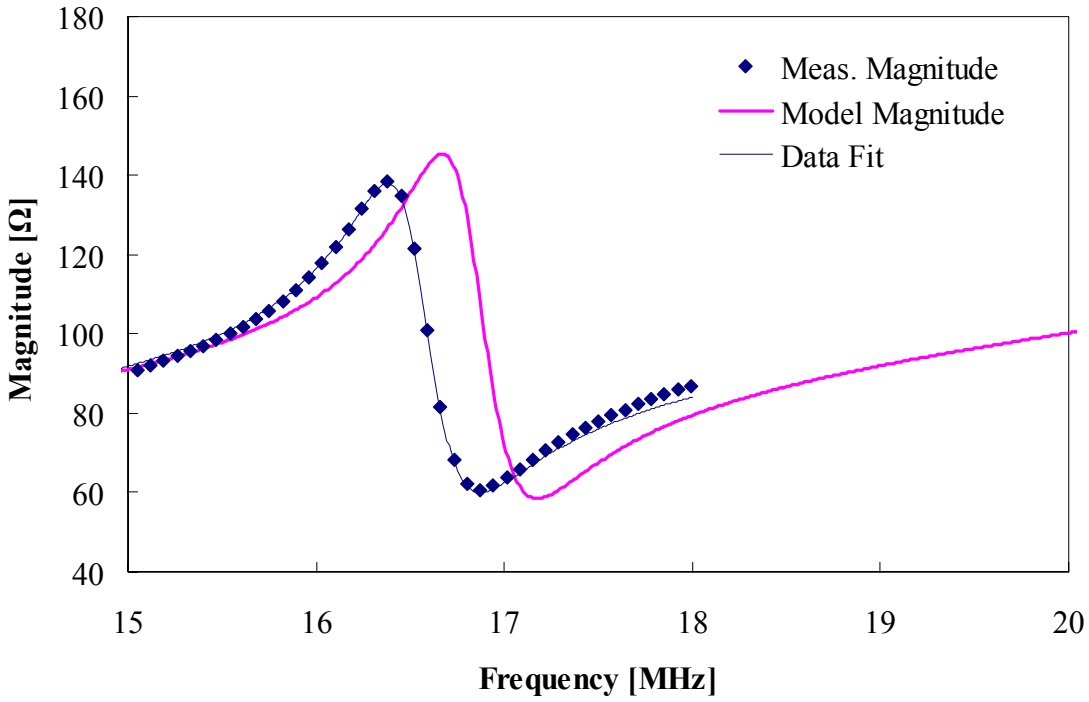

(a) Impedance magnitude.

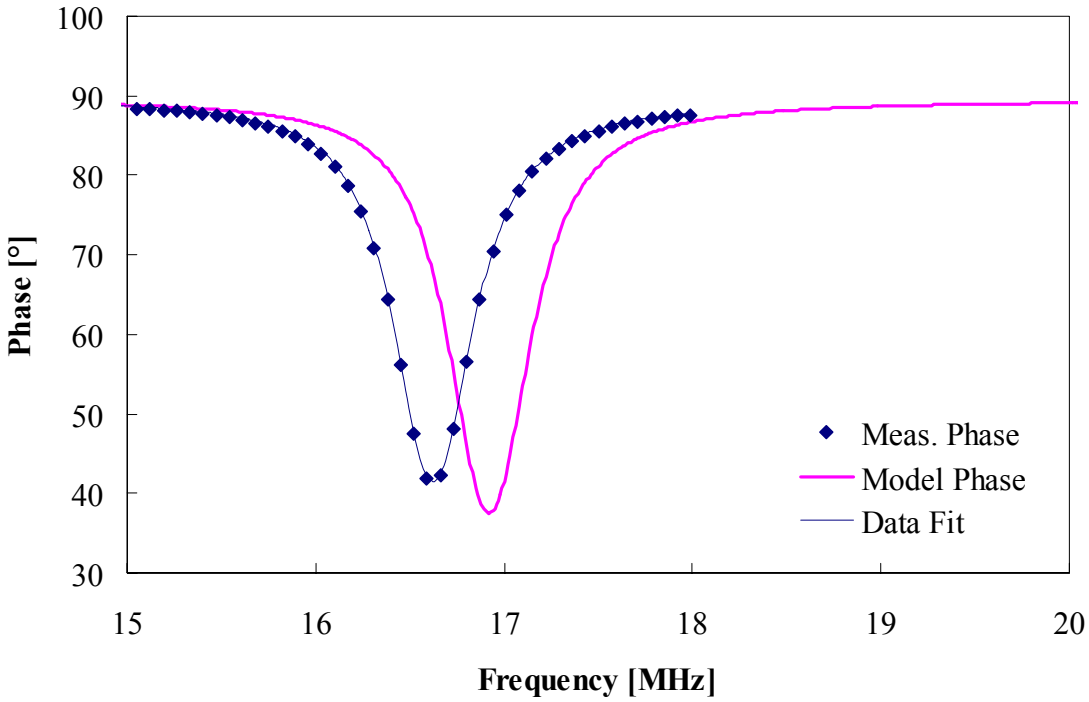

(b) Impedance phase.

Figure 3.13: Comparison between the measured and calculated impedance magnitude and phase for an embedded circuitry LTCC pressure sensor.

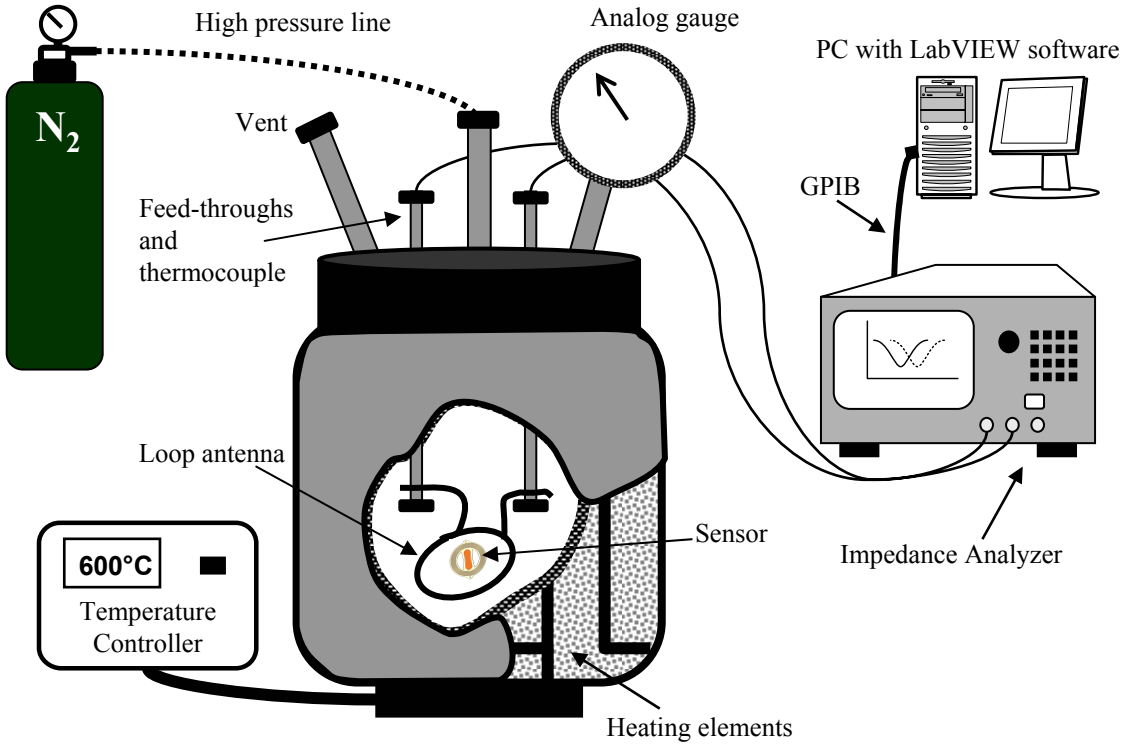

(a) Ceramic pressure sensor test system setup.

(b) Ceramic pressure sensor test system image.

Figure 3.14: Test setup (a) and system image (b) used to characterize pressure and temperature response of ceramic pressure sensors.

be mounted on moving parts. The frequency dependent antenna impedance was measured using an HP9141A impedance analyzer (Figure C.6 in §C.2). Feed-throughs in the vessel shell provided connections between the antenna and impedance analyzer. The magnitude and phase of a sensor as a function of frequency and parameterized by the applied pressure is shown in Figure 3.15.

The pressure dependence of the sensor can be obtained by determining the frequency at which the phase minimum of each curve occurs, f_{min}, and by plotting this frequency as a function of pressure. The pressure dependence of the sensor determined in this manner is shown in Figure 3.16a. Since no sensor data were taken at ambient vacuum (i.e., ambient pressure of zero bar), the first data points are at 1 bar. In order to compare with the theoretical development, which assumes a minimum differential pressure (as well as absolute pressure, since the reference pressure sealed in the cavity is ideally zero bar), The experimental data were extrapolated to a pressure of zero bar to extract the zero-pressure resonance frequency $f_0(P = 0)$. Figure 3.16b shows the normalized resonance frequency (f_0(P)/f_0(P=0)) as a function of the applied pressure and compares the experimental results with the analytical model according to Eq. (2.94).

The sensitivity of the sensor in Figure 3.16 is -83.3 kHz bar^{-1} from 1-5 bar. The theoretical sensitivity calculated from Eq. (2.94) is -82 kHz bar^{-1} for 0-5 bar and is in good agreement with measured data. The device was operated up to 450 ℃ in a pressure range of 1-5 bar. The sensitivity of the sensor ranges from -70 to -245 kHz bar^{-1} over the temperature excursion, which is shown in Figure 3.17. Since no sensor data were taken at vacuum, the first data points are again at 1 bar in Figure 3.17. The experimental data were again extrapolated to a pressure of zero bar to extract the zero-pressure resonance frequency $f_0(0)$). Figure 3.18 shows the normalized frequency response as a function of pressure for different temperatures. At low pressures, f_0 depends approximately linearly on P. The pressure sensitivity in the range from 1 to 5 bar is -70 kHz bar^{-1} from room temperature to 300 ℃ and increases to -245 kHz bar^{-1} from 300 ℃ to 450 ℃. The increase in sensitivity with increasing temperature is attributed to changes in the LTCC mechanical properties from

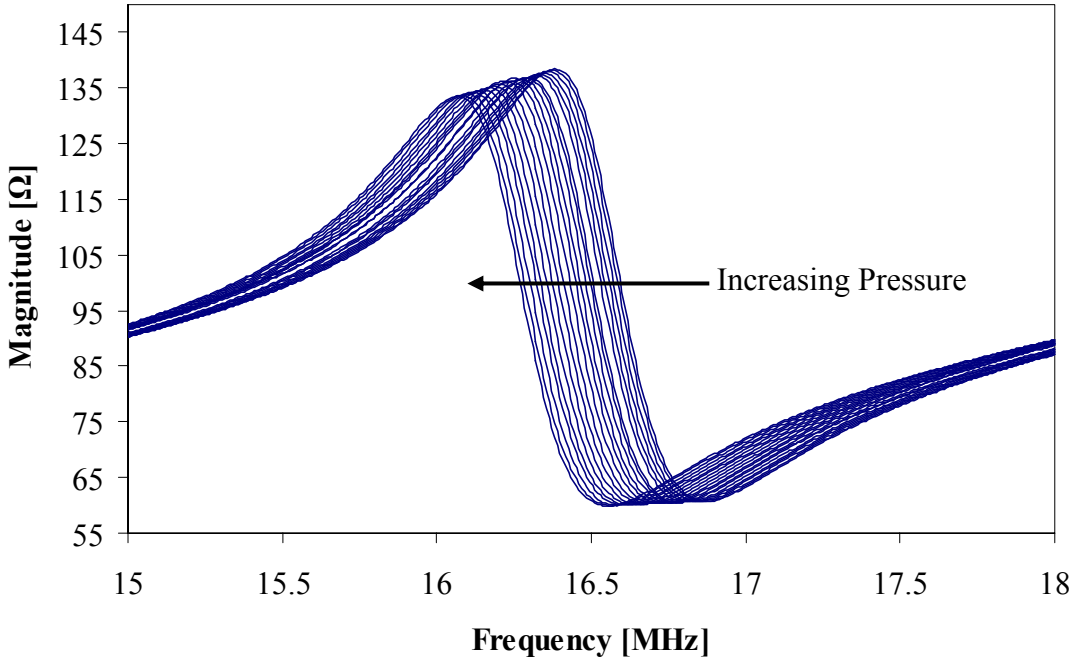

(a) Impedance magnitude over 1-5 bar pressure range.

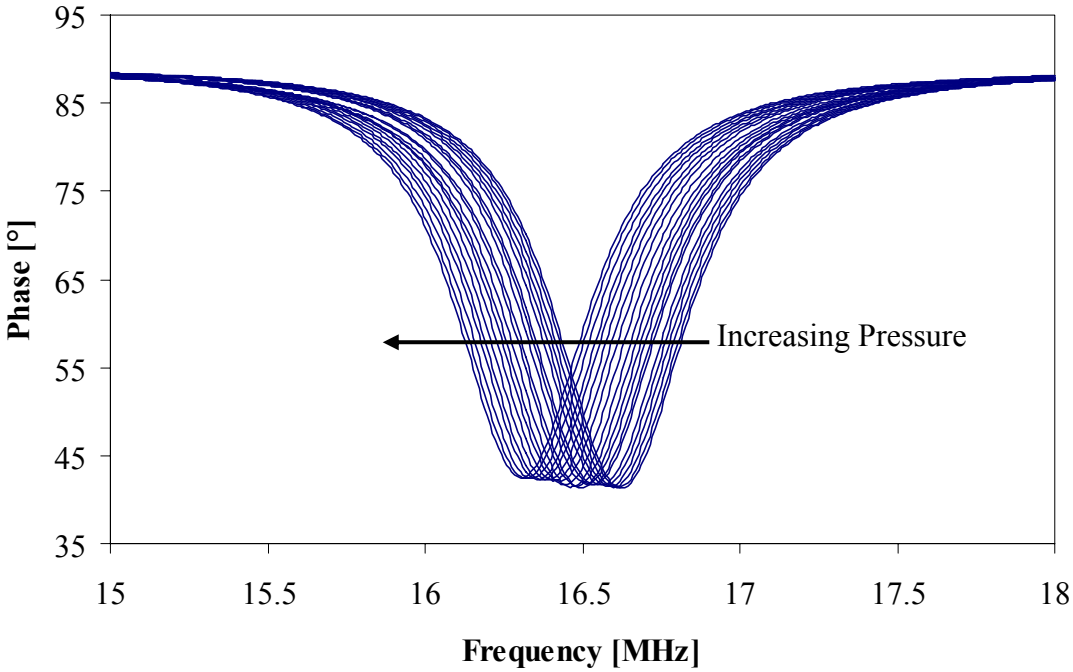

(b) Impedance phase over 1-5 bar pressure range.

Figure 3.15: Impedance magnitude (a) and phase (b) over a pressure excursion from 1-5 bar.

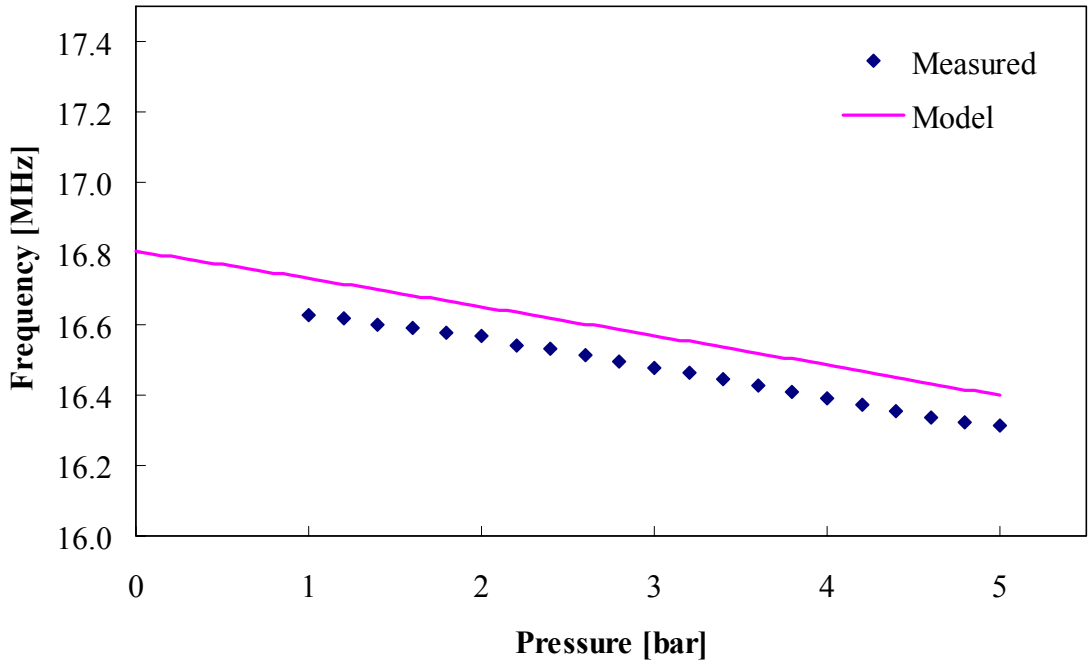

(a) Frequency versus pressure.

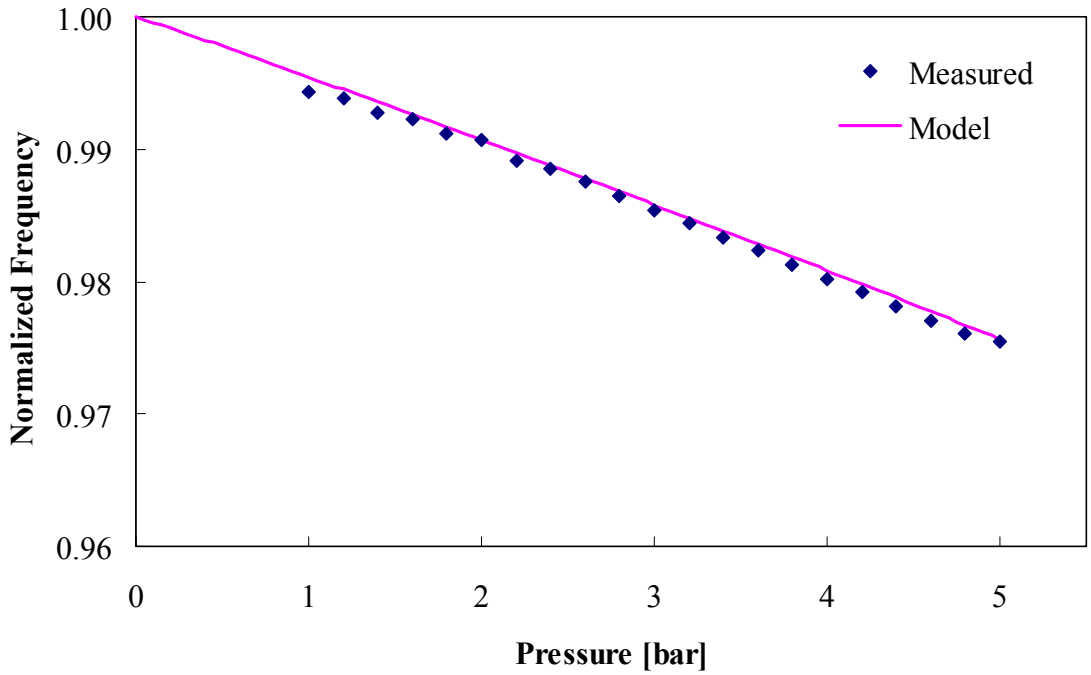

(b) Normalized frequency versus pressure.

Figure 3.16: Frequency (a) and normalized frequency (b) versus pressure for and embedded circuitry LTCC sensor.

the glass that is typically contained (≈10%) in LTCC materials. The decrease in resonance frequency with increasing tempeature is due to the increase in dielectric constant, which is grpahed in Figure 3.1.

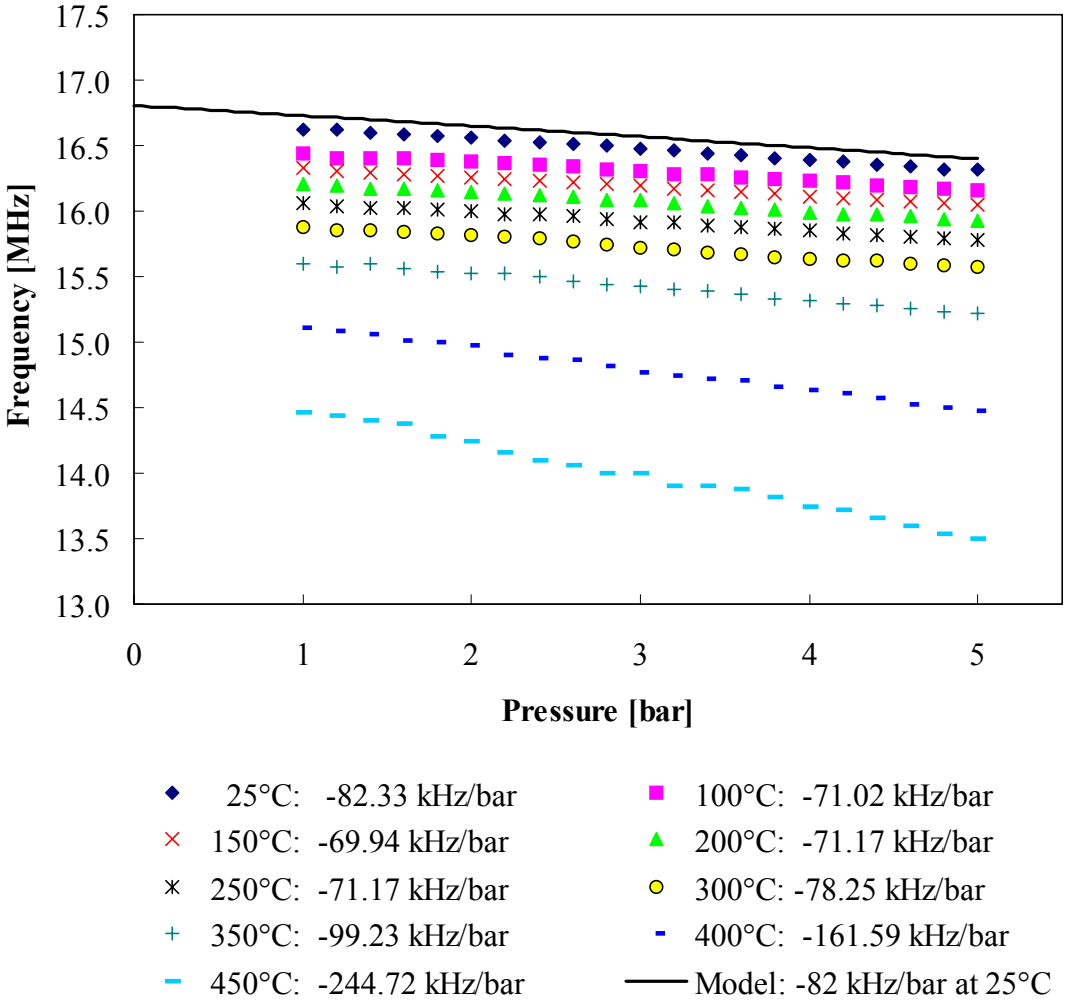

Figure 3.17: Sensor frequency response versus pressure from 1-5 bar over a temperature excursion from 25 ℃ to 450 ℃.

In section §3.1 we characterized the ceramic LTCC permittivity $\epsilon_r(T)$ versus temperature, graphed in Figure 3.1. The increase in permittivity would indicate that the sensors should have a parasitic temperature sensitivity. This can be modeled using Eq. (2.69), where C_{eq} from Eq. (2.68) is redefined as

$$C_{eq}(T) = 2\left[C_{ove}(T) + C_{plate}(T)\right] + C_{par}(T) + C_{sub}(T)\ , \tag{3.2}$$

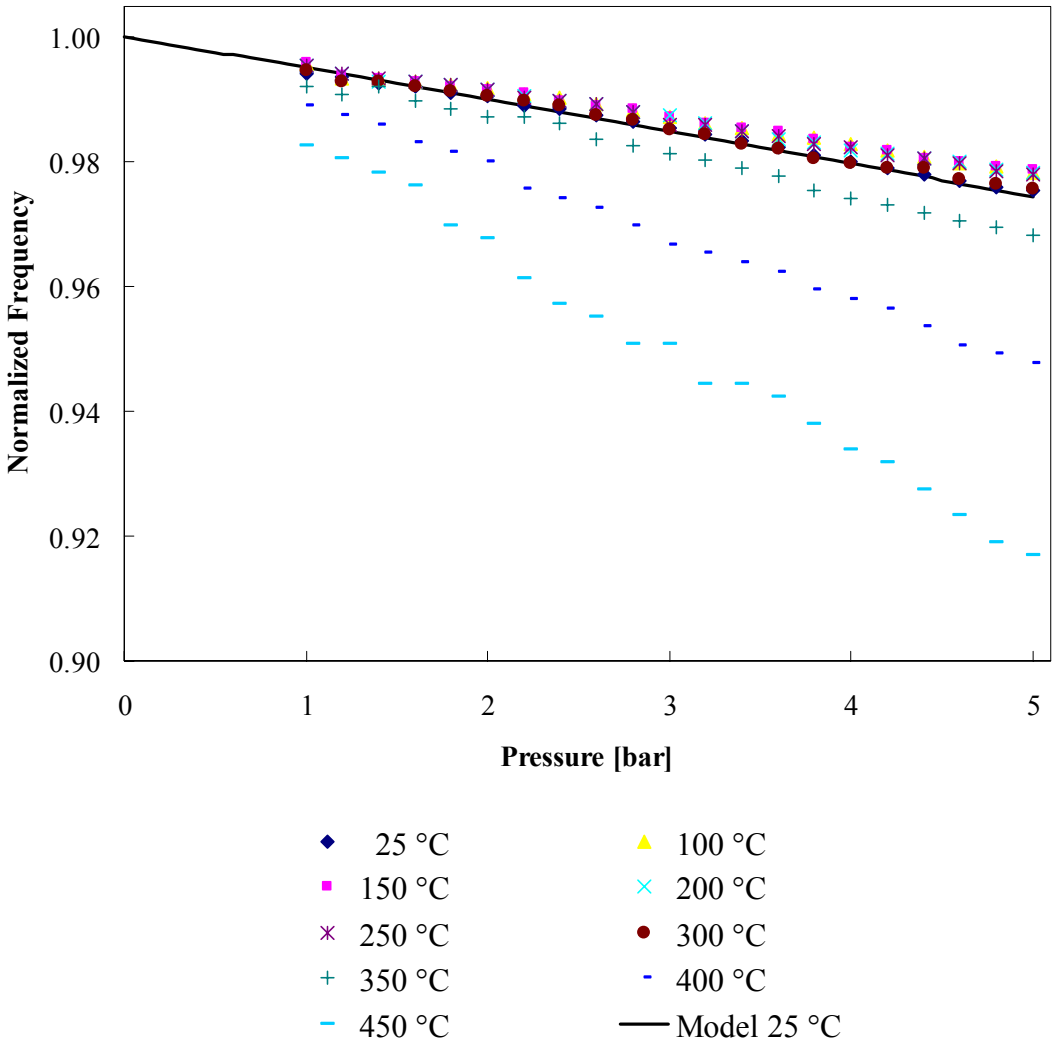

Figure 3.18: Sensor normalized frequency response versus pressure from 1-5 bar over a temperature excursion from 25 ℃ to 450 ℃.

where for each capacitive value the relative dielectric constant ϵ_r is replaced with the measured temperature sensitive dielectric constant $\epsilon_r(T)$ graphed in Figure 3.1.

To determine the parasitic temperature sensitivity, the resonance frequency was measured as a function of temperature. Figure 3.19 shows the sensor calculated and measured frequencies f_0 (measured at 1 bar) between 25 ℃ and 450 ℃, which are in good agreement. The average slope is -4.6 kHz ℃ $^{-1}$ between 25 ℃ and 450 ℃. A possible compensation scheme utilizes integration of a second sensor with no pressure dependence on the same substrate (i.e. a sensor without cavity).

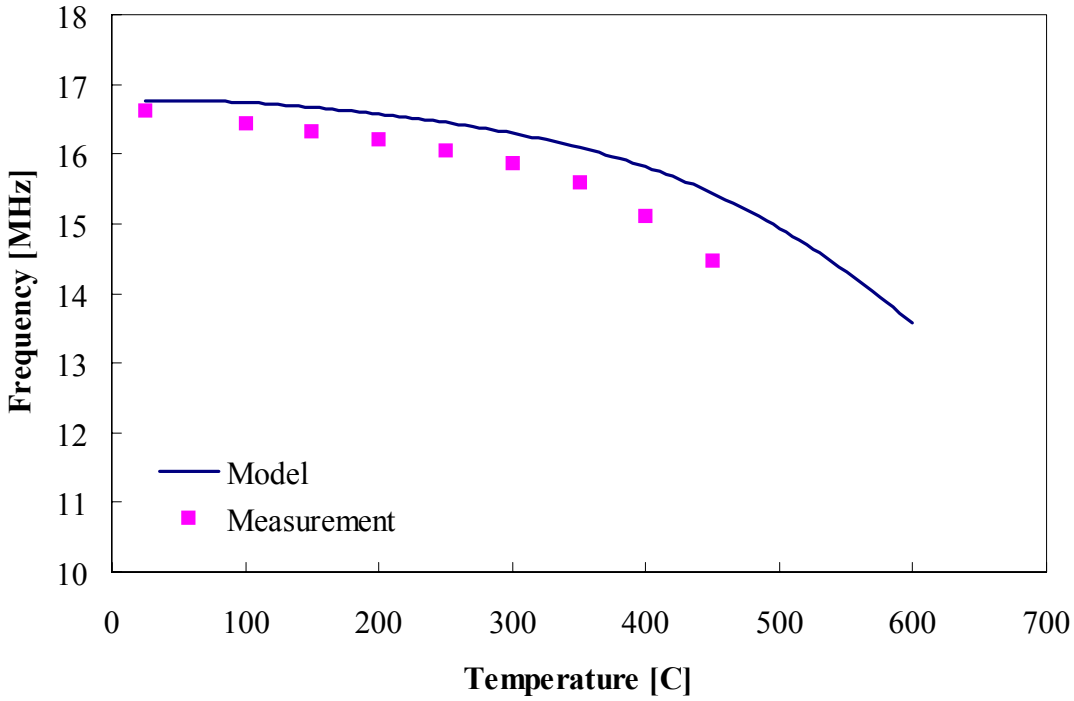

Figure 3.19: Measured and calculated resonance frequency of the LTCC-based sensor versus temperature for temperatures from 25 ℃ to 450 ℃.

Similar to permittivity, the conductivity of the ceramic material also increases as a function of temperature, discussed in section §3.1 and shown in Figure 3.2. The increase in conductivity can be translated to an increase in dielectric loss through the $tan\delta(T)$, which would indicate that the sensors quality factor should be reduced with temperature. In

addition, the metal resistivity increases with temperature, shown in Figure 3.10b and modeled by Eq. (3.1). By including both temperature dependent losses into the model for Q, Eq. (2.66b) can be rewritten as

$$Q = \frac{\omega_0 L_{eq}}{R_s(T) + Req(T)} \ , \tag{3.3}$$

where $R_s(T)$ includes the metal resistivity as a function of temperature and R_{eq}, defined in Eq. (2.70), includes the dielectric loss as a function of temperature. Figure 3.20 shows the measured and calculated quality factor Q as a function of temperature, which are in good agreement. Figure 3.20 also shows the calculated Q for each contributing loss mechanism, metal resistivity, and dielectric loss. As temperature increases, the dielectric loss dominates the Q for this design. This data shows that Q is reduced from 36 at 25 ℃ to 6.5 at 450 ℃, which limits the range of operation of sensors fabricated from these materials. Improved Q at higher temperatures can be obtained if the devices are fabricated in ceramics whose conductivity has lower temperature dependence.

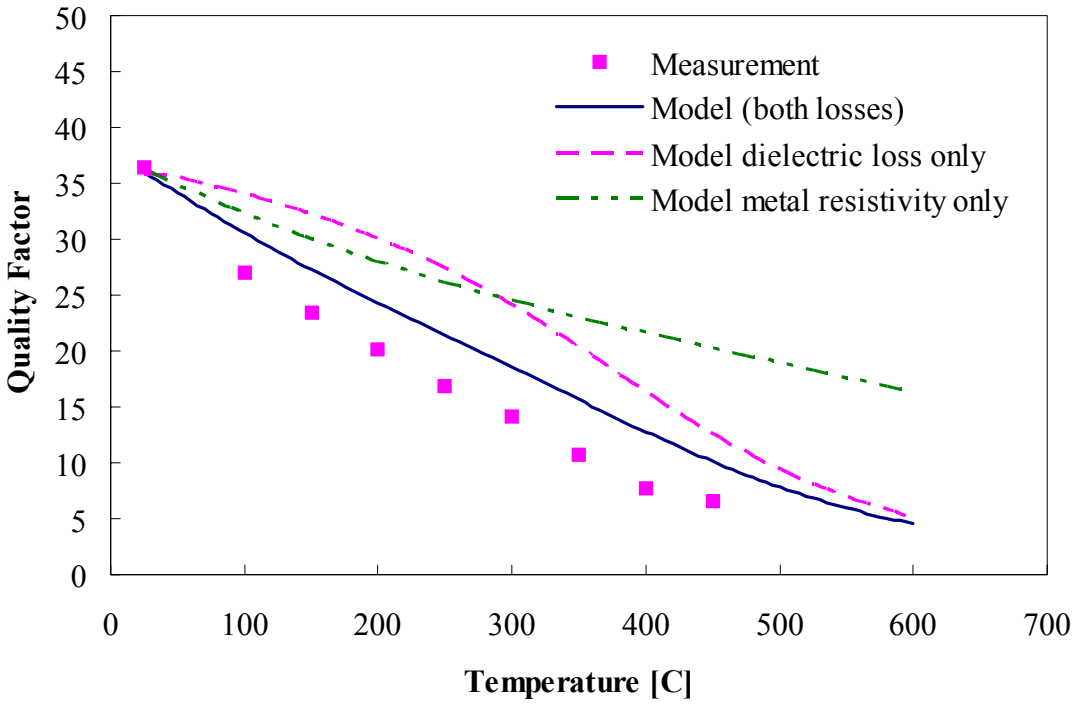

Figure 3.20: Measured and calculated quality factor of LTCC-based sensor versus temperature for temperatures from 25 ℃ to 450 ℃.

3.2.3 Embedded Multi-Layer-Inductor Sensors

The previous section, §3.2.2, presented devices fabricated using two embedded metal layers implementing two planar spiral inductors. This section presents the design and fabrication of a device implementing four metal layers with four planar spiral inductors interconnected through vias. Figure 3.21 illustrates a perspective view of the design with three embedded vias at opposite ends and an embedded cavity at the center of the spirals. The top-most spiral was left exposed for simplicity of fabrication, however, it can be embedded by simply adding an additional ceramic layer to the top section.

The fabrication sequence is illustrated in Figure 3.22. First, two sheets are laminated together and the bottom spiral is screen printed on to form the bottom section (Figure 3.22a). Next, two sheets that contain the cavity hole and via holes are laminated over the bottom coil (Figure 3.22b). The via is filled and the first inner-layer spiral is screen printed over the via (Figure 3.22c). Another two ceramic sheets are laminated over the spiral (Figure 3.22d). This section contains the cavity hole and via hole. The vias are alternated to keep them from overlapping. So far, the fabrication sequence has used six ceramic sheets and two metal layers interconnected with two vias. Next, the second via is filled and a second inner-layer spiral is screen printed over the via (Figure 3.22e). Two more sheets are laminated over the second inner-layer spiral, which contains the last via hole (Figure 3.22g). The via is filled and the top spiral is screen printed over the last via. Finally, the device is sintered in a furnace. The top-view of the sintered device is shown in Figure 3.22h.

The device resonance frequency f_0 was measured at 8.01 MHz with a quality factor Q of 29.3. The antenna L_a used had an inductance of 0.727 μH and the coupling coefficient k_a was 0.086. The data is graphed in Figure 3.23. The advantage of this design is the ability to reduce the resonance frequency while maintaining the same dimensional foot-print; this design resulted in a resonance frequency of approximately half that of two-layer designs.

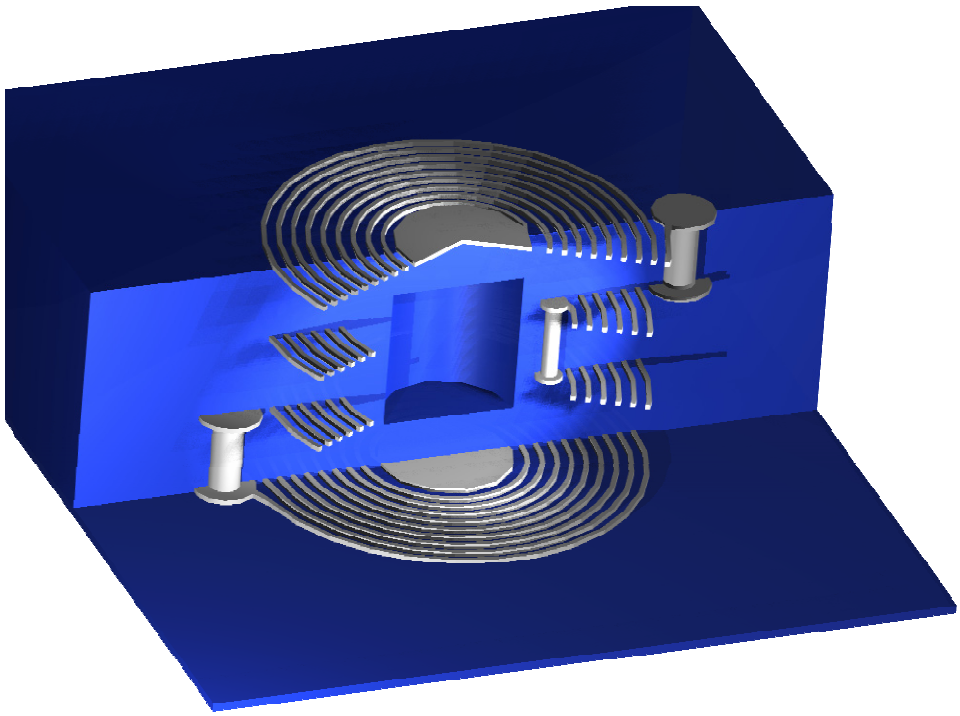

Figure 3.21: Perspective view of a four-layer sensor design.

3.2.4 Conclusions

Devices designed with embedded circuitry and fabricated on LTCC ceramic substrates demonstrated operation up to 450 ℃ for pressure ranges of 1-5 bar. Designs with different diaphragm flexural rigidity are possible, which allow higher or lower pressure ranges as well as sensitivities. The model derived for embedded passive structures was in good agreement with measured data and parasitic temperature effects. The reduction in Q and softening point of the ceramic material beyond 500 ℃ ultimately limit the operational temperature of this design. The use of HTCC materials could improve or increase the operational range of high temperature pressure sensors, which is researched in the next section.

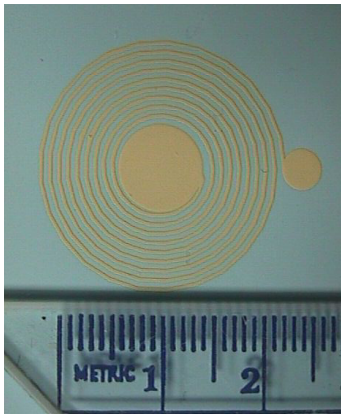

(a) Screen printed bottom coil over two sheets.

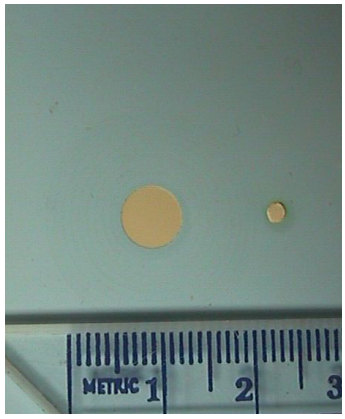

(b) Laminated sheet over bottom coil. Sheet has via holes and cavity hole.

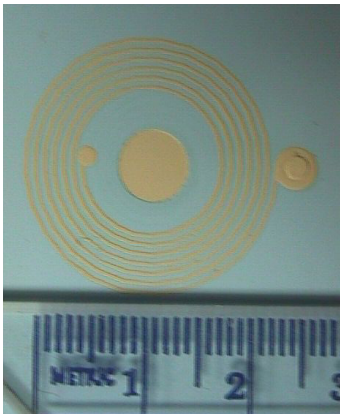

(c) Fill via and screen print first inner-layer spiral coil.

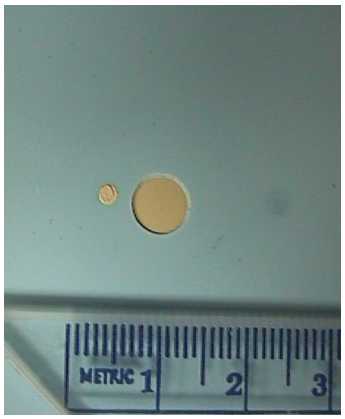

(d) Laminate sheet over first inner-layer spiral. Sheet has second via and cavity holes.

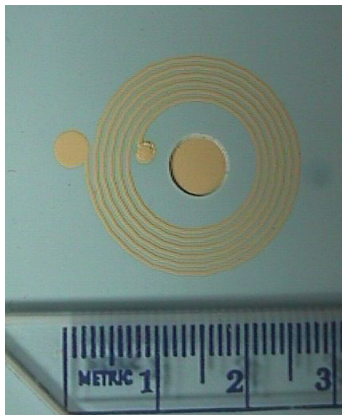

(e) Fill via and screen print second inner-layer spiral.

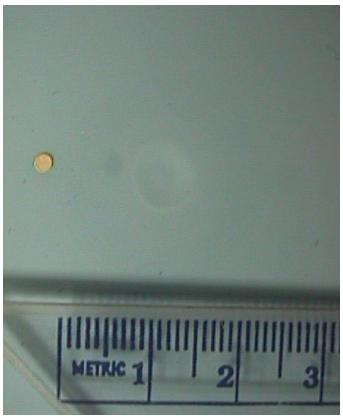

(f) Laminate sheet over second inner-layer spiral. Sheet has third via and cavity hole.

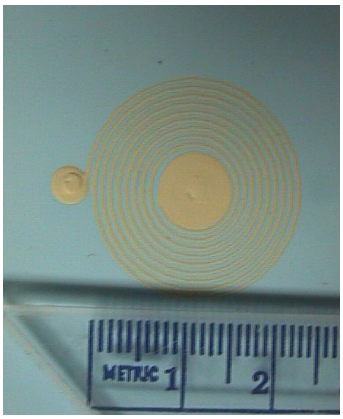

(g) Fill via and screen print top coil.

(h) Device after sintering.

Figure 3.22: Fabrication sequence for a four-layer sensor.

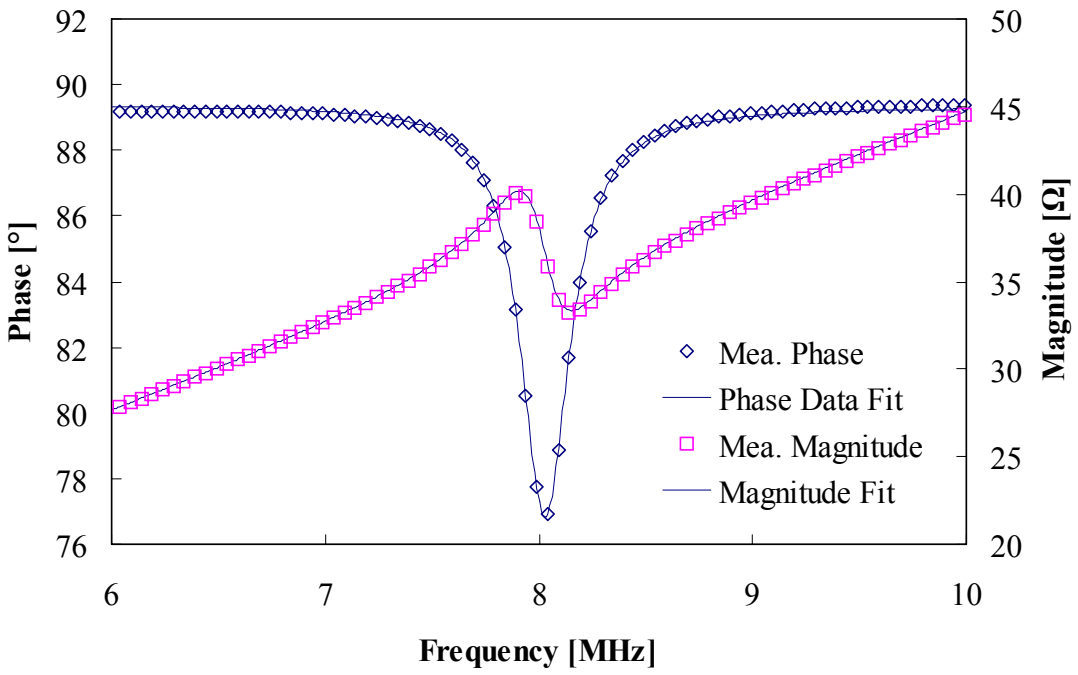

Figure 3.23: Measured magnitude and phase versus frequency for a multi-layer (4) spiral pressure sensor.

3.3 Development of HTCC Pressure Sensors

This section discusses the design, fabrication, and characterization of embedded circuitry HTCC sensors. To research higher temperature pressure sensor performance, embedded circuitry devices fabricated on alumina HTCC substrates are investigated. The results from section §3.2.2 concluded that improved performance can be achieved if the substrate has a lower dielectric loss and better mechanical properties at temperatures greater than 500 ℃. The design concept is the same as that for LTCC devices shown in Figure 3.6 in the previous section.

3.3.1 Design and Fabrication

The design and fabrication, illustrated in Figure 3.6 and Figure 3.7 respectively, of a device fabricated from 96% alumina ceramic is identical to that of embedded designs implemented in LTCC ceramic sbustrates. The only difference is the sintering temperature of

1500 ℃ and the use of Platinum-based 9141 Pt ink instead of silver-based ink. Figure 3.24 shows a fabricated device, which is backlit allowing the visualization of the embedded conductor lines, vias, and embedded channels.

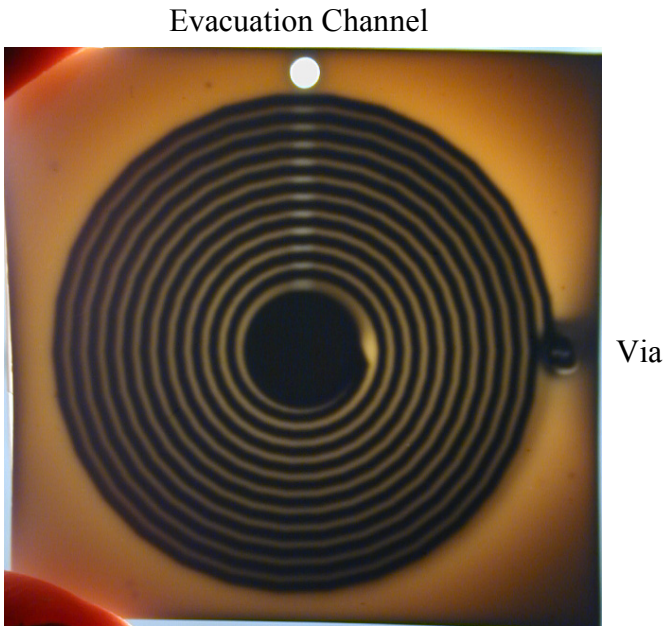

Figure 3.24: Top view of fabricated HTCC device in transmission light showing embedded coils and cavities.

3.3.2 Characterization

A device fabricated from HTCC was characterized at high temperature. The phase was measured from 350 ℃ to 600 ℃, shown in Figure 3.25. From the phase data measurement, the resonant frequency is extraced. The frequency temperature dependence is graphed in Figure 3.26 and is -2.7 kHz ℃ $^{-1}$. The quality factor for this device at room temperature was measured to be 14, which is low because of the high resistance of the Pt spiral. One of the drawbacks of this design is the relatively limited selection of metals that can be sintered with alumina ceramic at 1500 ℃. Most metals that withstand this temperature have relatively high resistivity (Pt is 10.6×10^{-8} Ωm) compared to good conductors like copper (1.7×10^{-8} Ωm), silver (1.6×10^{-8} Ωm), or gold (2.2×10^{-8} Ωm). One way to

overcome this limitation is to increase the spiral inductance through multi-layered designs while minimizing the resistance by keeping the length of the turns as short as possible.

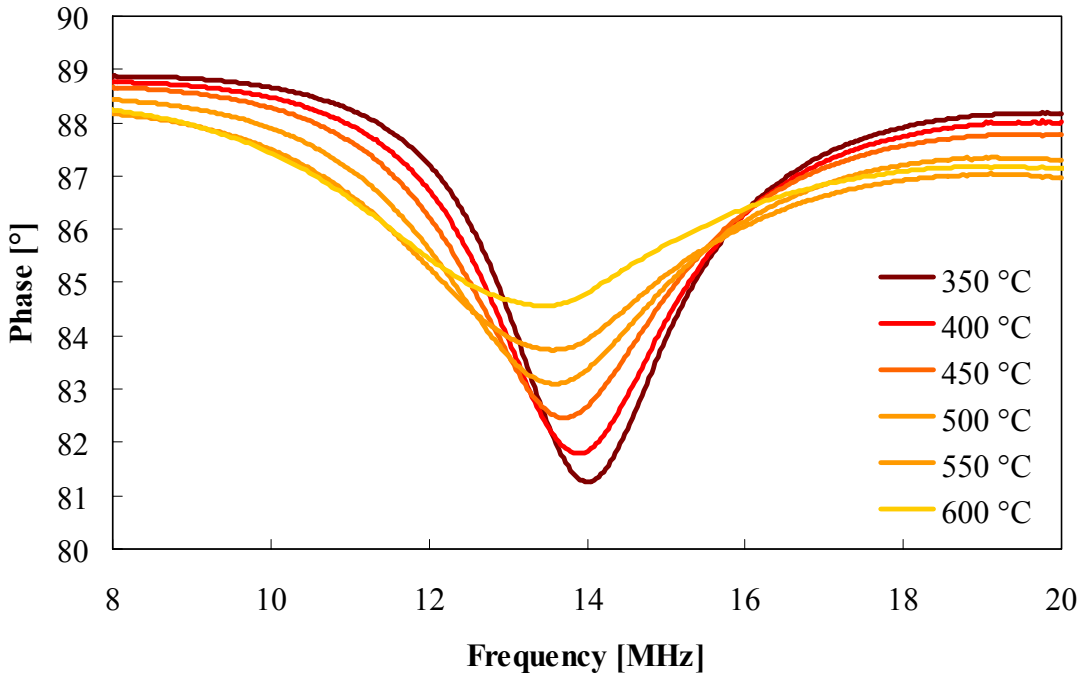

Figure 3.25: Measured impedance phase versus frequency for an HTCC device at temperatures from 350 ℃ to 600 ℃.

3.4 Summary and Conclusions

Devices fabricated from multi-layered LTCC ceramics with embedded Au metallization was operated at 450 ℃ and with pressure excursions over 5 bars. The models derived in Chapter 2 were used to predict the electrical, mechanical, and loss behavior for pressure sensors operating in high temperature environments. The devices were limited in temperature operation to below 450 ℃ due to the reduction in quality factor, with the dielectric loss dominating the Q above 300 ℃. Additionally, deterioration of the mechanical properties of LTCC substrate was observed at 350 ℃ with a drifting pressure sensitivity with increasing temperature as illustrated in Figure 3.18.

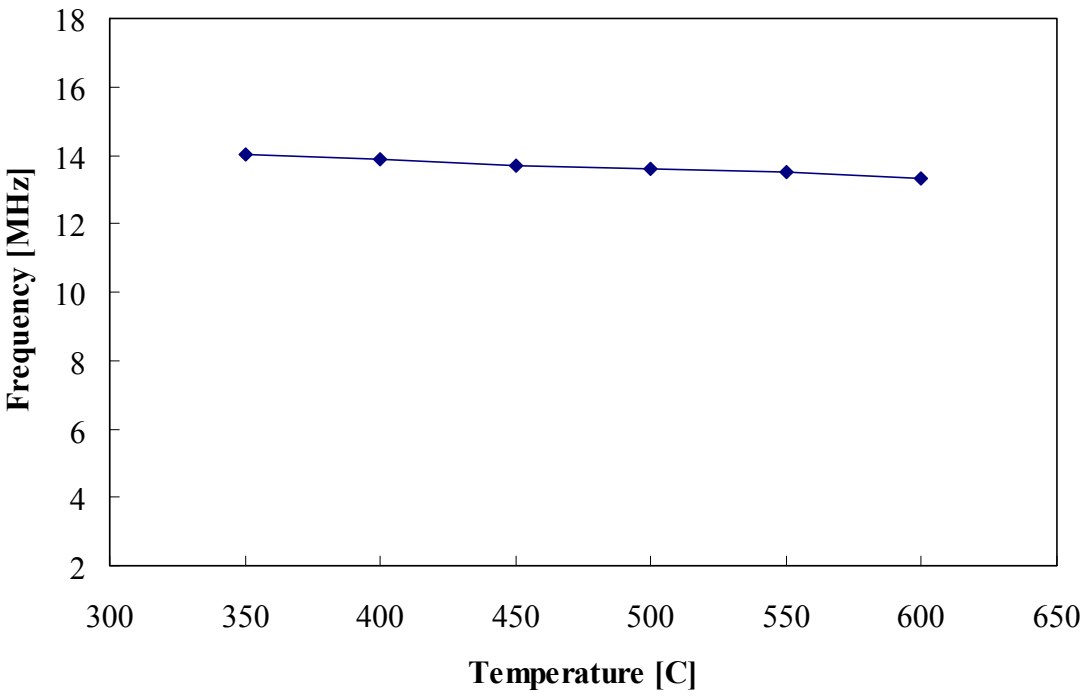

Figure 3.26: Resonant frequency versus temperature for an HTCC device.

Looking toward higher operating temperatures, alternate ceramic materials and metallizations suitable for operation at high temperatures were characterized. The high temperature alumina ceramic, consisting solely of alumina particles and organic binder (i.e. no glass filler), had typical firing temperatures in excess of 1400 ℃. Structures were fabricated from this material with embedded screen-printed Pt metallization and successful detection of resonance signals was achieved at 600 ℃, which was the maximum possible temperature of the test setup. One drawback of the fabricated devices from HTCC was their low quality factor, which is attributed to the high resistivity metal.

CHAPTER 4

BIOMEDICAL DESIGN CONSTRAINTS

Several sensor designs were developed and characterized to advance flexible polymer-based passive pressure sensors for wireless telemetry in biomedical applications. However, first it is necessary to define the design space and constraints associated with operation in such an environment. The list below describes the research objectives for designing wireless flexible polymer pressure sensors for biomedical applications.

- Implement passive LC resonant circuits for wireless telemetry.
- Use parallel-plate capacitors fabricated on and integrated into pressure-deflectable plates or membranes.
- Leverage standard microelectronics flex-circuit packaging technology used for ICs to achieve batch-fabrication.
- Fabricate devices from biocompatible flexible polymer materials.
- Be capable of catheter-based delivery for biomedical applications. This limits the design space by constraining physical dimensions.
- Leverage multi-layer fabrication approaches to achieve embedded passives.
- Develop designs without via interconnects between planar spiral layers to increase robustness as a flexible device.
- Use materials with the potential for micro-fabrication processes to create micro-scale mechanical and electrical features.
- Demonstrate applicability in biomedical applications.

An important research objective is the demonstration of pressure sensor applicability in biomedical applications. This is achieved by implanting devices into animal models using catheter-based delivery systems and wirelessly interrogating sensors to measure continuous pressure waveforms. The scope of this part of the dissertation is the design, fabrication, and characterization of polymer pressure sensors designed to be catheter delivered and operated

in vivo. To achieve these objectives, additional design constraints are considered, which are listed below.

- Catheter-based delivery limits physical dimensions. Catheters selected to demonstrated delivery have an inner diameter of < 5 mm. The application selected to demonstrate feasibility is abdominal aortic aneurysm (AAA), which is described further in Chapter 8, section §8.1.
- Materials selected to fabricate the devices should be flexible and biocompatible.
- Operate devices in a pulse pressure fluid environment.
- Use of commercial interrogation telemetry systems require high quality factor resonators and operational frequencies ranging from $30 < f_0 < 42$ MHz.
- Interrogate sensors with available telemetry electronics when operating through several inches of tissue.

To refine these requirements into specific design inputs, a better understanding of the relationship between the catheter, interrogation system, materials, environment, and sensors is required. Section §4.1 below presents electrical performance requirements for the sensor designs and how they relate to the interrogation system. Section §4.2 discusses catheter delivery system requirements. Section §4.3 introduces flex-circuit material properties, while §4.4 discusses environmental effects related to lossy electrical medial. Finally, section §4.5 summarizes the design requirements from this chapter.

4.1 Readout Telemetry Design Constraints

The readout telemetry system used to interrogate the sensors during animal implants was supplied and operated by engineers at CardioMEMS, Inc. A brief description of the system follows. Then, sensor design constraints are discussed as they relate to the interrogation distance.

The readout telemetry system consists of switched transmit and receive magnetic loops, a switched RF amplifier, and a high-sensitivity RF receiver. The system is driven by a microprocessor and a phase synchronous oscillator, illustrated in Figure 4.1. The system sends a burst of RF energy at the resonant frequency of the devices lasting several microseconds, which is optimized to be long enough to energize the sensor. Soon afterward, the transmit signal is turned off and the receive channel is opened. For a short period of time, based on the sensor quality factor Q, the sensor will continue to oscillate at the resonant frequency and exponentially decay to zero; this is repeated at the sampling rate of the system. In order to track the sensor real-time frequency response, a phase-locked-loop was implemented. Since the sensors are not absolute pressure sensors, a barometric pressure sensor is incorporated into the system to adjust for atmospheric pressure changes in order to report pressure in the aneurysm sac relative to atmospheric pressure. Additional interface inputs were added to the system to be able to read-out various catheter-based transducers used to compare to wireless pressure sensor readings. Finally, the system is controlled through a LabVIEW software interface, shown in Figure 8.5c.

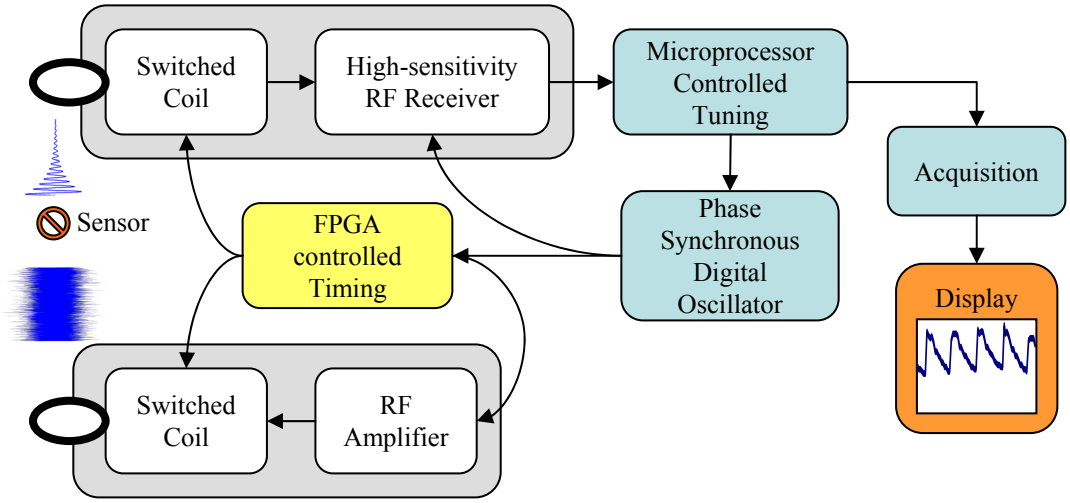

Figure 4.1: Block diagram of readout telemetry system.

Interrogation detection and allowable distance between the sensor and telemetry electronics are dependent on the sensors quality factor Q and coupling coefficient k, since they

affect the ring-down time and returned signal strength. Q impacts the ring-down time: the higher the Q value, the longer the circuit oscillates before exponentially decaying to zero. The magnitude of the oscillations are proportional to k. Both effects can be modeled using a basic lumped element model for the sensor, illustrated in Figure 2.3. Analysis of the circuit, which is derived in Appendix A section §A.4, yields the transfer function

$$H(s) = k\sqrt{\frac{L_s}{L_a}}\left(\frac{\omega_0 s + Q\omega_0^2}{(1-k^2)Qs^2 + \omega_0 s + Q\omega_0^2}\right) . \tag{4.1}$$

Using Eq. (4.1), the effects of varying Q and k are illustrated in Figure 4.2. For the data in Figure 4.2, a circuit resonant frequency of 35 MHz was used. The square root term at the beginning of Eq. (4.1) is ignored, and would act to scale the time response signal. This term should be $<<$ 1 because of the small mm-scale pressure sensors compared to a relatively large scale antennas with a diameter of several inches resulting in $L_s < L_a$.

The telemetry electronics uses a square wave to active the sensor, where high-signal charges up the oscillator and low-signal is used for detection. Then it can be determined that maximizing the sensor Q will increase detectability. This is because the oscillator will take longer to decay, allowing the electronic system more time to lock on in a phase-synchronous way. Also, increasing the coupling coefficient k between the sensors and readout antenna will increase the detection distance by amplifying the signal strength at the receive channel.

The last requirement that should be mentioned regarding the electronic telemetry system is the alloted operational frequency bandwidth for this system. The telemetry system receive pass band filters roll off below 30 MHz and above 42 MHz, thereby setting the frequency range of the sensors. This in turn sets the maximum allowable pressure sensitivities to maintain the device resonance frequency f_0 within 30-42 MHz. Assuming a pressure dynamic range from 600 to 1020 mmHg (absolute) to include both low and high altitudes, and using a linear sensitivity, practical sensitivities of $<$ 20 kHz·mmHg^{-1} can be achieved. This is because the set of allowable frequencies (at atmospheric pressure) that

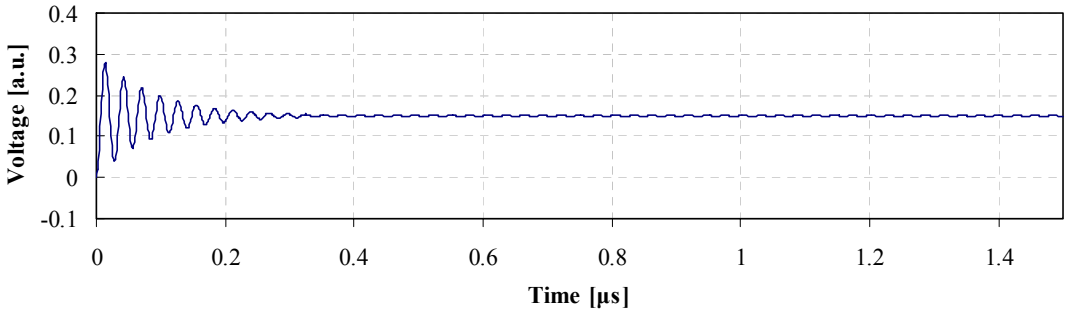

(a) $Q = 10$, $k = 0.15$

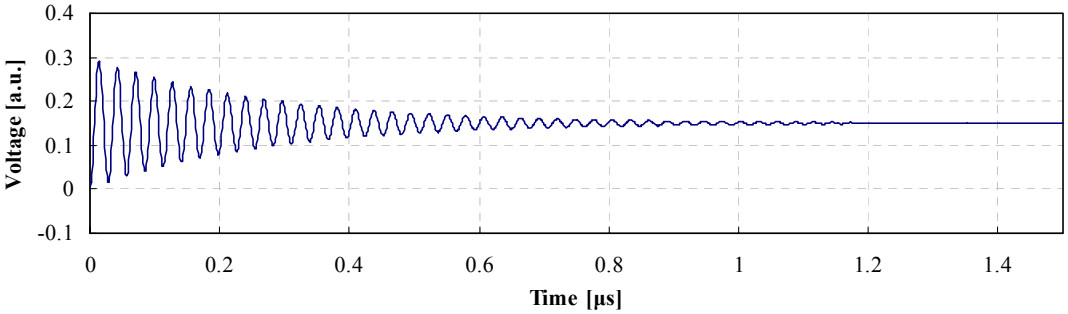

(b) $Q = 30$, $k = 0.15$

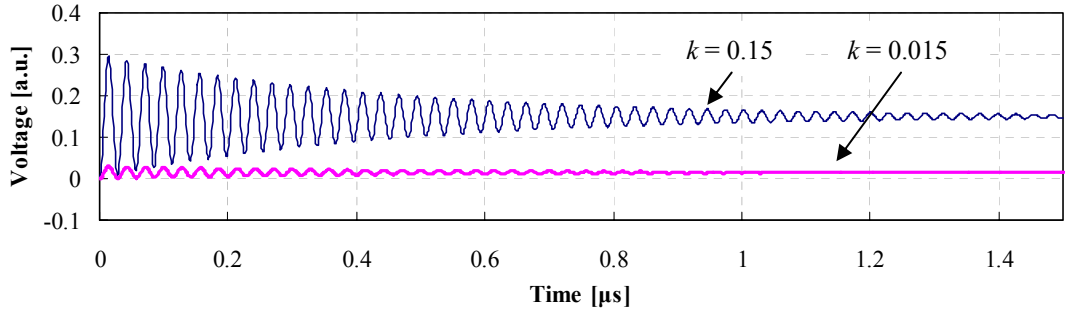

(c) $Q = 50$, $k = 0.15$ and $k = 0.015$

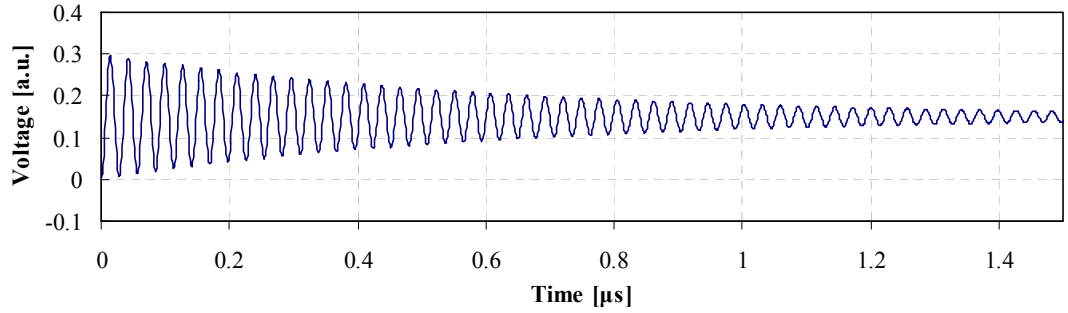

(d) $Q = 70$, $k = 0.15$

Figure 4.2: Lumped element model time step response for Q of 10 (a), 30 (b), 50 (c), and 70 (d). Also, effects of k scaling from 0.15 to 0.015 are shown in (c).

operate within the desired frequency band of 30-42 MHz across the entire dynamic pressure range are contained between 35.5 and 39.3 MHz. This represents a target band of 3.8 MHz, which is reasonable with level repeatability in the fabrication of the sensors. Beyond 20 kHz·mmHg^{-1}, the frequency bandwidth of allowable f_0 becomes increasingly narrow, illustrated by the minimum and maximum frequency lines Figure 4.3. To achieve higher pressure sensitivities better repeatability of the resonance frequency would be required.

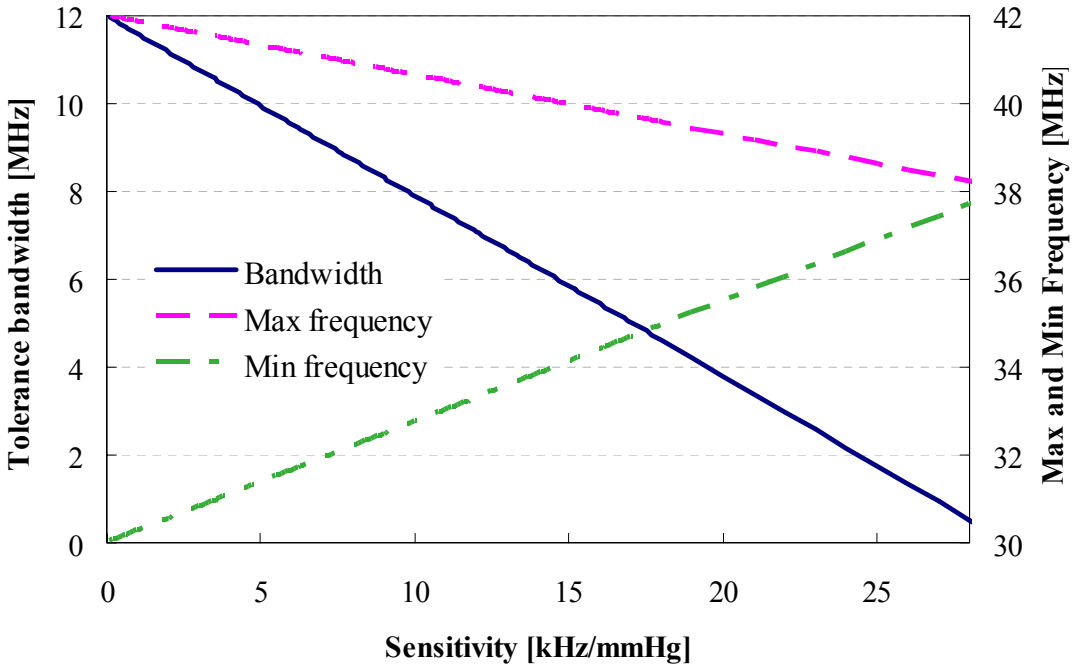

Figure 4.3: Plot of estimated frequency bandwidth and maximum and minimum allowable frequencies versus linear pressure sensitivity.

4.2 Catheter-based Delivery Design Constraints

For minimally invasive implantable devices, catheter-based delivery systems are preferable. The flexible sensors could be rolled or folded into catheters that have internal diameters < 5 mm, which limit the size and shape of the sensors. Additionally, during delivery the sensors will be in systemic blood flow prior to reaching the final delivery location. Therefore, it is required that the sensor be secured while the endovascular repair of a mock aneurysm

is in progress. This requires the use of a tethering system to keep the sensor from flowing downstream from the intended delivery site and occluding a main arterial branch. Specific details of the animal study and selected application are described further in Chapter 8. Also, the delivery catheter was developed by CardioMEMS, Inc. During the design of the sensor, collaboration with CardioMEMS, Inc staff was required to ensure proper integration between the sensor and delivery system.

The catheter main system consists of an extruded dual lumen catheter tube, a guide wire tube, a tether guiding tube and an outer sheath, illustrated in Figure 4.4a and Figure 4.4b. The outer sheath provides a smooth outer surface for delivery through arterial vessels and prevents damage to the tissue during insertion. The guide wire tube is used for a common delivery technique that requires the insertion of a guide wire though the artery all the way to the desired delivery site; this is done prior to using the delivery system. The delivery catheter tracks over the guide wire to reach the delivery site. The tether tube guides the tethering system up the catheter. The tether system holds onto the sensor during delivery in order to keep it in position in systemic blood flow during the procedure.

From Figure 4.4b, dimensional constraints for the sensor physical dimensions are extracted. The sensor will be positioned in the gap between the guide wire tube and tether tube, which is 0.7 mm. Additionally, the sensor will need to be rolled up in order to fit within the outer sheath ID of 4.78 mm. Apart from the catheter requirements, it is desirable that permanent implantable wireless pressure sensors be small and have rounded edges or corners to minimize perturbation or damage of the surrounding tissue.

Catheter deliverability ultimately limits the overall size and thickness of the implantable devices, which for the catheter discussed in this section is approximately 15 mm in diameter and 0.7 mm in thickness for flexible sensors. If the devices are not flexible, the overall width is limited to < 4.78 mm with a variable maximum thickness, which depends on the width. This is due to the circular profile of the catheters and the general rectangular profile of pressure sensors. The length is not strictly fixed; however, minimizing this dimension is

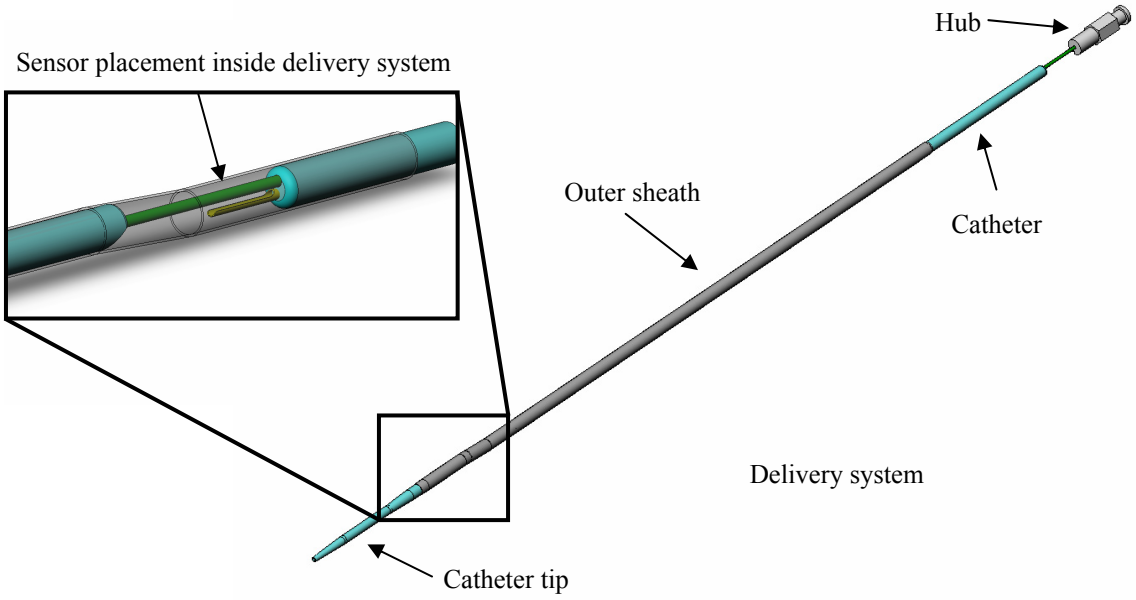

(a)

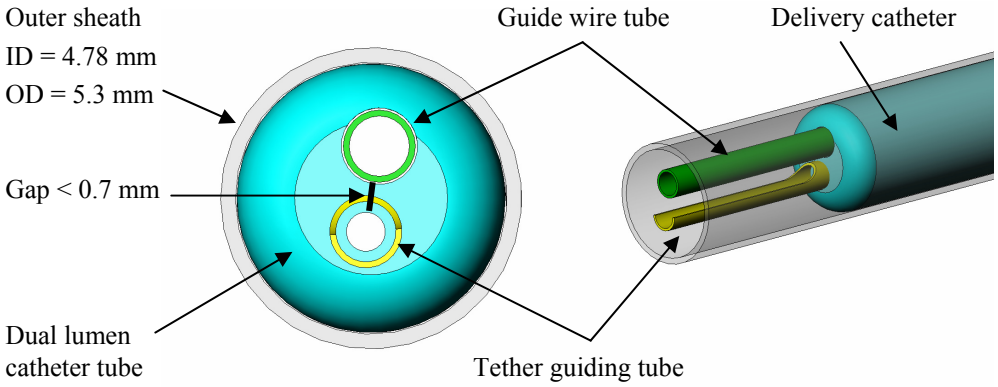

(b)

Figure 4.4: Delivery system (a) and close up view (b) of sensor placement location within the delivery system

a good practice as a general rule of thumb. Clearly, flexible devices have an advantage over rigid ones in that they can have larger footprints, which for wireless telemetry has the potential to increase detection distance. Increased flexibility can be achieved by selecting fabrication technologies that minimize the cross-section or thickness. For many of the flex-circuit technologies available, laminate sheets of thickness ranging from 25-100 μm are available. These will be used to fabricate passive wireless devices whose thicknesses will range from 200-700 μm.

4.3 Material Properties

There exist several flex-circuit fabrication technologies. One of the most common is Kapton® based, from DuPont™, within which several different product lines exist. In this research, the Pyralux® product line is investigated. The limitation of this technology is the acrylic bonding films and the relatively high dissipation factor. Other lower loss materials include LCP and fluorinated polymers, such as PTFE and FEP. Table 4.1 summarizes some of the material properties for these polymer and bonding film technologies.

Table 4.1: Polymer Material Properties.

Property	**Kapton®**	**Pyralux®**	**LCP**	**SpeedBoard®**	**PTFE**	**FEP**
Density [g·cm^{-3}]	1.42	-	1.4	-	2.15	2.14
CTE [ppm·C^{-1}]	20 - 30	-	17	56	80 - 130	130 - 200
Melt Temperature [℃]	-	200	315	-	-	260
Water Absorption [%]	2.8	-	0.04	-	0.004	0.004
E [GPa]	2.5	-	2.26	-	0.5	0.4
Poisson's Ratio	0.34	-	-		0.46	0.48
ϵ_r	3.6-4	4	2.9	2.6	2.1	2.06
$tan\delta$	0.002 *	0.02 - 0.03	0.0025	0.004	0.0008	0.0008

* When combined with Pyralux® adhesive, the $tan\delta$ increases to 0.02 - 0.03.

4.4 Operational Environment

An important aspect in designing implantable passive wireless devices is to consider the effect of the environment the device is required to operate within. It is well documented that living tissues have high permittivity and dielectric loss. Table 4.2 lists some of the more common body tissues encountered by implantable devices. The variability of the relative permittivity and dielectric loss of the body tissues and fluids can have parasitic effects on passive LC resonant sensor designs. Both the resonance frequency f_0 and quality factor Q can be affected. To research this effect, 2D FEA modeling on the cross-section of a typical device was performed, investigating the displacement flux density as the dielectric media surrounding the sensor changes.

Table 4.2: Summary of dielectric properties of body tissues [95].

Tissue or Fluid	ϵ_r	$tan\delta$
Air	1	0
Saline (0.9%)	80	0.2
Blood	119.5	5.5
Body fluid	69.3	11
Brain gray matter	152.6	1.65
Brain white matter	100.6	1.4
Bone	40.2	2
Cartilage	85.6	2.7
Fat	8.1	2.2
Muscle	91.8	3.9

The 2D FEA modeling is based on a static analysis, which is valid considering the wavelength of 10 m at 30 MHz in air and a physical device size of approximately 1cm in diameter and 35 cm of conductor length (wound length of a typical spiral). The analysis is used to gain basic insight on the displacement flux D and electric field E as the relative dielectric constant ϵ_r of the surrounding media changes. Figure 4.5 graphs a representation of the 2D cross-section used for modeling a typical pressure sensor, which closely resembles Figure 2.21 from section §2.1.5. In the center is the cross-section of a typical sensor with a cavity (ϵ_0), the polymeric substrate (ϵ_{r1} and ϵ_{r2}) and metal traces.

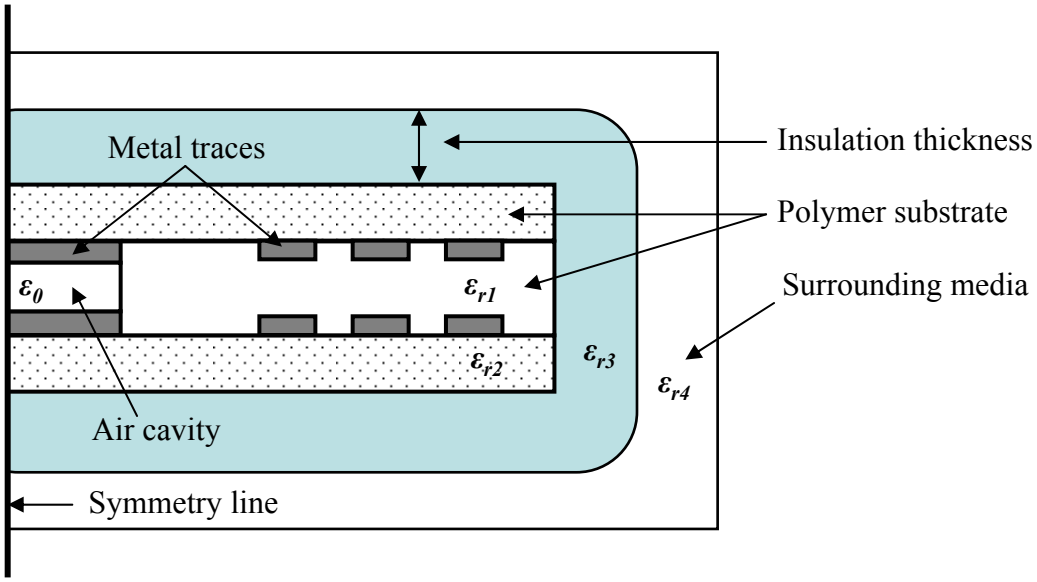

Figure 4.5: Sensor cross-section used for 2D FEA static analysis for changing relative permittivity of the surrounding media.

It is expected that to counteract some of the media dielectric effects on f_0 and Q, a layer of additional insulation will be required with a thickness t_{ins} and dielectric constant ϵ_{r3}. This is because as the surrounding media permittivity ϵ_{r4} changes, so will the displacement flux. With larger permittivity, more displacement flux passes through the media, which increases the system capacitance and reduces the resonance frequency f_0. If the media is lossy, then more electric energy is dissipated, thereby reducing the quality factor Q of the sensor. The insulation, which is just additional dielectric material (ϵ_{r3}), acts to contain the displacement flux from going into the media, thereby reducing the amount of electric energy dissipated.

In Figure 4.5, the voltage difference between the top and bottom metal traces is held constant while the relative permittivities are changed. Using sub-domain integration, the electric energy densities ($W_e = \frac{1}{2}\epsilon E^2$) of the different sub-domains are calculated and compared. The quantity of interest is the percent change in electric energy density of the surrounding media normalized to the total energy density of the system as a function of insulation thickness (ϵ_{r4} in Figure 4.5). The percent energy stored in the media W_{media} is

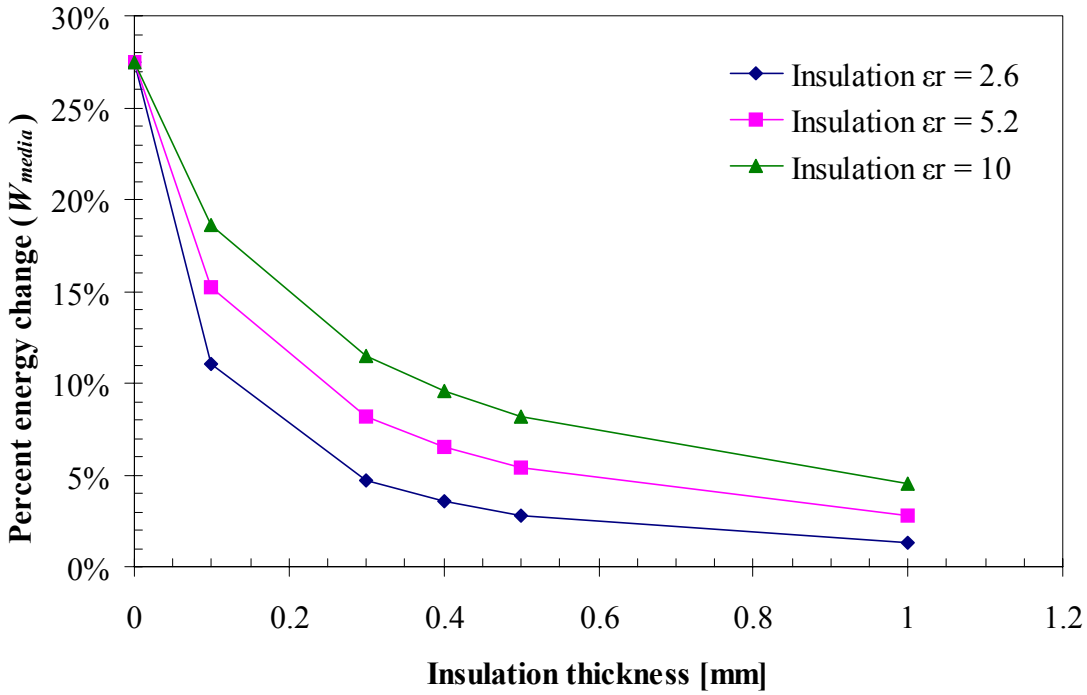

Figure 4.6: Percent electric energy stored in the surrounding media W_{media} versus insulation thickness t_{ins} for insulation permittivities of 2.6, 5.2, and 10.

given by

$$W_{media} = \frac{W_e(media)}{W_e(total)} \ . \tag{4.2}$$

The energy percent is used instead of the calculated value because the absolute value does not have a physical meaning. Figure 4.6 plots the percent energy stored in the media as a function of the insulation thickness for three different insulation dielectric constants (ϵ_{r3} = 2.6, 5.2, and 10). The insulation thickness was varied from 0 to 1 mm thick. All dielectric materials where held constant while t_{ins} varied. The media dielectric, ϵ_{r4}, was set to 80. In a similar fashion, W_{media} can be calculated as a function of the media relative permittivity ϵ_{r4} (see Figure 4.7). From these calculations, it is clear that the thicker insulation in combination with the lowest possible dielectric constant will achieve the best performance. This combination minimizes the amount of electric energy being dissipated into the lossy media. Although this result was expected, it is useful to predict the resonance frequency and quality factor of various designs when the design requirements have specific thicknesses or a limited material set.

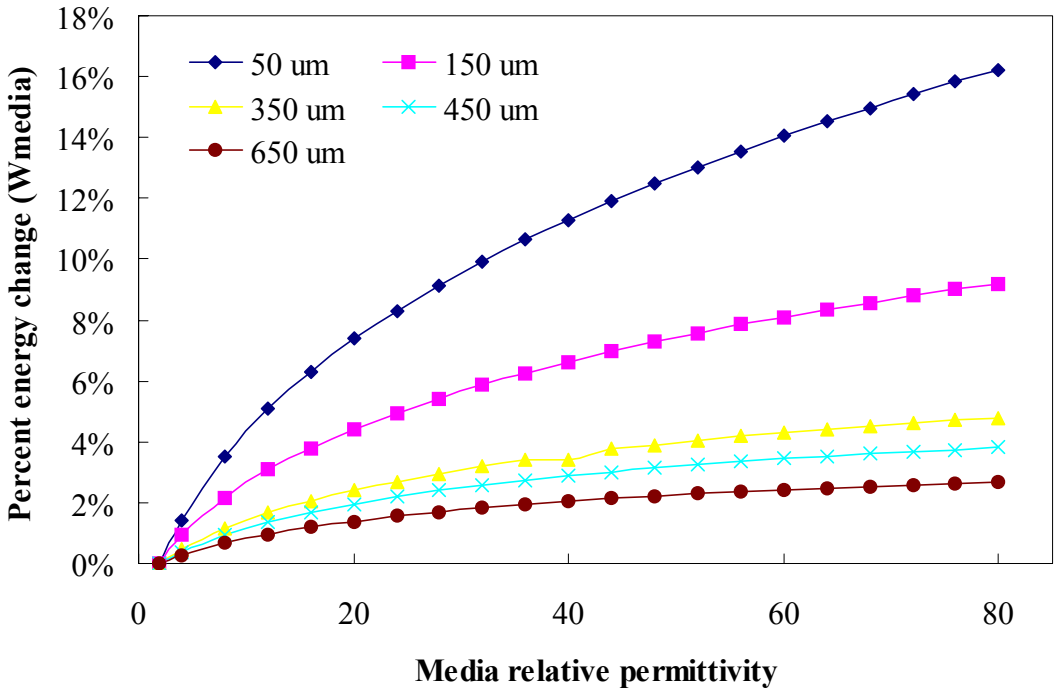

Figure 4.7: Percent electric energy stored in the surrounding media W_{media} versus media relative permittivity ϵ_{r4} for insulation thicknesses ranging from 50 to 650 μm.

Another dielectric parameter that should be considered is the substrate permittivity. The embedded traces are surrounded by this dielectric, and just like the insulator, lower permittivity should result in better performance. To verify this assumption, two designs are compared. The first design (Der1) has substrate relative permittivities of $\epsilon_{r1} = 2.5$ and $\epsilon_{r1} = 3$, while the second design (Der2) has both ϵ_{r1} and $\epsilon_{r2} = 2.1$. Also, the insulation thickness was held constant at 0.5 mm. Figure 4.8 plots the calculated stored energy change W_{media} as a function of media relative permittivity for both designs, Der1 and Der2.

A design trade off from the analysis above is maximizing the insulation thickness while keeping the overall thickness < 700 μm and maintaining device flexibility. These requirements must be met while in a narrow design space, which includes the material set, required for biocompatibility as well as fabrication technologies. To achieve the above requirements, medical grade silicone was selected. The coating can be applied post-fabrication through a potting or dipping procedure. The material has a long history as a medical device material and meets the required electrical characteristics (low loss and relative dielectric constant).

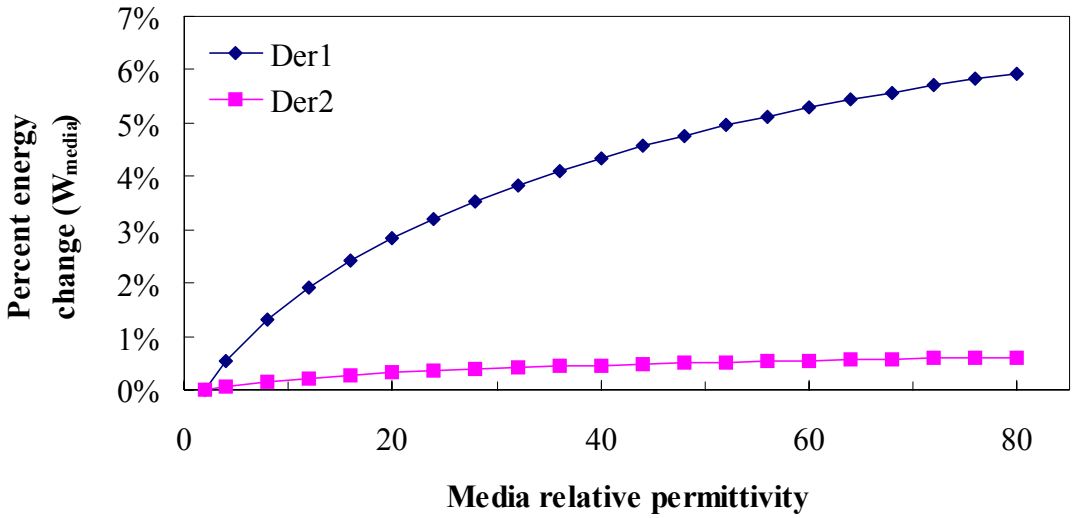

Figure 4.8: Percent electric energy stored in the surrounding media W_{media} versus media relative permittivity ϵ_{r4} for two sensor designs implementing different substrate relative permittivities. Der1 uses $\epsilon_{r1} = 2.5$ and $\epsilon_{r1} = 3$ and Der2 uses both ϵ_{r1} and $\epsilon_{r2} = 2.1$.

Finally, it has a low modulus of elasticity and high elongation, which allow for the coating to stretch and bend as the devices are folded and flexed into the delivery system. For the polymer-based devices fabricated in the subsequent chapters, silicone will be used for insulation to reduce the effects of the lossy media.

4.5 Summary of Design Constraints

To meet the sensor design detection and delivery requirements a round shape is chosen. This is the optimal shape for a planar spiral inductor, achieves the smallest possible footprint, and eliminates corners. A summary of sensor design requirements from the constraints discussed in the sections above are listed in Table 4.3. Further discussion on the design of polymer-based pressure sensors follows in Chapter 5 and Chapter 6.

Table 4.3: Summary of Polymer Sensor Design Requirements.

Parameter	**Requirement**
Operating Environment	Electrically lossy fluid or tissue
	Mean pressure range 0-260 mmHg
	Pulse pressures $>$ 40 mmHg at 76 bpm
Frequency	$30 < f_0 < 42$ MHz
Sensitivity	$> \|1\|$ kHz·mmHg^{-1}
Q	$>$ 40 in saline solution
k	Maximum for given Q
Drift	Application dependent
Thickness	$<$ 0.7 mm
Shape	Circular, rounded edges, and no corners
Diameter	$<$ 15 mm
Substrate	Flexible polymer
Reliability	Design concept and simplicity
Biocompatibility	Material selection

CHAPTER 5

POLYMER PRESSURE SENSORS

Several sensor designs were developed and characterized to advance flexible polymer-based pressure sensors for wireless telemetry in biomedical harsh environments. Standard flexible electronic packaging techniques were used to fabricate sensors from polymer materials, which include polyimide and LCP. The designs implement embedded circuitry with two oppositely wound planar spiral inductors interconnected to parallel plate capacitors introduced in Chapter 2 Figure 2.1b. Section §5.1 details the development LCP polymer-based pressure sensors, and sections §5.2 and §5.3 summarize designs implemented in Kapton® and PTFE substrates respectively.

5.1 Development of LCP-based Sensors

5.1.1 Design and Fabrication of LCP-based Sensors

The sensor design consists of three sections, illustrated in Figure 5.1, which form the outer and inner layers. The outer layers are patterned LCP copper-clad while the inner film is an ePTFE with infused adhesive resin. The inner layer bonds the three sections together and has a cutout to create the embedded cavity. This approach results in an intrinsically packaged structure in which only an LCP polymer outer surface is exposed to the environment.

The sensors are fabricated from laminated sheets of GORE™ copper-clad LCP and ePTFE-based inner bonding layers. The batch process uses 4 inch sheets with 4 rows and 4 columns, yielding 16 devices per fabrication run. First, the copper cladding is patterned into the

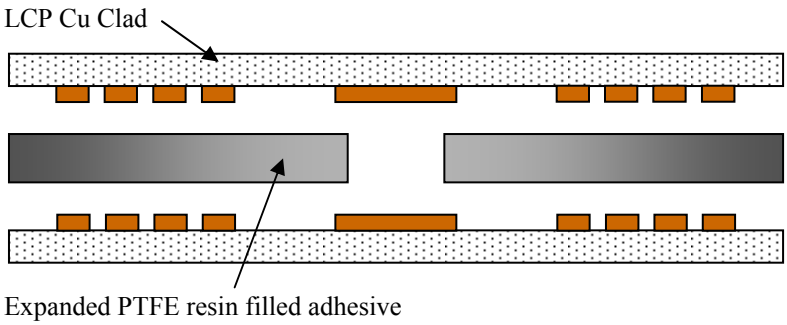

Figure 5.1: Cross-sectional view of a LCP-based pressure sensor.

desired inductor structures prior to lamination. This is done through standard photolithography and wet-chemical etching. The inner layer is laser-cut using an excimer laser (248 nm wavelength) to achieve accurate dimensions. Then, the two outer layers and inner layer with its corresponding cavity design are aligned via registration pins on platens, assembled together, and laminated at 180 ℃ for 80 minutes with 431 kPa of pressure. A perspective view is illustrated in Figure 5.2. The sensors are individualized using the same excimer laser from above to achieve various shapes for minimally-invasive delivery. A fabricated sensor is illustrated in Figure 5.3a and Figure 5.3b. Also, further details on the fabrication process, photolithography masks, assembly blocks, press platens and fabrication equipment are described in Appendix B section §B.3 and Appendix C section §C.1.

5.1.2 Modeling of LCP-based Sensors

The inductor layout, illustrated in Figure 5.4a, uses a planar spiral inductor with n=12 turns, line width (lw) of 60 μm, line spacing (ls) of 80 μm, and copper line thickness (lt) of 18 μm; the starting radius for the spiral inductor is 3.8 mm and the capacitor plate area (A_{cap}) is 13.1 mm^2 (length of 6.68 mm and width of 2.08 mm). Using the model for inductance derived in section §2.1.3, the calculated series inductance L_s, series resistance R_s, and self-capacitance C_{par} can be calculated for the spiral given in Figure 5.4a, and are 2.27 μH [Eq. (2.32)], 6.9 Ω [Eq. (2.44)], and 0.536 pF [Eq. (2.41)] respectively. The measured inductance and DC resistance of 2.3 μH and 6.93 Ω compare well with the model

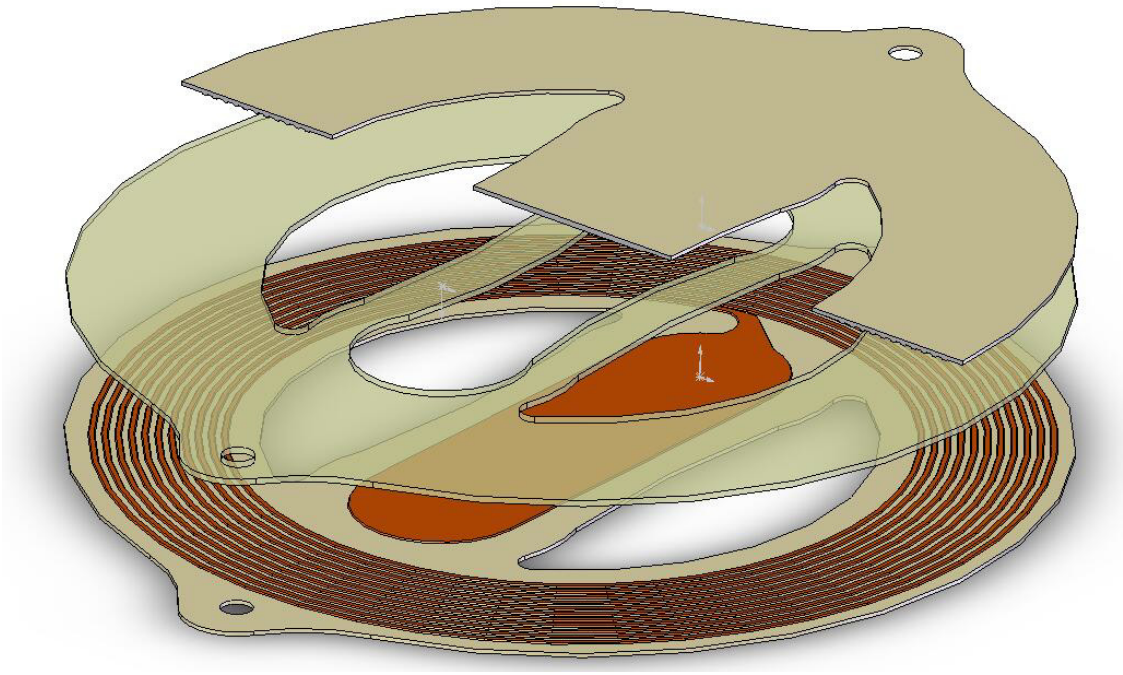

Figure 5.2: Perspective view of the assembly for an LCP-based pressure sensor.

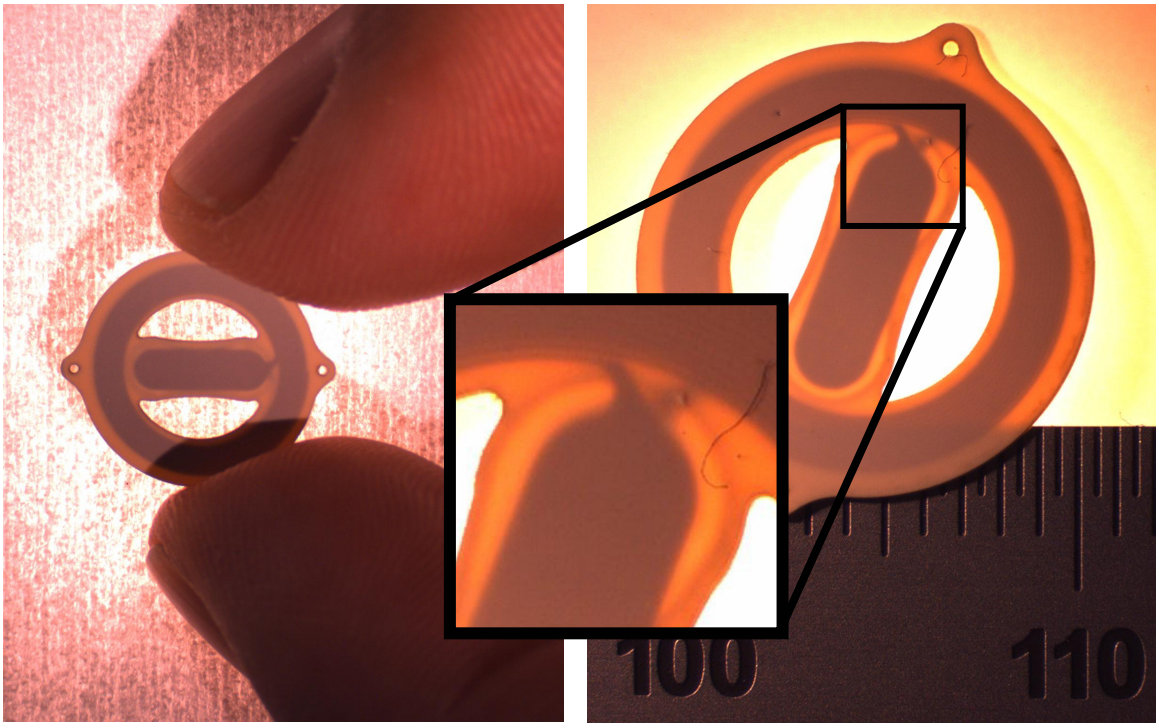

(a) (b)

Figure 5.3: Photographs of fabricated LCP polymer wireless pressure sensors using two reference scales: (a) hand-held and (b) millimeter ruler. The inset gives a magnified view of embedded cavity and capacitive electrodes.

estimates of 2.27 μH and 6.9 Ω. The design from above is equivalent to the spiral termed Design1 from Chapter 2, section §2.1.3 in Table 2.3 except for the substrate being LCP and not PTFE. This difference only impacts the parasitic capacitance and hence the coil self-resonance. Figure 2.14, Figure 2.15, and Figure 2.16 graph the measured inductance, resistance, and quality factor versus frequency, respectively, for Design1 from Chapter 2, which closely match the spiral design in this chapter.

The pressure variable capacitance C_{plate} for the pressure sensor consists of the top and bottom metal electrodes separated by a cavity with gap t_g, shown in Figure 5.1, and is equivalent to the model shown in Figure 2.36b. Before calculating the pressure variable capacitance, the mechanical diaphragm designs are discussed. Four cavity designs were implemented. The embedded cavity designs are illustrated in Figure 5.4b, with the base design having the same length as the capacitive electrode of 6.68 mm. The cavity was designed to span 2.08 mm at the ends and 1.4 mm in the center, resulting in an area of 10.93 mm^2. To achieve the taper in the center of the cavity, an arc is used with a radius of 7.95 mm; this taper reduces the deflection of the membrane and avoids shorting out the capacitor during fabrication and over pressure excursions of interest. Three other variations of the cavity design were researched, which include offsets of +100, +250, and +300 μm increments, with the +300 μm design illustrated in Figure 5.4b. Table 5.1 lists the dimensions for each of the cavity designs.

Table 5.1: Cavity designs for LCP-based pressure sensors.

Parameter	**Cavity Designs**			
	Base	**Base+100μm**	**Base+250μm**	**Base+300μm**
Length [mm]	6.68	6.88	7.1	7.28
Width [mm]	1.4	1.6	1.9	2
Area [mm^2]	10.93	12.54	14.5	15.95
End radius [mm]	1.04	1.14	1.25	1.34
Taper radius [mm]	7.95	8.02	7.16	8.275

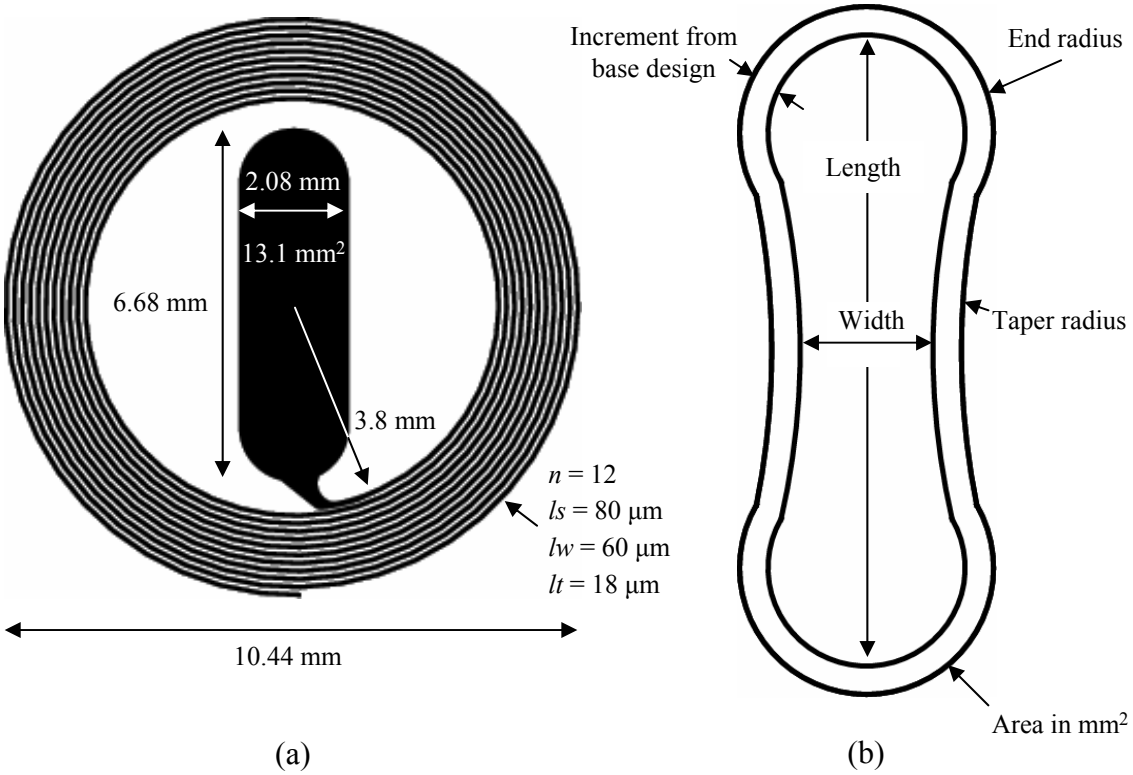

Figure 5.4: Planar spiral inductor (a) and cavity design (b) for LCP-based sensors.

The capacitance at zero applied pressure is estimated from Eq. (2.92b) and is equal to $C_{plate}(P = 0) = 1.25$ pF, which assumes no initial pre-deflection. Although the pre-deflection was not measured for this device, it is reasonable to assume that for some devices there will exist some level of residual pre-deflection from the lamination fabrication process. Also, note that zero applied pressure ($P = 0$) corresponds to atmospheric pressure, which is 760 mmHg (absolute) at sea level. Using Eq. (2.86) and Eq. (2.91), the deflection d_0 and pressure variable capacitance $C_{plate}(P)$ are calculated, respectively.

Figure 5.5 graphs the deflections for d_0 versus absolute pressure for the four different cavity designs for pressure ranges of 600-1020 mmHg (absolute). Note that the deflections are negative for pressure below atmospheric and they intersect zero at atmospheric pressure of 760 mmHg at sea level. For the deflection calculation, the flexural rigidity given by Eq. (2.75) of 0.217 mN·m overestimates the stiffness of the copper/LCP bi-layer by a factor of 3.4 times. The flexural rigidity was adjusted down to 0.0637 mN·m. It is possible that the

overestimation is due to the complex polymer-metal interface, which is beyond the scope of this work. Also, to simplify the deflection calculation, the shape from Figure 5.4b was assumed to be rectangular. In Eq. (2.86) the width dimension a was set equal to the average width for each cavity design.

Figure 5.6 graphs the pressure variable capacitance $C_{plate}(P)$ versus pressure for each cavity design from Table 5.1. Since the electrode dimension is constant, all capacitances start at 1.25 pF for a normalized pressure of 760 mmHg. Also for the cavity design Base+300μm, the electrodes should short out for the given pressure range, shown by the curve approaching infinity in Figure 5.6.

5.1.3 Impedance Measurements of LCP-based Sensors

The sensor is placed in the plane of a loop antenna L_a and the impedance is measured. The inductance of the antenna L_a was estimated as 1 μH. Using the model derived in section §2.1.5, the impedance magnitude and phase of the sensor can be calculated from Eq. (2.65) and are graphed in Figure 5.7a and Figure 5.7b respectively. Below and above resonance, the phase is close to the ideal value of 90° for an inductor and the magnitude depends linearly on the frequency. The data in Figure 5.7 was taken at atmospheric pressure. At resonance, the sensor induces a change in impedance phase and magnitude. The phase minimum f_{min} occurs at 36.91 MHz. Curve fitting, using Eq. (2.9), was used to extract frequency, coupling coefficient, and quality factor from the measured data (see Figure 5.7). The resonance frequency f_0, the coupling coefficient k, and the quality factor Q obtained from the fit are 36.86 MHz, 0.0726, and 50.1 respectively. Note that the phase minimum f_{min} is 0.14% higher than f_0. In this case, the difference is significantly less because the coupling k is low and the quality factor Q is high.

The calculated and measured self-resonances are 38.24 and 36.86 MHz, which are in good agreement. The difference of 3.61% in frequency is likely caused by an initial pre-deflection

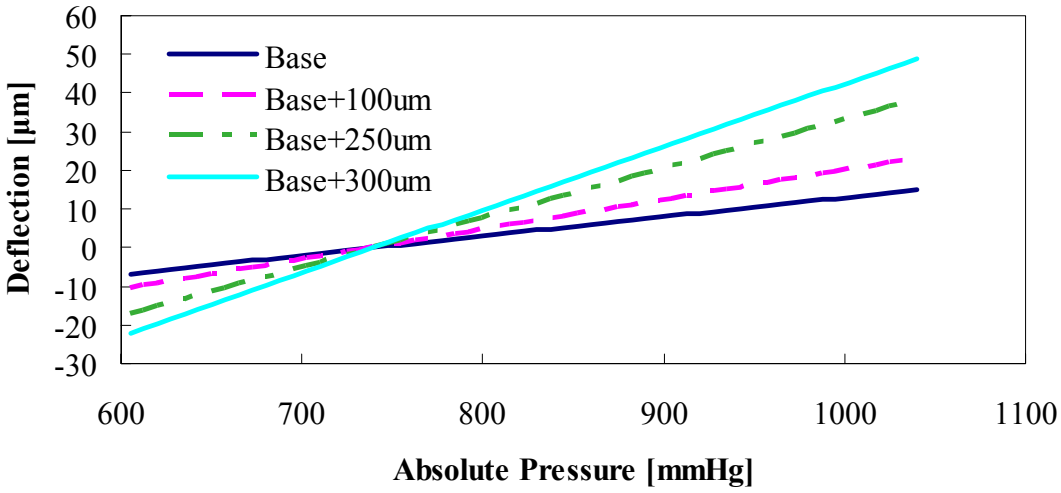

Figure 5.5: Simulated diaphragm deflection for cavity designs specified in Table 5.1 versus absolute pressure.

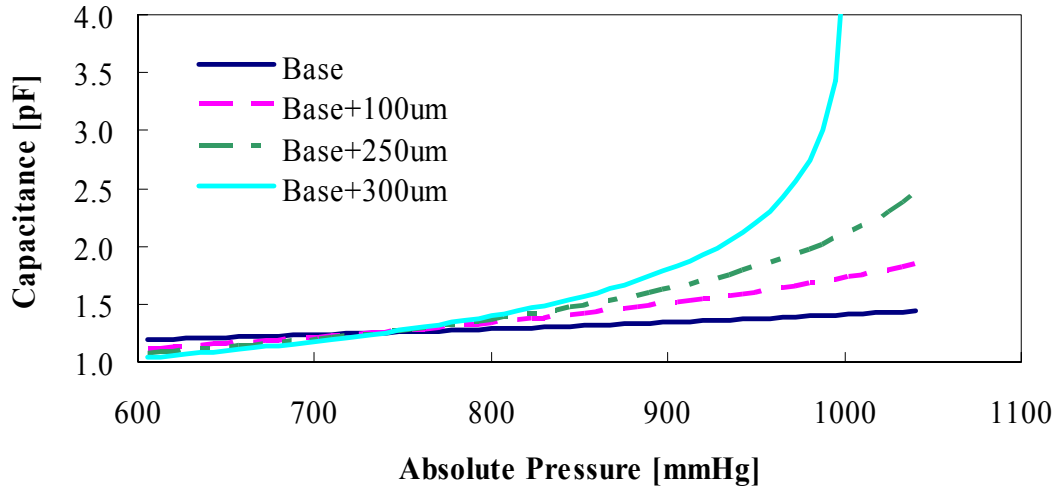

Figure 5.6: Simulated pressure variable capacitance $C_{plate}(P)$ versus absolute pressure.

of the diaphragm, which would increase the capacitance C_{plate} and, thus, reduce f_0. The calculated and measured quality factors Q are 61.3 and 50.1 respectively, which are also in reasonable agreement. The variation in Q is likely due to spiral trace thickness lt and width lw variations from the etching process.

5.1.4 Air Pressure Characterization Test Setup

The pressure dependence of sensors designed for biomedical applications is predominantly characterized in an air environment. This allowed for quick measurements as well as comparison between different designs while not include any dielectric or pressure effects of the surrounding media. This section describes the test setup used to characterize the pressure dependence of both polymer-based and polymer-ceramic-based sensor designs discussed in this work.

The pressure sweep and frequency measurements were taken using a computer controlled system. The system uses LabVIEW software to control all the necessary hardware (see Figure 5.8). The list below includes the necessary hardware and the software interface is illustrated in Figure 5.9. The software allows programmability of the channels, pressure, and time interval during testing as well as records the pressure, temperature, and frequency data.

- LabVIEW Software version 7.1
- Agilent E5100 Network Analyzer (300 kHz - 300 MHz)
- Mensor PCS 400 Pressure controller (0-2000 mmHg Absolute, 0.025% F.S. accuracy)
- Measurement Advantage USB-TC temperature acquisition unit
- Nitrogen gas
- Agilent 34905A RF 4:1 multiplexers in cascade to form a 16:1 switching system
- Windows PC with GPIB controller card
- Array of loop antennas
- Pressure chamber array for 16 devices

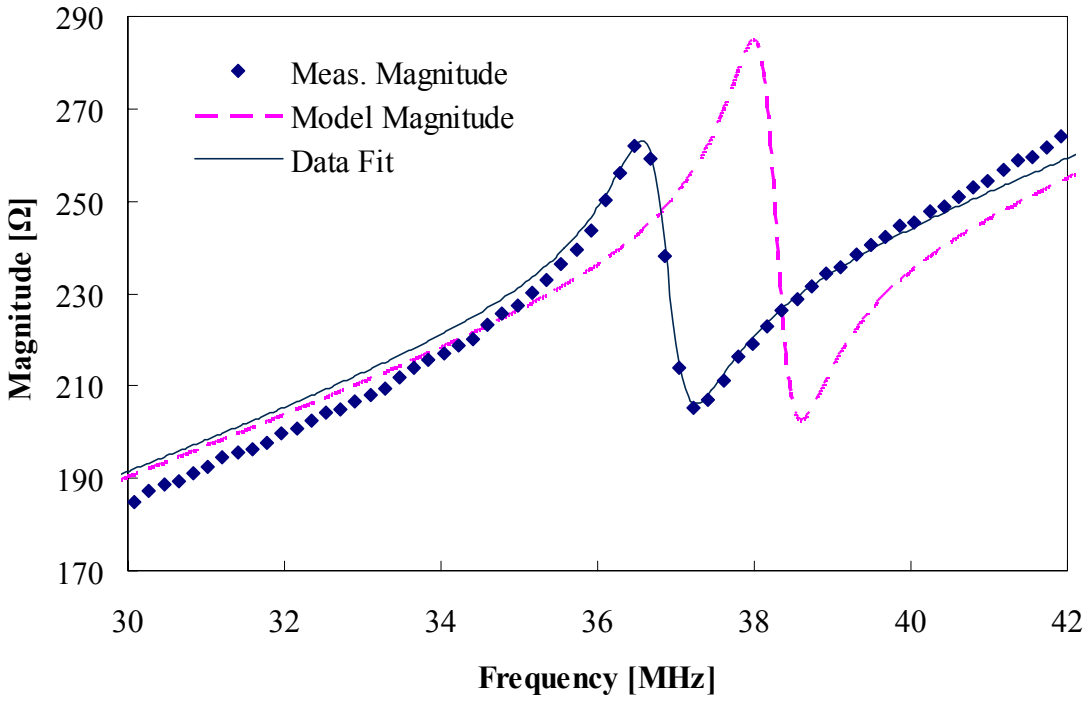

(a) Impedance magnitude.

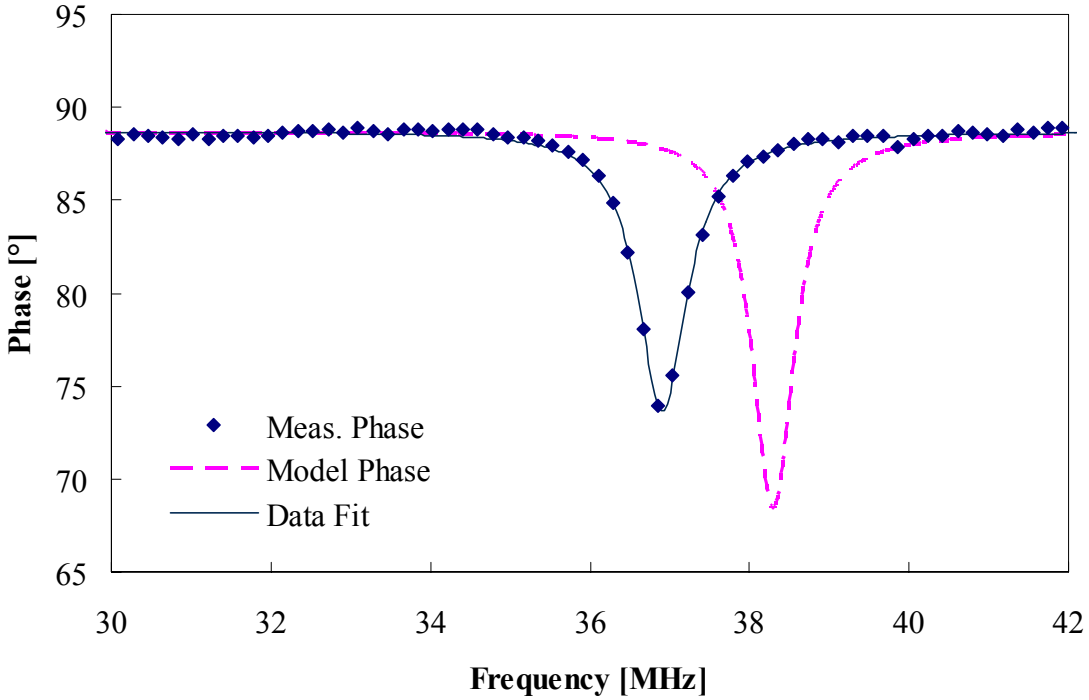

(b) Impedance phase.

Figure 5.7: Comparison between the measured and calculated impedance magnitude and phase for an embedded circuitry LCP pressure sensor.

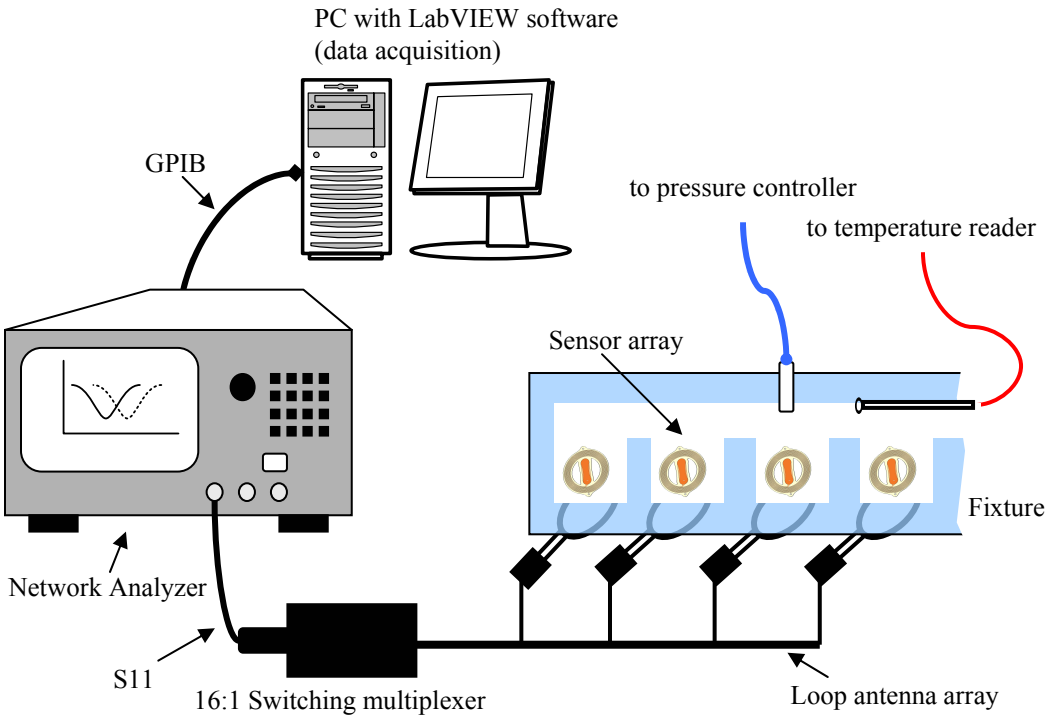

Figure 5.8: Experimental test setup used to characterize pressure sensors in air environments.

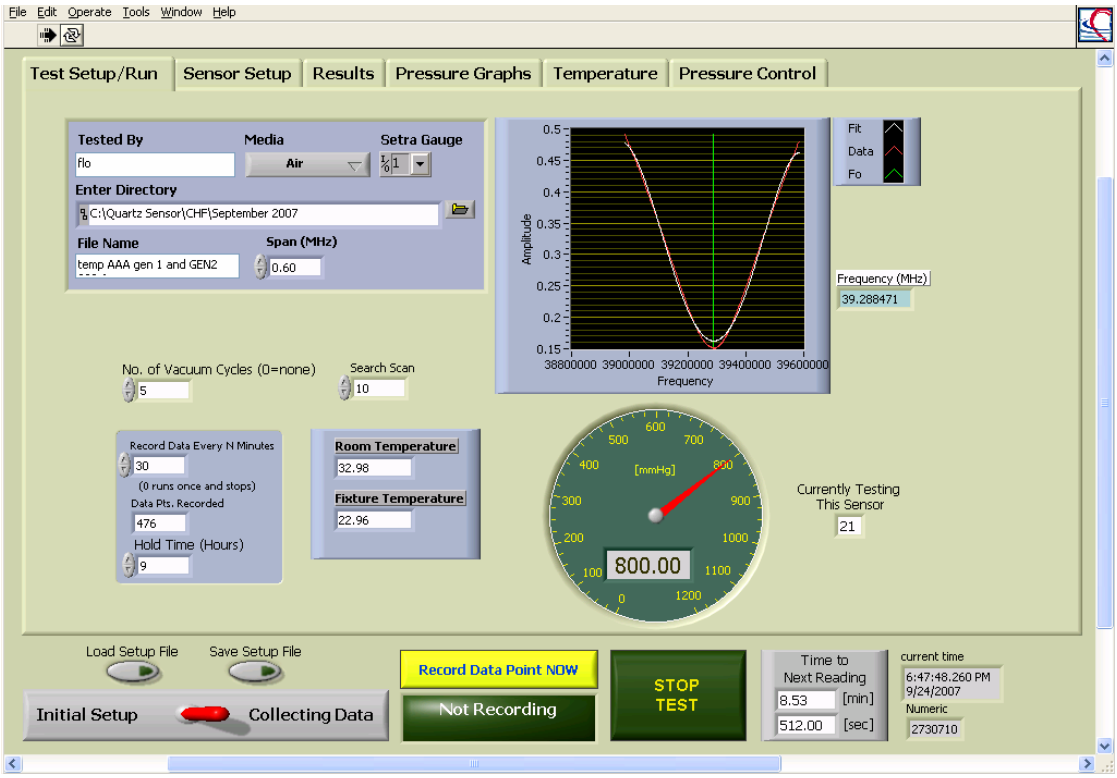

Figure 5.9: Screen capture of LabVIEW software used to collect frequency data for characterization of sensors in air environments.

5.1.5 Pressure Characterization of LCP-based Sensors

The pressure dependence of the sensor can be obtained by determining the frequency at which the phase minimum of each curve occurs, f_{min}, and plotting this frequency as a function of pressure. The magnitude and phase of a sensor as a function of frequency and parameterized by the applied pressure for ceramic pressure sensors was previously shown in Chapter 3 Figure 3.15. The pressure dependence of a LCP-based sensor is shown in Figure 5.10a. The frequency was normalized to 760 mmHg to compare the measured data with theory, shown in Figure 5.10b. The linear sensitivity of the sensor in Figure 5.10 is -9.13 kHz·mmHg^{-1} from 600-1020 mmHg. The theoretical linear sensitivity calculated from Eq. (2.94) is -9.36 kHz·mmHg^{-1} for the same pressure range, and is in good agreement with the measured data.

Several devices were fabricated implementing different cavity designs, as discussed above, and achieving a range of frequencies and sensitivities. Figure 5.11a graphs the resonance frequencies f_0 at atmospheric pressure versus the sample number for each cavity design, and Figure 5.11b plots the corresponding pressure sensitivities. In both graphs, the samples are sorted in descending order of the sensitivity. The average resonance frequency f_0 for the data set is 36.4 MHz with a standard deviation of $\pm$1.55 MHz, which meets the target frequency range of 30-42 MHz, given in the design requirements in Chapter 4 [1]. A slight decrease in frequency is observed as the sensitivity increases (note that the samples are arranged in descending order with respect to their sensitivity, which places the devices with highest sensitivity last since all sensitivities are negative). This trend is expected, since a lower frequency would indicate a smaller gap and hence a greater change in C_{plate} with pressure and therefore an increased sensitivity. Even though the pressure sensitivities meet the design requirements of > 1 kHz·mmHg^{-1}, they do not follow the theory as expected. From Figure 5.5, it was expected to see a trend of increasing sensitivity with

[1] As expected, the resonance frequency is essentially independent of the cavity design, as inductance and capacitance are mostly unchanged

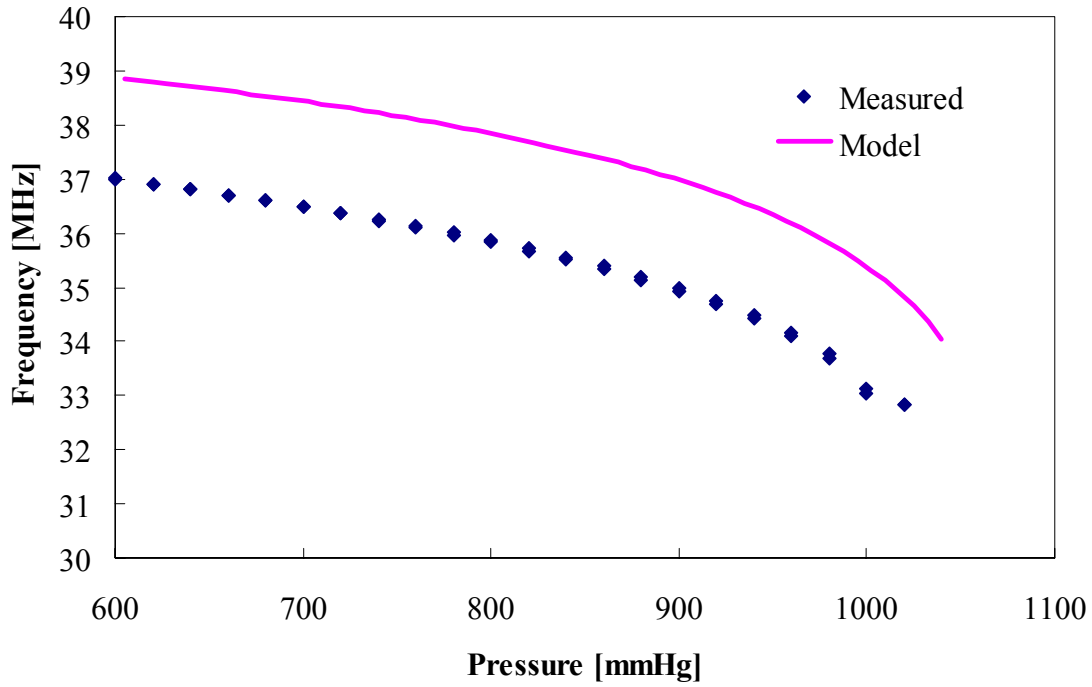

(a) Frequency versus pressure.

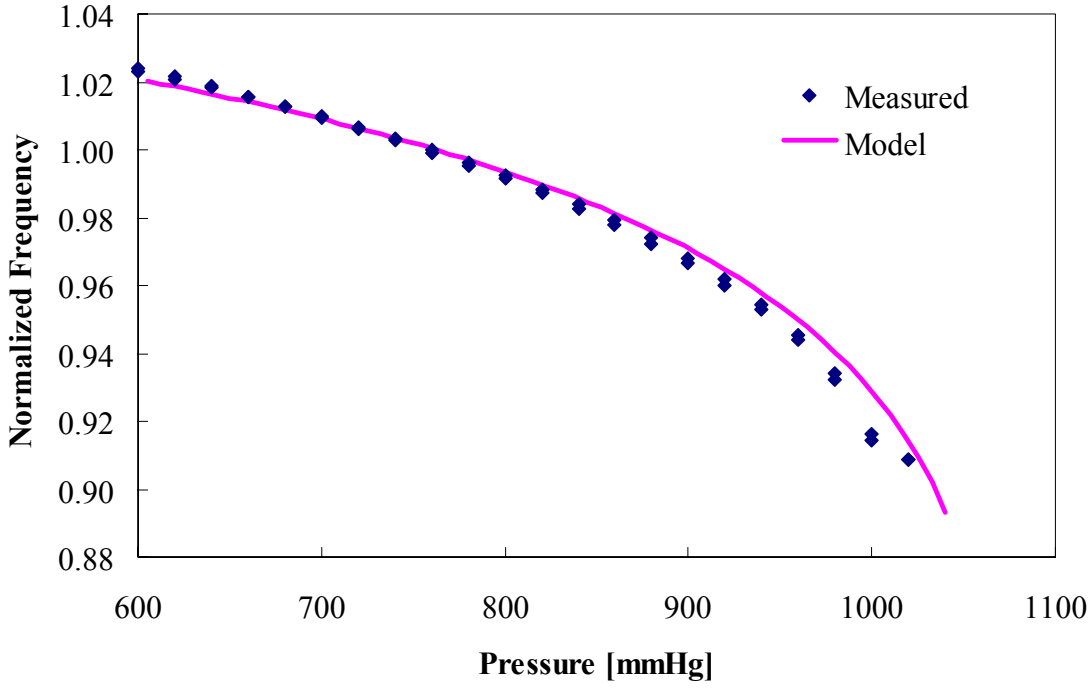

(b) Normalized frequency versus pressure.

Figure 5.10: Frequency (a) and normalized frequency (at 760 mmHg) (b) versus pressure for an LCP-based sensor with Base+250μm cavity design.

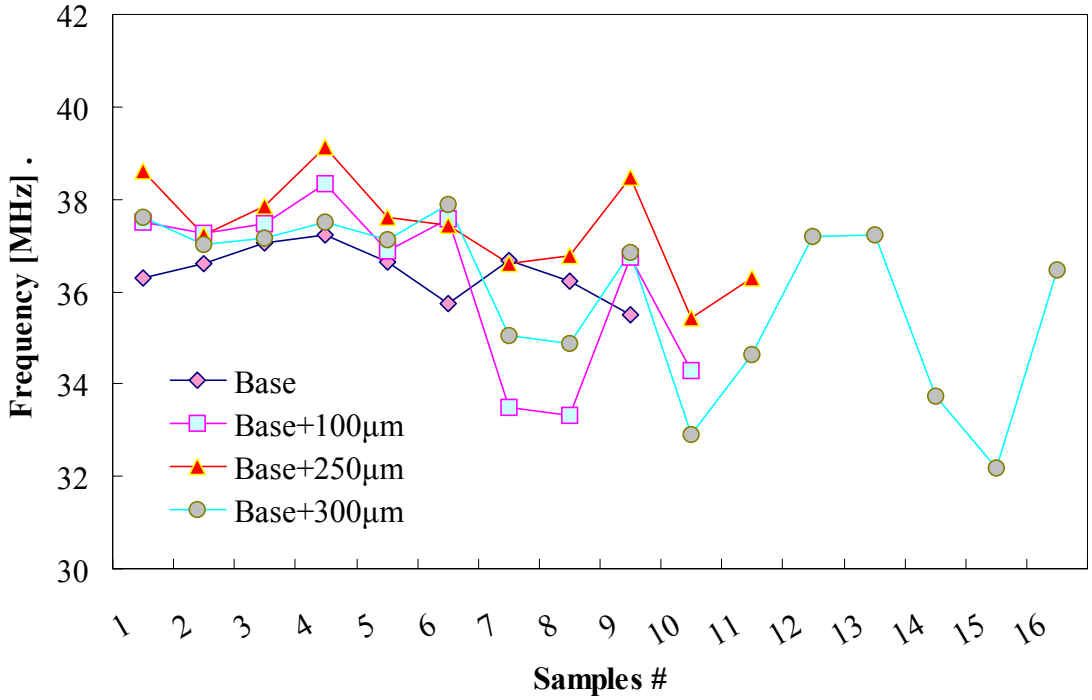

(a)

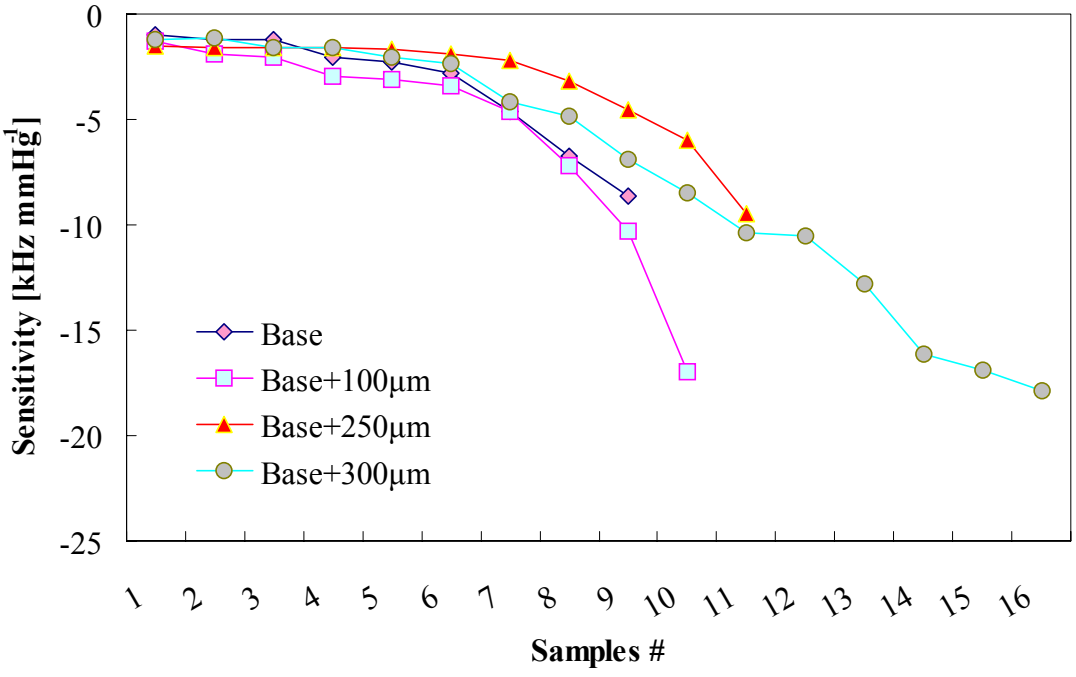

(b)

Figure 5.11: Frequencies (a) and pressure sensitivities (b) versus sample number for different cavity designs. The data set is arranged in descending order with respect to the sensor sensitivity.

increasing cavity width, which is not apparent in Figure 5.11b. The large variation in sensitivity can most likely be accounted for by two phenomena. The first is the variation in residual diaphragm pre-deflection resulting from the lamination process. The second is the dimensional variability of the cavity perimeter. Since the inner layer contains a resin adhesive, the adhesive might flow during lamination. For some samples the amount of resin flow is large, creating large variability in cavity perimeter and hence pressure sensitivity (recall from Eq. (2.86) that sensitivity is proportional to the diaphragm width a to the fourth power). Figure 5.12 compares a dissected sensor whose resin flow rendered the pressure sensitivity < 1 kHz·mmHg^{-1} to a sensor whose sensitivity was close to 10 kHz·mmHg^{-1} with very little resin flow.

5.1.6 Effects of Surrounding Dielectric Media on Sensor Resonance Frequency and Quality Factor for LCP-based Sensors

The LCP-based devices were measured in 0.9% saline to simulate the implant environment. Two main effects are considered: the reduction in sensor resonance frequency f_0 when submerged into the fluid environment due to the increase in the system capacitance caused by the high dielectric constant of the fluid, and the reduction in quality factor Q if the solution is lossy. From Chapter 4 section §4.4, it is observed that as the relative permittivity surrounding the sensor increases, there is an increase in electric energy density W_e, thereby increasing the system capacitance. From Table 4.2, we observe that the devices will operate in a lossy media, therefore a reduction in Q is expected. Minimizing the reduction of both f_0 and Q are important for device stabilty and signal detectability. To minimize both effects, Chapter 4 discussed an additional sensor passivation with low relative permittivity dielectric material. Medical grade silicone was selected as a good option for insulating the present devices.

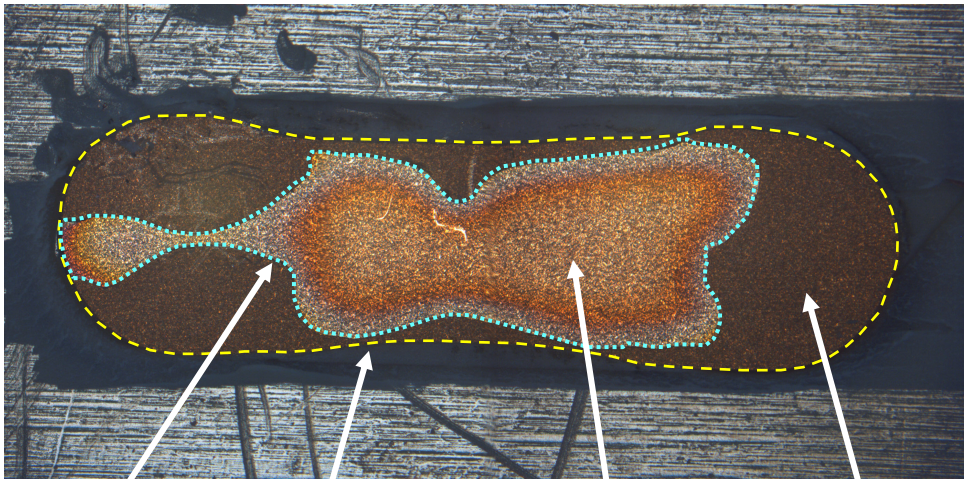

(a) Large resin flow.

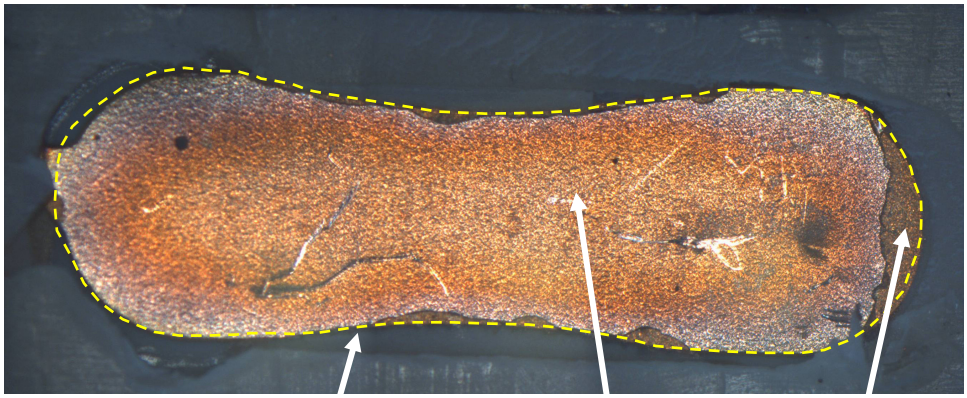

(b) Low resin flow.

Figure 5.12: Top-view of dissected pressure sensor cavity demonstrating large resin flow (a) and low resin flow (b) during lamination resulting in resonance frequency and pressure sensitivity variations.

To model the increase in surrounding permittivity, the circuit in Figure 2.24 includes the substrate and environmental capacitances C_{sub} from Eq. (2.64) as

$$C_{sub} = (C_{ove\ eq} + C_{par})(1 + W_{media})(1 - tan\delta_{media}) \tag{5.1}$$

where W_{media} is the percent increase in energy density in the surrounding media and $tan\delta_{media}$ is the loss factor for the surrounding media. Section §4.4, Figure 4.6 presents 2D FEA results, modeling the change in energy density as a function of the insulation thickness. The test devices are approximately 300 μm thick and are coated with $\approx$ 200 μm silicone per side, resulting in a total sensor thickness of $\approx$ 700 μm. For this device cross-section, the percent change in energy density in the surrounding media W_{media} was estimated to be 15% for a media relative dielectric constant of 80. A second data point was chosen to verify the model, using an insulation thickness of 1000 μm per side, with W_{media} estimated at 1.33% for a media relative dielectric constant of 80. Figure 5.13 graphs measured and calculated normalized resonance frequencies f_0 versus media relative permittivity. Figure 5.14 graphs the measured and claculated normalized quality factor Q versus media relative permittivity for $tan\delta_{media}$ of 0.2. Without any silicone coating, both the resonance frequency and quality factor would decrease dramatically, rendering the devices virtually undetectable by the remote query electronics. By coating the sensors with at least 200 μm of silicone, the decrease of f_0 and Q can be minimized.

5.1.7 Temperature Characterization of LCP-based Sensors

In biomedical applications, temperature is generally considered constant at a typical 37 ℃. Although there usually is some variation of a few degrees, large temperature excursions are not expected. LCP pressure sensors were characterized for temperature sensitivity from 30-40 ℃ to determine the temperature sensitivity for temperatures of interest in this application. Figure 5.15 plots the frequency response versus temperature. The measured temperature sensitivity for this device was 4.27 kHz· ℃ $^{-1}$. For several measured devices,

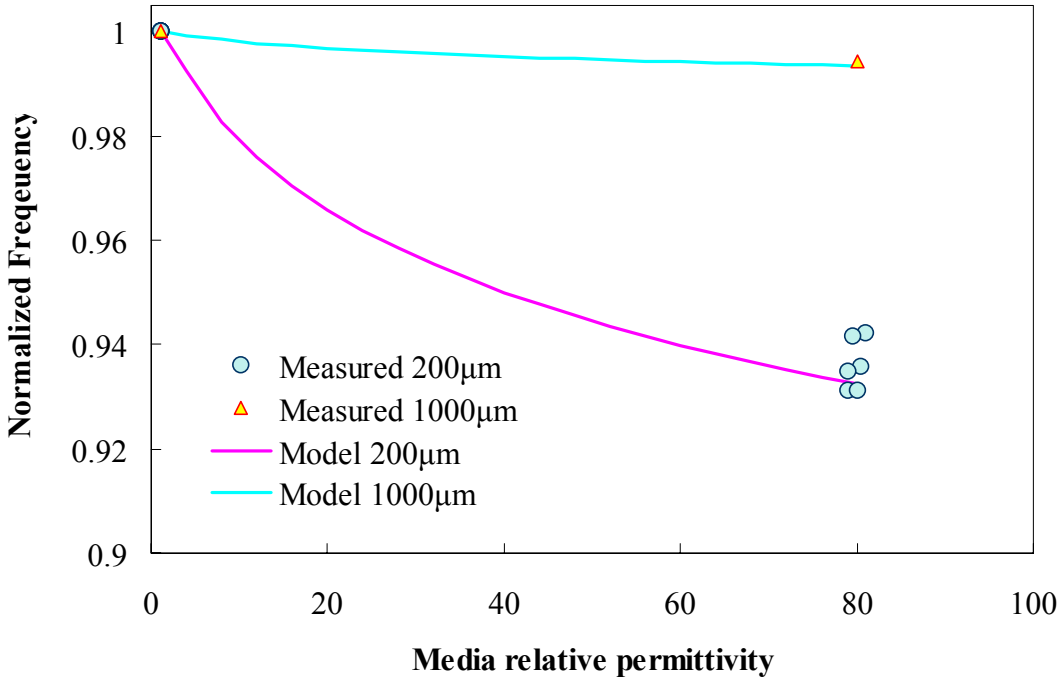

Figure 5.13: Measured and calculated normalized resonance frequencies f_0 of silicone coated LCP-based pressure sensors versus media relative permittivity (air $\epsilon_r = 1$ and water $\epsilon_r = 80$). Note that for the measured data (silicone thickness 200 μm), the x axis values were offset slightly around $\epsilon_r = 80$ to ensure better visibility of the data set.

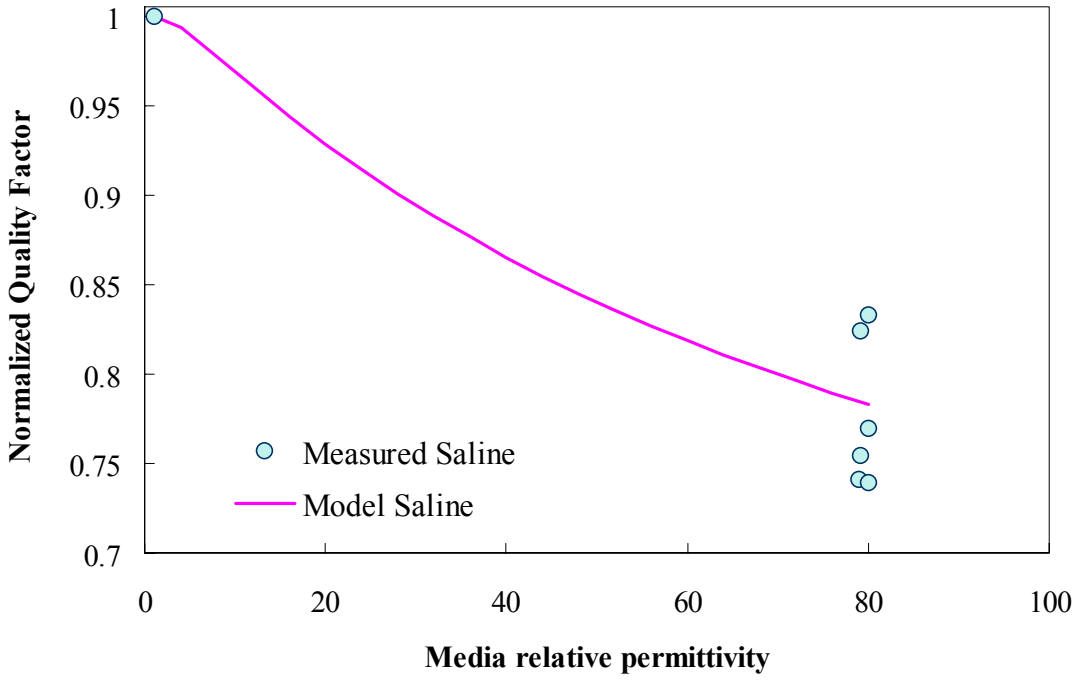

Figure 5.14: Measured and calculated normalized quality factor Q of silicone coated LCP-based pressure sensors versus media relative permittivity (air $\epsilon_r = 1$ and water $\epsilon_r = 80$) for $tan\delta_{media} = 0.2$. The devices were coated with 200 μm of silicone insulation. Note that for the measured data (silicone thickness 200 μm), the x axis values were offset slightly around $\epsilon_r = 80$ to ensure better visibility of the data set.

the temperature sensitivities are found to range between -5 to -8.5 mmHg· ℃ $^{-1}$. The temperature sensitivity appears to be proportional to the pressure sensitivity; therefore, it is likely that the temperature sensitivity is due to an increase in gas pressure within the cavity as temperature increases or due to the CTE mismatch in the polymer-metal diaphragm composite.

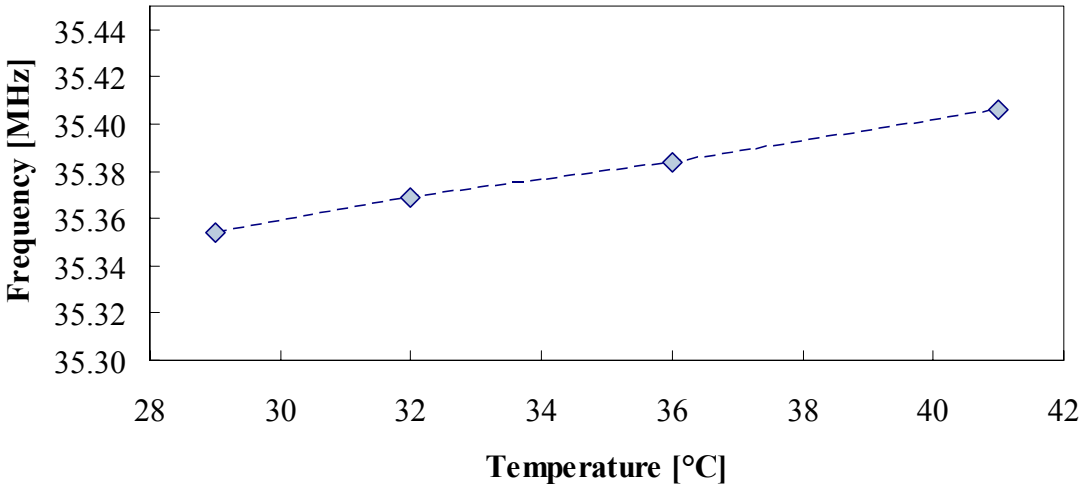

Figure 5.15: Measured resonance frequency versus temperature for LCP polymer sensors.

5.2 Development of Polyimide-based Sensors

5.2.1 Design and Fabrication of Polyimide-based Sensors

Similar to the LCP-based pressure sensors, polyimide-based devices have the same three essential parts, which include formation of a pressure-deformable diaphragm, a cavity, and the integration of an *LC* resonant circuit. In this design the circuitry is also completely embedded within the polymer substrate, illustrated in Figure 5.16.

The sensors are fabricated from laminated sheets of Kapton® copper-clad, Kapton® inner layers, and DuPont™ Pyralux® LF1500 acrylic adhesive. The batch process is the

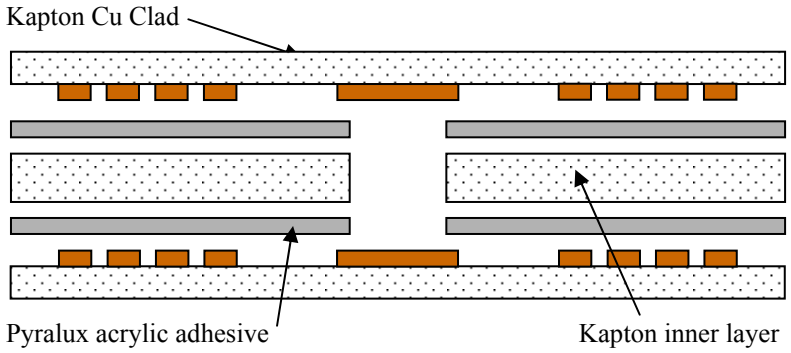

Figure 5.16: Cross-sectional view of Kapton®-based pressure sensors.

same as that for LCP sensors, which uses 4-inch sheets with 4 rows and 4 columns, yielding 16 devices per fabrication run. First, the copper cladding is patterned into the desired inductor structures prior to lamination. This is done through standard photolithography and wet-chemical etching. The inner Kapton® and adhesive layers are laser-cut using an excimer laser (248 nm wavelength) to achieve accurate dimensions. Then, the two outer layers and the inner layer with its corresponding cavity design are aligned via registration pins on platens, assembled together, and laminated at 200 ℃ for 60 minutes under 2400 kPa of pressure. The sensors are individualized using an excimer laser from above to achieve various shapes for minimally-invasive delivery. A fabricated sensor is illustrated in Figure 5.17. Further details on the fabrication process, photolithography masks, assembly blocks, press platens, and fabrication equipment are described in Appendix B section §B.3 and Appendix C section §C.1.

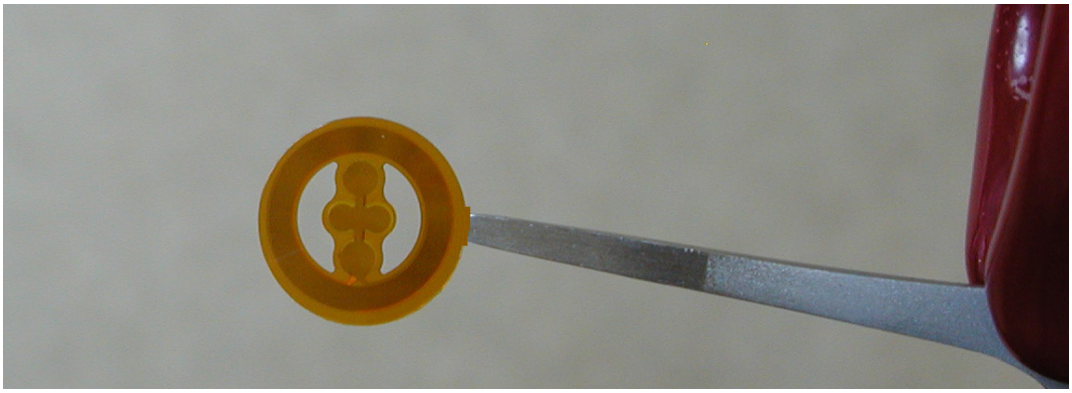

Figure 5.17: Fabricated Kapton® polymer wireless pressure sensor held by tweezers.

The spiral design for polyimide-based sensors implements the same geometry as that for LCP devices, shown in Figure 5.4a. Also, the modeling of polyimide sensors is performed in a similar fashion to LCP-based sensors. The cavity design is equivalent to those used for LCP sensors shown in Figure 5.4b. The Kapton® copper clad is formed from 50 μm of Kapton® HN and 18 μm of copper. The Pyralux® acrylic adhesive inner layers have a thickness of 25 μm (two sheets of LF1500 are used with a thickness of 12.5 μm each), and are placed between an inner Kapton® sheet of 50 μm and the outer cladding, shown in Figure 5.16. Therefore, the overall inner stack has total thickness of approximately 100 μm and the overall sensor thickness is approximately 200 μm.

5.2.2 Impedance Measurements of Polyimide-based Sensors

The sensor is placed in the plane of a loop antenna L_a and the impedance is measured. The inductance of the antenna L_a was estimated as 1 μH. Using the model derived in section §2.1.5, the impedance magnitude and phase of the sensor can be calculated from Eq. (2.65) and are graphed in Figure 5.18a and Figure 5.18b respectively. Below and above resonance, the phase is close to the ideal value of 90° for an inductor and the magnitude depends linearly on the frequency. The data in Figure 5.18 was taken at atmospheric pressures. At resonance, the sensor induces a change in impedance phase and magnitude. The phase minimum f_{min} occurs at 39.87 MHz. Curve fitting, using Eq. (2.9), was used to extract frequency, coupling coefficient and quality factor from the measured data, shown in Figure 5.18 as the solid line. The resonance frequency f_0, the coupling coefficient k, and the quality factor Q obtained from the fit are 39.82 MHz, 0.0747, and 33.8 respectively.

The calculated and measured self-resonances are 41.07 (Model 1), 39.39 (Model 2), and 39.82 MHz, which are in good agreement. Model 1 assumes a thickness of the adhesive layer of 25 μm. Model 2 assumes that the layer is reduced to 20 μm during the lamination. This reduction increases the overlap capacitance C_{ove}, thereby reducing f_0. The calculated and measured quality factors Q are 34.3 (Model 1), 34.8 (Model 2), and 33.8 respectively,

which are also in good agreement. The variation in Q is likely due to variations in spiral trace thickness lt and width lw from the etching process.

5.2.3 Pressure Characterization of Polyimide-based Sensors

The pressure dependence of the sensor can be obtained by determining the frequency at which the phase minimum f_{min} occurs and plotting this frequency as a function of pressure (the magnitude and phase of a ceramic pressure sensor as a function of frequency and parameterized by the applied pressure was previously shown in Chapter 3, Figure 3.15). The resulting pressure dependence of a polyimide-based sensor is shown in Figure 5.19 together with modeling results. Three cases for the model were compared to the measured data. The inner layer adhesive thickness was set at the original material thickness of 25 μm and two other compressed thicknesses of 22.2 and 20 μm. The value of 22.2 μm best fits this sensor. These values are corroborated by overall sensor thickness measurements of between 170 and 200 μm. Therefore a variation of 5 to 15 μm in adhesive thickness is plausible. The linear pressure sensitivity of the sensor in Figure 5.19 is -1.54 kHz·mmHg^{-1} from 600-1020 mmHg. The theoretical linear sensitivities calculated from Eq. (2.94) are -1.59, -1.67, and -1.74 kHz·mmHg^{-1} for the adhesive thicknesses (25, 22.2, and 20 μm) and for the same pressure range, which are in good agreement with measured data.

Several devices were fabricated, achieving relatively good consistency in both resonance frequency and quality factor as shown in Figure 5.20a, which graphs the resonance frequencies f_0 and quality factors at atmospheric pressure versus the sample number. Figure 5.20b plots the corresponding pressure sensitivities, which are also fairly constant. The average resonance frequency f_0 for the data set is 39.53 MHz with a standard deviation of $\pm$0.36 MHz, which meets the target frequency range of 30-42 MHz given in the design requirements in Chapter 4. The average Q and pressure sensitivity are 28.9 and -1.8 kHz·mmHg^{-1} with a standard deviation of 1.8 and 0.26 kHz·mmHg^{-1}, respectively. The improved fabrication consistency compared to the LCP-based devices is due to the reduced flow of the adhesive

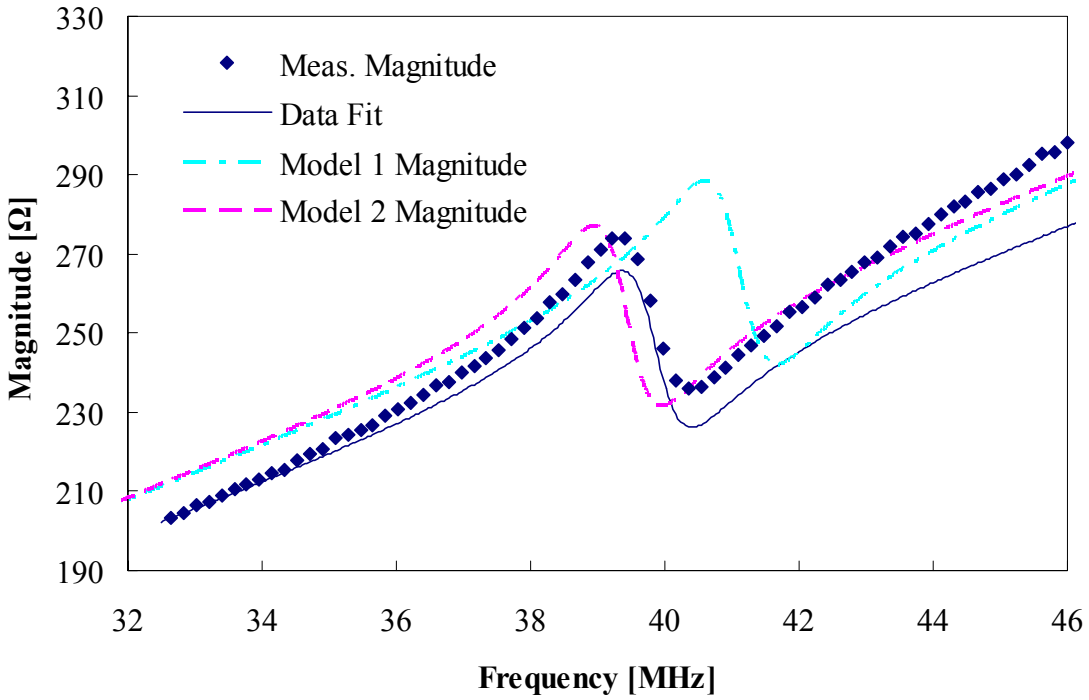

(a) Impedance magnitude.

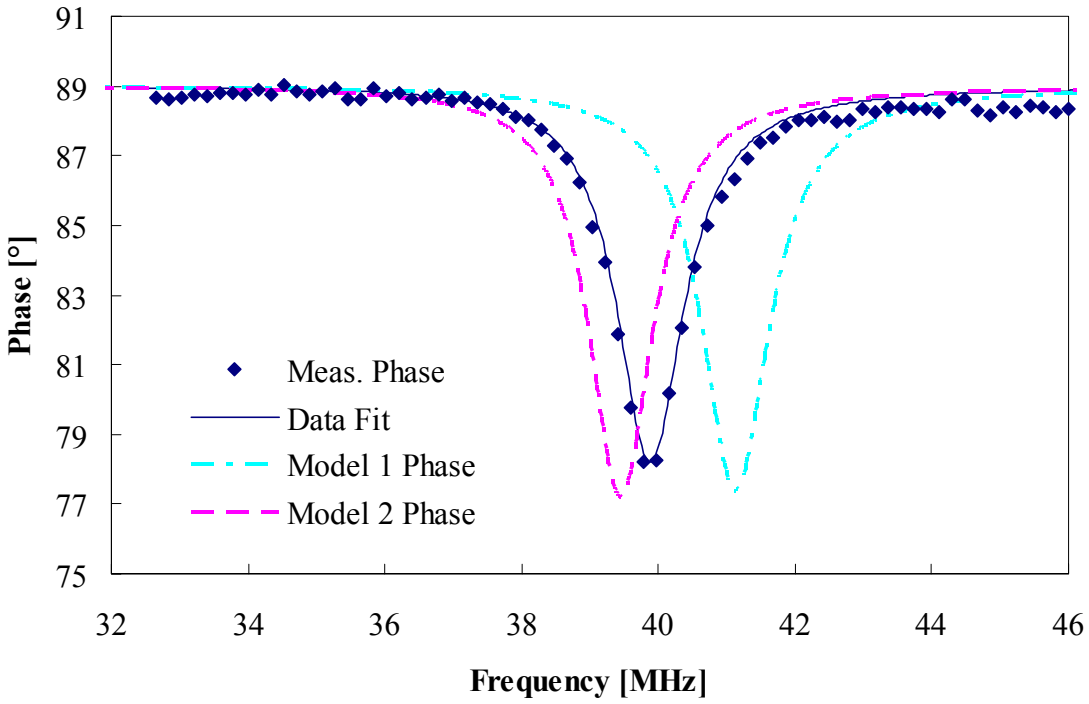

(b) Impedance phase.

Figure 5.18: Comparison between the measured and calculated impedance magnitude and phase for an embedded circuitry polyimide pressure sensor. Model 1 assumes a thickness of the adhesive layer of 25 μm. Model 2 assumes that the layer is reduced to 20 μm during the lamination.

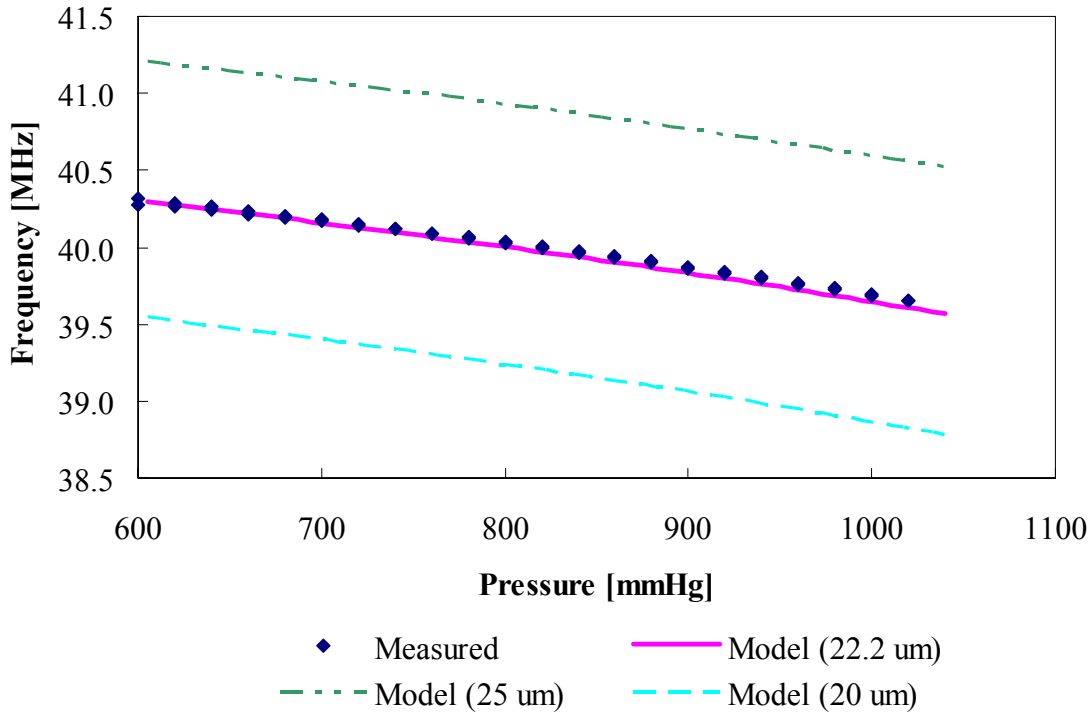

Figure 5.19: Measured and calculated resonance frequency versus applied pressure for a polyimide-based sensor. Three models are shown, with adhesive thicknesses of 25, 22.2, and 20 μm.

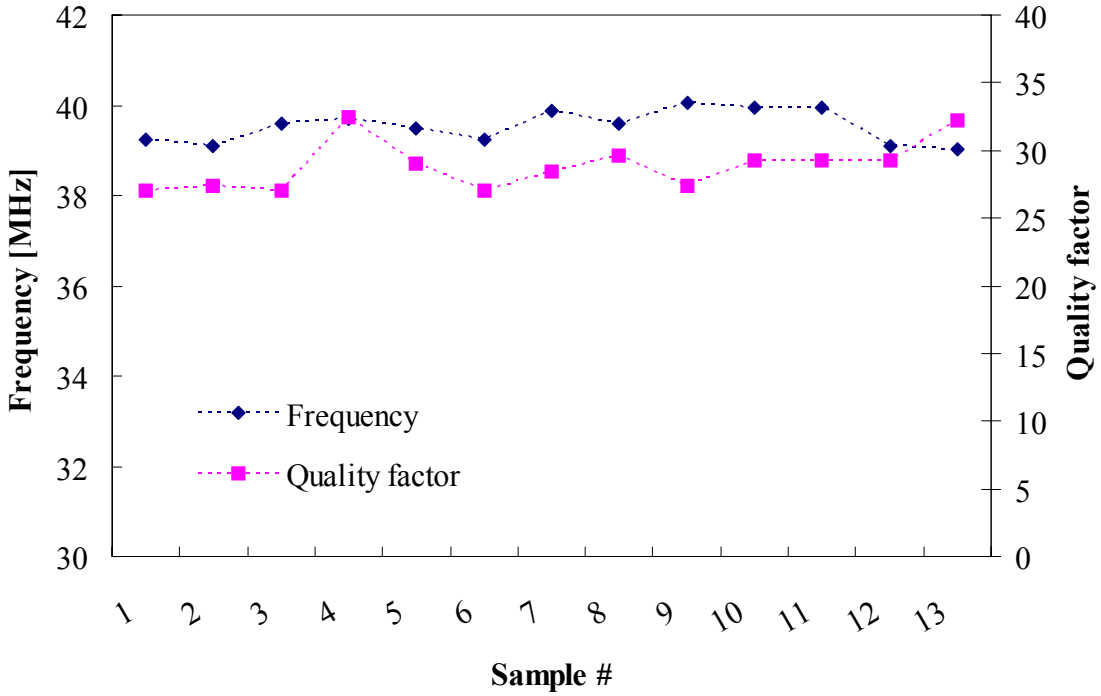

(a) Frequencies and quality factors.

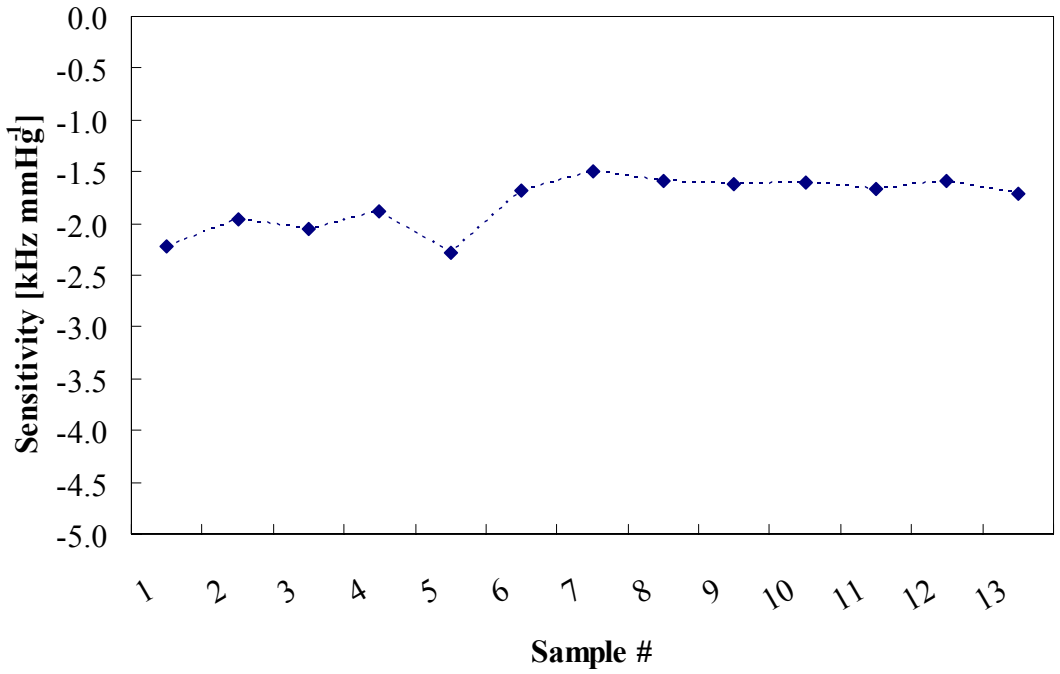

(b) Pressure sensitivity.

Figure 5.20: Frequencies and quality factors (a) and pressure sensitivities (b) of various tested polyimide-based pressure sensors.

layer. The quality factor Q is lower than for LCP-based devices by as much as 20. This reduction in Q is due to the increased dielectric loss of the Pyralux® acrylic adhesive, which can have $tan\delta$ as high as 0.03 (the value used in this modeling). Finally, the sensitivities are also very consistent with very small deviation. This is again due to the fact that the cavity shape is maintained during lamination processing with very little adhesive flow when compared to the LCP-based devices.

5.3 Development of PTFE-based Sensors

From the LCP-based device, we know that large flow from the adhesive layer can cause inconsistencies of the frequency and pressure sensitivity and from the polyimide-based device we see the effects of dielectric loss on the quality factor. To try to overcome these issues, we investigated PTFE as a polymer substrate. This material can be chemically treated to achieve bondability at high temperatures (> 300 ℃). Also, the dielectric loss is low ($tan\delta < 0.001$), allowing for high quality factors using the same spiral design. Frequencies from 30-50 MHz were achieved with quality factors as high as 75 for same spiral layout used for LCP and Kapton® sensors. Some of the electrical characteristics of PTFE-based circuits were already presented during the development of the analytical model, shown in Figure 2.28 and Figure 2.29. The main difference between the data presented in Figure 2.28 and this section is that in this section the devices are fabricated with a FEP adhesive layer while the devices fabricated to verify the model in Chapter 2 were made entirely from PTFE. Finally, although pressure-sensitive devices were fabriated, the high gas permeability of the PTFE rendered the reference chamber non-hermetic and resulted in higly nonliner pressure dependences, which will not be presented in this work. The sections below describe the development of PTFE-based resonant circuits.

5.3.1 Design and Fabrication of PTFE-based Devices

Similar to LCP-based pressure sensors, PTFE-based devices have the same three essential parts, which include formation of a pressure-deformable diaphragm, a cavity, and the integration of an *LC* resonant circuit. In this design, the circuitry is again completely embedded within the polymer substrate, illustrated in Figure 5.21. Although a cavity is shown in Figure 5.21, most devices fabricated solely from PTFE and FEP do not include the cavity.

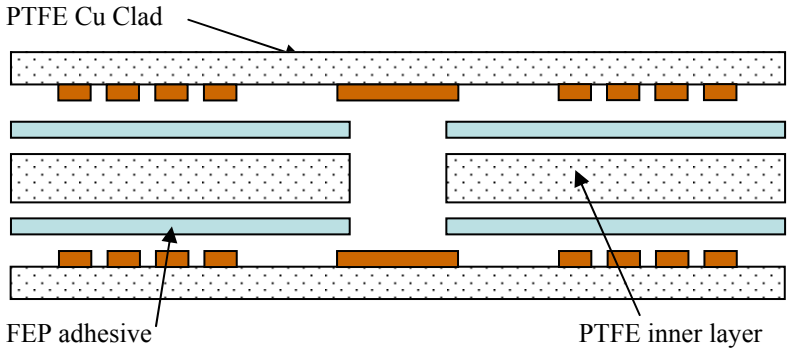

Figure 5.21: Cross-sectional view of PTFE-based pressure sensors.

The sensors are fabricated from laminated sheets of PTFE copper-clad, PTFE inner layers, and FEP bonding film. The batch process is the same as that for the LCP sensors, which uses 4-inch sheets with 4 rows and 4 columns, yielding 16 devices per fabrication run. First, the copper cladding is patterned into the desired inductor structures prior to lamination. This is done through standard photolithography and wet-chemical etching. The inner PTFE layer and FEP bonding film are laser-cut using a CO_2 laser (10.6 μm wavelength) or die-cut to achieve accurate cavity dimensions.

Prior to lamination, the inner layers are treated to increase their bondability. This is because fluoropolymers have low surface energy, which reduces their adhesion. The PTFE layer is chemically treated with FluoroEtch®. FluoroEtch® is a fluoropolymer pre-bonding etchant. The chemical etches the surface making the fluoropolymer bondable by increasing the surface energy. The chemical works by using a metallic sodium in solution form to react

with the fluorine atom of the polymer, leaving the carbon-fluorine molecule on the surface unbalanced. The process is performed in a nitrogen purged and oxygen-free environment because the metallic sodium oxidizes with moisture or oxygen, rendering the etchant inert. The FEP bonding film is acquired with a corona pre-treatment. Corona treatment of films is another common way to increase the surface energy of the film, which increases wettability and adhesion. In brief, the treatment is achieved by generating ionized air above the film. In general, two electrodes are separated by the film, which is near the ground electrode, and an air-gap. The air-gap becomes ionized creating a corona when a high potential is applied, treating the film. The outer PTFE copper-clad layers do not require further activation because they are inherently pre-activated. The pre-activation is performed by the manufacturer of the film during the lamination of the copper film. Etching of the copper leaves the film ready for lamination.

The process continues by aligning and assembling the two outer layers and the inner layers with their corresponding cavity design on registration pins on platens, and laminating at 265 ℃ for 60 minutes with 420 kPa of pressure. The sensors are individualized using the same CO_2 laser from above or die-set to achieve various shapes for minimally-invasive delivery. A fabricated sensor is illustrated in Figure 5.22. Further details on the fabrication process, photolithography masks, assembly blocks, press platens, and fabrication equipment are described in Appendix B, section §B.3 and Appendix C, section §C.1.

The spiral design for the PTFE-based sensors implements the same geometry as that for LCP devices, shown in Figure 5.4a. Also, the modeling of PTFE sensors is performed in a similar fashion to LCP-based sensors. The cavity design is equivalent to those used for LCP sensors shown in Figure 5.4b. The PTFE copper clad is formed from 75 μm of PTFE and 18 μm of copper. The PTFE and FEP inner layers have a thickness of 75 and 25 μm respectively. Therefore, the overall sensor thickness is approximately 275 μm.

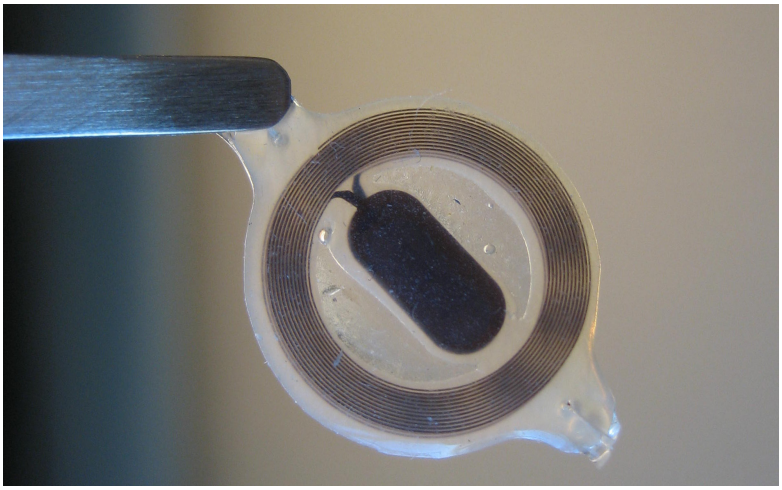

Figure 5.22: Fabricated PTFE polymer wireless pressure sensor held by tweezers.

5.3.2 Impedance Measurements of PTFE-based Sensors

The sensor is placed in the plane of a loop antenna L_a and the impedance is measured. The inductance of the antenna L_a was estimated as 0.219 μH. Using the model derived in section §2.1.5, the impedance magnitude and phase of the sensor can be calculated from Eq. (2.65) and are graphed in Figure 5.23a and Figure 5.23b, respectively. The data in Figure 5.23 were taken at atmospheric pressures. The phase minimum f_{min} occurs at 47.48 MHz. Curve fitting, using Eq. (2.9), was used to extract frequency, coupling coefficient, and quality factor from the measured data, shown in Figure 5.18 as a solid line. The resonance frequency f_0, the coupling coefficient k, and the quality factor Q obtained from the fit are 47.42 MHz, 0.0743, and 71.9 respectively. Note that the phase minimum f_{min} is 0.13% higher than f_0.

The calculated and measured self-resonances are 47.84 (Model 1), 47.05 (Model 2), and 47.42 MHz, which are in good agreement. Again the thicknesses of the adhesive layer was varied, being 27 μm in Model 1 and 25 μm in Model 2 to account for compression during lamination. This decreasein film thickness increases the overlap capacitance C_{ove}, thereby reducing f_0. The calculated and measured quality factors Q are 73.2 (Model 1), 73.4 (Model 2), and 71.9 respectively, which are also in good agreement. The variation in Q is likely due to variations in spiral trace thickness lt and width lw from the etching process.

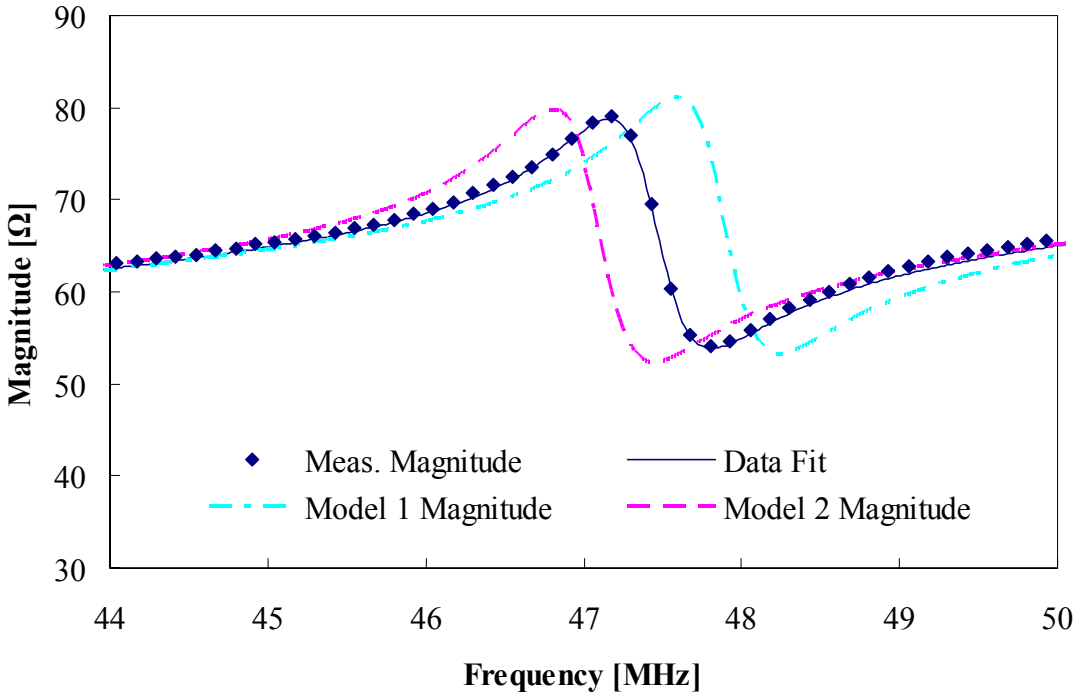

(a) Impedance magnitude.

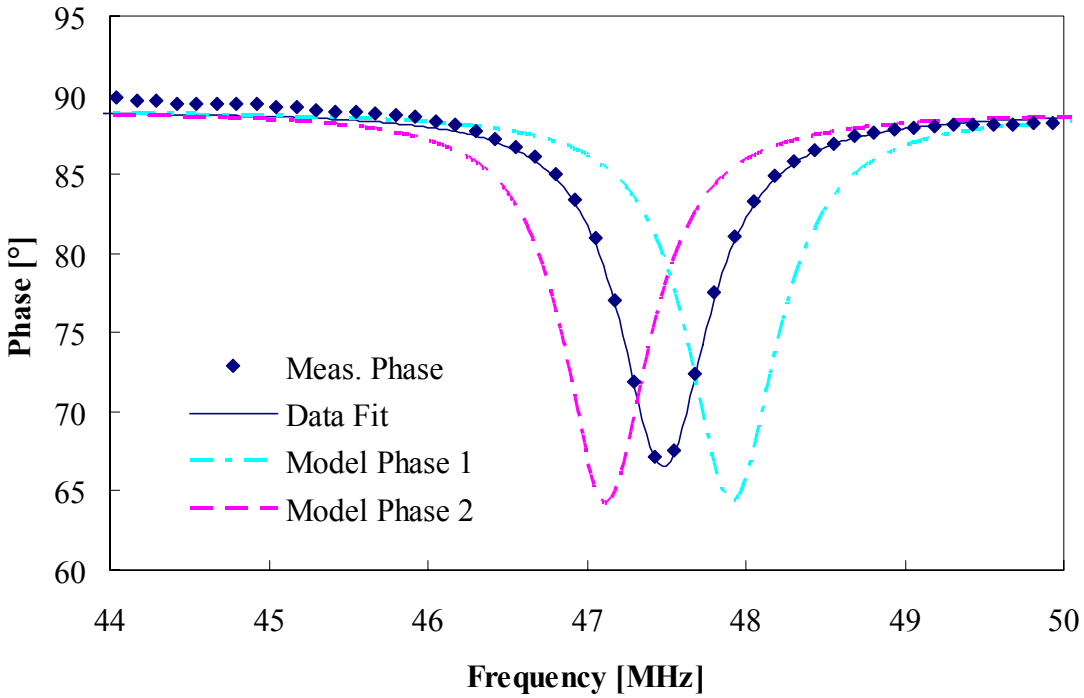

(b) Impedance phase.

Figure 5.23: Comparison between the measured and calculated impedance magnitude and phase for an embedded circuitry PTFE-based pressure sensor.

5.4 Summary of Polymer-Based Pressure Sensor Development

Batch-fabrication of polymer pressure sensors using lamination-based techniques was demonstrated in LCP, Kapton®, and PTFE substrates. Each substrate presented different fabrication advantages and disadvantages as well as electrical properties resulting in a range of quality factors Q, illustrated in Figure 5.24. LCP-sensors suffered from inconsistent resin flow during fabrication resulting in a variation of pressure sensitivities, while Kapton®-based sensors had relatviely low quality factors Q primarily from the high dielectric loss of the acrylic adhesive. The PTFE-based sensors presented the highest quality factors; however, they had very high nonlinear pressure dependence due to the high gas permeability.

The device electrical properties were characterized including frequency f_0 and quality factor Q. Device dependence to pressure, temperature, and surrounding dielectric media was also characterized for the LCP-based sensors and compared to models derived in Chapter 2, showing excellent agreement.

One design drawback for polymer-based sensors is that they are not considered hermetic. This means that some level of drift is expected over time when subject to an average mean pressure differential between the environment and embedded cavity. Additionally, polymer substrates are known to absorb moisture; this effect is likely to increase the system capacitance and thereby change the resonance frequency of the sensors, both of which are unwanted effects. For these reasons, this work investigates an alternate design intended to minimize the drift and maximize the quality factor through the integration of polymer and ceramic substrates while maintaining a flexible platform. Therefore, Chapter 6 presents the development of polymer-ceramic-based pressure sensors intended for chronic use in biomedical applications.

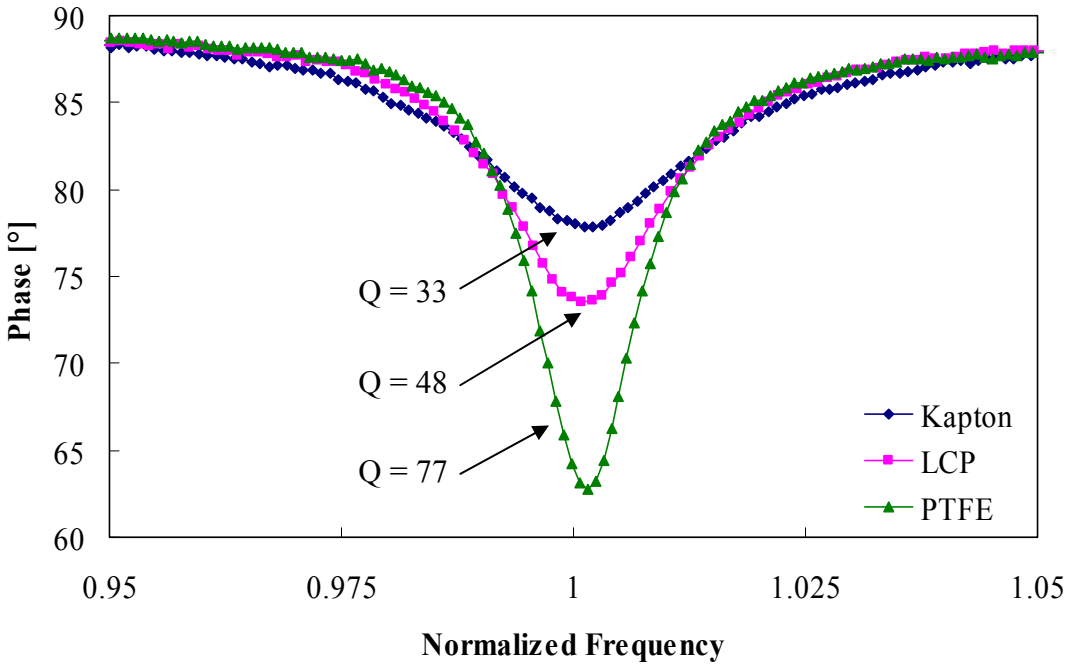

Figure 5.24: Comparison of measured quality factors Q for polymer-based pressure sensors.

CHAPTER 6

POLYMER-CERAMIC PRESSURE SENSOR

6.1 Design and Fabrication of Polymer-Ceramic-based Sensors

Sensors designed for chronic use are fabricated from both copper-clad and non-clad PTFE layers, FEP inner layers, and an encapsulated ceramic chamber (housing the hermetic pressure reference), resulting in a self-packaged structure. Only a PTFE outer surface is exposed to the environment.

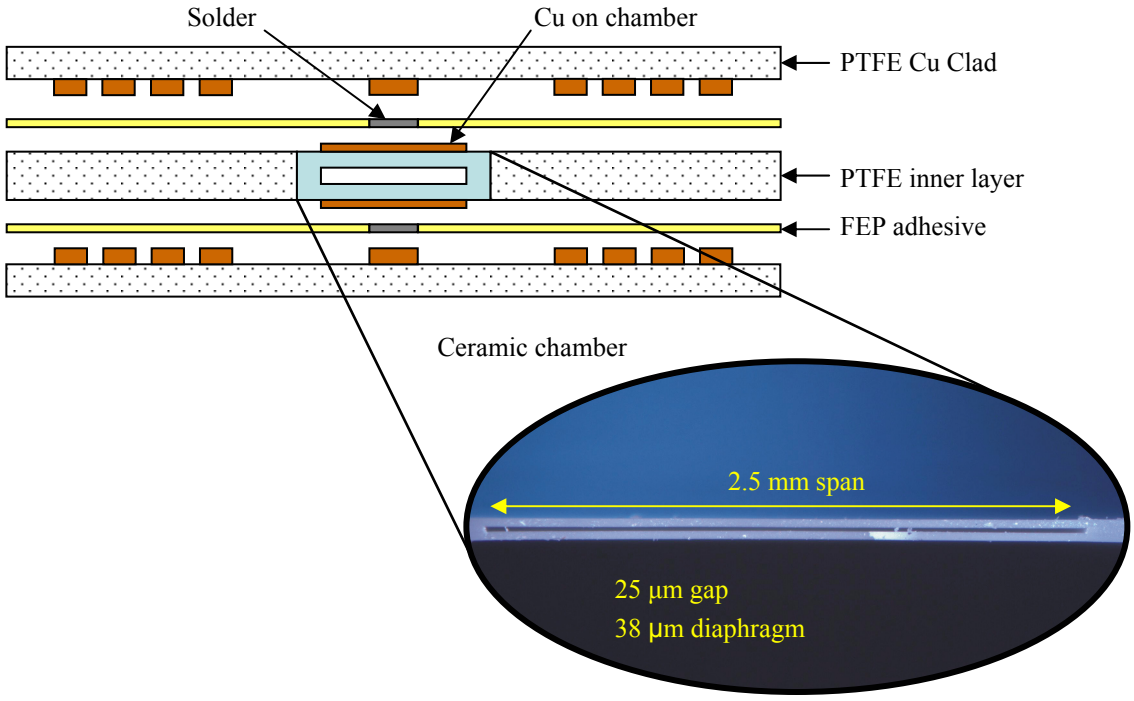

Figure 6.1: PTFE-ceramic sensor cross-sectional view including inset with ceramic chamber cross-section.

The planar inductor coil layout for the PTFE-based sensor design, illustrated in Figure 6.2, has the same physical dimensions as for the LCP-based design described in Chapter 5. The spiral is defined using photolithography and wet-chemically etched with ferric chloride acid,

which is commonly used to etch copper-cladding films. Although the assembly of the polymeric layers is similar to previously presented polymer-based devices, an additional ceramic hermetic chamber (CHC) is included to increase the pressure stability of the devices. The following subsection describes the design, fabrication, and testing of ceramic capacitive elements.

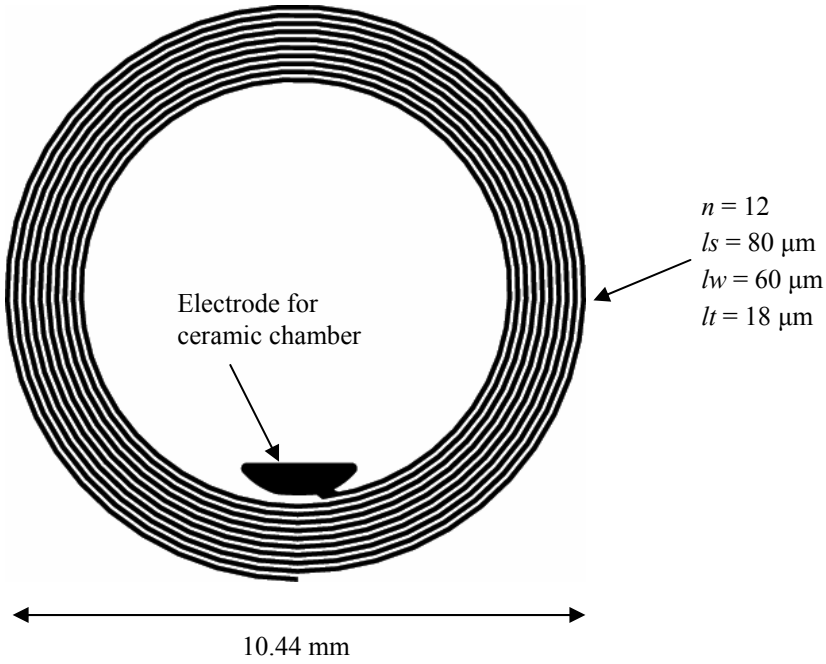

Figure 6.2: Planar spiral inductor for PTFE-ceramic-based sensors.

6.1.1 Ceramic Chamber Design, Fabrication and Characterization

The ceramic chambers are fabricated through the use of layers of zirconia ceramic powders using a standard green-tape approach presented in Chapter 3. The membrane layout ranges from 1.7-2.6mm in width, between 6-9 mm in length, and are separated by gaps ranging from 25-50 μm, illustrated in Figure 6.3. The inner layer of the chamber is laser-cut in a green state using a Nd:YLF infrared laser (1 micron wavelength). The sheets are aligned and assembled, three sheets per stack, with thicknesses between 25-35 μm, laminated in a press, and sintered in a box furnace at temperatures between 1300-1500 ℃. The ceramic

chambers are batch-fabricated on 2 inch sheets with 9 chambers per sheet. After the ceramic chambers are sintered, the capacitive electrodes are defined using photolithography and electrodeposited copper. Once metalized, the chambers are individualized using the an infrared laser and assembled into each polymer sensor.

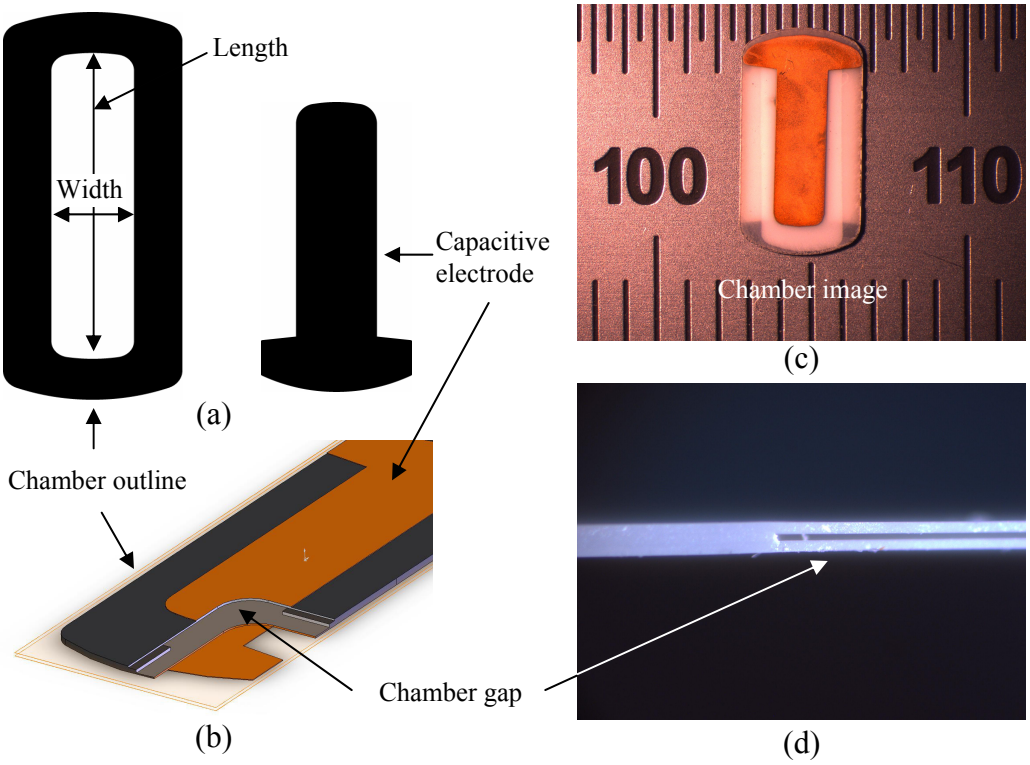

Figure 6.3: Zirconia ceramic hermetic chamber used with PTFE-ceramic-based sensors. The chamber top layout and capacitive electrode (a), perspective view (b), photograph on a mm scale (c), and cross sectional view of the gap (d).

Table 6.1 lists the dimensional values and measured capacitances for three designs. To measure the capacitance for each design, leads were soldered to each electrode. The devices were measured at room pressure using a Keithley 3322 LZC meter and have values of 15.46, 15.79, and 16.83 pF. The capacitors were characterized for pressure response. Each design was placed in a sealed jar and pressurized from 100 to 1800 mmHg (absolute) using a Mensor PCS 400 pressure controller and the capacitances were measured as a function of pressure, illustrated in Figure 6.4. The pressure sensitivities for the three designs are 1.77, 3.48, and 4.37 fF/mmHg. As expected, the widest design has the largest sensitivity.

Table 6.1: Dimensions and capacitances for ceramic chamber designs used in PTFE-ceramic sensors.

Parameter	Chamber Designs		
	CHC1	**CHC2**	**CHC3**
b [mm]	8.5	8.5	9
a [mm]	2.4	2.5	2.6
b/a	>2		
Electrode Area [mm^2]	8.34		
t_m [μm]	34.2		
t_g [μm]	35		
Meas. C_0 [pF][a]	15.46	15.79	16.83
Avg. Sensitivity [fF/mmHg]	1.77	3.48	4.37

[a] The capacitance values were measured with a Keithley 3322 LZC meter at room pressure.

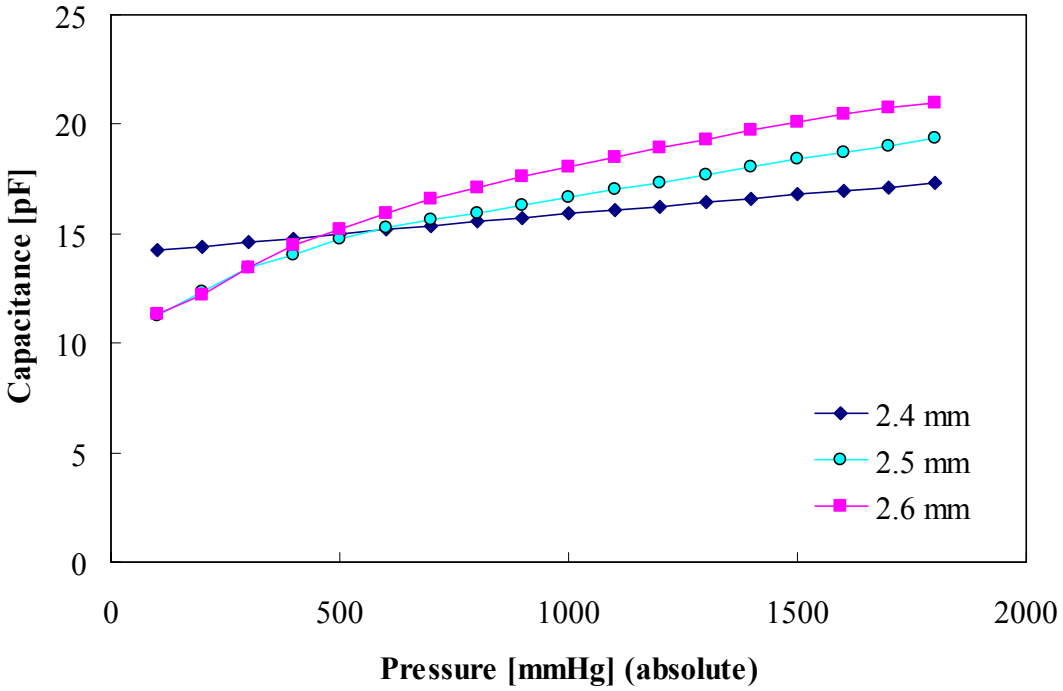

Figure 6.4: Pressure response for capacitive ceramic hermetic chambers with different widths as a function of applied pressure; for dimensional details, see Table 6.1.

6.1.2 Final Assembly and Lamination of Polymer-Ceramic-based Sensors

The PTFE and FEP inner layers are laser cut using a CO_2 ($\lambda = 10.6$ μm) laser to create cavities for the solder connection shown in Figure 6.1 and the chamber assembly shown in Figure 6.3. The copper clad, inner PTFE and FEP layers, ceramic chambers, and Sn-Ag solder pellets are aligned and assembled (16 devices per run on 4-inch sheets), shown for one device in Figure 6.5. The sheets are vacuum laminated in a hot press at 280 ℃, for 60 minutes with 431 kPa of pressure. The vacuum eliminates trapped air pockets between the layers of FEP, PTFE, and the ceramic chamber. The sensors are individualized using a CO_2 laser to achieve various shapes for minimally-invasive delivery. A fabricated sensor is illustrated in Figure 6.6.

6.2 Results for Polymer-Ceramic-based Sensors

6.2.1 Impedance Measurements for Polymer-Ceramic-based Sensors

The sensor is placed in the plane of a loop antenna L_a and the impedance is measured. The inductance of the antenna L_a was estimated as 0.71 μH. Using the model derived in section §2.1.5, the impedance magnitude and phase of the sensor can be calculated from Eq. (2.65) and are graphed in Figure 6.7a and Figure 6.7b respectively. Below and above resonance, the phase is close to the ideal value of 90° for an inductor and the magnitude depends linearly on the frequency. The data in Figure 6.7 was taken at atmospheric pressures. At resonance, the sensor induces a change in impedance phase and magnitude. The measured phase minimum f_{min} occurs at 43.12 MHz. Curve fitting, using Eq. (2.9), was used to extract frequency, coupling coefficient, and quality factor from the measured data,

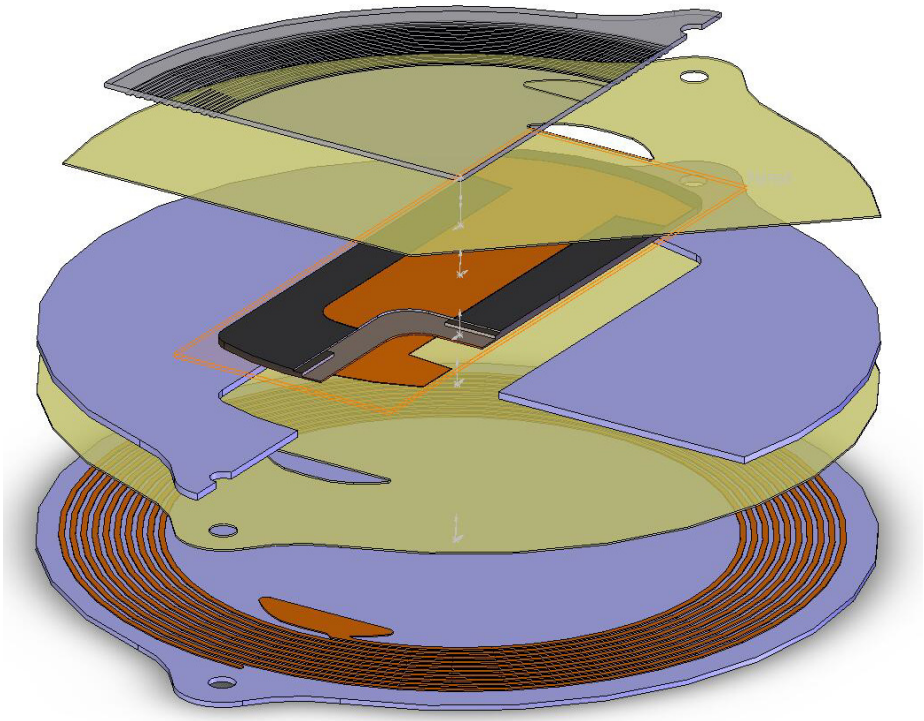

Figure 6.5: Perspective view of the assembly for a PTFE-ceramic-based pressure sensor.

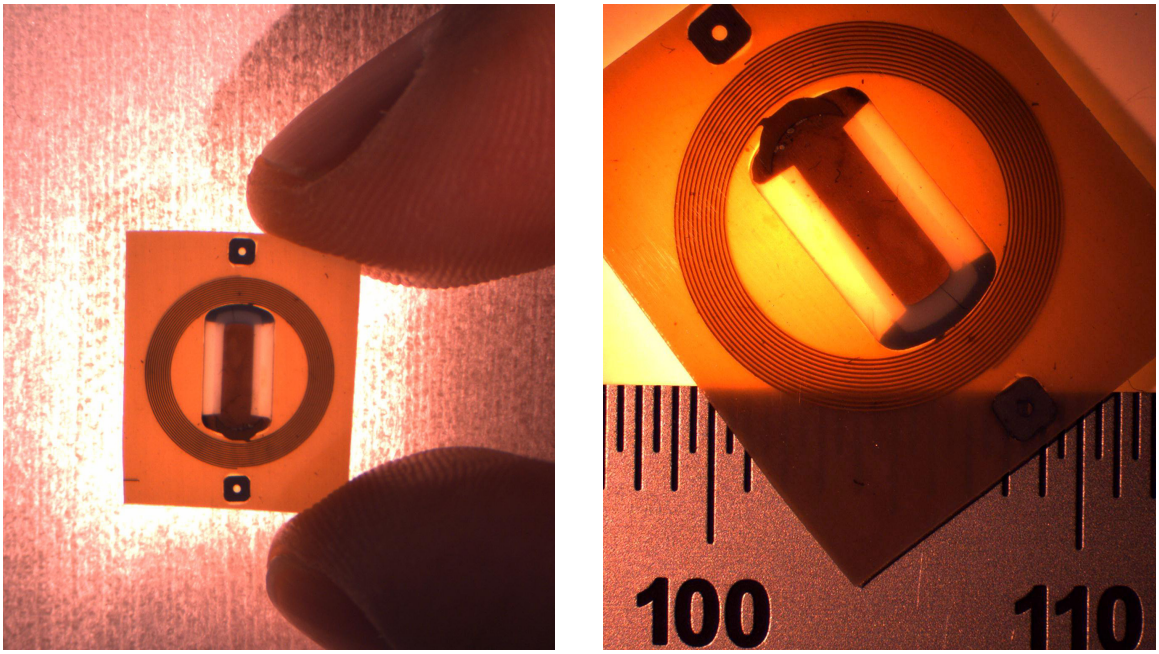

(a) (b)

Figure 6.6: Fabricated PTFE-ceramic wireless pressure sensors using two reference scales, (a) hand-held and (b) millimeter ruler.

shown in Figure 6.7 as the solid line. The resonance frequency f_0, the coupling coefficient k, and the quality factor Q obtained from the fit are 43.07 MHz, 0.0716, and 61.47 respectively.

The calculated and measured self-resonances are 42.99 and 43.07 MHz, which are in excellent agreement due to improved dimensional measurements of the gap between the spirals (performed by disecting the device). The calculated and measured quality factors Q are 73.5, and 61.47 respectively, which are also in reasonably good agreement. The variation in Q is likely due to variations in the spiral trace thickness lt and width lw from the etching process.

6.2.2 Pressure Characterization of Polymer-Ceramic-based Sensors

The pressure dependence of the sensor can be obtained by determining the frequency at which the phase minimum f_{min} occurs and plotting this frequency as a function of pressure. The resulting pressure dependence of a sensors is shown in Figure 6.8. Table 6.2 lists the dimensional and material property values used to fabricate and model the device in Figure 6.8. The linear sensitivity of the sensor in Figure 6.8 is -0.53 kHz·mmHg^{-1} from 600-1020 mmHg. The theoretical linear sensitivity calculated from Eq. (2.94) is -0.47 kHz·mmHg^{-1} for the same pressure range, which is in good agreement with measured data. The difference is likely due to the ceramic membrane geometrical variability.

Several devices were fabricated, achieving relatively good consistency in both resonance frequency and quality factor as shown in Figure 6.9a. Figure 6.9b plots the corresponding pressure sensitivities, which are also relatively consistent. The average resonance frequency f_0 for the data set is 42.49 MHz with a standard deviation of $\pm$1.21 MHz, which is near the target frequency range of 30-42 MHz given in the design requirements in Chapter 4. The average Q and pressure sensitivity is 57.08 and -0.63 kHz·mmHg^{-1} with standard deviations of $\pm$7.12 and $\pm$0.23 kHz·mmHg^{-1} respectively. The frequency can be reduced by increasing the inductance (increase the number to turns). Although some of the devices

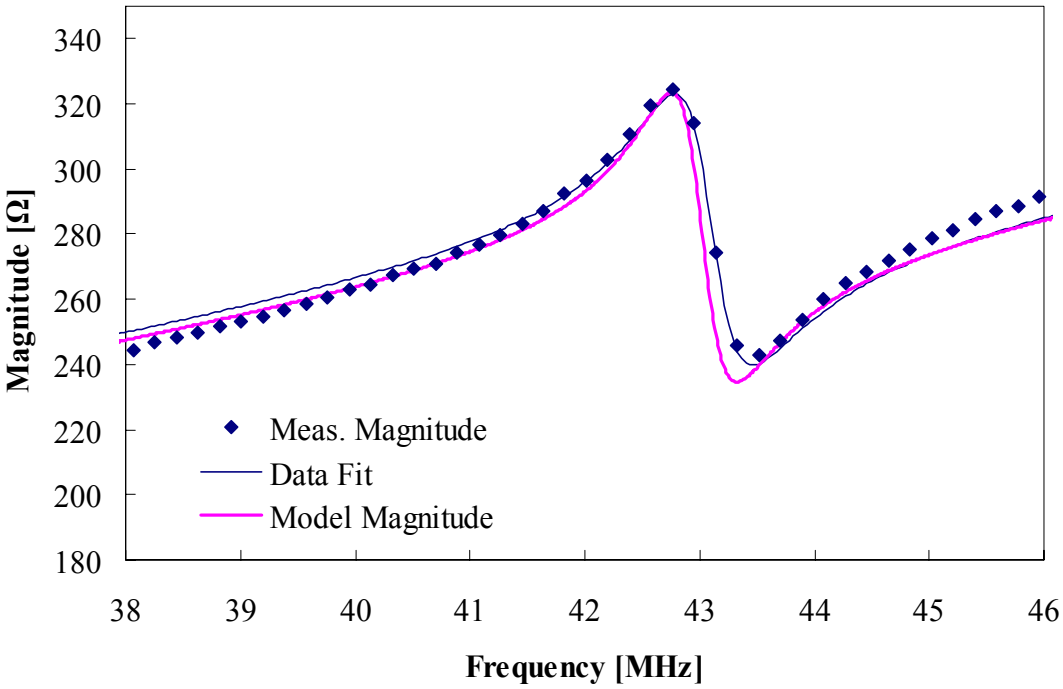

(a) Impedance magnitude.

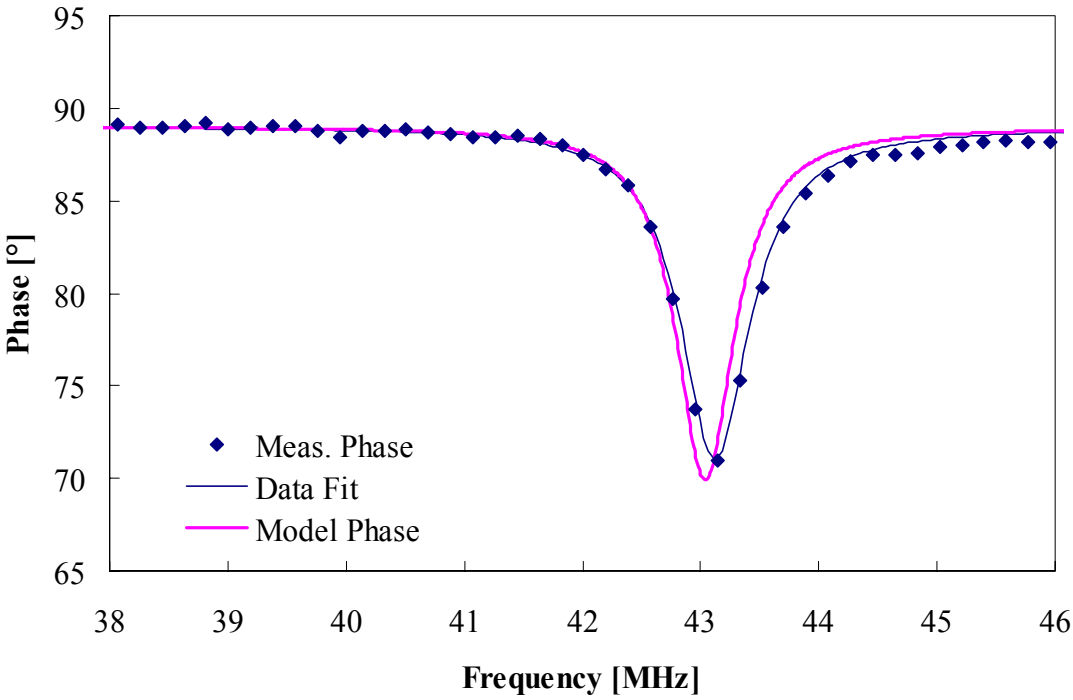

(b) Impedance phase.

Figure 6.7: Comparison between the measured and calculated impedance magnitude and phase for a PTFE-ceramic-based pressure sensor.

Table 6.2: PTFE-ceramic sensor geometrical (measured) and material characteristics used to model the sensor behavior.

Spiral Geom.		**Zr Chamber Geom.**	
n	12	a	2.6 mm
lw	60 μm	b	6.6 mm
ls	65 μm	a_e	1.84 mm
lt	17 μm	b/a	> 2
r_s	3.8 mm	t_g	25.3 μm
PTFE-clad Sub.	75 μm	t_m	34 μm
PTFE inner Sub.	134 μm		
Electrical Properties[a]		**Mechanical Properties**[a]	
PTFE ϵ_r	2.06	Zr E	210 GPa
PTFE $tan\delta$	0.0008	Zr ν	0.32
Zr ϵ_r	30	Cu E	120 GPa
Zr $tan\delta$	0.0001	Cu ν	0.34
Cu ρ	1.72×10^{-8} Ωm	PTFE E	0.5 GPa
		PTFE ν	0.46

[a] From supplier literature or bulk material property.

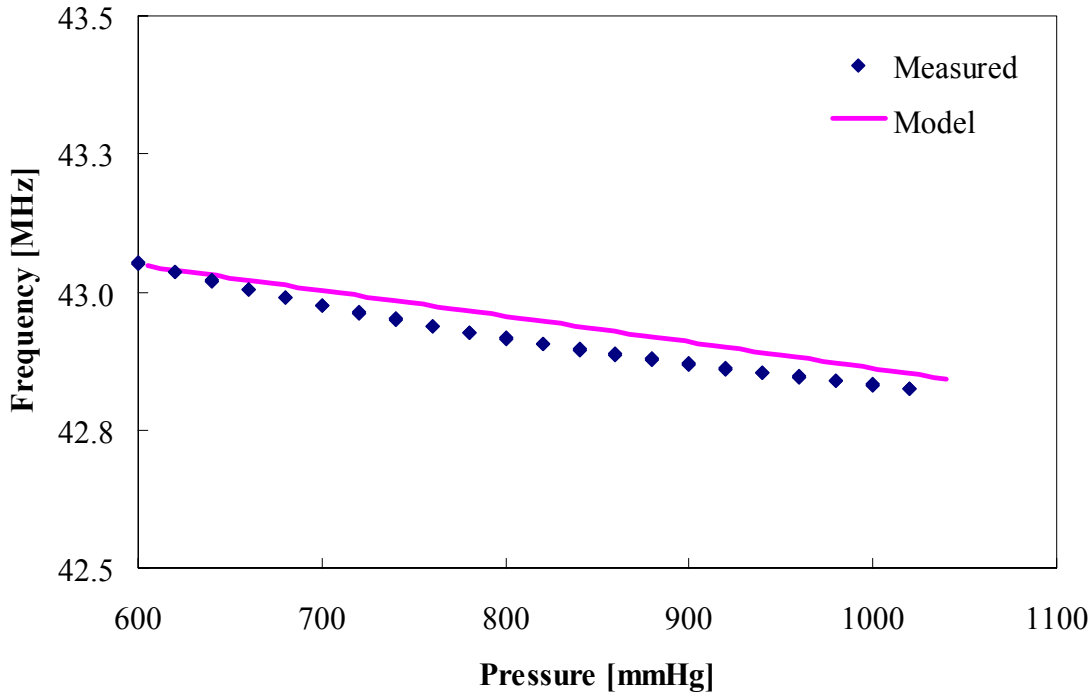

Figure 6.8: Measured and calculated frequency versus pressure for a PTFE-ceramic-based sensor.

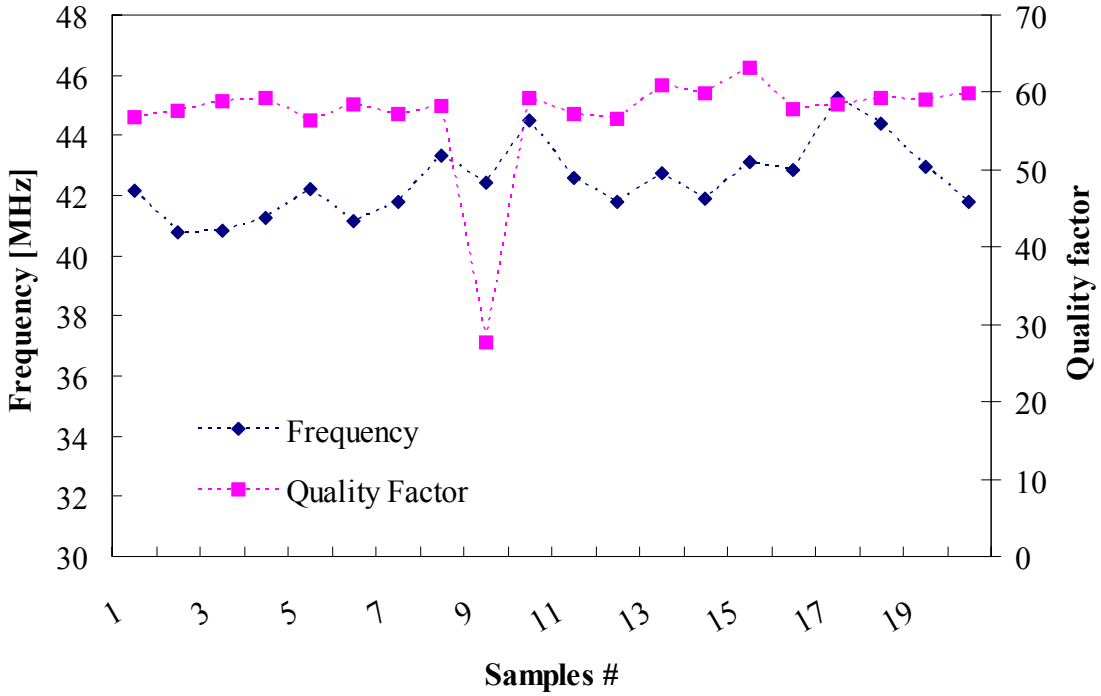

(a) Frequencies and quality factors.

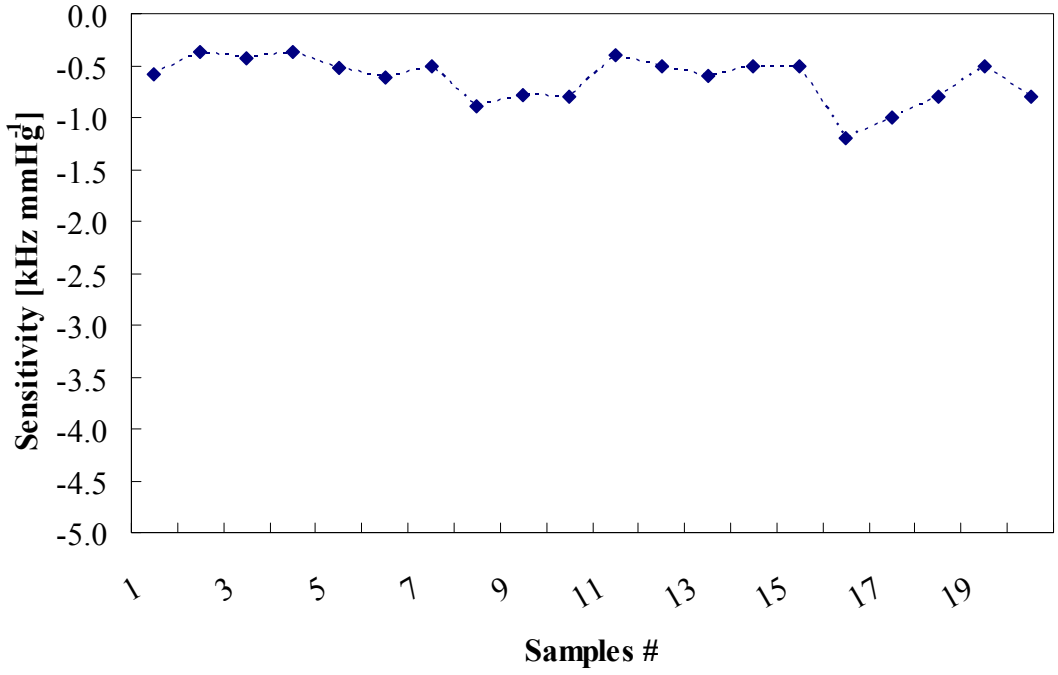

(b) Pressure sensitivity.

Figure 6.9: Frequencies and quality factors (a) and pressure sensitivities (b) versus sample number for PTFE-ceramic pressure sensors.

have pressure sensitivities of $> |1|$ kHz·mmHg^{-1}, most are closer to $> |0.6|$ kHz·mmHg^{-1}. These are limited by the fabrication of the ceramic chamber dimension and separation gap of the electrodes. Improvements in fabrication technology of the chamber could lead to mechanically more sensitive structures. Also, additional designs could increase the electrical sensitivity of the component to overcome its mechanical stiffness. The quality factor Q is lower than expected for PTFE-based devices by as much as 10-20. This reduction in Q is attributed to increased conductive loss of the Sn-Ag solder used to connect the spiral terminals to the electrodes of the ceramic chamber.

CHAPTER 7

PRESSURE SENSOR *IN VITRO* STABILITY TESTING

Implantable pressure sensors for biomedical applications generally require high reliability. This usually translates to exhaustive measures to guarantee device performance. Some aspects that are usually considered during reliability testing are mechanical integrity from cyclic loading and drift performance. In this work, an initial subset of reliability testing includes hydrostatic air and fluid pressure testing as well as cyclic-pressure loading.

For the hydrostatic environments, the mean frequency drift performance of devices fabricated from LCP, Kapton®, and PTFE [1] polymeric substrates are considered because these are the most common flex-circuit technologies available. The devices are characterized over sufficient time to gain an understanding of the basic drift behavior.

For the cyclic-pressure environments, the pressure-sensitivity drift and the mechanical integrity of the pressure sensors fabricated from the polymeric substrates listed above are investigated. This test accelerates the pressure-cycles by a factor of ≈31 times. This acceleration applies only to effects that are a function of the cyclic loading. The mean frequency drift is not accelerated through faster cycling. Therefore, the mean frequency drift during this experiment will be considered as real-time. The sections below outline the experimental test setup and results.

[1] For PTFE devices, this includes both PTFE-only and PTFE-ceramic devices

7.1 Sensor Stability in Hydrostatic Air Pressure

Chapter 5 and Chapter 6 discussed sensors fabricated from polymer and polymer-ceramic substrates. To compare the mean frequency stability of polymer and polymer-ceramic sensors, hydrostatic air pressure testing was performed for over 60 hours. This time-frame was sufficient to be able to compare different design architectures. The following sections describe the test setup and the experimental results.

7.1.1 Experimental Setup

Pressure sensor devices were subjected to 960 mmHg constant air pressure over a period of 60 hrs. Throughout this time, frequency measurements were automatically recorded using a Network Analyzer. The sensors wer mounted in a pressurizable fixture with coupling antennas, a Mensor PCS 400 pressure controller, and a Measurement Advantage USB-TC temperature acquisition unit. Signals were routed via an Agilent 34970A data acquisition system and Agilent 34905A RF 4:1 multiplexers in cascade to form a 16:1 switching system. The system is computer controlled by a LabVIEW program on a computer. The setup is shown in Figure 5.8 and a screen-capture of the software is shown in Figure 5.9. The software allows programmability of the channels, pressure, and time interval during testing as well as records the data.

7.1.2 Sensor Air-Pressure Stability Results

Figure 7.1 graphs the measured average normalized resonance frequency for 14 PTFE-ceramic, 7 LCP, and 9 Kapton® sensors, with maximum standard deviations of 0.06%, 1.1%, and 1.2%, respectively. From Figure 7.1, it is clearly shown that both the LCP-based and Kapton®-based devices exhibit a larger mean frequency drift than the PTFE-ceramic sensors. As expected, the devices housing a ceramic hermetic chamber maintain a greater level of stability. There is some variation in the data due to changes in temperature, which was not controlled during the test. The temperature did not vary by more than >3.8 ℃ and averaged 25.9 ℃ with a standard deviation of ±1 ℃.

The linear drift slope for LCP, Kapton®, and PTFE-ceramic devices is -0.02%, 0.02%, and <0.0003%, respectively, for the time frame of the test, which is over 60 hours. It is interesting to note that the drift for the LCP and Kapton® sensors is in opposite direction. The LCP devices have a decreasing mean frequency drift over time while the Kapton® devices have an increasing mean frequency drift. From theory, it is expected that for non-hermetic devices the mean frequency drift should occur in an increasing fashion when greater than atmospheric pressure is applied. This is, as the surrounding pressure is increased, the mechanical membranes deflect inward, thereby increasing the system capacitance and reducing the resonance frequency. As gas penetrates the non-hermetic chamber to equilibrate the pressure differential, the membranes should relax back to their original location (assuming no hysteresis). This phenomena appears to be true for the Kapton®-based devices. The LCP sensors, however, do not behave in this fashion. It is possible that for LCP-based devices, other more dominant effects overcome the expected non-hermetic behavior, such as plastic deformation of the membrane or creep.

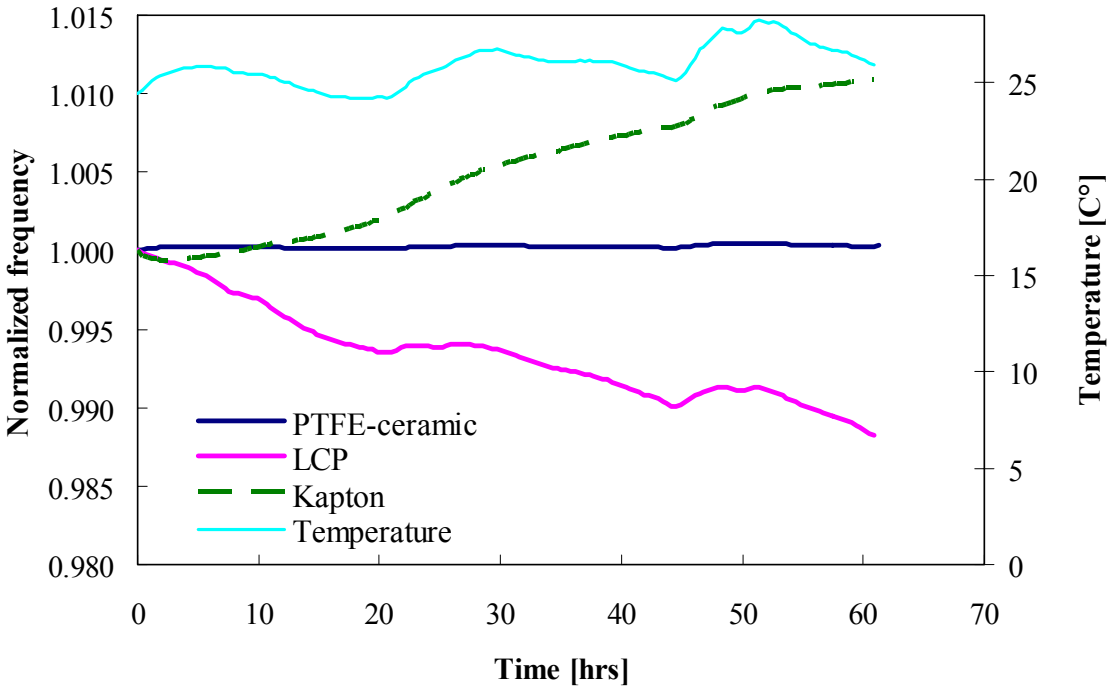

Figure 7.1: Normalized resonance frequency of LCP, Polyimide, and PTFE-ceramic pressure sensors versus time under hydrostatic pressure in air (960 mmHg absolute).

7.2 Sensor Stability in a Hydrostatic Saline Fluid Environment

To compare the mean frequency stability of sensors fabricated from polymer and polymer-ceramic substrates, devices were tested under hydrostatic saline fluid pressure for a time-frame of 150-1300 hrs. This period was sufficient to be able to compare the design architectures. The following sections describe the test setup and experimental results.

7.2.1 Experimental Setup

Devices fabricated from LCP, Kapton®, PTFE, and PTFE-ceramic substrates were subjected to hydrostatic pressure in a saline-fluid environment at room temperature and room pressure (≈740 mmHg, absolute). The experimental setup consisted of an array of sealed jars filled with approximately 2.5 inches of saline. The saline fluid level was normalized and marked for each jar to ensure both consistent and constant pressure over the duration of the experiment. Then each jar was sealed. The resonance frequencies were measured versus time for the period of the experiment and the results are discussed in the next section.

7.2.2 Saline-Fluid Stability Results

The test samples included in this experiment are various non-pressure sensitive devices and two PTFE-ceramic pressure sensors (see Table 7.1 for details). The first subgroup of non-pressure sensitive devices were used to characterize the stability of LC resonant circuits fabricated from different polymeric substrates. Non-pressure sensitive devices were used to isolate fluid effects due to material properties and pressure sensitivity. From the material properties listed in Table 4.1 (Chapter 4), it is expected that resonators built on polymers

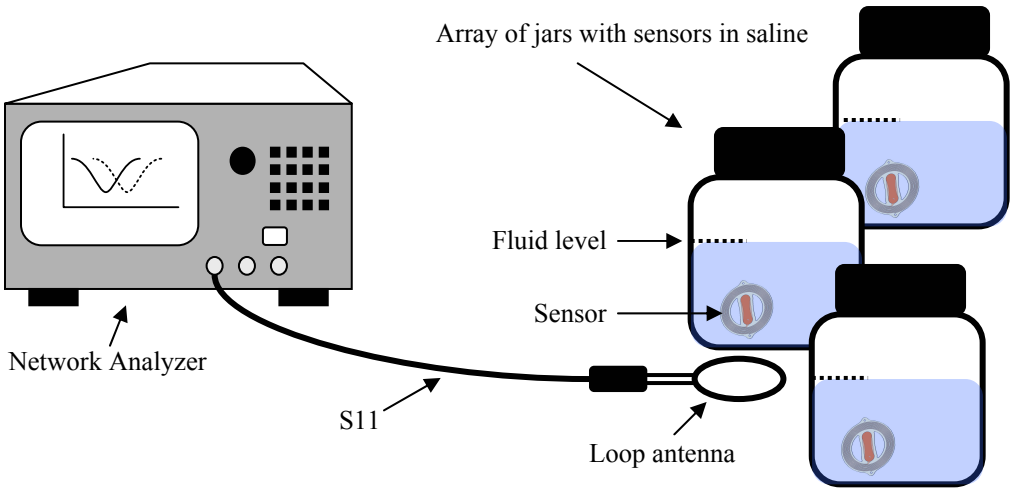

Figure 7.2: Experimental test setup used to characterize pressure sensors in a hydrostatic saline fluid environment.

with higher water absorption will have a larger mean frequency drift since the relative permittivity of the polymer will increase with increased water content [96].

Figure 7.3 graphs the normalized resonant frequency over time for the devices tested. The Kapton®-based and LCP-based devices have the largest mean frequency drift of between -2% to -5% for the time frame of >400 hours. The drift is attributed to their 2.8% and 0.04% water absorption, respectively. The PTFE-based structures appear to have close to zero (<0.09%) mean frequency drift when compared to Kapton® or LCP. Their lower mean frequency drift is attributed to the lower water absorption of PTFE, which is ≈0.004%. Additionally, PTFE-ceramic pressure sensors behave in a similar fashion.

Table 7.1: Device configurations used for hydrostatic saline stability testing.

Device	Configuration	Pressure sensitive [Y/N]	Test Duration [hrs]
PTFE-1	PTFE	N	>1300
PTFE-2	PTFE	N	>1300
LCP-1	LCP	N	>400
LCP-2	LCP	N	>150
Kapton	Polyimide	N	>500
PTFE Sensor 1	PTFE-ceramic	Y	>500
PTFE Sensor 2	PTFE-ceramic	Y	>300

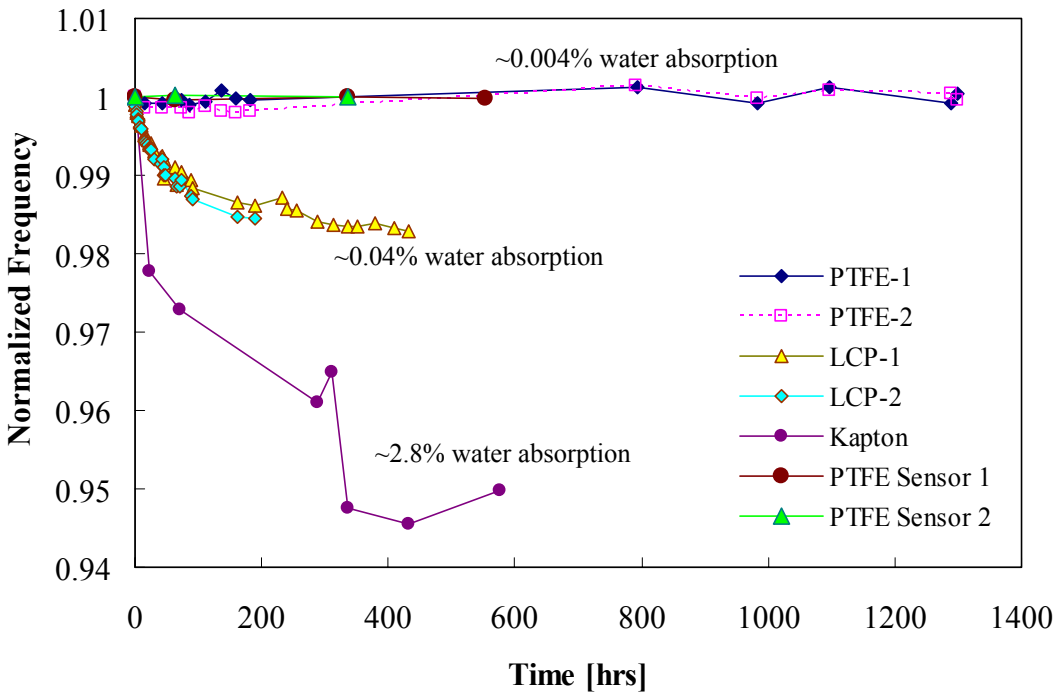

Figure 7.3: Normalized resonance frequency of LCP, Polyimide, PTFE, and PTFE-ceramic devices versus time measured in saline, at atmospheric pressure and at room temperature.

7.3 Cyclic Pressure Testing

Implantable pressure sensors intended for the human cardiovascular systems must be capable of withstanding millions of pressure cycles in body fluids and at body temperature. This environment can lead to fatigue, corrosion, or both, and eventually cause the devices to fail. To investigate the durability of polymer-based pressure sensor designs, simulated accelerated testing was performed.

The cycle test simulates aspects of the cardiovascular system, which include pressure, chemistry, and temperature. It characterizes sensor pulse pressure performance in physiological saline at body temperature for millions of cycles. The objective of this cycle test is to expose and characterize mechanical fatigue associated with repetitive fluid pulsation. Additionally, any material property effects, such as corrosion, can be exposed by subjecting

the devices to physiological saline at body temperature, which is not accelerated in this test setup.

Device performance related to mechanical pulsation, corrosion, or both, are monitored indirectly through frequency and sensitivity measurements. This is because any effect associated with mechanical fatigue or corrosion will cause either a change in device geometry or material property, altering the sensor's resonance frequency, quality factor, or pressure sensitivity. The pressure sensitive membrane is coupled to the electromagnetic domain through the integrated sensing capacitor as discussed in Chapter 2. From frequency, quality factor, and sensitivity measurements, effects of mechanical cycling or corrosion can be characterized.

Table 7.2: Cycle test environmental parameters for accelerated testing.

Environment	**In vivo conditions**	**Simulated conditions**
Medium	Blood	Saline (0.9% NaCl)
Mean Pressure	860 mmHg*	$\geq$ 860 mmHg*
Pulse Pressure	40 mmHg	$\geq$60 mmHg
Temperature	37 ℃	37 ℃

* Pressure in absolute values

The cycle test pressure parameters should meet or exceed those expected in the human cardiovascular systems. From Table 4.3 in Chapter 4, it is expected that devices should be able to operate in mean pressures ranging from 0-260 mmHg (0-34.66 kPa) above atmospheric pressure with pulse pressures $>$ 40 mmHg (8 kPa). Table 7.2 lists the cycle test environmental conditions compared to typical human cardiovascular systems. The expected pulse pressure rate of approximately 76 bpm is equivalent to 109,440 heart beats per day, which is approximately 40 million beats per year. To simulate $>$5 years of device operation in a reasonable time, the pulse pressure frequency was accelerated to oscillate at 40 Hz, a factor of 31.6 times, achieving 1 year of simulated cycling in 11.6 days. Table 7.3 lists respective time frames and test durations for accelerated testing. In the next section, the test setup, test equipment, and software for the cycle test are described in detail followed by

experimental results for polymer and polymer-ceramic sensor designs. It should be noted that only failure mechanisms associated with the pressure cycles are accelerated. Failure mechanisms originating from the exposure to the saline solution or body temperature are not accelerated.

Table 7.3: Simulated time frame for accelerated cycle testing.

Simulated Time frame	Approximate # of heart beats	Test Duration (approximate)
1 day	109,440	≈1 hr
1 week	766,000	5.3 hrs
1 month	3,300,000	22.8 hrs
1 year	40,000,000	278 hrs (11.6 days)
5 years	200,000,000	1388 hrs (58 days)

7.3.1 Experimental Setup

7.3.1.1 Equipment and Software

The experimental setup for cycle testing of wireless pressure sensors consisted of an environmental control and logging system (pressure and temperature) along with frequency data acquisition, which are illustrated in Figure 7.4 and Figure 7.5, respectively.

Mean and pulse pressures were achieved through the use of a peristaltic pump to generate pulse a pressure and a column of fluid for the mean pressure. Temperature was controlled though the use of a temperature-controlled water bath. A pressure gauge and temperature reader connected in line with the sensor chamber were used to log the environment during testing. The equipment required for the cycle test system is listed below.

Environmental control:

- Cole-Parmer peristaltic pump, digital drive 0-600 rpm
- Omega temperature reader and probe
- Cole-Parmer temperature-controlled water bath

- Setra pressure gauge Model 204, 0-25 PSIA
- GPIB PC with LabVIEW software
- Saline reservoir
- Pressure chamber

Frequency data acquisition:

- Network Analyzer, Agilent E5100
- GPIB PC with LabVIEW software
- Loop antenna

7.3.1.2 Test Methodology

The bench-top pressure cycle test system, illustrated in Figure 7.4, is mainly comprised of a peristaltic pump, a heated water bath, and a computer to control, monitor, and record the environmental conditions. Additionally, a network analyzer connected to the computer and controlled with LabVIEW was used to record frequency data over time and is illustrated in Figure 7.5.

The pressure sensors were placed in sealed chambers (jars) filled with saline. Four chambers were used with 2 sensors per chamber for a total of 8 sensors. Each chamber was connected in parallel to a pressure line and submerged in a heated bath. Although this configuration allows pressure gradients to exist in the system, each device was measured during initial setup to ensure pulse pressure excursions of at least 100 mmHg. The system setup is illustrated in Figure 7.4 and images of the test system are graphed in Figure 7.6 through Figure 7.9. Throughout cycle testing, the devices were interrogated to measure the resonance frequency. This was achieved by intermittently stopping the pressure cycling and measuring the frequency with a data acquisition system. Stopping the pressure pulsation was necessary to improve accuracy of the intermittent frequency measurements since a dedicated frequency acquisition system was not accessible for the extended period of

testing. An improvement to this setup would be to continuously monitor the frequency of each device. This would require a more elaborate system and dedicated interrogation units. The method used, however, allowed for sufficient data collection to compare the selected designs.

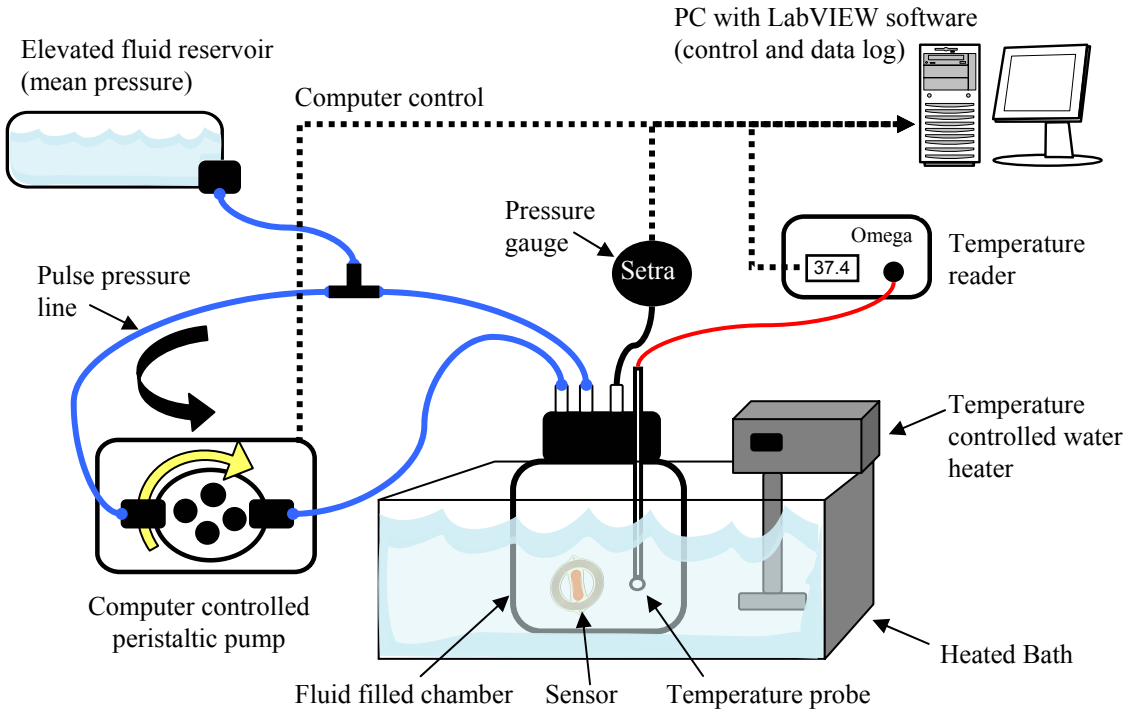

Figure 7.4: Pressure cycle test system used to evaluate mechanical fatigue of implantable pressure sensors.

7.3.1.3 Test Samples

Three different designs were selected for cyclic loading, termed Designs 1-3 (D1, D2, and D3). Two are polymer-based and fabricated from LCP (D1) and Kapton® (D2) while the third is polymer-ceramic-based fabricated from PTFE-ceramic (D3). The device frequency, quality factor, and pressure sensitivity were characterized in air prior to the experiment and are listed in Table 7.4.

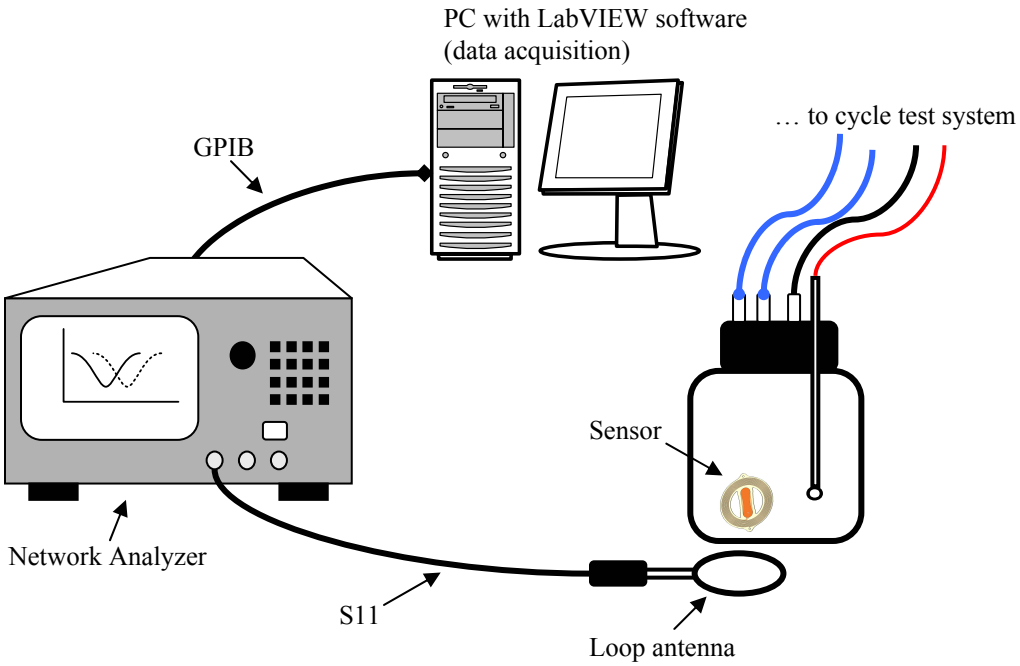

Figure 7.5: Pressure cycle test system frequency data acquisition system.

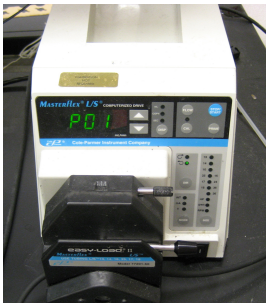

Peristaltic pump

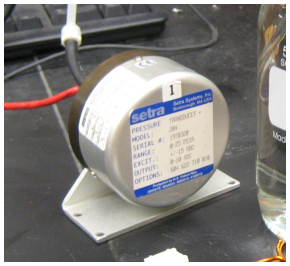

Setra pressure gauge

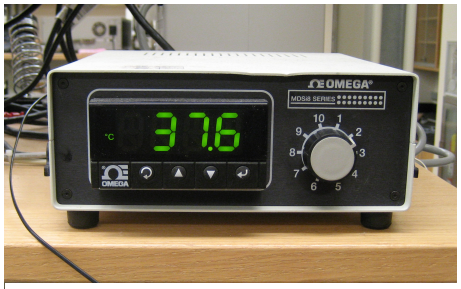

Omega temperature reader

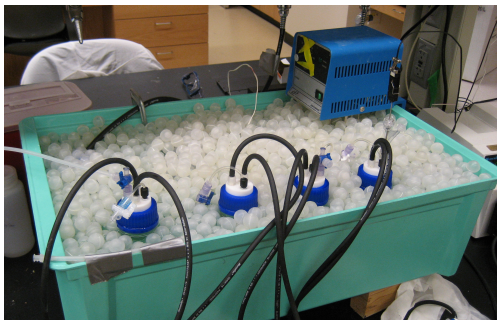

Heated water bath with 4 pressurized jars

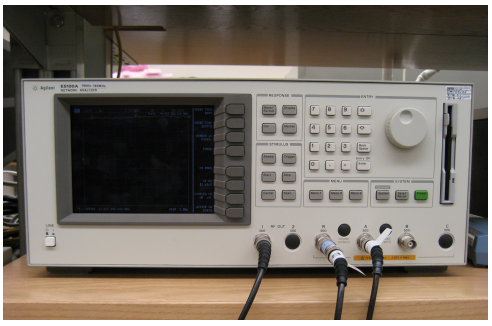

Network Analyzer

Figure 7.6: Pressure cycle test system images.

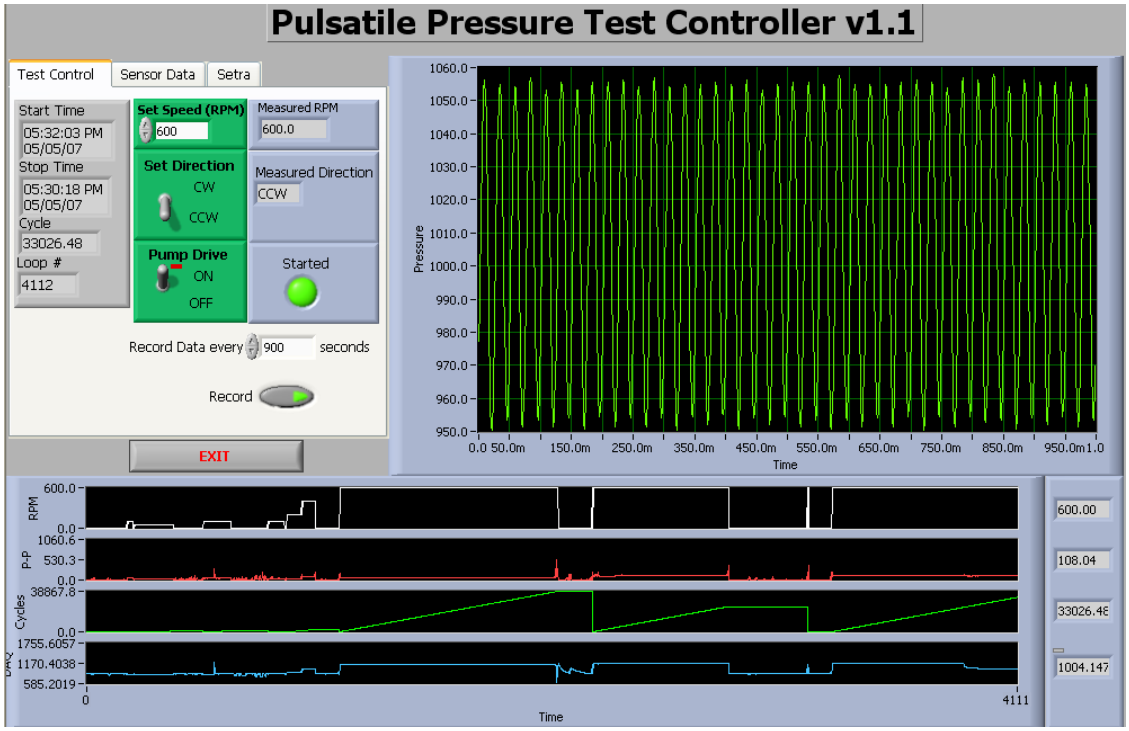

Figure 7.7: Pressure cycle test system software for pressure data logging and control.

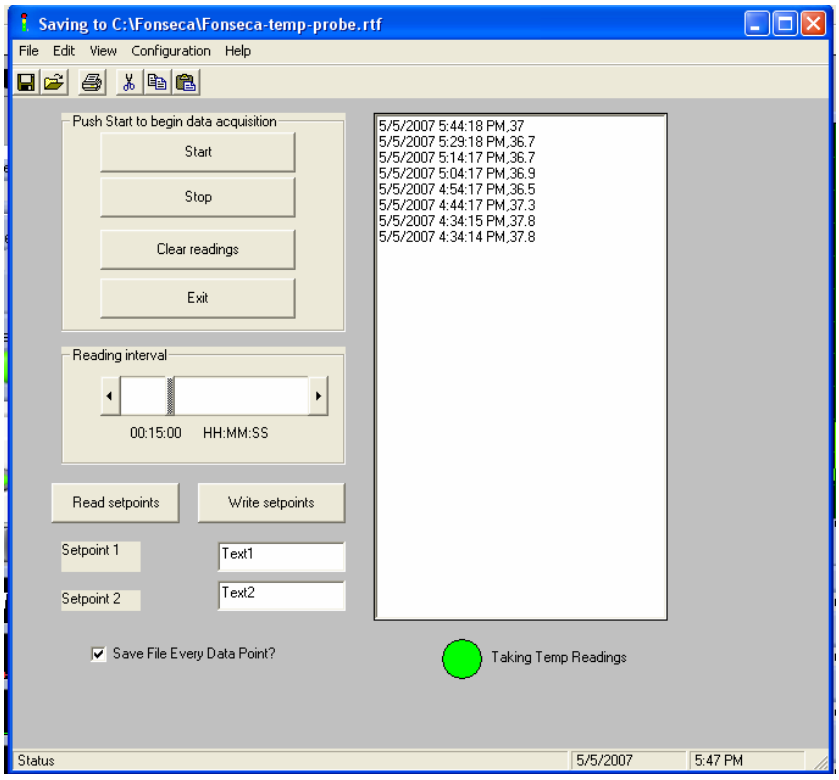

Figure 7.8: Pressure cycle test system software for temperature data acquisition.

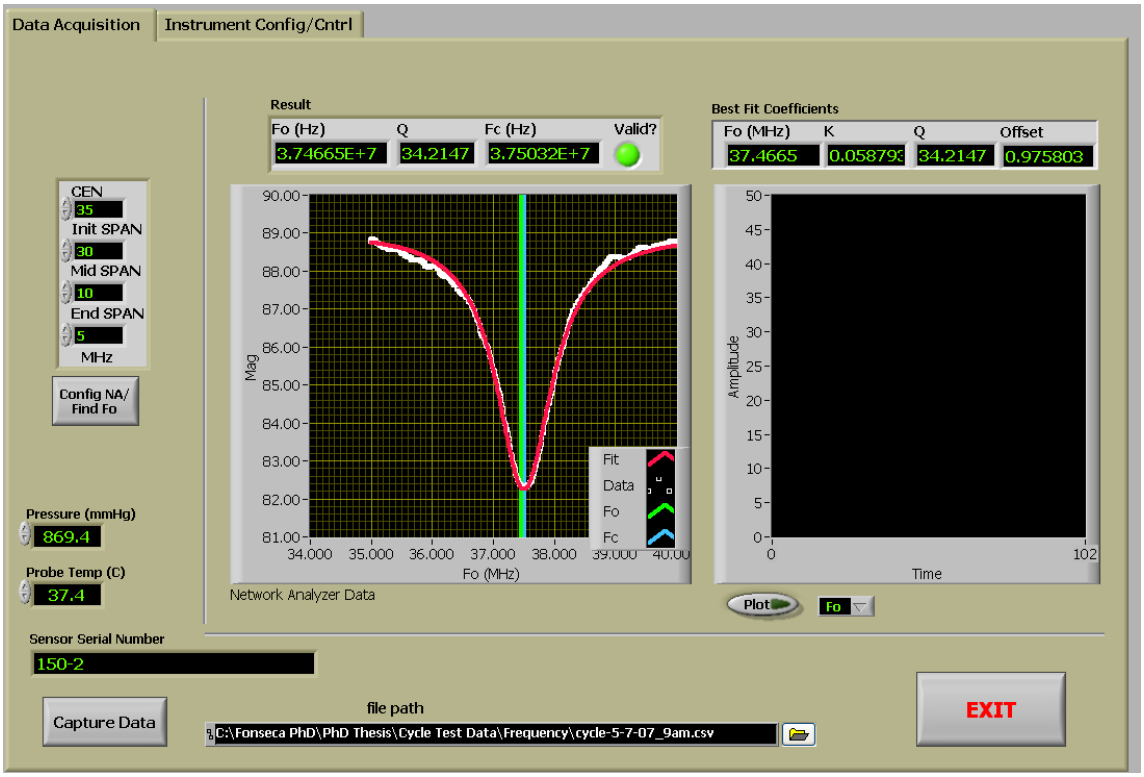

Figure 7.9: Pressure cycle test system software for frequency data acquisition.

Table 7.4: Device configurations used for cyclic loading stability testing.

Design		**Characteristics**		
Label	**Substrate**	**Frequency [MHz]**	**Pressure sensitivity [kHz·mmHg^{-1}]**	**Quality Factor**
D1	LCP	36.1	9.78	49.8
D2	Kapton	45.7	1.97	29.1
D3-a	PTFE-ceramic	41.8	0.47	56.6
D3-b	PTFE-ceramic	42.9	0.54	59.1
D3-c	PTFE-ceramic	45.3	0.97	58.5
D3-d	PTFE-ceramic	41.9	0.48	59.8
D3-e	PTFE-ceramic	44.5	0.79	59.3
D3-f	PTFE-ceramic	42.7	0.62	61.0

7.3.2 Cycling Test Results

7.3.2.1 Environmental Conditions

Temperature and pressure environmental conditions were monitored throughout the progression of cycle testing. The temperature, mean pressure, and pulse pressure were measured intermittently at 30 minute intervals during the experiment, which are illustrated in Figure 7.10 and Figure 7.11. The fluid temperature had an average of 37.26 ℃ with a standard deviation of ±0.23 ℃. The average mean and pulse pressures were measured at 1129 and 169 mmHg with standard deviations of ±16.4 and ±19.03 mmHg respectively.

7.3.2.2 Sensor Performance Results

The resonance frequency was intermittently measured during the experiment using the methodology described in the previous section. The results are graphed in Figure 7.12. In Figure 7.12, the data presented for PTFE-ceramic is an average of the six devices tested. The graph also includes error bars representing the standard deviation for each data point, which ranges from ±46 to ±250 kHz. At ≈300 million cycles, which is equivalent to ≈7.5 years (88 days of real-time), the experiment was stopped. The mean frequency drift was measured to be -7.65, -9.36, and -0.258 MHz for LCP, Kapton®, and PTFE-ceramic sensors respectively. Additionally, the device resonant frequencies, quality factors, and pressure sensitivities were measured post-cycling in air to compare to pre-cycling data. The comparison results are listed in Table 7.5 as percent difference and calculated using

$$\Delta X[\%] = \frac{X_{post} - X_{pre}}{X_{pre}} \ , \tag{7.1}$$

where X_{post} is the data post-cycling and X_{pre} is the data pre-cycling. From both Figure 7.12 and Table 7.5, it is clearly visible that the PTFE-ceramic devices have greater stability under simulated *in vivo* conditions. The improvement is attributed to the ceramic hermetic chamber and low moisture absorption of the design.

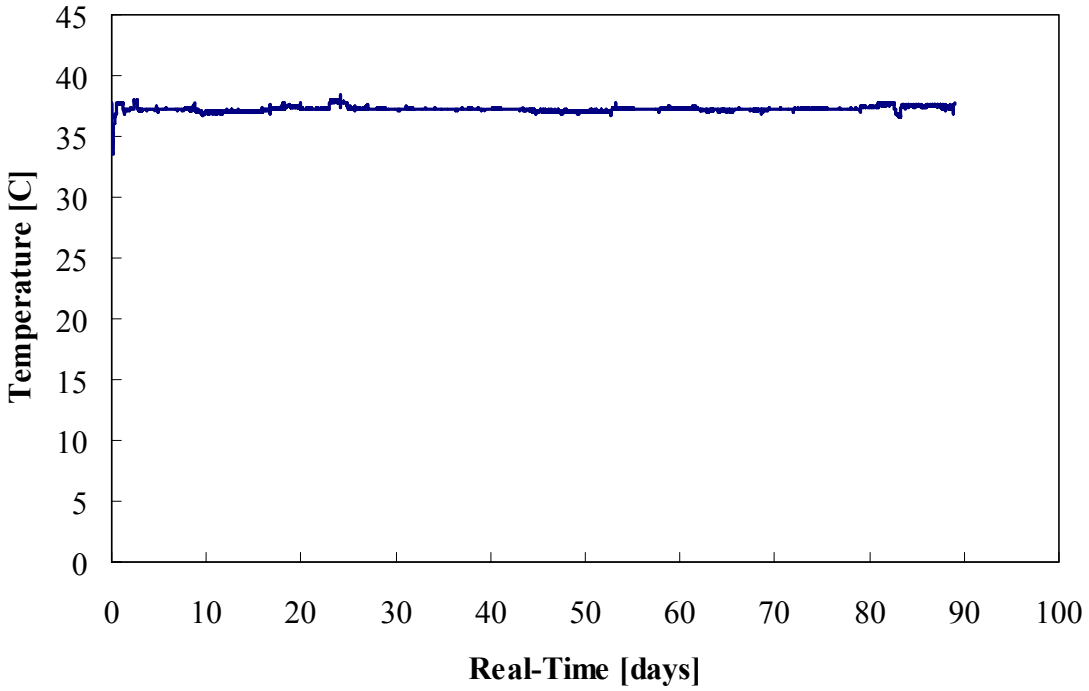

Figure 7.10: Measured temperature of fluid within the vessel containing a sensor during cycle testing.

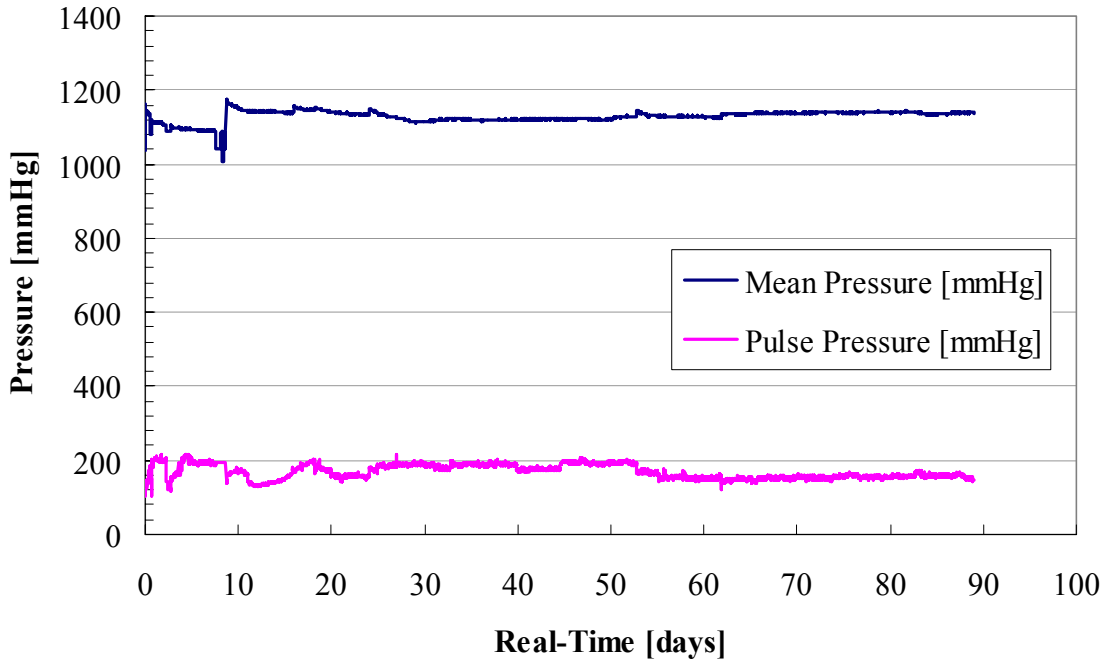

Figure 7.11: Measured mean and pulse fluid-pressure during cycle testing.

Table 7.5: Device resonant frequency, quality factor, and pressure sensitivity comparison for pre- and post-cycle testing. Characterization was performed in air.

Design		Characteristics		
Label	**Substrate**	**Delta Frequency [%]**	**Delta Pressure sensitivity [%]**	**Delta Quality Factor [%]**
D1	LCP	-11.00	61.5	-77.9
D2	Kapton	-17.42	-28.8	-63.3
D3-a	PTFE-ceramic	-0.06	1.1	-0.7
D3-b	PTFE-ceramic	-0.03	6.6	-21.2
D3-c	PTFE-ceramic	0.02	-6.7	-3.1
D3-d	PTFE-ceramic	-0.031	3.8	-32.0
D3-e	PTFE-ceramic	-0.63	5.4	-25.0
D3-f	PTFE-ceramic	-0.17	3.4	-36.0

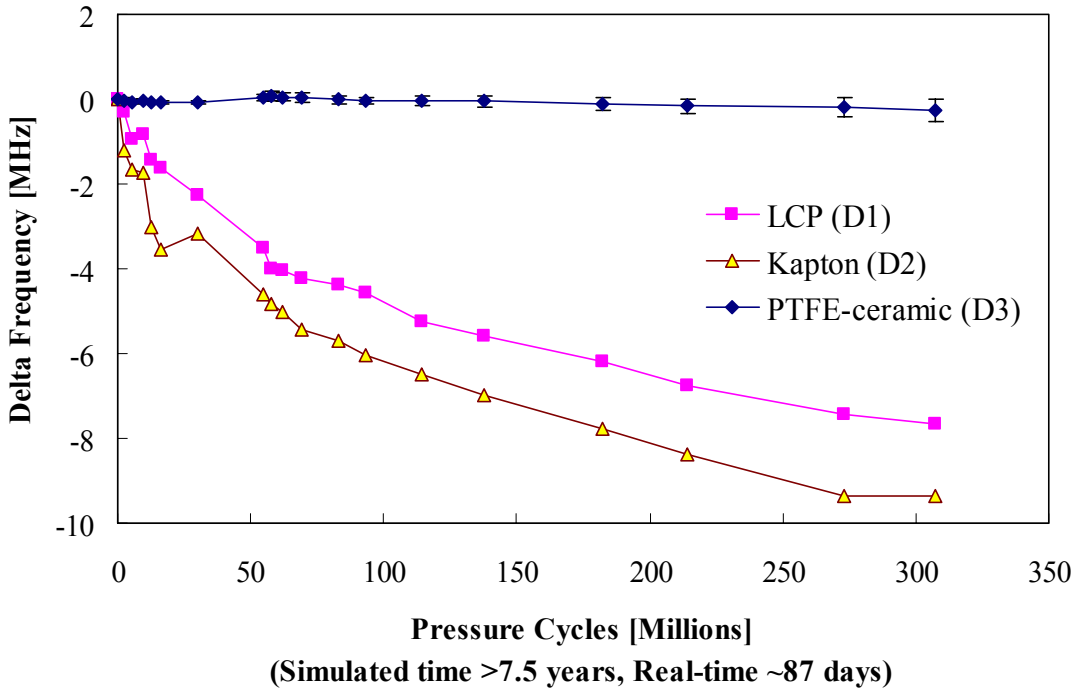

Figure 7.12: Delta frequency versus pressure cycle for cycle testing. Data shown for PTFE-ceramic sensors is an average of 6 devices.

CHAPTER 8

IN VIVO EXPERIMENTAL TESTING

During this research, verification of sensor operation *in-vivo* was possible through collaboration with a biomedical device company, CardioMEMS, Inc. All of the animal testing, catheter prototype designs, and electronic readout systems were designed, operated, and performed by CardioMEMS personnel. Additionally, all appropriate protocols and procedures specified by the Institutional Animal Care and Use Committee (IACUC) for animal testing were followed during the study, which were implemented by CardioMEMS personnel. The only material supplied from this research were polymer-based pressure sensing devices. Permission to present the collected data from the animal study, which is the main topic of this chapter, was granted by CardioMEMS, Inc.

In this chapter, section §8.1 gives an introduction and background on abdominal aortic aneurysm (AAA) to support the need for wireless pressure sensors. A description of the *in-vivo* animal model is presented in section §8.2. The catheter-based delivery of the sensors is discussed in section §8.3. Finally, the animal study results are presented in section §8.4 and a brief summary is given in section §8.5.

8.1 Abdominal Aortic Aneurysms

Aneurysms are a bulging of the blood vessels in weak areas. These commonly occur in the aorta, a large artery that supplies oxygenated blood from the heart to all parts of the body in systemic circulation. The aorta begins at the left ventricle of the heart and proceeds through the thorax and down through the abdomen. Abdominal aortic aneurysms (AAA), illustrated in Figure 8.1, are a swelling of the aorta caused by weakening of the vessel wall in the abdominal region, usually above the aortic bifurcation to the common

iliac arteries. The swelling or ballooning (aneurysm), if untreated, can have the risk of rupture and cause massive internal hemorrhaging, which can quickly result in death [97]. AAAs are currently the thirteenth leading cause of death with approximately 1.5 million cases, and approximately 200,000 new cases per year [46].

Abdominal aortic aneurysms range in size from <4 cm to >8 cm in diameter. As the aneurysm diameter increases, so does the risk of rupturing. The decision to treat is generally made when the risk of rupture exceeds the operative risks [98]. Consensus on estimated risk of rupture of AAAs based on diameter alone per year is shown in Table 8.1, with aneurysms >8 cm having up to 50% rupture risk per year. Additionally, from Table 8.1, a significant rupture rate increase occurs when aneurysm size increases from 5 cm to 6 cm. Moreover, other risk factors, including atherosclerosis, high blood pressure, smoking, gender, and genetics are considered when diagnosing AAAs.

Table 8.1: Estimated rupture-risk of AAAs for a given diameter per year [98].

AAA Diameter [cm]	**Rupture Risk [% per year]**
<4	0%
4-4.9	0.5 to 5%
5-5.9	3 to 15%
6-6.9	10 to 20%
7-8	20 to 40%
>8	30 to 50%

8.1.1 Treatment of AAAs

Prior to treatment, patients are monitored through imaging studies conducted with ultrasound, angiography, computer tomography (CT), or magnetic resonance angiography (MRA). Once the decision is made that treatment is needed, the patients undergo procedures to isolate systemic blood flow from the aneurysm. This is because prolonged systemic pulse pressure on the weakened vessel wall can lead to rupture. There are two methods for treatment of AAAs: open surgical repair and endovascular repair (EVAR), illustrated in Figure 8.2 (a) and (b) respectively.

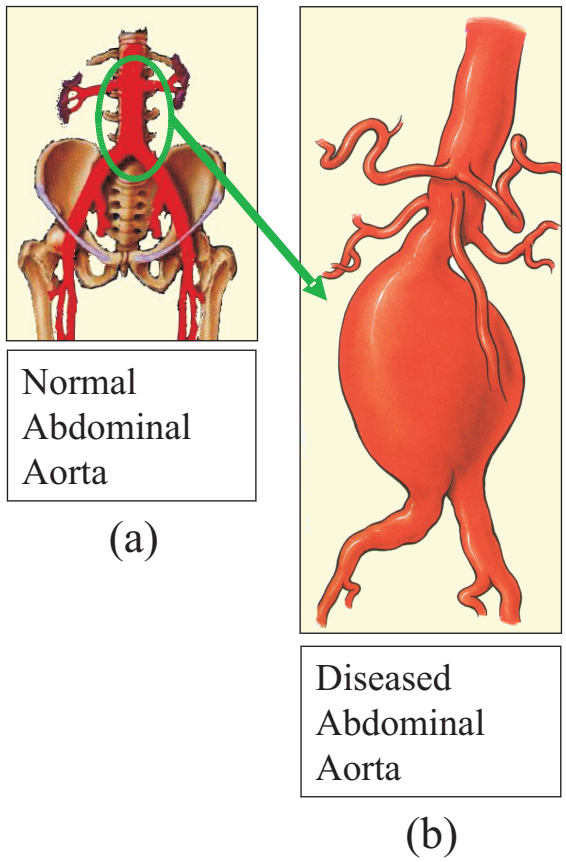

Figure 8.1: Abdominal aorta for (a) normal and (b) diseased blood vessels.

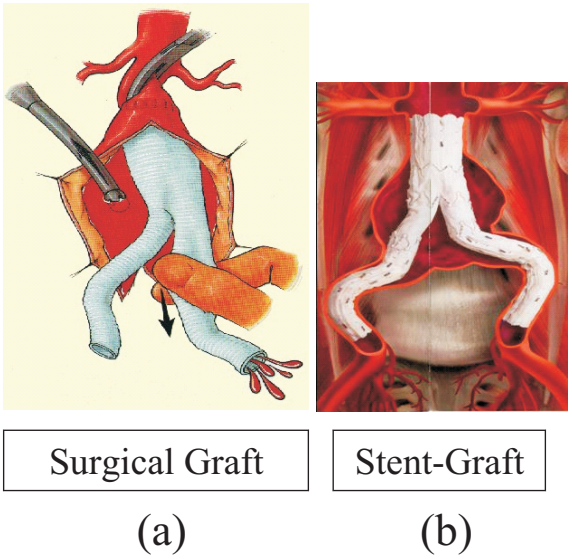

Figure 8.2: Methods to repair AAAs include (a) surgical and (b) endovascular.

Surgical repair of AAAs has been around since the 1950s with the first successful repair performed by Dubost in 1952 [98]. Open surgical repair replaces the diseased portion of the aorta with a synthetic vascular graft. The procedure starts with an incision of approximately 10" from the chest to the abdomen. Then, a graft is sewn to the proximal and distal portions of the aorta. The new graft redirects blood flow, replacing the diseased vessel with an artificial tube. Surgical repair of AAAs have reported 1% to 5% mortality rate post repair, with additional risk factors including major complications, prolonged hospitalization, prolonged recuperation, and sexual dysfunction [98]. Furthermore, comorbididy can limit patients from surgical treatment proceedures suffering from AAAs. These factors led to the development of new methods for treatement, such as EVAR, with the first procedure reported by Dr. Juan Parodi in the early 1990s [98].

In contrast to open surgical repair, EVAR does not replace the diseased aorta. Instead, this procedure lines the aorta with a stent graft, redirecting blood flow within. The procedure involves minimally invasive percutaneous methods through the iliac arteries to access the aorta. Catheter-based delivery systems are used to introduce the stent graft in a compact form (pre-deployment) into the aneurysm. The stent graft, usually comprised of two or three sections (main body and limbs), is deployed within the aneurysm and relies on mechanical expansion force of the stent struts to hold it in place as well as create a seal between healthy aorta and the graft. Imaging with contrast is performed at the end of the procedure to ensure proper seal is achieved between the stent graft and aorta. Major advantages to EVAR versus open surgical repair is the lower early (during or immediately following the procedure, 30-day) mortality rate of approximately 1.5% compared to open surgery's 3-5%, along with reduced hopitalization [98]. Another advantage to EVAR is reduced morbidity by up to 30-70%, due to a significant reduction in anesthesia time, blood loss, and other complications [98]. Yet, the Food and Drug Administration (FDA) estimates a higher aneurysm related mortality rate of 0.4% per year for EVAR compared to 0.1% per year for open surgical repair due to stent graft failures [98]. However, the 30-day operative mortality rate for open surgical repairs increases up to 2% to 50% when additional risk

factors are present such as ischemia, congestive heart failure, age older than 75, as well as others [98]. This increase in operative mortality from additional risk factors increases the number of EVAR procedures for this patient population, since it is sometimes the only option for repair.

8.1.2 Commercial need for wireless pressure monitoring of AAAs

One of the drawbacks to EVAR is related to how effectively the stent graft isolates the aneurysm from systemic blood flow, which is termed an endoleak. These are classified into four types, listed below [99].

Type I Leak that occurs due to poor or inadequate seal between the stent graft and aorta vessel wall (seal, graft-related endoleak).

Type II Leak from collateral blood vessels supplying blood flow into the aneurysm sac (non-graft related endoleak).

Type III Leak that allows blood flow into the aneurysm sac from a tear in the fabric of the stent graft or due to defective grafts (fabric, graft-related endoleak).

Type IV Leak through the porosity of the graft material (porosity, graft-related endoleak).

Another drawback is increased pressurization of the aneurysm sac without blood flow, known as endotension. The possibility of endoleaks or endotension post-EVAR procedures can still lead to ruptures. Given this possibility, lifelong patient management post-EVAR has become a priority with CT imaging becoming the prevailing method of surveillance to measure and monitor sac diameter as a link to sac pressurization [99]. However, repeated use of CT scans, which require the use of nephrotoxic contrast dye, is associated with reduced kidney function in patients who have undergone EVAR [46]. An improved method of patient management is achieved through direct monitoring of sac pressure by permanently implanting a wireless pressure sensor in between the stent graft and excluded aneurysm [46].

8.2 Animal Model

Polymer-based pressure sensors were tested *in vivo* in canine models simulating abdominal aortic aneurysms, illustrated in Figure 8.3, with LCP-based acute devices being implanted via a catheter and measured. The aneurysms were created by surgically implanting a graft and wired reference pressure transducer into the aorta. The canine model is described in greater detail in [100–102]. After the animal was allowed to heal, the sensors were implanted through catheter delivery, following which a stent graft was used to perform endovascular repair. The following sections §8.3 and §8.4 describe the catheter-based delivery and measurement results from this animal study.

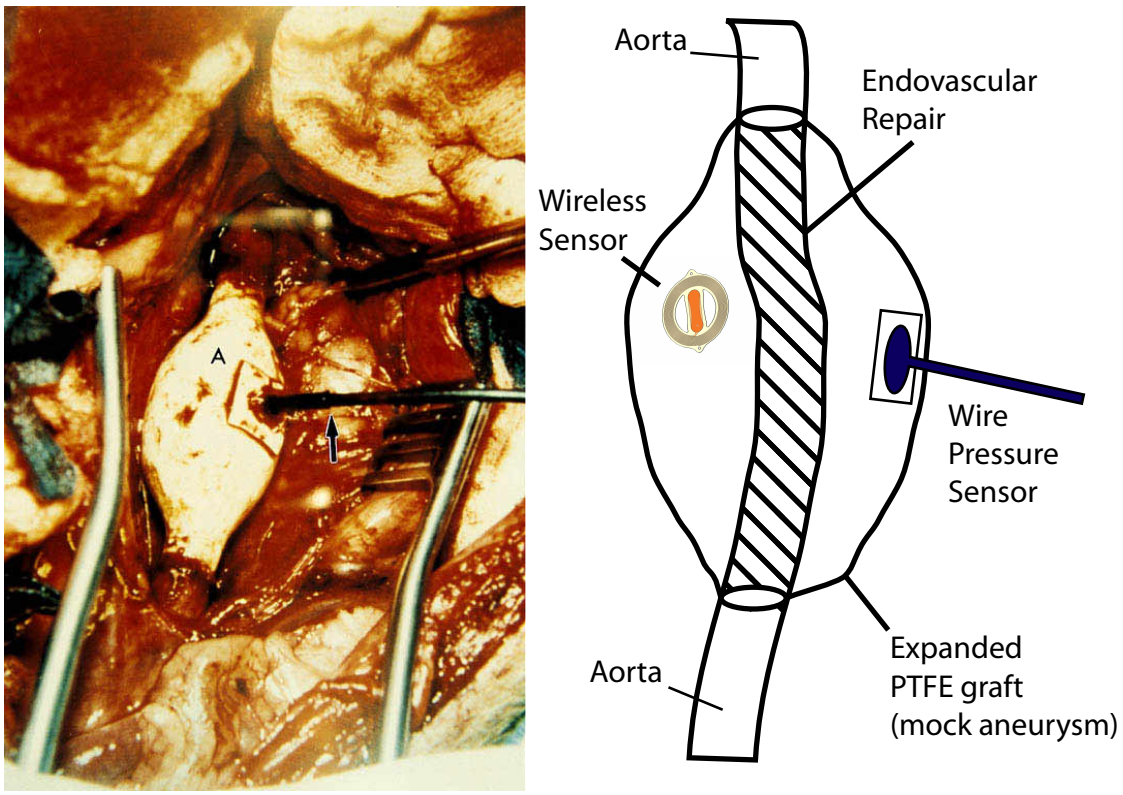

Figure 8.3: Creation of mock aneurysms in canine model and positioning of wired and wireless pressure sensors.

8.3 Catheter Delivery

For minimally invasive implantable devices, catheter-based delivery systems are preferable. The flexible sensors could be rolled or folded into catheters that have internal diameters of 4 mm. The delivery system used for this study consisted of a delivery catheter, sheath, deployment-clip, and sensor-tether, illustrated in Figure 8.4 (a). The sensor is attached to a small diameter (0.020" OD) 'tether tube', Figure 8.4 (b), by threading a small diameter (0.008") nitinol wire through the length of the tube and through holes on the top and bottom portion of the sensor, which are shown in Figure 8.4 (a). The tether tube maintains control over device position in the aneurysm sac by the user until completion of the endovascular repair with the stent graft. At the time of release, the thin wire is pulled by the user to release the sensor in the desired location within the aneurysm.

In order to facilitate folding, additional cut-out features were added to the sensor design in between the planar spiral coils and center pressure-variable capacitor; these are observed in Figure B.5 from Appendix B, section §B.3.1. The cut-outs allow for the sensor to be rolled up inside the catheter, illustrated in Figure 8.4 (c). The delivery procedure introduces the catheter through a cut-down in the femoral artery and the system is advanced into position within the mock aneurysm. Next, the catheter is retracted, exposing the sensor on the tether tube, which allows the aneurysm repair to continue.

The sensor is retained on the tether tube until endovascular repair of the aneurysm is completed with a stent graft. Once the sensor is trapped in the space created between the outer surface of the stent graft and the inner surface of the mock aneurysm, the tether wire is pulled, releasing the sensor. Finally, the tether tube and delivery catheter are removed, leaving the sensor in the "excluded" portion of the aneurysm sac, from which wireless measurements can be performed.

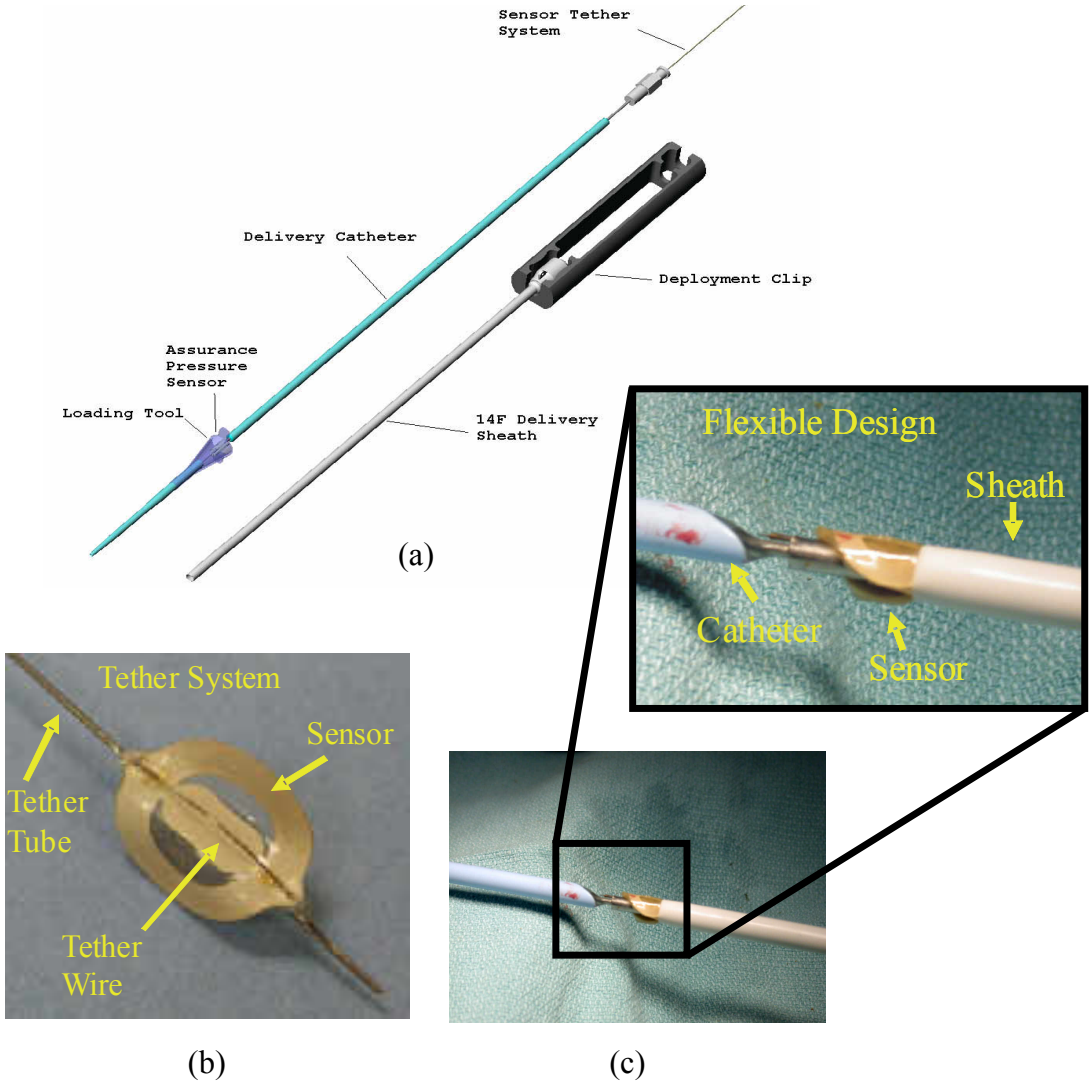

Figure 8.4: Sensor delivery system: (a) Schematic of delivery system, (b) sensor on tether, and (c) sensor rolled up into sheath prior to implantation.

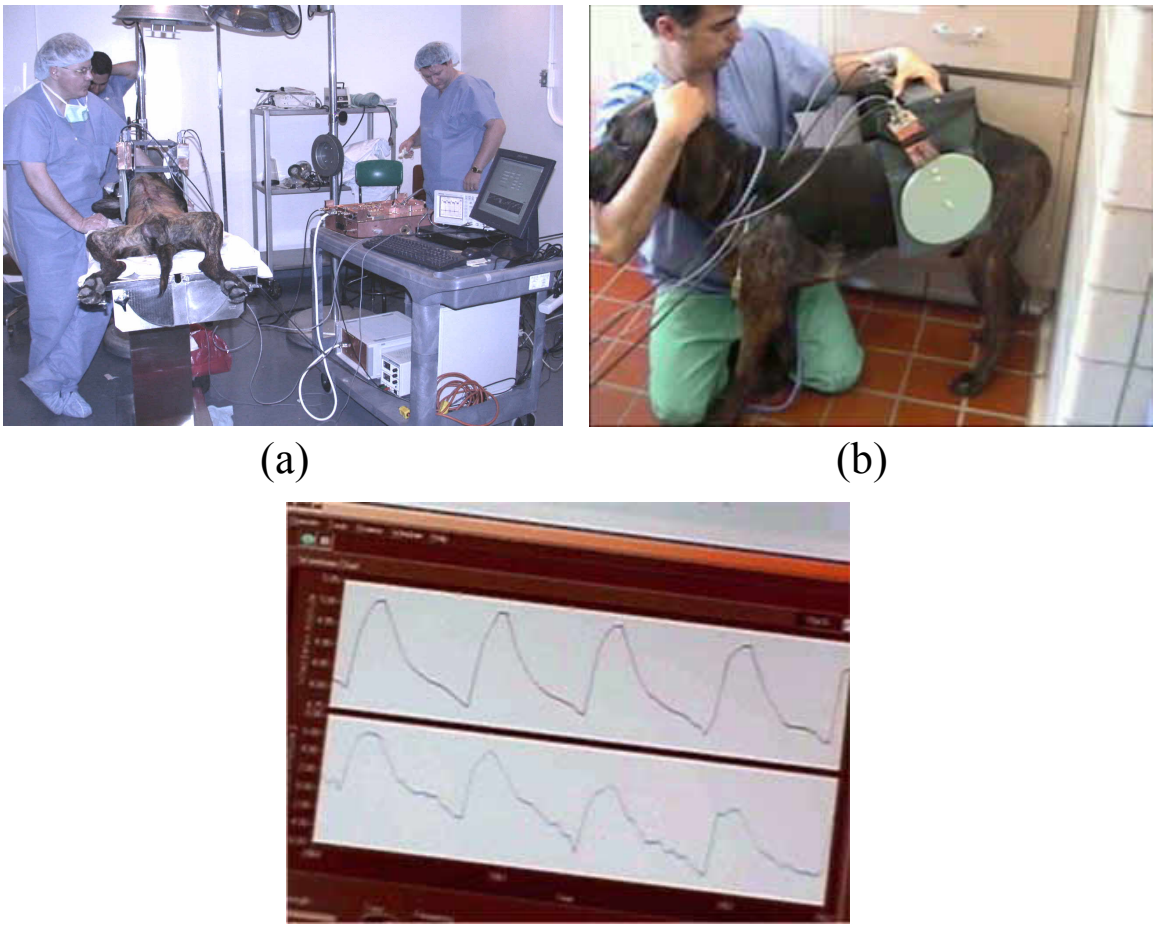

Figure 8.5: Readout telemetry system: (a) system during a measurement while the animal was sedated, (b) antenna on canine during un-sedated measurement, and (c) LabVIEW screen-shoot of measurement with the reference signal on the top and wireless pressure sensor on the bottom.

8.4 Animal Study Results

A total of four devices were implanted into four different animals for a period ranging between 30-60 days. Throughout the study some of the wired reference pressure transducers failed. No failure of the wireless sensors during the study was observed. Also, throughout the study, the telemetry system was improved, which increased the fidelity of the data. Images of the telemetry during a post-implant follow-up measurement are presented in Figure 8.5 (a). Figure 8.5 (b) illustrates a canine with an antenna during an un-sedated measurement and Figure 8.5 (c) shows a screen capture of the pressure waveform for both the wireless and wired sensors. The data reported below represents typical results from the four devices, which was recorded in 60 to 120 second intervals at sampling rates of > 120 Hz. This sampling rate was sufficient to capture the highest frequency content of interest in the pulse train, illustrated in Figure 8.6.

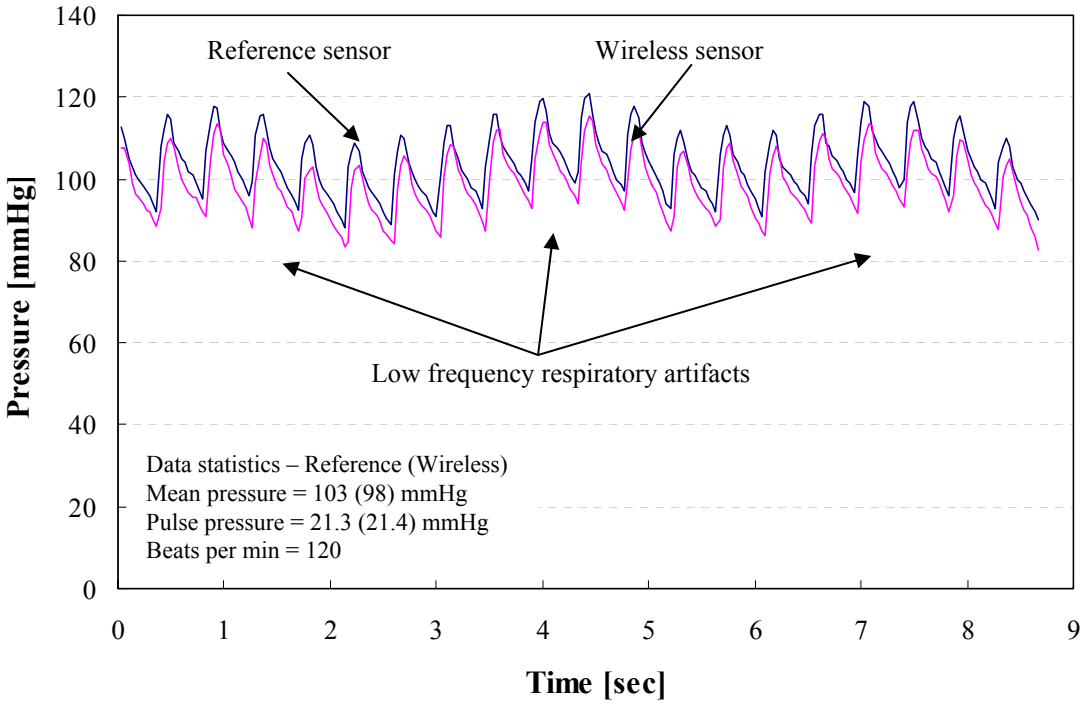

Figure 8.6: Continuous pressure waveform of a wired and wireless pressure sensor during a follow-up procedure.

The sensor frequency response to pressure change was determined by pre-implant calibration testing. This was achieved by characterizing f_0 versus absolute pressure during sensors characterization and discussed in Chapter 5. At the time of implant, a fluid-filled catheter was placed in the aneurysm to baseline the mean pressure and was used to calibrate the wireless and wired pressure sensors. Data was collected beyond 30 days for most of the devices, with pulse pressures ranging between 12-37 mmHg and mean pressures ranging from 70-120 mmHg about atmospheric pressure.

To assess the measurement results of the animal feasibility study, a key statistical principle for comparing clinical measurements is discussed. In clinical settings, it can often be extremely difficult or impractical to perform direct measurement of parameters of interest without adverse affects. Over time, specific test benchmarks, termed the gold standard, become definitive methods of measurement even if the true values remain unknown. Therefore, when developing new methods of measurement, they must be evaluated by comparing them to the gold standard rather than true quantities. If the new method is in good agreement with the old gold standard, then the old method may be replaced. Since two methods are being compared and neither provides an unequivocally correct value, then a procedure for assessing agreement is used as opposed to a more common method of correlation, which can be misleading [103]. Assessing agreement is different from determining correlation because correlation measures the strength of a relation between two measurements and not the agreement between them [103]. By assessing agreement, a determination of how the two measurements differ is established. A well known method for assessing agreement is the use of a Bland and Altman plot to compare the level of agreement between two clinical measurements [103].

Figure 8.7 graphs a Bland and Altman plot of the continuous pressure waveforms from Figure 8.6 for the wired reference and wireless pressure sensors. The mean pressure difference (d_{Diff}) and standard deviation of the differences (s_{Diff}) are determined to be $d_{Diff} = -4.368$ mmHg and $s_{Diff} = \pm 2.2$ mmHg respectively. Ideally d_{Diff} would be zero, however,

for this case the offset is partially attributed to poor calibration of either the wired or wireless pressure sensors from the fluid-filled catheter during implant. Additional measurement error could include the fact that the wired reference pressure transducer was sutured to the mock aneurysm, inducing stress, and thereby applying a bias. Despite this offset, the two measurement methods are in good agreement, demonstrated by the 95% confidence interval. The confidence interval is an estimated range of values that is likely to include the parameter of interest 95% of the time. The confidence level of 95% is comonly used, though 90 and 99% are also used. The 95% confidence interval is calculated from d_{Diff} $\pm$ 1.96$\cdot s_{Diff}$, which assumes a normal distribution. For the measured pulse pressure data from Figure 8.6, it can be stated that there is 95% confidence the mean difference between the two measurements will lie between the limits d_{Diff} + 1.96$\cdot s_{Diff}$ = $-$0.06 mmHg and d_{Diff} $-$ 1.96$\cdot s_{Diff}$ = 8.68 mmHg, which is plotted in Figure 8.7.

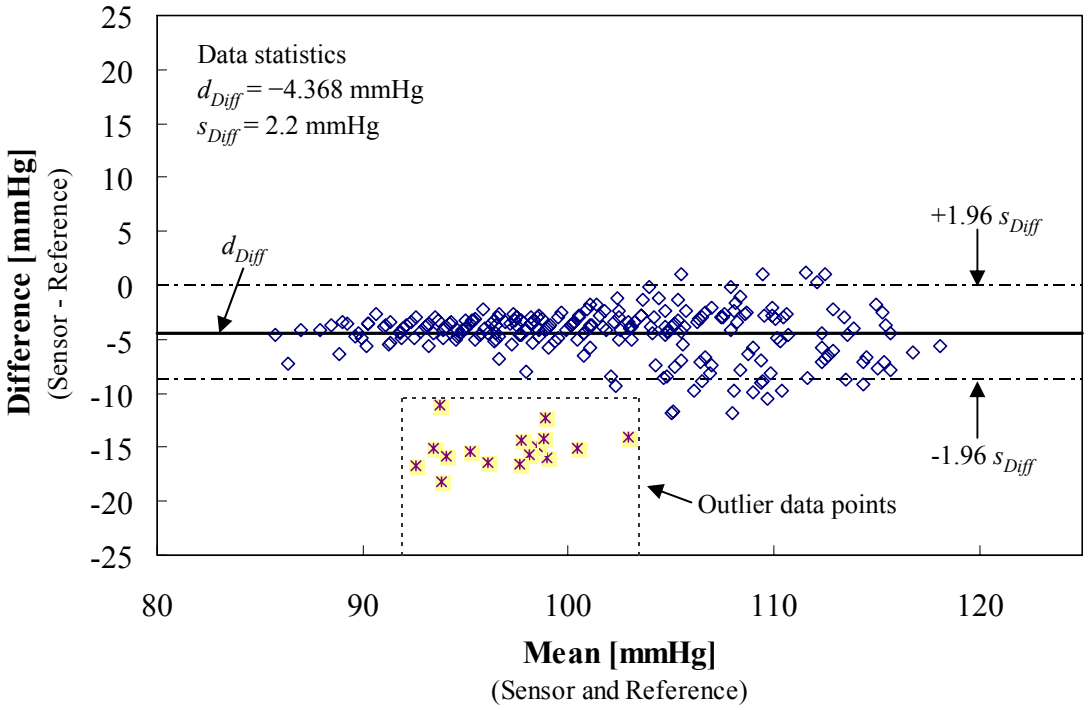

Figure 8.7: Bland and Altman plot of the wired and wireless pressure sensors.

Figure 8.8 illustrates the pulse pressure readings over 41 days for the wired reference and wireless pressure sensors for two animals. The wireless sensor readings were within the

error bars of the reference sensor, indicating low to zero change in response to dynamic pressure changes (pulse pressure). For the first animal, three data points were collected corresponding to 0, 8, and 41 days from implant, with pulse pressures ranging from 12 to 14 mmHg. For the second animal, two data points were collected corresponding to 0 and 33 days from implant with pulse pressures ranging from 14 to 20 mmHg. Figure 8.9 graphs the Bland and Altman plot for all the pulse pressure data for both animals and all time periods. From this plot, the mean pulse pressure difference and standard deviation of the differences are determined to be $d_{Diff} = -0.3755$ mmHg and $s_{Diff} = \pm 3.43$ mmHg respectively. The two measurement methods are in good agreement, demonstrated by the low mean error and the 95% confidence interval limits $d_{Diff} + 1.96 \cdot s_{Diff} = 6.35$ mmHg and $d_{Diff} - 1.96 \cdot s_{Diff} = -7.1$ mmHg, plotted in Figure 8.9.

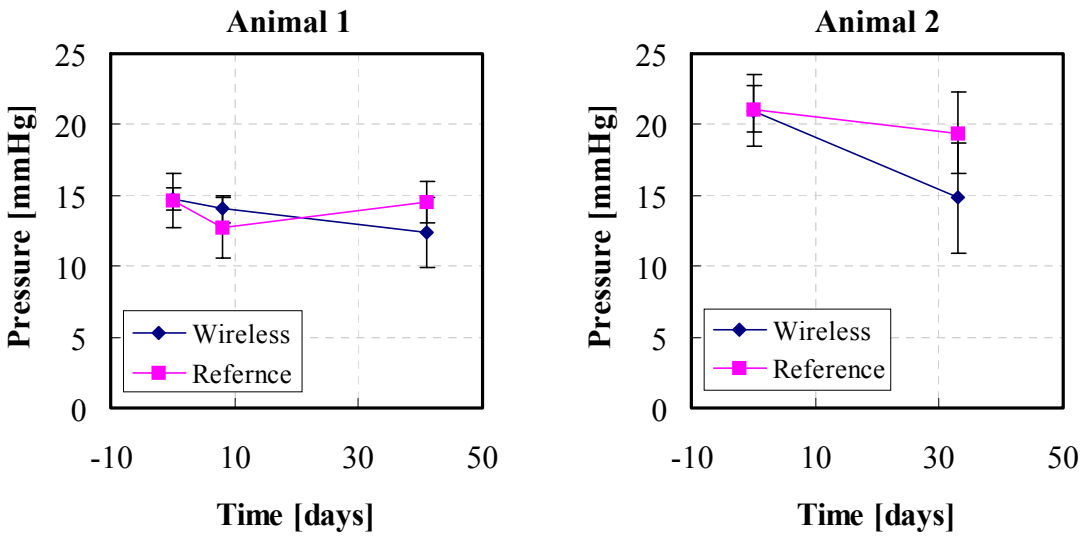

Figure 8.8: Pulse pressure vs. time for animals 1 and 2.

The mean (baseline) frequency drift over the same time period as above is graphed in Figure 8.10. Over the first eight days for animal 1, the mean frequency drifted by -154 kHz, which is equivalent to an increase in pressure of 28.52 mmHg. Beyond six days the mean frequency continued to drift downward, which was observed during bench testing (see Section §7.3 in Chapter 7).

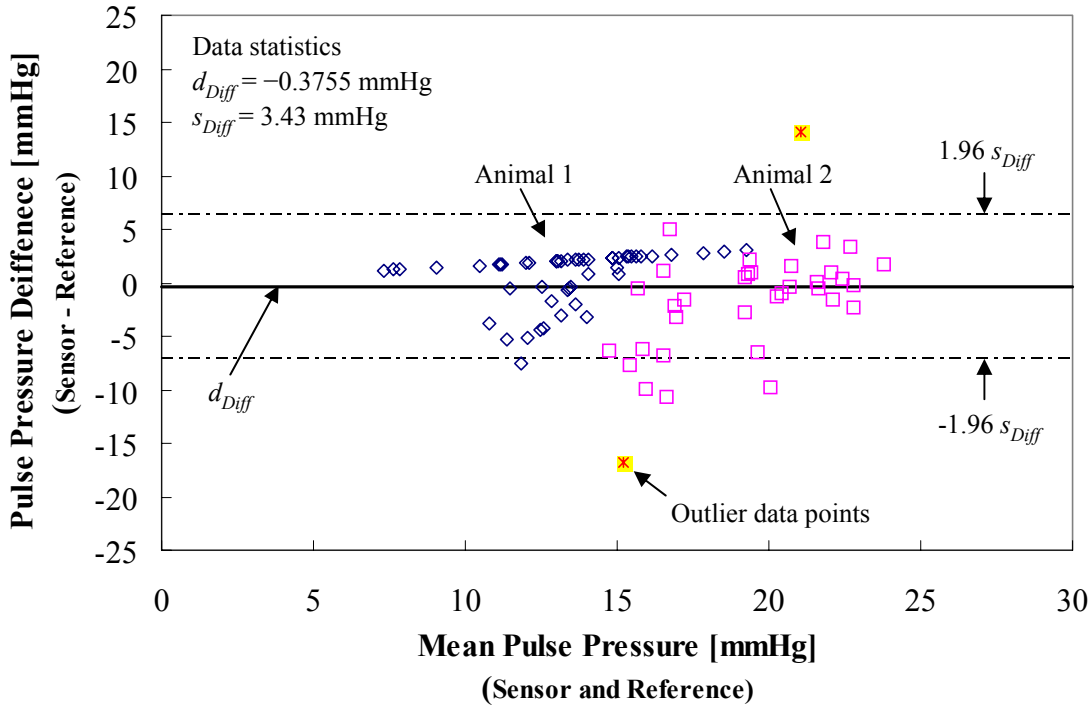

Figure 8.9: Bland and Altman plot of pulse pressure data.

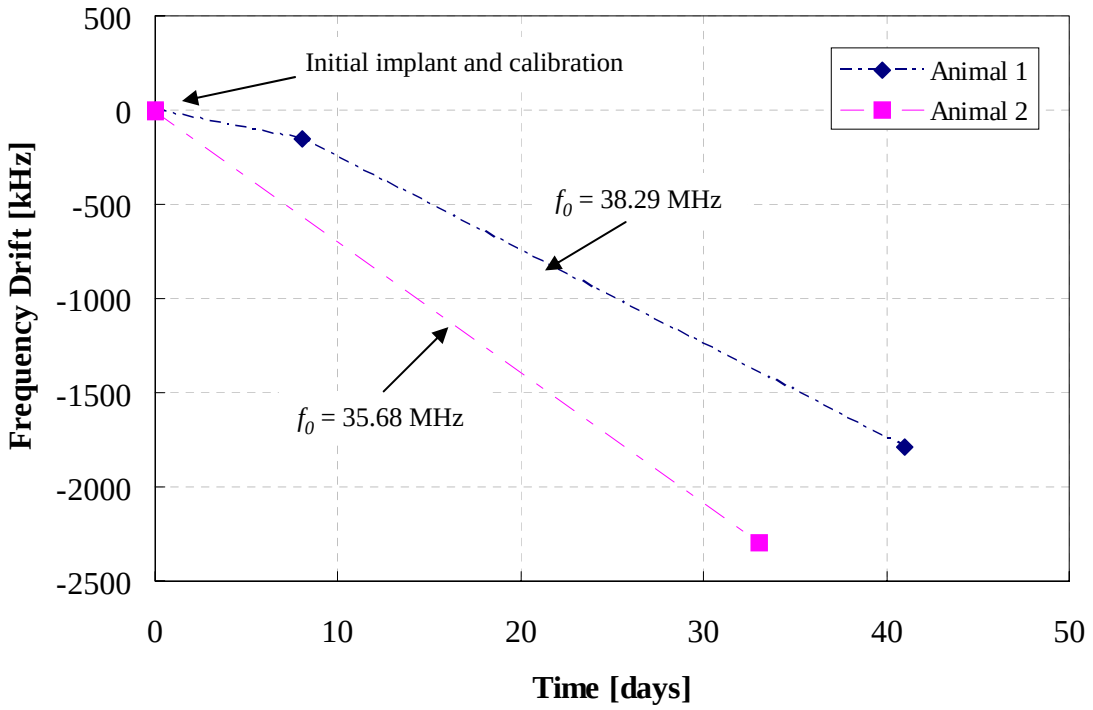

Figure 8.10: Mean resonant frequency drift vs. time for wireless sensor in both animal implants.

8.5 Summary and Conclusions

From the data collected and results presented in Chapter 7, it is clear that the LCP-based sensors are not suitable for applications where an accurate mean pressure reading beyond a few days is important. From Chapter 7, it was expected that the pressure sensivity drift would be larger. However, for the *in vivo* data the pressure sensitivity drift is much lower or insignificant. The difference could be related to the magnitude of the applied pulse pressure. For the bench-testing performed in Chapter 7, the pulse pressure was > 100 mmHg while the pulse pressure measurements from the animials was < 20 mmHg. Since the pressure sensitivity drift for *in vitro* testing in Chapter 7 is derived from the before and after measurements, a pressure sensitivity drift rate could not be defined. Therefore, for the time-frame of the *in vivo* testing of 40 days, it is difficult to determine the amount of pressure sensitivity drift that whould be expected for LCP-based pressure sensors. Although polymer-ceramic-based pressure sensors were not tested *in vivo*, it is possible that based on results from Chapter 7 they would have significantly lower mean pressure drift in applications that required long-term stability.

CHAPTER 9

CONCLUSIONS

9.1 Summary of the Research

Chapter 1 introduced the need for wireless pressure sensing in harsh environments and reviewed the current work done in the area of passive wireless sensing for high temperature and biomedical applications. The chapter concluded with the thesis outline for the developed work.

Chapter 2 developed the sensor concept and modeling. First, the sensor electromagnetic theory was presented, which included a simplified lumped-element model and a more accurate semi-distributed analytical model. Although the model is not fully distributed, it is sufficient to capture most of the dominant effects for this work. Additionally, the analytical model is based on a literature survey of the electrical elements of inductance and capacitance. These form the basis for the electromagnetic model of the sensor. The electromagnetic model was verified through measurement of fabricated devices using both polymer and ceramic substrates. Next, a mechanical model for both circular and rectangular plates was presented and verified against results from Finite Element Analysis (FEA). Then, both the electromagnetic and mechanical models were integrated to form the electromechanical model and establish the pressure-dependent frequency of the LC resonator. Verification of the electromechanical model was achieved throughout the rest of the thesis. The derived model can be used to optimze design configurations implementing multi-layered planar spiral inductors that have distributed capacitances. The effects of temperature, humidity, and loss of dielectric materials used to fabricate the wireless pressure sensors were included.

Chapter 3 presented the design, fabrication, and characterization of high-temperature pressure sensors. This included designs fabricated from low temperature cofireable ceramics LTCC with exposed and embedded circuitry operating up to 450 ℃, as well as high

temperature cofireable ceramics (HTCC) with embedded circuitry operating up to 600 ℃. Devices fabricated from HTCC materials demonstrated feasability, operating in temperature ranges beyond that of conventional silicon-based sensors.

Chapter 4 defined the design space for the development of implantable wireless pressure sensors for biomedical applications. This chapter narrowed the design to a specific telemetry systems, method of delivery into the body, which is based on catheter-deliverability, and operational environment. The chapter concluded with a list of specific requirements for the sensor design. Using the model derived in Chapter 2, designs that achieve these requirements were presented in Chapter 5 and Chapter 6.

Chapter 5 presented the design, fabrication, and characterization of polymer-based pressure sensors fabricated from LCP, Kapton®, and PTFE substrates. These devices had drift characteristics since they were fabricated from non-hermetic monolithic packages. This lead to the development of polymer-ceramice-based pressure sensors presented in Chapter 6.

Chapter 6 presented the design, fabrication, and characterization of polymer-ceramic-based pressure sensors fabricated from PTFE and Zirconia ceramic substrates. Zirconia ceramic substrates were used to create hermetic chambers housing the reference pressure for the pressure sensor and metalized to form the pressure-variable capacitance. These were then embedded within the polymer layers and interconnected to the planar spiral inductors to complete the *LC* circuit. These devices had improved drift performance because of increased stability of the PTFE polymeric substrate and hermetic Zirconia chamber, which was demonstrated in the *in vitro* stability testing presented in Chapter 7.

Chapter 7 presented *in vitro* sensor stability testing in hydrostatic air pressure environments for up to 60 hours, sensor stability testing in hydrostatic saline-fluid environments for up to 1300 hours, and sensor stability under cyclic saline-fluid pressure for over 300 millions pulses (simulating approximately 7 years of pulsation within the human body). In all cases of stability testing, the pressure sensors fabricated from polymer-ceramic substrates

outperformed the polymer-based sensors. Besides bench testing and characterization, the feasibility of the design requirements for operation *in vivo* was presented in Chapter 8.

Chapter 8 presented *in vivo* testing of an LCP-based pressure sensors in a mock-aneurysm in a canine model. At the time of animal protocol approval the PTFE-ceramic-based pressure sensors were still under development. Therefore, these were not available for implantation. Additionally, all the animal testing was performed by CardioMEMS, Inc staff as well as supplied equipment. The appropriate protocols and procedures specified by the Institutional Animal Care and Use Committee (IACUC) were followed. The results of the animal study demonstrated catheter-deliverability of the developed wireless pressure sensors into a mock-aneurysm model in four canines. During and post-implant, continuous wireless pressure data-measurements from within the aneurysms were recorded for a time-frame of approximately 30 days. Both the delivery and continous measurement was succesfully demonstrated in this animal study.

9.2 Future Outlook

The presented work on wireless MEMS pressure sensors demonstrated the feasibility of passive LC resonant circuits packaged in a monolithic housing that servers as the final package and offers the potential to operate them wirelessly in harsh environments (i.e. intrinsically packaged). The designs in this work leveraged existing manufacturing infrastructures found in the microelectronic's ceramic and flex-circuit packaging technologies to batch-fabricate laminated hermetic structures. These were tested in both simulated and actual environments with indications for further operational capabilities.

Improvements can be made to both the fabrication and performance of the wireless pressure sensors. With respect to performance, improved high temperature operation can be achieved through optimized designs to maximize the quality factor of the circuits. This can be achieved through better geometrical design of the spiral-inductors or better material

selection, using improved high-temperature conductors. Improved performance related to drift for biomedical applications can be achieved through material selection and encapsulation of the outermost layer to minimize the penetration of moisture into the polymeric substrate. An alternative could be to use only hermetic materials, if drift stability is the overriding requirement of the biomedical application. Sensors developed in the presented work used Cu metallization, which is not considered biocompatible. Further designs could implement designs implementing different metals such as Au or Ag to increase biocompatibility and reduce corrosion.

In Table 1.3, other types of wireless sensors were presented, including strain, chemical species, humidity, and flow rate. Although this work focused on pressure measurements, LC resonant circuit-designs and the models derived in Chapter 2 could be used to design sensor that measure other physical characteristics. This can be achieved by modulating the frequency, quality factor, or coupling coefficient while taking advantage of an intrinsically packaged device.

APPENDIX A

MODEL DERIVATIONS

A.1 Taylor Series Expansion

To further simplify Eq. (2.22), the Taylor series expansion is derived. First, new terms for Q and k are defined

$$Q' = \frac{1}{Q^2} \tag{A.1}$$

and

$$k' = k^2 \ . \tag{A.2}$$

Therefore, Eq. (2.22) can be re-written as

$$\Omega(Q', k') = \sqrt{\frac{(2 - Q' - k') - \sqrt{(Q' - 2 + k')^2 - 12(k' - 1)}}{2(k' - 1)}} \ . \tag{A.3}$$

The Taylor series expansion for $\Omega(Q', k')$ about $\Omega(0, 0)$ is given as

$$\Omega(Q', k') = \Omega(0,0) + \left[\frac{\partial}{\partial k'}\Omega\Big|_{(0,0)}\right] k' + \left[\frac{1}{2!}\frac{\partial^2}{\partial k'^2}\Omega\Big|_{(0,0)}\right] k'^2 + \left[\frac{\partial}{\partial Q'}\Omega\Big|_{(0,0)}\right] Q' + \left[\frac{1}{2!}\frac{\partial^2}{\partial Q'^2}\Omega\Big|_{(0,0)}\right] Q'^2 + \cdots \ . \tag{A.4}$$

The constants for the partial derivatives in Eq. (A.4) are

$$\begin{aligned} \Omega(0,0) &= 1 \\ \left[\frac{\partial}{\partial k'}\Omega\Big|_{(0,0)}\right] &= 1/4 \\ \left[\frac{\partial}{\partial Q'}\Omega\Big|_{(0,0)}\right] &= 1/8 \\ \cdots &\text{higher order terms} \end{aligned} \tag{A.5}$$

The higher order terms are ignored because they become increasingly smaller compared to the first terms. The expression from Eq. (A.4) and Eq. (A.5), and replacing Q' and k' is therefore

$$\Omega(Q', k') = 1 + \frac{k'}{4} + \frac{Q'}{8} = 1 + \frac{k^2}{4} + \frac{1}{8Q^2} \tag{A.6}$$

Since this equation was derived for $\Omega(Q', k')$ about $\Omega(0, 0)$, it is only valid for small values of k' and Q'. From the definition of k' and Q', it is therefore only valid for small values of k and large values of Q. Since $\Omega = f_{min}/f_0$, the minimum frequency for the phase of the input impedance Z_1 is given as

$$f_{min} = f_0 \left(1 + \frac{k^2}{4} + \frac{1}{8Q^2}\right) \ . \tag{A.7}$$

A.2 Deflection of a Circular plate

Circular plate deflection is given by

$$d_0 = \frac{Pa^4}{64D} \underbrace{\frac{1}{1 + 0.488\left(\frac{d_0}{t_m}\right)^2}}_{\text{Stretching Factor}} \ . \tag{A.8}$$

Solving for d_0 and selecting the real roots gives

$$\begin{aligned} d_0 &= \frac{0.0000677681K_x}{D} - \frac{10079.4Dt_m^2}{K_x} \\ K_x &= \sqrt[3]{5.14391e^{10}a^4D^2Pt_m^2 + \sqrt{2.64598e^{21}a^8D^4P^2t_m^4 + 3.29021e^{24}D^6t_m^6}} \ . \end{aligned} \tag{A.9}$$

A.3 Deflection of a Rectangular plate

The deflection is defined by the sum of two loads, one for bending and one for stretching, given by

$$P = \underbrace{\frac{Dd_0}{0.0026a^4}}_{\text{Bending}} + \underbrace{\left(\frac{d_0}{0.401a}\right)^3 \frac{2Et_m}{a}}_{\text{Stretching}} \ . \tag{A.10}$$

Next, a solution for d_0 is reached by selecting the real roots, resulting in

$$\begin{aligned} d_0 &= \frac{221.562a^4P(Et_m)^2 + 0.00853\sqrt{G_x} - 484.585DEt_mH_x^{1/3}}{Et_mH_x^{2/3}} \\ G_x &= (Et_m)^3(1.834D^3 + 6.747e^8a^8P^2Et_m) \\ H_x &= 25975a^4P(Et_m)^2 + \sqrt{G_x} \ . \end{aligned} \tag{A.11}$$

A.4 Transfer Function for Lumped Element Model

To evaluate the interrogation effects of Q and k between the sensor and selected telemetry electronics used for *in vivo* experimental studies, the transfer function for the circuit shown in Figure A.1 is derived from The transfer function for a systems can be derived from

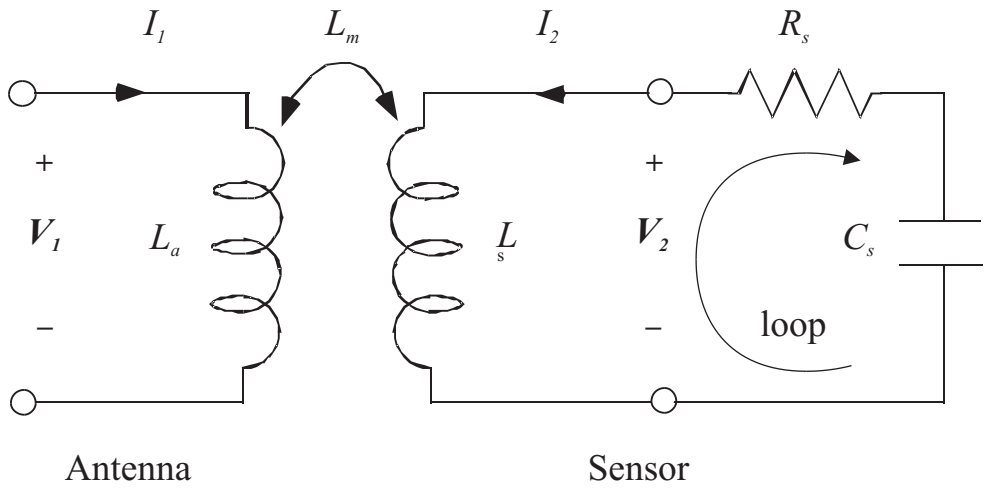

Figure A.1: Lumped element model for an inductively coupled system containing a loop antenna and a sensor.

$$Y(s) = H(s)X(s) \ , \tag{A.12}$$

where $s = \sigma + j\omega$ is the Laplace Transform, $Y(s)$ is the output signal of interest, $X(s)$ is the input and $H(s)$ is the transfer function. Solving for $H(s)$ gives

$$H(s) = \frac{Y(s)}{X(s)} \ . \tag{A.13}$$

From the circuit in Figure A.1, the desired output $Y(s) = V_2(s)$ and the input $X(s) = V_1(s)$. Then, the transfer function becomes

$$H(s) = \frac{V_2(s)}{V_1(s)} \ . \tag{A.14}$$

The voltages V_1 and V_2 from Figure A.1 are given by

$$V_1(s) = sL_aI_1 + sL_mI_2 \tag{A.15}$$

$$V_2(s) = sL_mI_1 + sL_sI_2 \ . \tag{A.16}$$

Using Kirchhoff's voltage law, the loop equation around the sensor is given by

$$-R_s I_2 - V_2 - \frac{1}{sC_s} I_2 = 0 \ . \tag{A.17}$$

Solving for I_2 in terms of I_1 by replacing V_2 in Eq. (A.17) with Eq. (A.16) yields the expression

$$I_2 = -\frac{C_s I_1 L_m s^2}{1 + C_s R_s s + C_s L_s s^2} \ . \tag{A.18}$$

Replacing I_2 in Eq. (A.15) and Eq. (A.16) with (A.18) yields

$$V_1(s) = I_s s \left(L_a - \frac{C_s L_m^2 s^2}{1 + C_s s (R_s + L_s s)} \right) \tag{A.19}$$

$$V_2(s) = I_1 \left(\frac{L_m s (1 + C_s R_s s)}{1 + C_s (R + L_s s)} \right) \ . \tag{A.20}$$

The transfer function $H(s)$ is calculated by substituting Eq. (A.19) and (A.20) in Eq. (A.14), which gives the expression

$$H(s) = \frac{V_2}{V_1} = \frac{L_m + C_s L_m R_s s}{L_a + C_s L_a R_s s + C_s (L_s L_a - L_m^2) s^2} \ . \tag{A.21}$$

The coupling coefficient k, quality factor Q, and resonant frequency f_0 are given by

$$k^2 = \frac{L_m^2}{L_s L_a} \tag{A.22}$$

$$Q = \frac{\omega_0 L_s}{R_s} = \frac{1}{\omega_0 R_s C_s} \tag{A.23}$$

$$\omega_0^2 = (2\pi f_0)^2 = \frac{1}{L_s C_s} \ . \tag{A.24}$$

Substituting Eq. (A.22), Eq. (A.23), and Eq. (A.24) in (A.21) and simplifying yields the transfer function

$$H(s) = k \sqrt{\frac{L_s}{L_a}} \left(\frac{\omega_0 s + Q \omega_0^2}{(1 - k^2) Q s^2 + s \omega_0 + Q \omega_0^2} \right) \ . \tag{A.25}$$

APPENDIX B

FABRICATION PROCESSES

B.1 LTCC Fabrication Processes

B.1.1 Exposed Circuitry Sensors

(Note: this process was used to fabricate devices in [5])

1. Cut 2.5"x2.5" blank sheets of ceramic tape.
2. Cut alignment holes using the die set, shown in Figure B.2(b).
3. Clean with methanol 3"x3" sheets of aluminum foil. Use die set to create alignment holes for press blocks. The foil is used to prevent the green sheets from sticking to the press blocks.
4. For the top section, laminate layers together to form the top diaphragm (if one sheet is used omit steps 4-6). Align the stack of sheets and foil in the press blocks, illustrated in Figure B.2(a).
5. Laminate top sections together in a vacuum press. The press platens are heated to 70 ℃. The press mold is centered in the platens. The vacuum is turned on prior to pressing. Set the force to 3000 psi (e.g., 9.38 tons for 6.25 in^2). Laminate for five minutes, vent chamber, and rotate samples 180°, then reseal and repeat process for another five minutes. Remove sheets from press blocks and peel aluminum foil.
6. Repeat steps 4 and 5 for the bottom sections.
7. For the inner sections, punch holes using the die set for both the alignment holes and center cavity hole. If multiple inner layers are used, laminate using step 5.
8. Align the top, inner section, and bottom section in the press blocks; ensure aluminum foil is between the ceramic sheets and press blocks. Laminate using procedure described in step 5. After lamination, remove from press blocks, peel aluminum foil, and trim edges (approximately 1/4").
9. Place laminated sections on a silicon substrate and then put in the box furnace. Sinter ceramic in air for 30 minutes at 500 ℃ (5 ℃ min^{-1} ramp rate) to bake off the organics and then for 20 minutes at 850 ℃ (5 ℃ min^{-1} ramp rate) to melt the glass particles and harden the sample [94].
10. After cooling remove from furnace.
11. Fabricate custom screen (mesh size 200 with 1 mil thick emulsion, Rigsby Screens) with circuitry pattern.

12. Clamp the screen on the screen printer.
13. Place the sensors on the vacuum chuck on the screen printer. Lower the screen temporarily and align the sensor prior to turning on the vacuum.
14. Load the screen with silver ink paste and set the squeegee force to 2.25. Screen-print the pattern onto the substrate.
15. Soft-bake in oven for 5 minutes at 120 ℃.
16. Repeat steps 12-15 for the bottom capacitor electrode.
17. Use a syringe to spread a bead of ink from the bottom electrode to the outer most winding of the coil.
18. Soft-bake in oven for 5 minutes at 120 ℃.
19. Cure the ink in a furnace by heating to 800 ℃ at 10 ℃ min^{-1} and dwell for 30 minutes.
20. Sample is ready for testing.

B.1.2 Embedded Circuitry Sensors

(Note: Improved process for multi-layered LTCC fabrication processes)

1. Cut 6"x6" section of ceramic tape from the roll. Leave ceramic on acrylic backing material.
2. Load section of ceramic onto IR Laser chuck on the XY motion stage.
3. Use the IR Laser to cut the sheets to achieve alignment holes, via holes, and cavity holes, illustrated in Figure B.1. The laser is used to cut the sheets to achieve a greater level of alignment accuracy for multi-layer fabrication processes. This process cuts the ceramic and acrylic backing material. Leave ceramic sections on the backing material for use as support during screen-printing of green ceramic tape.
4. Peel away chads left in holes from the laser process for all sections.
5. Fabricate custom screen (mesh size 200 with 1 mil thick emulsion, Rigsby Screens) with circuitry pattern (inductor-coil interconnected to capacitor electrodes). Due to symmetry, the same screen can be used for the top and bottom sections.
6. Fabricate custom vacuum chuck with alignment holes (aligns with press blocks) for the screen printer. This is needed for multi-layered screen-printing processes.
7. Clamp the screen on the screen printer.
8. Lower the screen and align with vacuum chuck alignment holes. Raise screen back to default position.

9. Place the un-sintered top section (still on acrylic backing material) on the vacuum chuck and align to the vacuum chuck.

10. Load the screen with silver ink paste and set the squeegee force to 2.25. Screen-print the pattern onto the substrate. Adhesion of the ceramic tape to acrylic backing material, which is held down by vacuum, prevents the ceramic from lifting during the printing process.

11. Soft-bake sample in oven for 5 minutes at 120 ℃.

12. Repeat steps 7-11 for the bottom section.

13. Peel inner section from acrylic backing material. Align the bottom and inner sections in the press blocks; bottom is still on acrylic backing material. Also, ensure aluminum foil is between the ceramic sheets and press blocks.

14. Laminate using procedure step 5 described above in §B.1.1.

15. Let cool, then peel away aluminum foil from inner section.

16. Fabricate custom stencil from brass or stainless steel with alignment holes (same as press blocks) and via holes.

17. Load stencil on press block alignment pegs. Use blade to squeegee ink through via hole. Soft-bake sample in oven for 5 minutes at 120 ℃.

18. Load top section onto press blocks. Ensure aluminum foil is between the ceramic sheets and press blocks.

19. Laminate all three sections together using procedure step 5 described above in §B.1.1 except without vacuum. The vacuum is not used in order to decrease the amount of deflection of the green membranes. After lamination, remove from press blocks, peel aluminum foil and trim edges (approximately 1/4").

20. Sinter sample using procedure step 9 described above in §B.1.1.

21. After cooling remove from furnace.

22. **Note:** Sample is ready for testing if not implementing evacuation channel.

23. Using CTE matched glass frit powder (ELAN number 19 glass frit), fill the evacuation channel. Ensure sufficient powder is used because it will shrink significantly.

24. Place sample in tube furnace (capable of vacuum) and seal tube.

25. Turn on vacuum pump and heat up furnace to 790 ℃ (2 ℃ min^{-1} ramp rate), past the melting temperature of the glass frit. Dwell for 30 min to ensure full melting of the frit, then allow to cool.

26. Remove sample from furnace. Sample is ready for testing.

B.1.3 Embedded Multi-Layer-Inductor Sensors

1. Repeat procedure steps 1-4 from above in §B.1.2.
2. Fabricate custom screen (mesh size 200 with 1 mil thick emulsion, Rigsby Screens) with circuitry pattern (inductor-coil interconnected to capacitor electrodes). Due to asymmetry and placement of vias, all four screens need to be fabricated, the two outer coils and the two inner coils.
3. For the next steps, repeat procedures 7-21 above in §B.1.2 to complete the screen-printing, lamination, and sintering of all four coil layers and three via interconnects.
4. After sintering, the sample is ready for testing.

B.2 HTCC Fabrication Processes

1. Repeat procedure steps 1-19 from above in §B.1.2.
2. Place laminated sections on an alumina setter-plate substrate (pre-sintered) and then place in the box furnace. Sinter ceramic in air for 30 minutes at 500 ℃ (5 ℃ min^{-1} ramp rate) to bake off the organics and then for 60 minutes at 1500 ℃ (5 ℃ min^{-1} ramp rate) to sinter the ceramic. Then let cool at 5 ℃ min^{-1} ramp rate or slower.
3. Follow steps 21-25 from above in §B.1.2.
4. The sample is ready for testing.

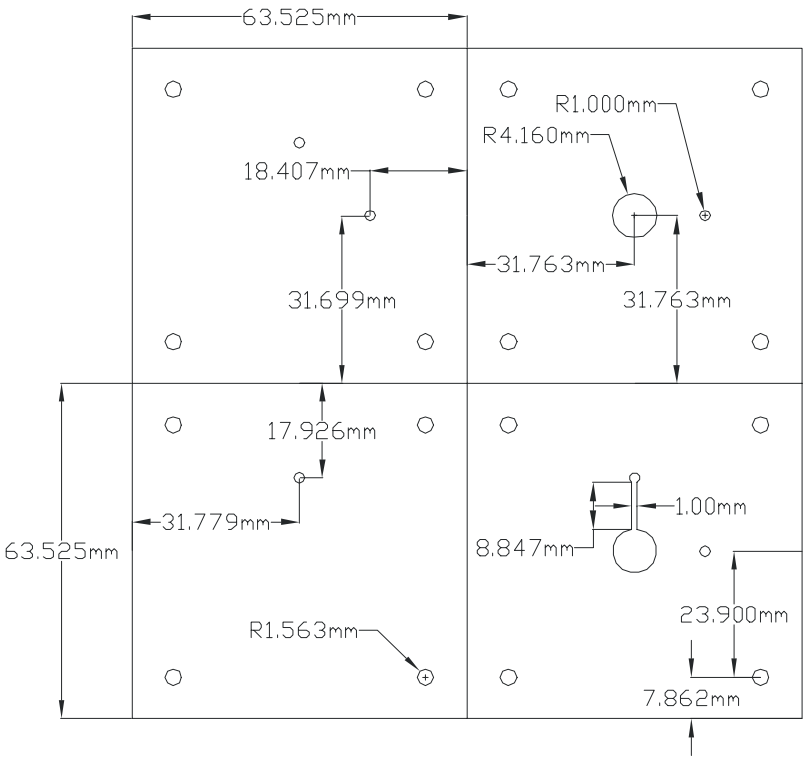

Figure B.1: Schematic layout for laser cutting green sheets of LTCC or HTCC tape.

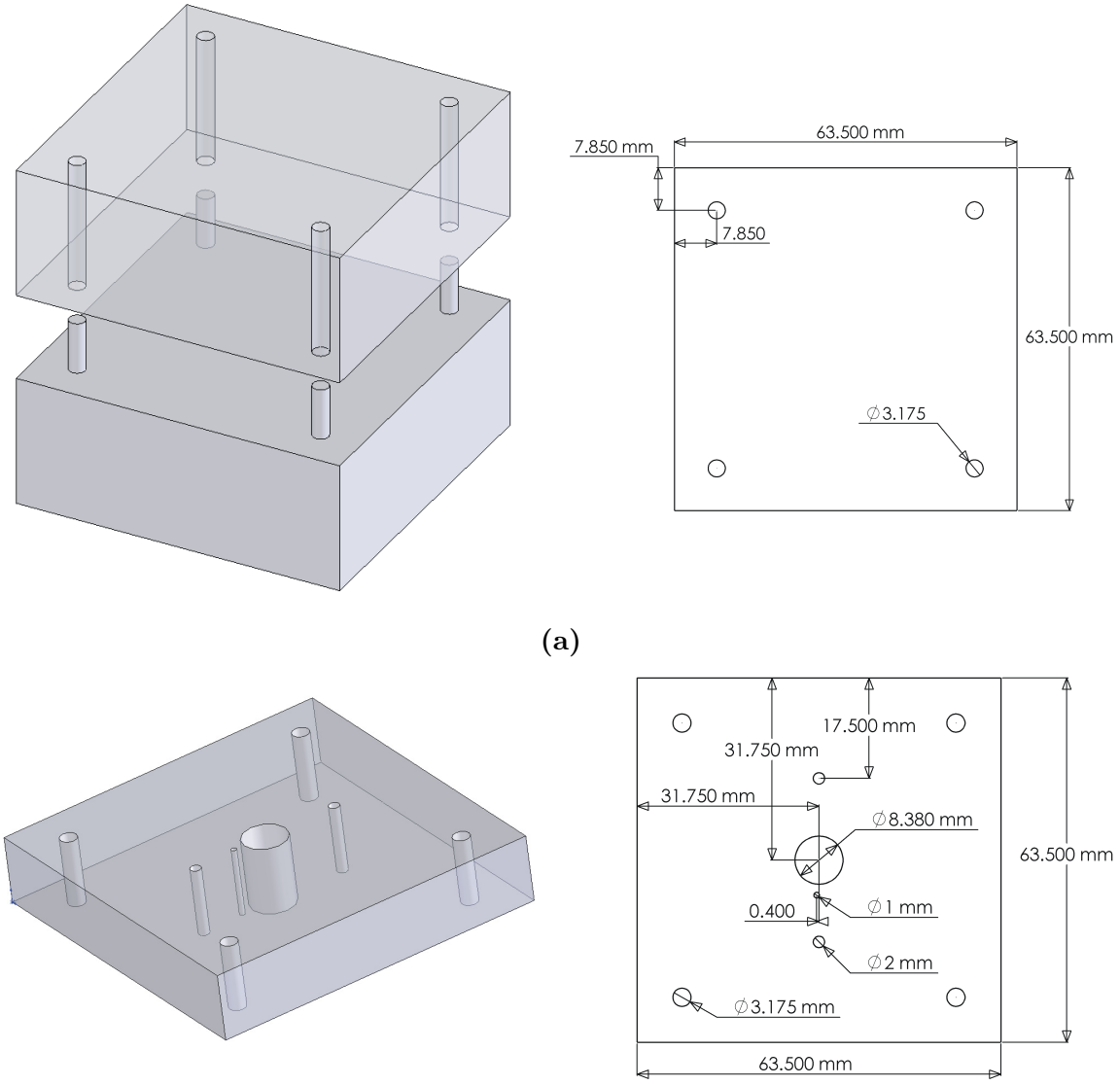

Figure B.2: Example of a press block with alignment pegs (a) and a die set (b).

B.3 Polymer Fabrication Processes

B.3.1 LCP-based Sensors

B.3.1.1 Photolithography

1. Cut LCP copper clad film to 4"x4" sheets.
2. Clean sheets by rinsing them in acetone, then methanol, and DI water. Then soak sheets in a 10:1 HCL solution for 2 minutes. Next, rinse in DI water, and finally dry with nitrogen gas.
3. The samples are mounted on 4"x4" glass plate. The sheets are secured to the glass plate to support the film during processing in the next steps.
4. Spin coat first layer of Shipley 1827 photoresist by placing the sample on the spinner. The spinner is programed to use two stages. The first stage is set to 700 rpm and lasts 5 seconds. The second stage is set to 2000 rpm and lasts 30 seconds. The sample is air dried for 5 minutes.
5. Spin coat the second layer of Shipley 1827 photoresist using the same settings as in the previous step.
6. Bake sample in an oven at 100 ℃ for 3 minutes.
7. Expose the photoresist using the OAI mask aligner. The mask layout is illustrated in Figure B.4. Then the sample is developed.
8. A bath of $FeCl_3$ solution is used to etch the copper from the film. Next, the sample is rinsed in DI water.
9. Samples are ready for lamination.

B.3.1.2 Lamination and Laser cutting Processes

1. Preheat Carver press (Figure C.1b) platens to 200 °F.
2. Assemble the outer and inner sheets on the press blocks. Ensure that there is aluminum foil between the polymer film and press blocks (Figure B.6). The inner SpeedBoard® sheets are laser cut using an excimer laser system (Figure C.5) using the cavity designs discussed in §5.1 illustrated in Figure B.3. The LCP copper cladding is processed using the photolithography steps above and patterned with the mask layout illustrated in Figure B.4; also, both outer sheets use the same mask.
3. Place the press blocks between the platens of the Carver press. Close the gap between the platens until they are in contact with press blocks.
4. Allow for the press blocks and film to reach the starting temperature of 200 °F.

5. Ramp temperature to 356 °F.
6. At 356 °F apply 1000 lbs of force (approximately 60 PSI) for 45 minutes.
7. Ramp temperature to 428 °F.
8. At 428 °F, apply 2500 lbs of pressure (approximately 155 PSI) for 1 hour.
9. Cool down platens to 400 °F naturally under constant force of 2500 lbs.
10. Actively cool down platens to 200 °F.
11. Remove press blocks from platens and let cool to room temperature.
12. Once cool, remove laminated sheets from press blocks. Carefully peel away aluminum foil.
13. Laser cut sensors with the excimer laser system using outline in Figure B.5.
14. Devices are ready for testing or silicone coating (§B.3.2).

B.3.2 Silicone Coating Process

Two methods of silicon coating were implented. Initially, devices were coated with medical grade silicone using a dip-coating method. Then, this was performed externally by Polyzen, Inc, a specialy medical device manufacturer with silicone dip-coating capabilities. Polyzen's methods improved uniformity, coverage, and reduced the number defects.

B.3.3 Polyimide-based Sensors

B.3.3.1 Photolithography

1. Follow photolithography steps described above in section §B.3.1.1 using mask layout equivalent to Figure B.4.
2. The sheets are for lamination.

B.3.3.2 Lamination and Laser cutting Processes

1. Preheat Carver press (Figure C.1b) platens to 250 °F.
2. Assemble the outer and inner sheets on the press blocks. Ensure that there is aluminum foil between the polymer film and press blocks (Figure B.6). The inner Kapton® and Pyralux® sheets are laser cut using an excimer laser system (Figure C.5) using the cavity designs discussed in §5.1 illustrated in Figure B.3. The Kapton® copper cladding is processed using the photolithography steps above and patterned with the mask layout illustrated in Figure B.4; also, both outer sheets use the same mask.
3. Place the press blocks between the platens of the Carver press. Close the gap between the platens until they are in contact with press blocks.
4. Allow for the press blocks and film to reach the starting temperature of 250 °F.
5. Ramp temperature to 395 °F.
6. At 375 °F, apply 1000 lbs of force (approximately 60 PSI) for 10 minutes.
7. Ramp temperature to 395 °F.
8. At 395 °F, apply 5500 lbs of pressure (approximately 300 PSI) for 1 hour.
9. Cool down platens to 250 °F naturally under constant force of 5500 lbs.
10. Actively cool down platens to 100 °F.
11. Remove press blocks from platens and let cool to room temperature.
12. Once cool, remove laminated sheets from press blocks. Carefully peel away aluminum foil.
13. Laser cut sensors with the excimer laser system using outline in Figure B.5.
14. Devices are ready for testing or silicone coating (§B.3.2).

B.3.4 PTFE-based Sensors

B.3.4.1 Photolithography

1. Follow photolithography steps described above in section §B.3.1.1 using mask layout equivalent to Figure B.4.
2. The sheets are for lamination.

B.3.4.2 Pre-Lamination Processes

1. The PTFE copper cladding is processed using the photolithography steps above and patterned with the mask layout equivalent to that illustrated in Figure B.4; also, both outer sheets use the same mask.
2. The inner FEP and PTFE sheets are laser cut using a CO_2 laser (10.6 μm wavelength) or die-cut with a die set to achieve accurate cavity dimensions.
3. The inner PTFE sheet is treated with FluoroEtch® in an oxygen free environment to activate the surface prior to lamination.
4. The sheets are ready for assembly.

B.3.4.3 Lamination and Laser cutting Processes

1. Preheat Carver press (Figure C.1b) platens to 75 ℃.
2. Assemble the outer and inner sheets on the press blocks. Ensure that there is aluminum foil between the polymer film and press blocks (Figure B.6).
3. Place the press blocks between the platens of the Carver press. Close the gap between the platens until they are in contact with press blocks.
4. Allow for the press blocks and film to reach the starting temperature of 265 ℃.
5. Ramp temperature to 265 ℃.
6. At 265 ℃, apply 420 kPa of force (approximately 60 PSI) for 60 minutes.
7. Cool down platens to 75 ℃.
8. Remove press blocks from platens and let cool to room temperature.
9. Once cool, remove laminated sheets from press blocks. Carefully peel away aluminum foil.
10. Laser cut using a CO_2 laser system using outline in Figure B.5.
11. Devices are ready for testing or silicone coating (§B.3.2).

B.3.4.4 Polymer-based fabrication masks, press-blocks, and device outlines

This section includes the masks, laser outlines and layouts, and press-blocks for polymer-based pressure sensors.

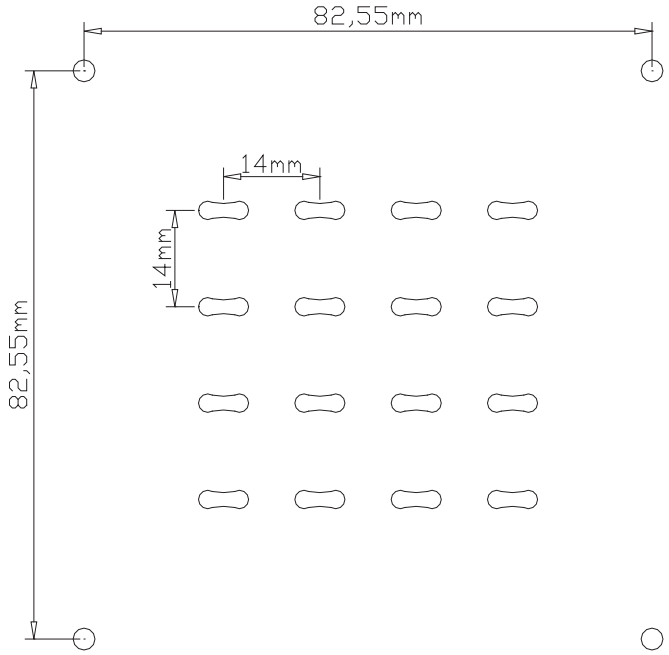

Figure B.3: Example layout of cavity patterns for laser cutting SpeedBoard® used to create inner layer bonding film.

B.4 Polymer-Ceramic Fabrication Processes

B.4.0.5 Photolithography

1. Follow photolithography steps described above in section §B.3.1.1 using mask layout equivalent to Figure B.4.

2. The sheets are for lamination.

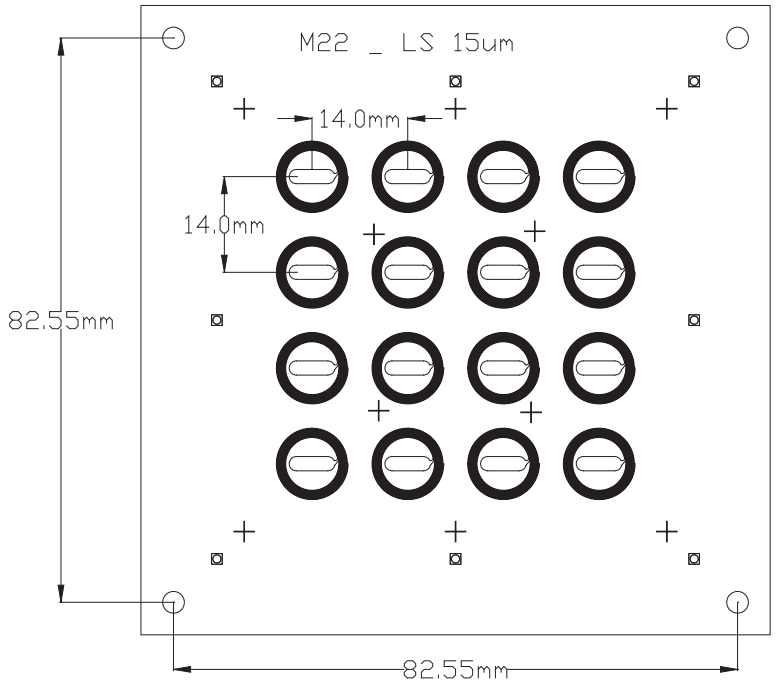

Figure B.4: Mask layout for circuitry used to perform photolithography on LCP copper cladding.

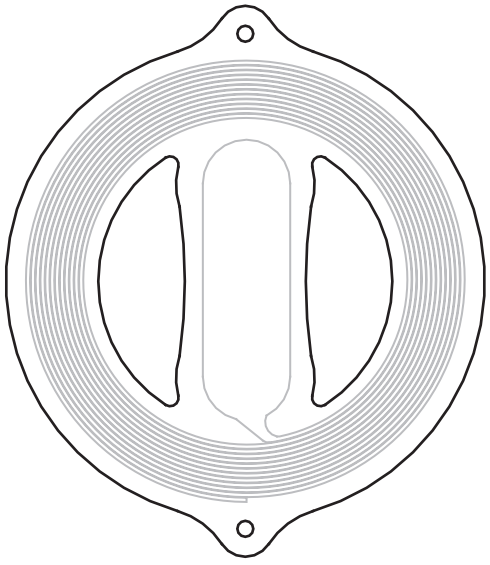

Figure B.5: Sensor outline for laser cutting process to achieve shapes capable of minimally invasive catheter-based delivery.

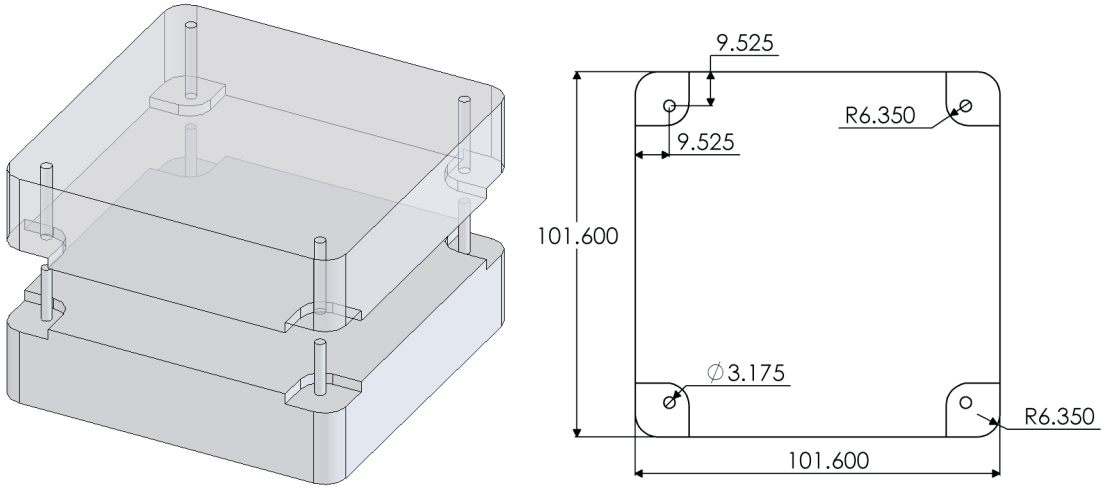

Figure B.6: Press block with alignment pegs used for lamination of polymer-based films. The recessed section near the alignment pegs eliminate pressure force from being applied during lamination. This ensures that there is little to no adhesion between the laminated film and pegs.

B.4.0.6 Ceraic Hermetic Chamber Fabrication

1. Repeat procedure steps in section §B.1.1 from above in to prepare green Zirconia ceramic sheets. Thesre are approximately 1.5 inches square.
2. The cavities are laser-cut using an IR laser system (Nd:YLF infrared) to achieve various configurations. Generally the layout was a $3x2$ array pattern.
3. Most designs implemented a 3-sheet stack, each sheet with a thickness between 25-35 μm. These were assembled and laminated in a press at 70 ℃ with 500 lbs of force for 10 minutes.
4. After lamination, the sheets were sintered at 1450 ℃ for 60 minutes.
5. Next, a seed layer of chrom-copper is sputter deposited.
6. Photolithography was used to pattern ≈ 10 μm thick resist molds.
7. Electrodeposition of copper was used to deposit the copper metal electrodes that formed the capacitor electrodes of the ceramic chamber.
8. After electrodeposition, the seed layer was removed using wet-chemical etching.
9. Next, the chambers were idividualized using the same infrared laser systems.
10. The chambers are ready for assembly.

B.4.0.7 Pre-Lamination Processes

1. The PTFE copper cladding is processed using the photolithography steps above and patterned with the mask layout equivalent to that illustrated in Figure B.4; also, both outer sheets use the same mask.
2. The inner FEP and PTFE sheets are laser cut using a CO_2 laser (10.6 μm wavelength) or die-cut with a die set to achieve accurate cavity dimensions.
3. The inner PTFE sheet is treated with FluoroEtch® in an oxygen free environment to activate the surface prior to lamination.
4. The sheets are ready for assembly.

B.4.0.8 Lamination and Laser cutting Processes

1. Preheat Carver press (Figure C.1b) platens to 75 ℃.
2. Assemble the outer and inner sheets and ceramic chambers on the press blocks. Ensure that there is aluminum foil between the polymer film and press blocks (Figure B.6).
3. Place the press blocks and a stainless steel bag. The bag is sealed with a single outlet port. The port was used to pull vacuum during the entire lamination process.
4. Place the press blocks/bag between the platens of the Carver press. Close the gap between the platens until they are in contact with press blocks.
5. Allow for the press blocks and film to reach the starting temperature of 265 ℃.
6. Ramp temperature to 280 ℃.
7. At 280 ℃, apply 420 kPa of force (approximately 60 PSI) for 60 minutes.
8. During this time, the FEP and solder melts. Additionally, the vacuum removes any trapped gas between the polymer layers.
9. Cool down platens to 75 ℃ and remove vacuum system.
10. Remove press blocks from platens and let cool to room temperature.
11. Once cool, remove laminated sheets from press blocks. Carefully peel away aluminum foil.
12. Laser cut using a CO_2 laser system using outline in Figure B.5.
13. Devices are ready for testing or silicone coating (§B.3.2).

APPENDIX C

FABRICATION AND TEST EQUIPMENT

C.1 Fabrication Equipment

- Wabash 15-50VH Press (Figure C.1a)
- Carver Press (Figure C.1b)
- Blue M Box Oven model 0V-12A (Figure C.2)
- Lindberg Blue Box Furnace 51848A
- Crystal Mark Screen Printer Model 35 (Figure C.3)
- IR (Nd:YLF) Laser System (Figure C.4)
- Excimer Laser System (Figure C.5)
- CO_2 Laser System
- Resist spin coater
- Mask Aligner (OAI)

C.2 Test Equipment

- Agilent Network Analyzer E5100A
- HP4194A Impedance Analyzer (Figure C.6)
- Keithley LCZ Meter 3322
- Cole-Parmer peristaltic pump, digital drive 0-600 rpm
- Omega temperature reader and probe
- Temperature controlled water bath
- Setra pressure gauge Model 204, 0-25 PSIA
- GPIB PC with LabVIEW software
- Mensor Pressure Controller Figure C.7
- High temperature and pressure test system (Figure 3.14b)

(a) (b)

Figure C.1: Wabash 15-50VH Press (a) and Press (b).

Figure C.2: Blue M Box Oven model 0V-12A.

Figure C.3: Crystal Mark Screen Printer Model 35.

Figure C.4: IR Laser System.

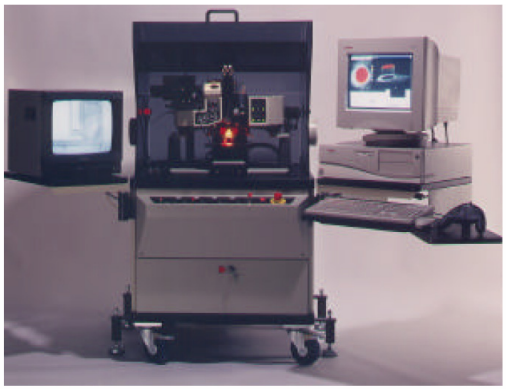

Figure C.5: Excimer Laser System.

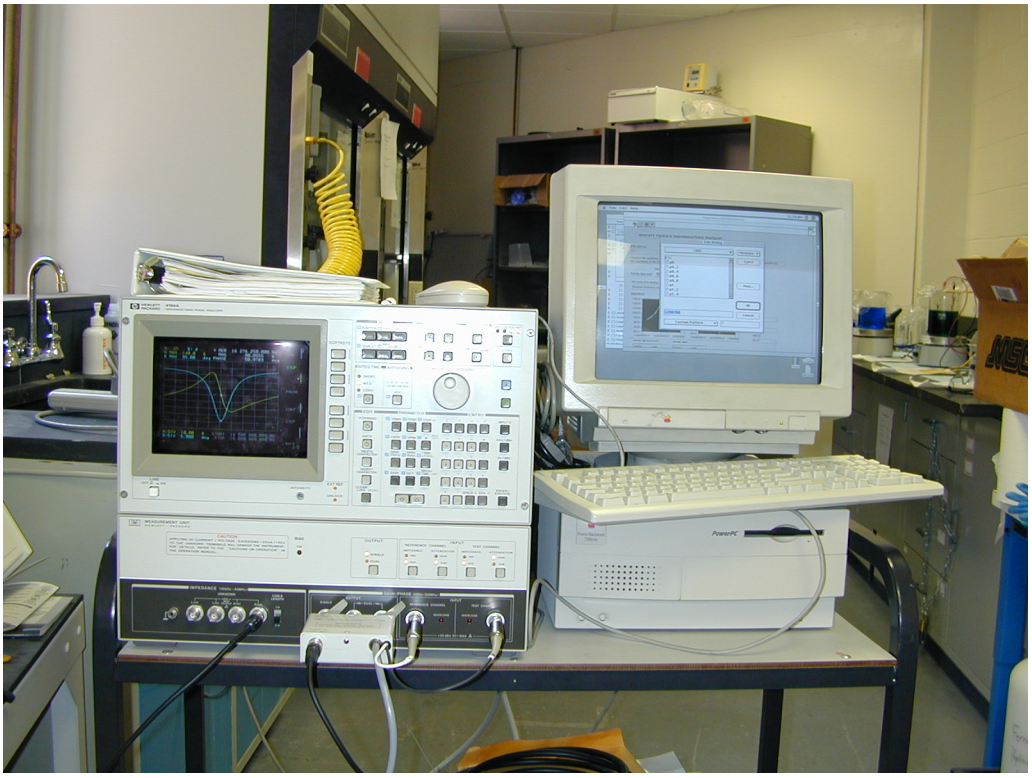

Figure C.6: HP4194A Impedance Analyzer connected through GPIB to computer for data acquisition.

Figure C.7: Mensor PCS400 Pressure controller. Range of 0-2000 mmHg (absolute) with 0.025% F.S. accuracy.

APPENDIX D

NUMERCIAL SIMULATIONS IN MATLAB

The following code was written in MATLAB. The exact code might have varied from one sensor design to another.

D.1 Electromagnetic Analytical Model

In Listing 1,

```
%%%% Element Calculation
%%% Modified 6-2-07


clc
clear all


%%% Calc Circuit Elements
%%% Material Properties

mu = 4*pi*1e-7;
eo = 8.854e-12;
omega=2*pi*30.34e6;

%% Speed Board
erSB = 2.6;
lossSB = 0.004;
%% LCP
erLCP = 2.9;
lossLCP=0.0025;
%% Kapton
erK = 3.7;
lossK = 0.0014;
%% LF1500 Acrylic
erLF = 3.8;
lossLF = 0.03;
%% PTFE
erPTFE = 2.06;
lossPTFE = 0.0008;
%% FEP
```

```
erFEP = 2.06;
lossFEP = 0.0008;
%% Deionized H2O
erDWater = 80;
lossDWater = 2e-4/omega/erDWater/eo;
%% Saline
erSaline = 80;
lossSaline = 1/omega/erSaline/eo;

erM = [erK erLF erSB erLCP erPTFE erFEP erDWater erSaline];
lossM = [lossK lossLF lossSB lossLCP lossPTFE lossFEP
   lossDWater lossSaline];

%%%%%%%%%%%%%%%%%%%%%%%%%%%%%%%%%%%%%%%%%%%%%%%%%%%%%%%%
%% Mask Design
%% Inductor Dimensions %%%

ri = 3.8e-3; %4.296e-3; %3.80e-3./2;
Din = 2.*ri;

width = 54.5e-6; %54.5e-6; %437e-6; %54.5e-6;
ls = 66.7e-6; %66.7e-6; %427e-6; %66.7e-6;
lt = 17e-6; %30e-6; %17e-6;

ppr = 60;

w = width;
s = ls;
pitch = s+w;

%% Capacitor Dimensions
PlateAreaTef = 13.92e-6;
PlateAraLCP = 13.1e-6;
gapPTFE106 = 110e-6; %97e-6; %97e-6;

%%% Cu electrical properties %
resistivity = 1.72e-8; %Ohm-m Cu
conductivity = 1/resistivity; %1/Ohm-m Cu
Rsheet = 1./conductivity./lt;
Rss = Rsheet;

SkinDepth = sqrt(2/omega/mu/conductivity);

%%%%%%%%%%%%%%%%%%%%%%%%%%%%%%%%%%%%%%%%%%%%%%%%%%%%%%%%

%%% Test Freq with PTFE sensor

%Nt = [4 6 8 10 12 14 15 16 17 20 22 24 26 28 30];
```

```
%Nt = [2 4 6 8 10 12 14 16 18 20];
%Nt = 15;
%Nt = 2:1:100;
Nt = 10:1:20;

for idx=1:length(Nt)
    Dint = Din;
    Doutt = Din + 2.*(pitch.*Nt(idx));
    Davgt = (Dint + Doutt)./2;
    ppt = (Doutt - Dint)./(Doutt + Dint);

    %%%%%%%%%%%%%% DEFINE SPIRAL GEMOETRY %%%%%%%%%%%%%%%
    ainc = 2.*pi./ppr;
    hinc = pitch./ppr;
    ang = 0;

    jx = 0:1:(ppr);
    rstart = 1.*((ri + w./2) + Nt(idx).*pitch);

    rii = ri;
    for ix = 0:1:(Nt(idx)-1);

        x(ix+1,:) = ((rii + (pitch.*ix) + w./2)+hinc.*jx).*
           cos(ang+ainc.*jx) + rstart;
        y(ix+1,:) = ((rii + (pitch.*ix) + w./2)+hinc.*jx).*
           sin(ang+ainc.*jx) + rstart;
        %rii = rii+pitch;
    end
    xm = x./1e-3;
    ym = y./1e-3;
    (x(idx,:)./1e-3)';
    (x(2,1)./1e-3)';

    %%%%% Get segment lengths %%%%%%

    for gx = 1:1:Nt(idx)
        for sx = 1:1:(ppr);
            dx(gx,sx) = x(gx,sx+1) - x(gx,sx);
            dy(gx,sx) = y(gx,sx+1) - y(gx,sx);
            lseg(gx,sx) = sqrt((dx(gx,sx)).^2 + (dy(gx,sx))
               .^2);
            seg(gx) = length(lseg(gx,:));
        end
        Lturn(gx) = sum(lseg(gx,:));

    end
```

```
        Lfirst(idx) = Lturn(1);
        Llast(idx) = Lturn(Nt(idx));
126     Ltot(idx) = sum(Lturn);

        Leff(idx) = Ltot(idx) - (Lfirst(idx) + Llast(idx))./8;

        %%%% Self inductance
131     L1t(idx) = mu.*Nt(idx).^2*Davgt./2.*(log(2.46./ppt)
           +0.2.*ppt.^2);

        %%%% spiral area
        Lareat(idx) = 0.45.*Ltot(idx).*w;

136     %%%% Resistance
        RdC = Ltot(idx)./conductivity./lt./w;
        RdCC(idx) = RdC;


141     FitCoeff = 20.*ri+0.78;
        %%%% Capacitance
        CparAir(idx) = eo.*Leff(idx)./(Nt(idx)).^(FitCoeff);
        CparTefx(idx) = erPTFE.*(1-j.*lossPTFE).*CparAir(idx);
        CoveTefx(idx) = eo*erPTFE.*(1-j.*lossPTFE).*Lareat(idx)
           /gapPTFE106; %%% Batch 106
146
    end
    CparAirm = CparAir';
    CparTefxm = CparTefx';
    CoveTefxm = CoveTefx';
151 Lmm = L1t';

    Rself = RdCC';
    wcritSelf = 3.1.*(s+w)./mu./w.^2.*Rss;

156 %%%%%%%%%%%%%%%%%%%%%%%%%%%%%%%%%%%%%%%%%%%%%%%%%%%%%%%%
    CplateTef = eo.*erPTFE.*(1-j.*lossPTFE).*PlateAreaTef./
       gapPTFE106;
    CplateAir = eo.*PlateAreaTef./gapPTFE106;
    Cove = CoveTefx+CplateTef;

161 CeqTef = CparTefx + 0.5.*Cove;
    CeqTefm = CeqTef';
    Leq = L1t.*(1.85);
    FoCalc = 1./2./pi./sqrt(L1t.*(1.85).*real(CeqTef));
    Fom = FoCalc';
166
    RtanD = real(1./(2.*pi.*FoCalc.*j.*CeqTef));
    RtanDxx = RtanD';
```

```
%%%% From Kuhn
wcrit = 3.1.*(s+w)./mu./w.^2.*Rss;
Reff = RdCC.*(1+(2.*pi.*FoCalc).^2./10./wcrit.^2);
Rss = RdCC';
Rfo = Reff';

xx = real(CparTefx).*L1t;
xw = 2.*pi.*FoCalc;
ReffwithF = Reff./(1-2.*xx.*xw.^2+(xx.*xw).^2+xx.^2.*xw.^4)
    ;
ReffwithFreq = ReffwithF';

Rtot = ReffwithF+RtanD;  %used for Q calulation not Z1
Rtotm = Rtot';

QoCalc = 2.*pi.*FoCalc.*Leq./Rtot;
Qm = QoCalc';
```

Listing 1: (Element091707SelfCapMF.m) The matlab algorithm in MATLAB

D.2 Analytical Model for LTCC Pressure Sensors

In Listing 2,

```
%%  M40-1 Calculations

clc
clear all

%%%%%%%%%%%%%%%%%%%%%%%%%%%%%%%%%%%
%%%%%%%% Read in Data
mdata = dlmread('EmbeddedCircLTCC 25C.txt','\t',2,0);
freqdata=mdata(:,1);
magdata=mdata(:,2);
phasedata=mdata(:,3);
ComplexData=magdata.*exp(j.*phasedata.*pi./180);

%%% Cu electrical properties %

Rsheet = 3.3e-3; %mOhm/sqr.
resistivity = Rsheet.*9e-6; %ohms-m
conductivity = 1./resistivity;

%%% Input
```

```
mu = 4*pi*1e-7;
eo = 8.854e-12;

freqmodel = (10e6:0.01e6:30e6)'; %freqdata+5e6;
fo = freqmodel;

omega=2.*pi.*fo;
SkinDepth = sqrt(2./omega./mu./conductivity);
erAl = 9;
lossAl = 0.0001;
erLTCC = 7.8;
lossLTCC = 0.014;

f=freqdata;

w = 300e-6;
s = 600e-6;
pitch = w+s;
ls = s;
n = 9;
ppr = 60;
t = 16e-6;
lt = t;
tLTCC = 95e-6;
tm1 = 2.*tLTCC;
tm2 = tLTCC;
di = 220e-6;
tgap = 4.*tLTCC;
teff = SkinDepth.*(1-exp(-t./SkinDepth));
weff = SkinDepth.*(1-exp(-w./SkinDepth));
%%%% Mechanical model
syms Pvar wo1 wo2
v = 0.17;
E = 152e9;
a = 4.2e-3.*0.85; %3.35e-3;%4.76e-3;
a1 = a+0.4e-3;
Pnum = (0:5e3:6e5).';

ri = 4.19e-3;
Din = ri*2;
Dout = (ri+(w+s)*n+w)*2;
rd = ri+(w+s)*n/2+w;
pd = n*w+(n-1)*s;
D = 2*rd;
Davg = 0.5*(Dout+Din);
pp = (Dout - Din)/(Dout + Din);

```

```
%%%%%%%%%%%%%%%%%%%%%%%%%%%%%%%%
%%%%%%%%%%%%%%%%%%%
```

```
        Lfirst(idx) = Lturn(1);
        Llast(idx) = Lturn(Nt(idx));
117     Ltot(idx) = sum(Lturn);


        Leff(idx) = Ltot(idx) - (Lfirst(idx) + Llast(idx))./8;

122     %%%% Self inductance
        Ls2(idx) = mu.*Nt(idx).^2*Davgt./2.*(log(2.46./ppt)
           +0.2.*ppt.^2);

        %%%% spiral area
        Lareat(idx) = 0.45.*Ltot(idx).*w;
127
        %%%% Resistance
        RdC = Ltot(idx)./conductivity./lt./w;
        RdCC(idx) = RdC;


132
        FitCoeff = 20.*ri+0.78;
        %%%% Capacitance
        CparAir(idx) = eo.*Leff(idx)./(Nt(idx)).^(FitCoeff);
        Cpar(idx) = erLTCC.*(1-j.*lossLTCC).*CparAir(idx);
137     CoveL(idx) = eo*erLTCC.*(1-j.*lossLTCC).*Lareat(idx)/
           tgap; %%% Batch 106


    end

142 CparAirm = CparAir';
    Cparm = Cpar';
    Covem = CoveL';
    Lmm = Ls2';

147 %%%%%%%%%%%%%%%%%%%%%%%%%%%%%%%%%%%%%%%%%%%%%%%%%%%%%%%%%%%%%%%%%%%%%%%
    %%%%%%% Circuit Element calculations
    Cplate = eo.*pi.*ri.^2./(tgap+tm1./(erLTCC.*(1-j.*lossLTCC)
       )./2)+(eo.*erLTCC.*(1-j.*lossLTCC).*pi.*(a1.^2-a.^2)./(
       tm1./2+tgap));

    %%%% Mechanical model
152 do1 = 3.*Pvar.*(1 - v.^2).*a.^4./(16.*E.*tm1.^4) - wo1./tm1
        - 0.488.*wo1.^3./tm1.^3;
    do2 = 3.*Pvar.*(1 - v.^2).*a.^4./(16.*E.*tm2.^4) - wo2./tm2
        - 0.488.*wo2.^3./tm2.^3;

    wo_roots1 = solve(do1,wo1);
```

```
wo_roots2 = solve(do2,wo2);
wo_1 = real(subs(wo_roots1(1),Pvar,Pnum));
wo_2 = real(subs(wo_roots2(1),Pvar,Pnum));

gamma = (wo_1 + wo_2 + di)./(tgap+tm1./erLTCC./2);
Cp = Cplate./sqrt(gamma).*atanh(sqrt(gamma));

Cplate0 = Cp(1);

%%%%% New R from Sieiro et all
RdC = Ltot./conductivity./t./w;
%%%%% From Kuhn
Rss = Rsheet;
wcrit = 3.1.*(s+w)./mu./w.^2.*Rss;
Reff = RdC.*(1+1./10.*(2.*pi.*fo./wcrit).^2);

Reff(1);
%%%%%%%%%%%%%%%
km = 0.85;
Lm = Ls2.*km;
Csub = 0;

Cove = CoveL+Cplate0;
Ceq = 2.*Cove+Cpar+Csub;
CeqP = 2.*(CoveL+Cp)+Cpar+Csub;
Leq = Ls2+Lm;
k = 0.15660;
La = 0.876e-6;
M = k.*sqrt(La*Ls2);
R = 10.38;
phase0=0.5;

s = j.*2.*pi.*freqmodel;


fcal = 1./2./pi./sqrt(real(Ceq).*Leq)
fcalP = 1./2./pi./sqrt(real(CeqP).*Leq);

ReffatF = RdC.*(1+(2.*pi.*fcal).^2./10./wcrit.^2);
RtanD = real(1./(2.*pi.*fcal.*j.*Ceq));

xx = real(Cpar).*Ls2;
xw = 2.*pi.*fcal;
ReffwithF = ReffatF./(1-2.*xx.*xw.^2+(xx.*xw).^2+xx.^2.*xw
   .^4);

R = ReffwithF;
Qcal1 = fcal.*2.*pi.*Leq./(R+RtanD)
```

```
Qcal2 = fcal.*2.*pi.*Ls2./(R+RtanD);

Zin = La.*s-(2.*Ceq.*M.^2.*s.^3./(1+Ceq.*R.*s+Ceq.*Leq.*s
   .^2));

Zin1=((freqmodel./fcal).^2./(1-(freqmodel./fcal).^2+j.*
   freqmodel./fcal./Qcal1));
Zin2=La.*2.*pi.*freqmodel.*j.*(1+k.^2.*(2./(1+km)).*Zin1);
ZmagModeEQ=abs(Zin2);
ZphaseModeEQ=angle(Zin2).*180./pi-phase0;

ZmagModel=abs(Zin);
ZphaseModel=angle(Zin).*180./pi-phase0;
Qzin = imag(Zin)./real(Zin);
figure(2)
plot(freqmodel,ZphaseModel,freqmodel,ZphaseModeEQ,'--',
   freqdata,phasedata,'.')

%%%%%%%%%%%%%%%%%%%%%%%%%%%%%%%%%%
%%%%%%%% Define Model\
ki=0.1;
qi=38;
L11=1.150e-6;
phase0=0.5; %5;
omega=freqdata.*2.*pi;
omegamod = freqmodel.*2.*pi;
freq0=16e6;
omega0=freq0.*2.*pi;

Z1=((omega./omega0).^2./(1-(omega./omega0).^2+j.*omega./
   omega0./qi));
Z2=L11.*omega.*j.*(1+ki.^2.*Z1);
Zmag=abs(Z2);
Zphase=angle(Z2).*180./pi-phase0;
%%%%%

mymagfun=@(x) abs(x(4).*omega.*j.*(1+x(1).^2.*((omega./x(2)
   ).^2./(1-(omega./x(2)).^2+j.*omega./x(2)./x(3)))));
myphasefun=@(x) angle(x(4).*omega.*j.*(1+x(1).^2.*((omega./
   x(2)).^2./(1-(omega./x(2)).^2+j.*omega./x(2)./x(3))))
   .*180./pi-phase0;
myerrorfun=@(x)std(phasedata-angle(x(4).*omega.*j.*(1+x(1)
   .^2.*((omega./x(2)).^2./(1-(omega./x(2)).^2+j.*omega./x
   (2)./x(3))))).*180./pi-phase0);
myerrorfunMag=@(x)std(phasedata-abs(x(2).*omega.*j.*(1+x(1)
   .^2.*((omega./freq0).^2./(1-(omega./freq0).^2+j.*omega./
   freq0./qi)))));
```

```
myerrorfunModel=@(x)std(ZphaseModel-angle(x(4).*omegamod.*j
   .*(1+x(1).^2.*(2./(1+km)).*((omegamod./x(2)).^2./(1-(
   omegamod./x(2)).^2+j.*omegamod./x(2)./x(3))))).*180./pi-
   phase0);


[x,fval,exitflag,output]=fminsearch(myerrorfun,[ki,omega0,
   qi,L11],optimset('MaxFunEval',10000,'MaxIter',1500));
xi2=x;
[x,fval,exitflag,output]=fminsearch(myerrorfun,xi2,optimset
   ('MaxFunEval',10000,'MaxIter',1500));

%[x,fval,exitflag,output]=fminsearch(myerrorfun,[ki,omega0,qi],optimset('
   MaxFunEval',10000,'MaxIter',1500))

xData = x;
x(1)
foData = x(2)./2./pi./1e6
x(3)
x(4)
fminData = foData.*(1+x(1).^2./4+1./8./x(3).^2);
fminH = (fminData-foData)./foData.*100;

MagDataFit = mymagfun([0.1566,(16.5184e6.*2.*pi)
   ,36.0611,0.876e-6]);
PhaseDataFit = myphasefun(xData);

[x,fval,exitflag,output]=fminsearch(myerrorfunModel,xData,
   optimset('MaxFunEval',10000,'MaxIter',1500));

xModel = x;
x(1)
x(2)./2./pi./1e6
x(3)
x(4)


figure(3)
plot(freqmodel,ZphaseModel,'-k',f,myphasefun(abs(xData)),'-
   r',f,phasedata);
%plot(f,myphasefun(abs(xData)),'-r',f,phasedata);
%figure(4)
%plot(f,myphasefun(abs(xData)))
figure(5)
plot(freqmodel,ZmagModel,'--',freqmodel,ZphaseModel,f,
   magdata,f,phasedata)
%%%%%%%%%%%%%%%%%%%%%%%%%%%%%%%%%%%%%%%%%%%%%%%%%%%%%%%%%%%%%%%%%%%%%%%%
```

```
erT = [7.83 7.93 7.96 8.05 8.17 8.44 8.9 9.09 9.64 10.39
   11.45 13.01]';
Temp = [25 102 154 203 255 307 378 401 454 501 552 600]';
DTemp = Temp-25;
tandT = [.0140 .0172 .0184 .0209 .0238 .0312 .0474 .055
   .0769 .1055 .1487 .2068]';
Temps = (25:5:600)';
erTs = 9.2373e-11.*Temps.^4-6.6154e-8.*Temps.^3+2.3848e-5.*
   Temps.^2-1.9667e-3.*Temps+7.886;
tandTs = 2.6125e-12.*Temps.^4-1.1899e-9.*Temps.^3+3.1083e
   -7.*Temps.^2-2.7638e-6.*Temps+1.427e-2;
DTemps = Temps-25;

resisT = resistivity.*(1+0.0031.*DTemps);
conducT = 1./resisT;

CparTemp = CparAirm.*erTs.*(1-j.*tandTs);
CplateTemp = eo.*pi.*ri.^2./(tgap+tm1./(erTs.*(1-j.*tandTs)
   )./2)+(eo.*erTs.*(1-j.*tandTs).*pi.*(a1.^2-a.^2)./(tm1
   ./2+tgap));

gammaT = (di)./(tgap+tm1./erTs./2);
CpT = CplateTemp./sqrt(gammaT).*atanh(sqrt(gammaT));
Cplate0T = CpT(1);

CoveLTemp = eo*erTs.*(1-j.*tandTs).*Lareat./tgap;
CoveTemp = CoveLTemp+Cplate0T;
CeqTemp = 2.*CoveTemp+CparTemp+Csub;

fcalTemp = 1./2./pi./sqrt(real(CeqTemp).*Leq);

RdCT = Ltot./conducT./t./w;
ReffatFTemp = RdCT.*(1+(2.*pi.*fcalTemp).^2./10./wcrit.^2);
RtanDT = real(1./(2.*pi.*fcalTemp.*j.*CeqTemp));

xx = real(Cpar).*Ls2;
xz = real(Cpar).*RdCT;
xw = 2.*pi.*fcalTemp;
ReffwithFT = ReffatFTemp./(1-2.*xx.*xw.^2+(xz.*xw).^2+xx
   .^2.*xw.^4);

RTemp = ReffwithFT+RtanDT;

QcalTemp = fcalTemp.*2.*pi.*Leq./(RTemp);
QcallossT = fcalTemp.*2.*pi.*Leq./(ReffwithF+RtanDT);
QcalresisT = fcalTemp.*2.*pi.*Leq./(ReffwithFT+RtanD);

xinit = xModel;
```

```
figure(11)
plot(Temps,fcalTemp);
figure(12)
plot(Temps,QcalTemp);
figure(13)
plot(Temps,tandTs);
figure(14)
plot(Temps,erTs);
```

Listing 2: (EmbeddedCircLTCCmf092307.m) The matlab algorithm in MATLAB

REFERENCES

[1] W. Merrill, "Commercialization of harsh environment microsystems -existing challenges," in *Proc. IEEE Sensors. First IEEE International Conference on Sensors*, vol. 2, 2002, pp. 1105–1108.

[2] R. W. Johnson, J. L. Evans, P. Jacobsen, J. R. Thomson, and M. Christopher, "The changing automotive environment: High-temperature electronics," *IEEE Trans. Electron. Packag. Manufact.*, vol. 27, no. 3, pp. 164–176, July 2004.

[3] S. J. Prosser, "Advances in sensors for aerospace applications," in *Proc. EUROSENSORS VI Sensors and Actuators, A: Physical*, San Sebastian, Spain, Oct. 1992, pp. 128–134.

[4] T. George, K. A. Son, R. A. Powers, L. Y. D. Castillo, and R. Okojie, "Harsh environment microtechnology for NASA and terrestrial applications," in *Proc. IEEE Sensors*, Irvine, CA, USA, Oct. 2005, pp. 1253–1258.

[5] J. M. English, "Wireless Micromachined Ceramic Pressure Sensors for High Temperature Environments," Ph.D. dissertation, Georgia Institute of Technology, Atlanta, GA, USA, 2000.

[6] M. R. Werner and W. R. Fahrner, "Review on Materials, Microsensors, Systems, and Devices for High-Temperature and Harsh-Environment Applications," *IEEE Trans. Ind. Electron.*, vol. 48, Apr. 2001.

[7] J.-M. Stauffer, "Market Opportunities for Advanced MEMS Accelerometer and Overview of Actual Capabilities vs. Required Specifications," in *Proc. IEEE PLANS Position Location and Navigation Symposium*, Monterey, CA, USA, Apr. 2004, pp. 78–82.

[8] K. Petersen, J. Brown, T. Vermeulen, P. Barth, J. J. Mallon, and J. Bryzek, "Ultrastable, High-temperature Pressure Sensors using Silicon Fusion Bonding," in *Proc. Transducers '89 Sensors and Actuators, A: Physical*, vol. 2, Montreux, Switzerland, June 1990, pp. 96–101.

[9] Z. Yulong, Z. Libo, and J. Zhuangde, "A novel high temperature pressure sensor on the basis of SOI layers," *Sensors and Actuators, A: Physical*, vol. 108, pp. 108–111, Nov. 2003.

[10] L. Toygur, X. Yu, and S. Garverick, "High-Temperature, Low-Power 8-MegΩ by 1.2 MegHz SOI-CMOS Transimpedance Amplifier for MEMS-Based Wireless Sensors," in *Proc. IEEE Int. SOI Conf.*, Charleston, NC, USA, Oct. 2004, pp. 179–181.

[11] M. Suster, W. H. Ko, and D. J. Young, "An Optically Powered Wireless Telemetry Module for High-Temperature MEMS Sensing and Communication," *J. MEMS.*, vol. 13, no. 3, June 2004.

[12] J. Xu, G. R. Pickrell, X. Wang, B. Yu, K. L. Cooper, and A. Wang, "Vacuum-sealed high temperature high bandwidth fiber optic pressure and acoustic sensors," in *Proc. of SPIE Sensors for Harsh Environments*, vol. 5998, 2005.

[13] W. Pullman, P. Russler, R. Mlcak, K. Murphy, and C. Kozikowski, "Micromachined, SiC fiber optic pressure sensor for high-temperature aerospace applications," in *Proc. of SPIE Sensors for Harsh Environments*, vol. 4202, 2000.

[14] Y. Zhu, K. L. Cooper, G. R. Pickrell, and A. Wang, "High-Temperature Fiber-Tip Pressure Sensor," *J. Lightwave Technology*, vol. 24, no. 2, Feb. 2006.

[15] R. S. Okojie, A. A. Ned, A. D. Kurtz, and W. N. Carr, "α(6H)-SiC Pressure Sensors at 350 ℃," *Int. Electron Devices Meeting, Technical Digest*, pp. 525–528, 1996.

[16] A. A. Ned, R. S. Okojie, and A. D. Kurtz, "6H-SiC Pressure Sensor Operating at 600 ℃," in *Proc. HITEC Fourth Int. High Temperature Electronics Conference*, 1998, pp. 257–260.

[17] E. Savrun, "Packaging Considerations for Very High Temperature Mircosystems," in *Proc. IEEE Sensors*, vol. 2, 2002, pp. 1139–1143.

[18] S. Dakshinamurthy, N. R. Quick, and A. Kar, "SiC-based optical interferometry at high pressure and temperature for pressure and chemical sensing," *J. Applied Physics*, vol. 99, 2006.

[19] J. M. English and M. G. Allen, "Wireless micromachined ceramic pressure sensors," in *Proc. of the Twelfth IEEE Microelectromechanical Systems Conference*, 1999, pp. 511–516.

[20] G. H. Kroetz, M. H. Eickhoff, and H. Moeller, "Silicon compatible materials for harsh environment sensors," *Sensors and Actuators*, vol. 74, pp. 182–189, 1999.

[21] K. Kasten, J. Amelung, and W. Mokwa, "CMOS-compatible capacitive high temperature pressure sensors," *Sensors and Actuators*, vol. 85, pp. 147–152, 2000.

[22] G. W. Hunter, P. G. Neudeck, R. S. Okojie, G. M. Beheim, J. A. Power, and L. Chen, "An Overview of High-Temperature Electronics and Sensor Development at NASA Glen Research Center," *Transactions of the ASME*, vol. 125, pp. 658–664, Oct. 2003.

[23] C. C. Collins, "Miniature passive pressure transensor for implantation in the eye," *IEEE Trans. Biomed. Eng.*, vol. 14, no. 2, pp. 74–83, Apr. 1967.

[24] Y. Bácklund, L. Rosengren, and B. Hök, "Passive silicon transensor intended for biomedical, remote pressure monitoring," *Sensors and Actuators*, vol. 21-23, pp. 58–61, 1990.

[25] L. Rosengren, Y. Bácklund, T. Sjöström, and B. Svedbergh, "A system for wireless intra-ocular pressure measurement using a silicon micromachined sensor," *J. Micromech. Microeng.*, vol. 2, pp. 202–204, 1992.

[26] L. Rosengren, P. Rangsten, and B. Hök, "A system for passive implantable pressure sensors," *Sensors and Actuators*, vol. 43, pp. 55–58, 1994.

[27] K. Schuylenbergh and R. Puers, "Passive telemetry by harmonic detection," in *Proc. IEEE 18th Annual Int. Conference of EMBS*, 1996, pp. 299–300.

[28] S. Ullerich, G. v. B. W. Mokwa, and U. Schnakenberg, "Micro coils for an advanced system for measuring intraocular pressure," in *Proc. IEEE 1st Annual Int. Conference of EMBS Special Topics*, 2000, pp. 470–474.

[29] R. Puers, G. Vandevoorde, and D. D. Bruyker, "Electrodeposited copper inductors for intraocular pressure telemetry," *J. Micromech. Microeng.*, vol. 10, pp. 124–129, 2000.

[30] U. Schnakenberg, P. Walter, G. vom Bögel, C. Krüger, H. C. Lüdtke-Handjery, H. A. Richter, W. Specht, P. Ruokonen, and W. Mokwa, "Initial investigation on systems for measuring intraocular pressure," *Sensors and Actuators*, vol. 85, pp. 287–291, 2000.

[31] T. Eggers, J. Draeger, K. Hille, C. Marschner, P. Stegmaier, J. Binder, and R. Laur, "Wireless intra-ocular pressure monitoring system integrated into an artifical lens," in *Proc. IEEE 1st Annual Int. Conference of EMBS Special Topics*, 2000, pp. 466–469.

[32] J. Coosemans, M. Catrysse, and R. Puers, "A readout circuit for an intra-ocular pressure sensor," *Sensors and Actuators*, vol. 110, pp. 432–438, 2004.

[33] S. L. Martínez, J. L. R. M. R. Giannetti, and B. Tellini, "Design of a system for continuous intraocular pressure monitoring," *IEEE Trans. Instrum. Meas.*, vol. 54, no. 4, pp. 1534–1540, 2005.

[34] U. Schnakenberg, C. Krüger, J.-G. Pfeffer, W. Mokwa, G. vom Bögel, R. Günther, and T. Schmitz-Rode, "Intravascular pressure monitoring system," *Sensors and Actuators*, vol. 110, pp. 61–67, 2004.

[35] N. Najafi and A. Ludomirsky, "Initial Animal Studies of a Wireless, Batteryless, MEMS Implant for Cardiovascular Applications," *Biomedical Microdevices, 6:1*, pp. 61–65, 2004.

[36] T. Salo, K.-U. Kristein, J. Šedivý, J. Grünenfelder, T. Vancura, G. Zünd, and H. Baltes, "Continuous blood pressure monitoring utilizing a CMOS tactile sensor," in *Proc. IEEE EMBS of the 26th Annual Int.*, 2004, pp. 2326–2329.

[37] P. Cong, D. J. Young, and W. H. Ko, "Novel long-term implantable blood pressure monitoring system," in *Proc. IEEE Sensors*, vol. 3, 2004, pp. 1359–1362.

[38] A. DeHennis and K. Wise, "A double-sided single-chip wireless pressure sensor," in *Digest MEMS Fifthteen MEMS Int. Conference*, 2002, pp. 252–255.

[39] R. S. Mackay and B. Jacobson, "Endoradiosonde," *Nature*, vol. 179, pp. 1239–1240, June 1957.

[40] J. T. Farrar, V. K. Zworykin, and J. Baum, "Pressure-sensitive telemetering capsule for study of gastrointestinal motility," *Science*, vol. 126, pp. 975–976, Nov. 1957.

[41] A. Arshak, K. Arshak, D. Waldron, D. Morris, O. Korostynska, E. Jafer, and G. Lyons, "Review of the potential of a wireless MEMS and TFT microsystem for the measurement of pressure in the GI tract," *Medical Engineering and Physics*, vol. 27, pp. 347–356, 2005.

[42] J. Coosemans and R. Puers, "An autonomous bladder pressure monitoring system," *Sensors and Actuators*, vol. 123-124, pp. 155–161, 2005.

[43] C. Hierold, B. Clasbrummel, D. Behrend, T. Schieter, M. Steger, K. Oppermann, H. Kapels, E. Landgraf, D. Wenzel, and D. Etzrodt, "Implantable low power integrated pressure sensors system for minimally invasive telemetric patient monitoring," in *Proc. IEEE 11th Annual Int. Workshop in MEMS*, Heidelberg, Germany, Jan. 1998, pp. 586–573.

[44] J. F. L. Goosen, D. Tanase, and P. J. French, "Silicon sensors for use in catheters," in *Proc. IEEE 1st Annual Int. EMBS Special Topic Conference on Microtechnologies in Medicine and Biology*, 2000, pp. 152–155.

[45] P. Holejšovská, Z. Peroutka, and J. Cengery, "Non-invasive monitoring of the human blood pressure," in *Proc. IEEE 16th Symposium on Computer-Based Medical Systems CBMS*, 2003, pp. 301–306.

[46] M. G. Allen, "Micromachined endovascularly-implantable wireless aneurysm pressure sensors: From concept to clinic," in *Proc. The 13th Int. Conference on Solid-State Sensors, Actuators and Microsystems. Digest of Technical Papers*, vol. 1, 2005, pp. 275–278.

[47] R. Puers, "Linking sensors with telemetry: impact on the system design," *Sensors and Actuators*, vol. 52, pp. 169–174, 1996.

[48] J. A. D. Romig, M. T. Dugger, and P. J. McWhorter, "Materials issues in microelectromechanical devices: science, engineering, manufacturability and reliability," *Acta Materialia*, vol. 51, no. 19, pp. 5837–5866, Nov. 2003.

[49] O. Akar, T. Akin, and K. Najafi, "A wireless batch sealed capacitive pressure sensor," *Sensors and Actuators*, vol. 95, pp. 29–38, 2001.

[50] K.-H. Shin, C.-Y. Moon, T.-H. Lee, C.-H. Lim, and Y.-J. Kim, "Implantable flexible wireless pressure sensor module," *Sensors and Actuators*, vol. 123-124, pp. 30–35, 2005.

[51] J. C. Butler, A. J. Vigliotti, F. W. Verdi, and S. M. Walsh, "Wireless, passive, resonant-circuit, inductively coupled, inductive strain sensor," *Sensors and Actuators*, vol. 102, pp. 61–66, 2002.

[52] A. Baldi, W. Choi, , and B. Ziaie, "Wireless, passive, resonant-circuit, inductively coupled, inductive strain sensor," *IEEE Sensors J.*, vol. 3, no. 6, Dec. 2003.

[53] M. Husák, "One-chip integrated resonance circuit with a capacitive pressure sensor," *J. Micromech. and Microeng.*, vol. 7, pp. 173–178, 1997.

[54] K. G. Ong, C. A. Grimes, C. L. Robbins, and R. S. Singh, "Design and application of a wireless, passive, resonant-circuit environmental monitoring sensor," *Sensors and Actuators*, vol. 93, pp. 33–34, 2001.

[55] K. G. Ong and C. A. Grimes, "A resonant printed-circuit sensor for remote query monitoring of environmental parameters," *Smart Mater. Struct.*, vol. 9, pp. 421–428, 2000.

[56] T. J. Harpster, B. Stark, and K. Najafi, "A passive wireless integrated humidity sensor," in *Proc. IEEE Digest. 14th Int.Conference on MEMS*, 2001, pp. 553–557.

[57] T. J. Harpster, S. Hauvespre, M. R. Dokmeci, and K. Najafi, "A passive humidity monitoring system for in situ remote wireless testing of micropackages," *J. MEMS.*, vol. 11, no. 1, Feb. 2002.

[58] K. G. Ong, J. Wang, R. S. Singh, L. G. Bachas, and C. A. Grimes, "Monitoring of bacteria growth using a wireless, remote query resonant-circuit sensor: application to environmental sensing," *Biosensors and Bioelectronics*, vol. 16, pp. 305–312, 2001.

[59] K. Takahata, A. DeHennis, K. D. Wise, and Y. B. Gianchandani, "A wireless microsensor for monitoring flow and pressure in a blood vessel utilizing dual-inductor antenna stent and two pressure sensors," in *Proc. IEEE of the 17th Int. Conference on MEMS*, 2004, pp. 216–219.

[60] R. N. Simons, D. G. Hall, and F. A. Miranda, "RF telemetry system for an implantable Bio-MEMS sensor," in *Proc. IEEE MTT-S International Microwave Symposium Digest*, vol. 3, 2004, pp. 1433–1436.

[61] ——, "Spiral chip implantable radiator and printed loop external receptor for RF telemetry in bio-sensor systems," in *Proc. IEEE Radio and Wireless Conference*, 2004, pp. 203–206.

[62] W. N. Carr, S. Chamarti, and X. Gu, "Integrated pressure sensor with remote power source and remote readout," in *Proc. IEEE 18th Int. Conf. on Solid-State Sensors and Actuators and Eurosensors IX*, vol. 1, Stockholm, Sweeden, June 1994, pp. 624–627.

[63] K. L. Su, *Fundamentals of Circuits, Electronics, and Signal Analysis.* Houghton Mifflin Company, 1978, pp. 587–614.

[64] K. Pham, K. Okada, and K. Masu, "Quality factor enhancement of on-chip inductor by using negative impedance circuit," *2006 Topical Meeting on Silicon Monolithic Integrated Circuits in RF Systems (IEEE Cat. No.06EX1204)*, pp. 4 pp. –, 2006.

[65] H. Greenhouse, "Design of planar rectangular microelectronic inductors," *IEEE Trans. Parts Hybrids Packag. (USA)*, vol. PHP-10, no. 2, pp. 101 – 9, 1974/06/.

[66] J. Hizon, M. Rosales, L. Alarcon, and I. Sabido, D.J., "Characterization of monolithic spiral inductors on a 0.25 um digital cmos process," *TENCON 2004. 2004 IEEE Region 10 Conference (IEEE Cat. No. 04CH37582)*, vol. Vol. 4, pp. 360 – 3, 2004.

[67] C. Yue and S. Wong, "Physical modeling of spiral inductors on silicon," *IEEE Trans. Electron Devices (USA)*, vol. 47, no. 3, pp. 560 – 8, 2000/03/.

[68] C. Yue, C. Ryu, J. Lau, T. Lee, and S. Wong, "A physical model for planar spiral inductors on silicon," *International Electron Devices Meeting. Technical Digest (Cat. No.96CH35961)*, pp. 155 – 8, 1996.

[69] A. Telli, I. Demir, and M. Askar, "Planar spiral inductor modeling for RFIC designs," *International Conference on VLSI - VLSI 2003*, pp. 138 – 42, 2003.

[70] J. Lescot, J. Haidar, and F. Ndagijimana, "Accurate and fast modeling of planar inductors in cmos technologies," *ESSDERC'99. Proceedings of the 29th European Solid-State Device Research Conference*, pp. 668 – 71, 1999.

[71] J. Park and M. Allen, "High Q spiral-type microinductors on silicon substrates," *IEEE Trans. Magn. (USA)*, vol. 35, no. 5, pp. 3544 – 6, Sept. 1999.

[72] J. Lescot, R. Ribas, F. Ndagijimana, and J. Karam, "Modeling of micromachined planar spiral inductors," *Proceedings 10th MICROCOLL*, pp. 355 – 8, 1999.

[73] S. Mohan, M. del Mar Hershenson, S. Boyd, and T. Lee, "Simple accurate expressions for planar spiral inductances," *IEEE J. Solid-State Circuits (USA)*, vol. 34, no. 10, pp. 1419 – 24, 1999/10/.

[74] R. Lutz, Y. Hahm, A. Weisshaar, V. Tripathi, A. Grzegorek, W. McFarland, and J. Meyer, "Modeling of spiral inductors on lossy substrates for RFIC applications," *1998 IEEE Radio Frequency Integrated Circuits (RFIC) Symposium. Digest of Papers (Cat. No.98CH36182)*, pp. 313 – 16, 1998.

[75] J. Crols, P. Kinget, J. Craninckx, and M. Steyaert, "An analytical model of planar inductors on lowly doped silicon substrates for high frequency analog design up to 3 ghz," *1996 Symposium on VLSI Circuits. Digest of Technical Papers (IEEE Cat. No.96CH35943)*, pp. 28 – 9, 1996.

[76] A. Balakrishnan, W. Palmer, W. Joines, and T. Wilson, "The inductance of planar structures," *APEC '93. Eighth Annual Applied Power Electronics Conference and Exposition. Conference Proceedings 1993 (Cat. No.93CH3271-4)*, pp. 912 – 21, 1993.

[77] W. Mo, D. Cheng, and Y. Lee, "Design and analysis of planar inductors," *IAS '95. Conference Record of the 1995 IEEE Industry Applications Conference. Thirtieth IAS Annual Meeting (Cat. No.95CH35862)*, vol. vol.1, pp. 817 – 23, 1995.

[78] W. Kuhn and N. Ibrahim, "Approximate analytical modeling of current crowding effects in multi-turn spiral inductors," *2000 IEEE MTT-S International Microwave Symposium Digest (Cat. No.00CH37017)*, vol. vol.1, pp. 405 – 8, 2000.

[79] S. Kythakyapuzha and W. Kuhn, "Modeling of inductors and transformers," *2001 IEEE Radio Frequency Integrated Circuits (RFIC) Symposium (IEEE Cat. No.01CH37173)*, pp. 283 – 6, 2001.

[80] W. Kuhn and N. Ibrahim, "Analysis of current crowding effects in multiturn spiral inductors," *IEEE Trans. Microw. Theory Tech. (USA)*, vol. 49, no. 1, pp. 31 – 8, 2001/01/.

[81] J. Sieiro, J. Lopez-Villegas, J. Cabanillas, and J. Samitier, "Accurate physical model for designing rf and microwave integrated planar inductors," *30th European Microwave Conference 2000. Conference Proceedings*, vol. vol.1, pp. 59 – 62, 2000.

[82] J. Cabanillas, J. Lopez-Villegas, J. Sieiro, and J. Samitier, "Analysis of rf monolithic transformers," *ESSDERC 2000. Proceedings of the 30th European Solid-State Device Research Conference*, pp. 456 – 9, 2000.

[83] J. Sieiro, J. Lopez-Villegas, J. Cabanillas, J. Osorio, and J. Samitier, "A complete physical frequency dependent lumped model for RF integrated inductors," *2001 IEEE Radio Frequency Integrated Circuits (RFIC) Symposium (IEEE Cat. No.01CH37173)*, pp. 121 – 4, 2001.

[84] ——, "A physical frequency-dependent compact model for RF integrated inductors," *IEEE Trans. Microw. Theory Tech. (USA)*, vol. 50, no. 1, pp. 384 – 92, 2002/01/.

[85] S. S. Mohan, "The Design, Modeling and Optimization of on-chip inductor and transformer circuits," Ph.D. dissertation, Stanford University, Stanford, CA, USA, 1999.

[86] F. Huang, J. Lu, and N. Jiang, "Scalable distributed-capacitance model for silicon on-chip spiral inductors," *Microwave and Optical Technology Letters*, vol. 48, no. 7, pp. 1423 – 7, 2006/07/.

[87] C.-H. Wu, C.-C. Tang, and S.-I. Liu, "Analysis of on-chip spiral inductors using the distributed capacitance model," *IEEE Journal of Solid-State Circuits*, vol. 38, no. 6, pp. 1040 – 4, 2003/06/.

[88] S. S. Mohan, C. P. Yue, M. d. M. Hershenson, S. S. Wong, and T. H. Lee, "Modeling and characterization of on-chip transformers," *Technical Digest - International Electron Devices Meeting*, pp. 531 – 534, 1998.

[89] C. H. Hsueh, C. R. Luttrell, and P. F. Becher, "Modeling of bonded multilayered disks subjected to biaxial flexure tests," *International Journal of Solids and Structures*, vol. 43, no. 20, pp. 6014–6025, Oct. 2006.

[90] S. P. Timoshenko and S. Woinowsky-Krieger, *Theory of Plates and Shells*. McGraw Hill, London, 1984.

[91] S. P. Chang, J. B. Lee, and M. G. Allen, "A robust 8x8 capacitive pressure sensor array," in *Proc. MEMS the American Society of Mechanical Engineers Winter Annual Meeting ASME*, Anaheim, CA, US, 1998, pp. 513–517.

[92] ——, "A robust capacitive pressure sensor array," in *Proc. Sensors and Actuators, A: Physical*, vol. A101, 2002, pp. 231–238.

[93] S. B. L. M. Jackson, M. Pecht and P.Sandborn. (2007, Nov.) Integral, embedded, and buried passive technolgies. [Online]. Available: http://www.calce.umd.edu/whats_new/

[94] "Green tape material system, design and layout guidelines," Dupont Applied Technologies Group, Tech. Rep., (available from E.I. Dupont Co.).

[95] (2001, Nov.) Dielectric properties of body tissue. Italian National Research Council. [Online]. Available: http://niremf.iroe.fi.cnr.it/cgi-bin/tissprop/htmlclie/uniquery

[96] J. Melcher, D. Yang, and G. Arlt, "Dielectric effects of moisture in polyimide," *IEEE Transactions on Electrical Insulation*, vol. 24, no. 1, pp. 31 – 38, 1989.

[97] (2007, June) Aortic aneurysm. [Online]. Available: http://en.wikipedia.org/wiki/Aortic_aneurysm\#Signs.2C_symptoms_and_diagnosis

[98] I. P. Casserly, R. Sachar, and J. S. Yadav, *Manual of Peripheral Vascular Intervention*. Philadelphia, PA: Lippincott Williams and Wilkins, 2005.

[99] F. J. Veith and R. A. Baum, *Endoleaks and Endotension*. New York, NY: Marcel Dekker, Inc., 2003.

[100] L. A. Sanches, P. L. Faries, M. L. Miran, T. Ohki, R. E. Parson, B. Marty, D. Soeiro, S. Olivieri, and F. J. Veith, "Chronic intraaneurysmal pressure measurement: An experimental method for evaluating the effectiveness of endovascular aortic aneurysm exclusion," *J. Vascular Surgery*, vol. 22, no. 2, pp. 222–230, Aug. 1997.

[101] P. L. Faries, L. A. Sanchez, M. L. Marin, R. E. Parsons, R. T. Lyon, S. Oliveri, and F. J. Veith, "An experimental model for the acute and chronic evaluation of intra-aneurysmal pressure," *J. Endovasc. Surg.*, vol. 4, pp. 290–297, Aug. 1997.

[102] T. Ohki, J. Yadav, N. Garuiulo, H. Kurvers, S. Rhee, F. J. Veith, and D. Stern, "Preliminary results of an implantable wireless aneurysm pressure sensor in a canine model: Will surveillance CT scan following evar become obsolete?" in *16th International Congress on Endovascular Interventions*, Phoenix, AZ (USA), Feb. 1998.

[103] J. M. Bland and D. G. Altman. (2007, Mar.) Statistical methods for assessing agreement between two methods of clinical measurement. [Online]. Available: http://www-users.york.ac.uk/\~mb55/meas/ba.htm

VITA

Michael A. Fonseca was born in Tegucigalpa, Honduras, in 1977. He received his B.S. and M.S. degrees in electrical and computer engineering at the Georgia Institute of Technology, Atlanta GA, in December of 1999 and May of 2004.

In the summer semester of 2000 he joined the Microsensros and Microactuators group under the direction of Dr. Mark Allen at the Georgia Institute of Technology, and researched wireless pressure sensors for high temperature applications. In May of 2001 he joined CardioMEMS, Inc as the second employee of the company where he directed research and development of implantable wireless pressure sensors for abdominal aortic aneurysms. Since then he has worked to develop wireless products for the medical diagnostic industry. Currently, Michael is pursuing his Ph.D. degree in Electrical and Computer Engineering at the Georgia Institute of Technology in the field of Microelectromechanical Systems (MEMS). His areas of interest are wireless pressure sensors for harsh environments such as high temperature and biomedical applications. Mr. Fonseca is a member of IEEE and Eta Kappa Nu.